Federal University of Goiás (UFG)
School of Electrical, Mechanical and Computer Engineering (EMC)
Graduate Program in Electrical and Computer Engineering

Henrique Pires Corrêa

Contributions to Modeling, Control and Integration of Photovoltaic Devices to Electrical Power Systems

Brazil

2023

Universidade Federal de Goiás (UFG)
Escola de Engenharia Elétrica, Mecânica e de Computação (EMC)
Programa de Pós-Graduação em Engenharia Elétrica e de Computação

Henrique Pires Corrêa

Contribuições à Modelagem, Controle e Integração de Dispositivos Fotovoltaicos a Sistemas Elétricos de Potência

Brasil

2023

UNIVERSIDADE FEDERAL DE GOIÁS
ESCOLA DE ENGENHARIA ELÉTRICA, MECÂNICA E DE COMPUTAÇÃO

TERMO DE CIÊNCIA E DE AUTORIZAÇÃO (TECA) PARA DISPONIBILIZAR VERSÕES ELETRÔNICAS DE TESES E DISSERTAÇÕES NA BIBLIOTECA DIGITAL DA UFG

Na qualidade de titular dos direitos de autor, autorizo a Universidade Federal de Goiás (UFG) a disponibilizar, gratuitamente, por meio da Biblioteca Digital de Teses e Dissertações (BDTD/UFG), regulamentada pela Resolução CEPEC nº 832/2007, sem ressarcimento dos direitos autorais, de acordo com a Lei 9.610/98, o documento conforme permissões assinaladas abaixo, para fins de leitura, impressão e/ou download, a título de divulgação da produção científica brasileira, a partir desta data.

O conteúdo das Teses e Dissertações disponibilizado na BDTD/UFG é de responsabilidade exclusiva do autor. Ao encaminhar o produto final, o autor(a) e o(a) orientador(a) firmam o compromisso de que o trabalho não contém nenhuma violação de quaisquer direitos autorais ou outro direito de terceiros.

1. Identificação do material bibliográfico

[ ] Dissertação [X] Tese [ ] Outro*:_____

*No caso de mestrado/doutorado profissional, indique o formato do Trabalho de Conclusão de Curso, permitido no documento de área, correspondente ao programa de pós-graduação, orientado pela legislação vigente da CAPES.

Exemplos: Estudo de caso ou Revisão sistemática ou outros formatos.

2. Nome completo do autor

Henrique Pires Corrêa

3. Título do trabalho

Contribuições à Modelagem, Controle e Integração de Dispositivos Fotovoltaicos a Sistemas Elétricos de Potência

4. Informações de acesso ao documento (este campo deve ser preenchido pelo orientador)

Concorda com a liberação total do documento [X] SIM [ ] NÃO[1]

[1] Neste caso o documento será embargado por até um ano a partir da data de defesa. Após esse período, a possível disponibilização ocorrerá apenas mediante:
a) consulta ao(à) autor(a) e ao(à) orientador(a);
b) novo Termo de Ciência e de Autorização (TECA) assinado e inserido no arquivo da tese ou dissertação.
O documento não será disponibilizado durante o período de embargo.
Casos de embargo:
- Solicitação de registro de patente;
- Submissão de artigo em revista científica;
- Publicação como capítulo de livro;
- Publicação da dissertação/tese em livro.

Obs. Este termo deverá ser assinado no SEI pelo orientador e pelo autor.

Documento assinado eletronicamente por **Henrique Pires Corrêa**, **Discente**, em 06/11/2023, às 19:44, conforme horário oficial de Brasília, com fundamento no § 3º do art. 4º do Decreto nº 10.543, de 13 de novembro de 2020.

Documento assinado eletronicamente por **Flavio Henrique Teles Vieira**, **Professor do Magistério Superior**, em 06/11/2023, às 23:05, conforme horário oficial de Brasília, com fundamento no § 3º do art. 4º do Decreto nº 10.543, de 13 de novembro de 2020.

A autenticidade deste documento pode ser conferida no site https://sei.ufg.br/sei/controlador_externo.php?acao=documento_conferir&id_orgao_acesso_externo=0, informando o código verificador **4174901** e o código CRC **E784C0BC**.

Henrique Pires Corrêa

Contributions to Modeling, Control and Integration of Photovoltaic Devices to Electrical Power Systems

Thesis presented to the Graduate Program in Electrical and Computer Engineering of the School of Electrical, Mechanical and Computer Engineering of the Federal University of Goiás (UFG), in fulfillment of the requirements for the degree of Doctor in Electrical and Computer Engineering.
Concentration area: Computer Engineering

Federal University of Goiás

School of Electrical, Mechanical and Computer Engineering

Graduate Program in Electrical and Computer Engineering

Supervisor: Prof. Dr. Flávio Henrique Teles Vieira

Brazil

2023

Henrique Pires Corrêa

Contribuições à Modelagem, Controle e Integração de Dispositivos Fotovoltaicos a Sistemas Elétricos de Potência

Tese apresentada ao Programa de Pós-Graduação em Engenharia Elétrica e de Computação, da Escola de Engenharia Elétrica, Mecânica e de Computação, da Universidade Federal de Goiás (UFG), como requisito para obtenção do título de Doutor em Engenharia Elétrica e de Computação.
Área de concentração: Engenharia de Computação

Universidade Federal de Goiás

Escola de Engenharia Elétrica, Mecânica e de Computação

Programa de Pós-Graduação em Engenharia Elétrica e de Computação

Orientador: Prof. Dr. Flávio Henrique Teles Vieira

Brasil

2023

Ficha de identificação da obra elaborada pelo autor, através do
Programa de Geração Automática do Sistema de Bibliotecas da UFG.

Corrêa, Henrique Pires
Contribuições à Modelagem, Controle e Integração de Dispositivos Fotovoltaicos a Sistemas Elétricos de Potência [manuscrito] / Henrique Pires Corrêa. - 2023.
239 f.

Orientador: Prof. Dr. Flávio Henrique Teles Vieira.
Tese (Doutorado) - Universidade Federal de Goiás, Escola de Engenharia Elétrica, Mecânica e de Computação (EMC), Programa de Pós-Graduação em Engenharia Elétrica e de Computação, Goiânia, 2023.

1. Sistema fotovoltaico. 2. Rastreamento do ponto de máxima potência. 3. Controle de tensão. 4. Redução de perdas. 5. Modelagem. I. Vieira, Flávio Henrique Teles, orient. II. Título.

CDU 621.3

UNIVERSIDADE FEDERAL DE GOIÁS

ESCOLA DE ENGENHARIA ELÉTRICA, MECÂNICA E DE COMPUTAÇÃO

ATA DE DEFESA DE TESE

Ata Nº **07** da sessão de Defesa de Tese de **Henrique Pires Corrêa** que confere o título de Doutor em **Engenharia Elétrica e de Computação**, na área de concentração em **Engenharia de Computação.**

Aos **três dias do mês de novembro de dois mil e vinte e três**, a partir das **08h30min.**, realizou-se a sessão pública de Defesa de Tese intitulada "**Contribuições à Modelagem, Controle e Integração de Dispositivos Fotovoltaicos a Sistemas Elétricos de Potência**". Os trabalhos foram instalados pelo Orientador, Professor Doutor **Flávio Henrique Teles Vieira - (EMC/UFG)** com a participação dos demais membros da Banca Examinadora: Professor Doutor **Reinaldo Martinez Palhares - (UFMG)** membro titular externo; Professor Doutor **Prof. Dr. Igor Kopcak - (EMC/UFG)** membro titular externo; Professora Doutora **Lina Paola Garcés Negrete - (EMC/UFG)** membro titular interno; Professor Doutor **Fernando Nunes Belchior - (FCT/UFG)** membro titular externo: **cujas participações ocorreram através de videoconferência** pelo link da videochamada: https://meet.google.com/iaa-yhgg-anq. Durante a arguição, os membros da banca **não fizeram** sugestão de alteração do título do trabalho. A Banca Examinadora reuniu-se em sessão secreta a fim de concluir o julgamento da Tese tendo sido o candidato **aprovado** pelos seus membros. Proclamados os resultados pelo Professor Doutor **Flávio Henrique Teles Vieira**, Presidente da Banca Examinadora, foram encerrados os trabalhos e, para constar, lavrou-se a presente ata que é assinada pelos Membros da Banca Examinadora, aos **três dias do mês de novembro de dois mil e vinte e três**.

TÍTULO SUGERIDO PELA BANCA

Documento assinado eletronicamente por **Lina Paola Garces Negrete**, **Professora do Magistério Superior**, em 03/11/2023, às 12:16, conforme horário oficial de Brasília, com fundamento no § 3º do art. 4º do Decreto nº 10.543, de 13 de novembro de 2020.

Documento assinado eletronicamente por **Igor Kopcak**, **Professor do Magistério Superior**, em 03/11/2023, às 12:17, conforme horário oficial de Brasília, com fundamento no § 3º do art. 4º do Decreto nº 10.543, de 13 de novembro de 2020.

Documento assinado eletronicamente por **Flavio Henrique Teles Vieira**, **Professor do Magistério Superior**, em 03/11/2023, às 12:17, conforme horário oficial de Brasília, com fundamento no § 3º do art. 4º do Decreto nº 10.543, de 13 de novembro de 2020.

Documento assinado eletronicamente por **Fernando Nunes Belchior**, **Professor do Magistério Superior**, em 03/11/2023, às 12:19, conforme horário oficial de Brasília, com fundamento no § 3º do art. 4º do Decreto nº 10.543, de 13 de novembro de 2020.

Documento assinado eletronicamente por **Henrique Pires Corrêa**, **Discente**, em 03/11/2023, às 12:29, conforme horário oficial de Brasília, com fundamento no § 3º do art. 4º do Decreto nº 10.543, de 13 de novembro de 2020.

Documento assinado eletronicamente por **Reinaldo Martinez Palhares**, **Usuário Externo**, em 06/11/2023, às 16:59, conforme horário oficial de Brasília, com fundamento no § 3º do art. 4º do Decreto nº 10.543, de 13 de novembro de 2020.

A autenticidade deste documento pode ser conferida no site https://sei.ufg.br/sei/controlador_externo.php?acao=documento_conferir&id_orgao_acesso_externo=0, informando o código verificador **4147868** e o código CRC **0FA8D2BC**.

Acknowledgements

My most sincere gratitude is due to:

My parents, who have always supported me in an untold number of ways and are the cause of all righteous choices I have made throughout my life.

My supervisor, Prof. Dr. Flávio Vieira, for his constant support and essential contributions to the development of this work. Aside from having a supervisor of admirable professionalism, it is especially gladdening to affirm I have a true friend.

My colleague Gilberto Filho, for his essential assistance in the experiments from Chapter 3. A further detailing of his contributions is given at the end of such Chapter.

My work colleague at EMC-UFG, Dr. Luiza Reino, for her very friendly presence and incentive to the pursuit of my doctoral studies.

The examining board members, for dedicating their time to the evaluation of this work and making important remarks which led to its significant improvement.

"It is difficult to find happiness within oneself, but it is impossible to find it anywhere else."
(Arthur Schopenhauer)

"The investigation of the truth is in one way hard, in another easy. An indication of this is found in the fact that no one is able to attain the truth adequately, while, on the other hand, no one fails entirely, but every one says something true about the nature of things, and while individually they contribute little or nothing to the truth, by the union of all a considerable amount is amassed."
(Aristotle)

Abstract

The prominence attained by photovoltaic (PV) power generation among the various available renewable energy resources has led to the need of analyzing and engineering such technology at a wide range of implementation scales, beginning from the electrical characteristics of PV cells, passing through the local control of PV generation systems, up to the massive integration of PV resources to wider electrical power systems, such as the distribution grid. This thesis is divided into three parts, each of which presents novel contributions to the study of PV systems in the three aforementioned scales of analysis. In the first part, analytical modeling of PV cell current-voltage (I-V) characteristics by means of explicit closed-form equations is addressed. A new piecewise quadratic model is proposed, which is shown to perform either better or comparably, for different solar cells, to state-of-the-art models in terms of accuracy. Two methods are established for computing the model parameters: the first one is analytical and only requires datasheet information, whereas the second one uses linear-complexity optimization with respect to I-V samples in order to further improve accuracy. In the second part, the problem of maximum power point tracking (MPPT) in two-stage PV systems is considered. First, a new hybrid MPPT method which uses direct duty cycle control for enhanced tracking efficiency is developed for grid-tied systems. Then, an analytical MPPT approach for single-phase off-grid variable-voltage systems is presented and subsequently generalized to consider current harmonics and three-phase loads. Both proposed MPPT methods are shown, by means of simulation, to perform better than existing methods with similar implementation complexities. In the third part, voltage control of distribution systems with photovoltaic penetration by means of PV inverter reactive power support is studied. Three novel decentralized methods for controlling the inverter reactive power setpoints are proposed. The first method considers voltage measurements are available at each PV inverter and consists in the heuristic specification of a cooperative decentralized Markov decision process (MDP), whose offline solution yields voltage control policies to be carried out by the grid zone controllers. On the other hand, the second method assumes voltage measurement and computational resources are scarce and establishes a decentralized strategy which only uses two voltage measurements per control zone and is directly compatible with droop-type controls usually found in PV inverters. At last, a third method is presented which combines cooperative MDP, droop control and a switching mechanism for achieving a compromise between voltage regulation and reduction of active power losses. All methods are compared to similar existing approaches, via simulations with real irradiance profiles in a large distribution grid, yielding favorable performances.

Keywords: Photovoltaic system, modeling, maximum power point tracking, voltage control, loss reduction, analytical methods, decentralized control.

Resumo

A proeminência alcançada pela geração fotovoltaica (FV), dentre as várias fontes de energia renováveis disponíveis, conduz à necessidade de análise e projeto desta tecnologia em uma ampla variedade de escalas para implementação, desde as características elétricas de células FV, passando pelo controle local dos sistemas de geração FV, até a integração massiva de fontes FV a sistemas elétricos de potência de grande porte, como a rede de distribuição. Esta tese é dividida em três partes, cada uma das quais apresenta novas contribuições ao estudo de sistemas FV nas três escalas de análise supracitadas. Na primeira parte, é abordada a modelagem analítica da característica corrente-tensão (I-V) da célula FV por meio de equações explícitas e em forma fechada. Um novo modelo quadrático por partes é proposto, cuja acurácia revela-se superior ou comparável, a depender da célula FV considerada, àquelas de modelos do estado da arte. Dois métodos são desenvolvidos para o cálculo dos parâmetros de modelo: o primeiro é analítico e requer apenas informações do *datasheet*, enquanto o segundo utiliza otimização de complexidade linear com relação a amostras I-V para refinar a acurácia do modelo. Na segunda parte, o problema de rastreamento do ponto de máxima potência (RPMP) em sistemas FV de dois estágios é considerado. Primeiramente, é desenvolvido um novo método híbrido de RPMP, para sistemas conectados à rede, que utiliza controle direto do ciclo de trabalho com vistas à melhoria da eficiência de rastreamento. Em sequência, um método RPMP analítico para sistemas monofásicos desconectados da rede e de tensão variável é proposto e, subsequentemente, generalizado para harmônicos de corrente e cargas trifásicas. É demonstrado, por meio de simulação, que ambos métodos de RPMP entregam desempenhos superiores aos de métodos existentes com complexidades de implementação similares. Na terceira parte, o controle de tensão em redes de distribuição com penetração fotovoltaica por meio do suporte de reativo dos inversores FV é estudado. Três novos métodos para controle descentralizado dos pontos de ajuste da potência reativa dos inversores são propostos. O primeiro método considera que medidas de tensão estão disponíveis em cada inversor PV e consiste na especificação heurística de um processo de decisão de Markov (PDM) descentralizado, cuja solução *offline* provê políticas para controle de tensão a serem seguidas pelos controladores de área da rede. Por outro lado, o segundo método assume que recursos computacionais e para medição de tensão são escassos e estabelece uma estratégia descentralizada que utiliza apenas duas medidas de tensão por área de controle e é diretamente compatível com controles de tipo *droop* usualmente encontrados em inversores FV. Por fim, é apresentado um terceiro método que combina PDM cooperativo, controle *droop* e um mecanismo de chaveamento visando o balanceamento dos objetivos de regulação de tensão e redução das perdas de potência ativa. Todos os métodos são comparados a abordagens similares existentes na literatura, via simulações considerando perfis de irradiância reais em uma rede de distribuição ampla, provendo desempenhos favoráveis.

Palavras-chave: Sistema fotovoltaico, modelagem, rastreamento do ponto de máxima potência, controle de tensão, redução de perdas, métodos analíticos, controle descentralizado.

List of Figures

List of Tables

List of abbreviations and acronyms

AC	Alternating current
AIIE	Analytical input impedance estimation
BEOG	Battery-equipped off-grid
BER	Bit error rate
BPSK	Binary phase shift keying
C-POMDP	Cooperative partially observable markov decision process
CV	Constant voltage
DC	Direct current
DDCC	Direct duty cycle control
DDC	Decentralized droop control
DRS	Distributed reactive support
DSO	Distribution system operator
DSSS	Direct sequence spread spectrum
EMC	Escola de Engenharia Elétrica, Mecânica e de Computação
FF	Fill factor
ETPQM	Explicit two-piece quadratic model
FOCV	Fractional open circuit voltage
FSCC	Fractional short circuit current
GT	Grid-tied
HAC	Hierarchical agglomerative clustering
IEEE	Institute of Electrical and Electronic Engineers
INC	Incremental conductance
INR	Incremental resistance

I-V	Current-voltage
JESP	Joint equilibrium-based search for policies
LDC	Local droop control
LoRa	Long range
MDP	Markov decision process
MOSFET	Metal-oxide semiconductor field-effect transistor
MPP	Maximum power point
MPPC	Maximum power point current
MPPDC	Maximum power point duty cycle
MPPV	Maximum power point voltage
MPPT	Maximum power point tracking
MVV	Maximum voltage violation
NAE	Normalized absolute error
NRMSE	Normalized root mean square error
OCV	Open circuit voltage
ODM	One-diode model
OF	Objective function
OLTC	On-load tap changer
OPF	Optimal power flow
PI	Proportional-integral
P&O	Perturb & observe
PRCU	Peak reactive capacity usage
PS	Partial shading
PV	Photovoltaic
PV-T	Photovoltaic-thermal
PWHS	Photovoltaic water heating system

PWM	Pulse-width modulation
RMSE	Root mean square error
ROT	Relative overvoltage time
RPS	Reactive power setpoint
RUT	Relative undervoltage time
RVT	Relative violation time
SCC	Short circuit current
SFOCV	Sensor-aided fractional open circuit voltage
UFG	Universidade Federal de Goiás
VC	Voltage control
VCZ	Voltage control zone
VPS	Variable-voltage photovoltaic system
VR	Voltage regulator
VRH	Variable resistance heater
ZC	Zone controller

Published Works

Journal publications (direct relation to thesis)

1. **Corrêa, H.P.**; Vieira, F.H.T. Cooperative Markov Decision Process for Voltage Control of Grid-Tied Photovoltaic Generators with Reactive Power Support. **IEEE Transactions on Sustainable Energy**, v. 13, p. 919-933, 2021.

2. **Corrêa, H.P.**; Vieira, F.H.T. Explicit Two-Piece Quadratic Current-Voltage Characteristic Model for Solar Cells. **IEEE Transactions on Electron Devices**, v. 68, p. 6273-6278, 2021.

3. **Corrêa, H.P.**; Vieira, F.H.T. Analytical MPPT for PV Water Heating System Based on Inverter Input Impedance. **International Journal of Energy and Environmental Engineering**, 2022.

4. **Corrêa, H.P.**; Vieira, F.H.T. Hybrid sensor-aided direct duty cycle control approach for maximum power point tracking in two-stage photovoltaic systems. **International Journal of Electrical Power & Energy Systems**, v. 145, 2023.

5. **Corrêa, H.P.**; Vieira, F.H.T.; Negrete, L.P.G. Double pilot node decentralized voltage control of distributed PV generators with droop-type inverter reactive support. **IEEE Access**, v. 10, p. 109476-109487, 2022.

6. **Corrêa, H.P.**; Vieira, F.H.T. Enhancing the Accuracy of an Explicit Solar Cell I-V Model via Low-Complexity Search-Based Parameter Extraction. **IEEE Access**, v. 10, p. 115823-115832, 2022.

7. **Corrêa, H.P.**; Vieira, F.H.T. An improved approach to analytical estimation of inverter input impedance and its application to MPPT in PV water heating systems. **Journal of Control, Automation and Electrical Systems**, 2023.

8. **Corrêa, H.P.**; Vieira, F.H.T. Analytical estimation of three-phase inverter input impedance applied to MPPT in off-grid variable-voltage photovoltaic systems. Accepted for publication in **International Journal of Electrical Power & Energy Systems**, 2023.

Journal submissions (direct relation to thesis)

1. **Corrêa, H.P.**; Vieira, F.H.T. Hybrid Cooperative MDP-Based Method for Decentralized Voltage Control and Loss Reduction via PV Generator Reactive Power Support, submitted to **Electric Power Systems Research**.

Journal publications (indirect relation to thesis)

1. **Corrêa, H.P.**; Vieira, F.H.T. An Approach for Impedance Matrix Computation Considering Phase Transposition on Distribution Lines. **IEEE Access**, v. 8, p. 168601-168610, 2020.

2. **Corrêa, H.P.**; Vieira, F.H.T.; Negrete, L.P.G. Assessment of Neutral Voltages in Distribution Networks via Monte Carlo Simulation and Load Flow Independent Grounding Approximation. **Advances in Electrical and Computer Engineering**, v. 20, p. 45-52, 2020.

3. **Corrêa, H.P.**; Vieira, F.H.T.; de Almeida, M.L.S. Reduced Complexity Estimation of Neutral Voltages in Terms of Grounding Impedances via Phasor Interpolation. **IEEE Access**, v. 8, p. 195946-195954, 2020.

4. **Corrêa, H.P.**; Vieira, F.H.T.; de Almeida, M.L.S. An Upper Bound on Magnitude Error of Voltage Drop Phasors in Distribution Lines Due to Phase Transposition Assumption. **Electric Power Components and Systems**, v. 48, p. 1-12, 2021.

5. **Corrêa, H.P.**; Vieira, F.H.T. An Approach to Steady-State Power Transformer Modeling Considering Direct Current Resistance Test Measurements. **Sensors**, v. 21, p. 6284, 2021.

6. **Corrêa, H.P.**; Vieira, F.H.T. Explicit three-piece quadratic model for accurate analytic representation of S-shaped solar cell current-voltage characteristics **Solar Energy**, v. 258, p. 143-147, 2023.

Journal submissions (indirect relation to thesis)

1. **Corrêa, H.P.** Improving an analytic SDM parameter extraction method via decoupled maximum power point derivative approximation, submitted to **Solar Energy**.

Conference publications (indirect relation to thesis)

1. **Corrêa, H.P.**; Vieira, F.H.T, de Castro, M.S. Aplicacão de Simulação Monte Carlo na Análise dos Impactos da Geração Distribuída Sobre um Alimentador Radial. **Escola Regional de Informática de Goiás (ERI-GO)**, 2020.

Contents

General Introduction

The combination of growing concerns regarding energy sustainability in society, decreasing implementation costs of alternative means for generating electrical energy and economic incentives often conferred by governments to those who take the initiative in leveraging such technologies has culminated in the rapid deployment of renewable energy resources for power generation. Photovoltaic (PV) systems have, in particular, enjoyed massive integration to the world energy matrix due to the unrivalled modularity and continuously decreasing manufacturing costs of PV panels. Aside from large PV power plants connected to national power systems at transmission level, the modularity of PV panels has enabled successful implementation of smaller-scale PV systems, which consist in consumer-owned PV units connected directly to distribution grids (grid-tied distributed generation) and off-grid PV arrays for entirely autonomous energy supply.

Precisely due to the aforementioned modularity of PV systems, their analysis and engineering is a complex task which must be tackled from significantly different viewpoints. In fact, a thorough understanding of PV generation can only be achieved if adequate consideration is given to the wide range of analysis which begins at PV cell electrical characteristics and reaches up to joint control of multiple grid-tied PV panels in distributed generation scenarios. The objective of this thesis is providing significant contributions to the analysis and engineering of PV systems at three implementation scales of interest, which can be conveniently termed as PV cell modeling, local PV generation control and voltage regulation of power grids with distributed PV generation. In this sense, the Chapters of this thesis are divided into three parts wherein each aforementioned scope of analysis is dealt with. In what follows, a concise description of each Part, Chapter and their associated contributions to the study of PV systems is carried out.

Part I

The modeling of PV cell current-voltage (I-V) characteristics is addressed. It is acknowledged that the widely used one-diode I-V model, despite its precision, poses some inconveniences in terms of mathematical tractability and parameter extraction due to it not being an explicit model. Taking this into account, a closed-form I-V model with excellent tractability is developed whose parameters can be determined in a very straightforward manner, either analytically (Chapter 1) or via low complexity optimization (Chapter 2).

Chapter 1

A novel I-V characteristic model is proposed, which is based on two quadratic curves that are referred to orthogonal coordinate systems and intersect at the PV cell maximum power point. Its main advantage lies in being a closed-form model, i.e., current is expressed directly as a function of voltage. Given the notable operating points available in PV cell datasheets (open circuit, short circuit and maximum power), the simple mathematical structure yielded by the quadratic segments of the proposed model enables derivation of analytical equations for computing its parameters. For validation purposes, the proposed model is applied to three different solar cells and has its performance compared to those yielded by three established closed-form models. Obtained results show that it can perform better or comparably to the model which is generally considered the most accurate in the literature. At last, it is shown that the proposed model has the unique feature of enabling analytical computation of cell operating points in terms of the PV cell load. Simulations with dynamic irradiance and temperature show that such computation yields output power values which strongly match those obtained with the one-diode model.

Chapter 2

An alternative parameter extraction method for the I-V model proposed in the previous Chapter is developed that further enhances its accuracy. A notable operating point is devised which, after being substituted for one of the original notable point conditions, permits expressing all model parameters in terms of a single auxiliary parameter, which is, in turn, demonstrated to be inside a subset of the unit interval. At last, the optimal auxiliary parameter value is obtained by means of the single-variable linear-complexity compass search optimization algorithm. Such approach avoids the main difficulties associated to multi-variable optimization required for extracting one-diode model parameters, namely the implementation of complex algorithms, since compass search is one of the simplest optimization procedures, and wide multi-dimensional search domains, since the required optimization is single-variable and restricted to a narrow interval. To validate the new parameter computation approach, it is compared to the analytical method derived in Chapter 1. The obtained results show that the proposed approach can yield expressive error reductions with a minor execution time trade-off.

Part II

The local control of grid-tied and off-grid PV systems for ensuring adequate power supply to their loads is the theme of this Part. More specifically, the problem of carrying out maximum power point tracking (MPPT) under varying ambient conditions (irradiance and temperature) is considered. In general, legacy MPPT algorithms are simple to implement but suffer from relatively slow tracking speeds, whereas modern algorithms are more efficient

but often require complex implementations and higher processing capabilities. Taking such facts as motivation, a novel MPPT algorithm for grid-tied systems that hybridizes two legacy MPPT methods is proposed which attains high efficiency while maintaining simple implementation requirements (Chapter 3). Then, an analytical MPPT algorithm designed for an emerging type of off-grid system (variable-voltage PV generators) is proposed (Chaper 4) that performs better and has even simpler computational implementation than the classic Perturb & Observe (P&O) method. Such analytical algorithm is then generalized to three-phase systems with output current harmonics (Chapter 5).

Chapter 3

A novel MPPT algorithm for two-stage grid-tied PV systems is proposed, which is a hybrid of P&O and a modified version of the Fractional Open Circuit Voltage (FOCV) method. In steady-state conditions, P&O is used with a small perturbation step so that precise tracking is achieved. Irradiance and temperature sensors detect rapid variations in ambient conditions and trigger the modified FOCV, which uses the measured values to estimate the new maximum power point voltage (MPPV). At last, knowledge of the approximately constant direct current (DC) bus voltage of two-stage systems is leveraged to convert the estimated MPPV into an estimation of DC-DC converter duty cycle. This step is particularly important since it enables direct duty cycle control (DDCC), thereby not requiring a proportional-integral controller and avoiding oscillations caused by such controller when it is used for MPPT via voltage reference control. The proposed method is straightforward to implement, since it combines two well-known legacy MPPT algorithms. Also, its efficiency is high due to the fast tracking yielded by FOCV and reduced oscillations losses of DDCC. It is first validated via simulations, whose results show it consistently outperforms P&O and a similar non-DDCC hybrid method. Finally, effectiveness of the proposed method is confirmed by means of a simple small-scale experiment.

Chapter 4

Aside from being applicable to two-stage grid-tied systems, the MPPT algorithm developed in Chapter 3 can also be used for battery-equipped off-grid PV systems, since they also satisfy the required assumption of approximately constant DC bus voltage. Quite notably, PV systems that are off-grid and do not employ batteries have seen increased application recently, mainly in the form of photovoltaic water heating systems (PWHS). The most unusual feature of such implementation is that it constitutes a variable-voltage PV system (VPS), which is therefore incompatible with the MPPT method developed in Chapter 3. Taking this into account, a VPS-specific MPPT algorithm is proposed that leverages the specific electrical characteristics of the VPS for achieving high efficiency and analytical tracking. The proposed algorithm is based on an expression derived for estimating DC input impedance of the PV system inverter. It also substitutes irradiance and

temperature sensors for the voltage and current ones used in most MPPT methods, whose measurements are used to estimate PV panel maximum power point resistance. Given both estimated impedance values, the DC-DC converter conversion ratio equation is then solved analytically for the maximum power point duty cycle (MPPDC). This approach provides an even simpler implementation than P&O, since it is entirely analytical (i.e., it does not rely on hill-climbing) and does not require specification of a perturbation parameter. Furthermore, it yields fast tracking due to the almost instantaneous computation of MPPDC after changes in ambient conditions. Simulations are carried out for validating the proposed algorithm; obtained results show it outperforms P&O and has the significant advantage of being highly insensitive to sample time.

Chapter 5

Two generalizations of the analytical MPPT method devised in the previous Chapter are proposed. When deriving the inverter DC input impedance in Chapter 4, a single-phase VPS was considered and it was further assumed that its output current was sinusoidal. Despite such assumption being often satisfied in practice due to inverter output filters, taking harmonics into account is of interest because resistive heating loads do not impose strict power quality requirements and PWHS may therefore be implemented with small (or even without) output filters. Hence, the first generalization consists in relaxing the sinusoidal current assumption and obtaining a more precise expression which incorporates the effect of current harmonics into DC input impedance. Subsequently, a second generalization is derived which, aside from considering current harmonics, computes the DC input impedance of a three-phase four-wire VPS with unbalanced loads. Both approaches are validated via simulations, whose results show that the single-phase generalization significantly improves performance of the MPPT method from Chapter 4 for small load power angles and that the three-phase generalization also outperforms and is simpler to implement than P&O.

Part III

The control of PV generators massively integrated to the distribution grid by means of grid-tied systems is considered. In particular, focus is given to the important problem of voltage control (VC) via reactive power support supplied by the PV systems. It is known that using local droop control at each PV inverter is an approach that, despite its simplicity, fails to adequately take the global grid voltage profile into account. In this context, decentralized reactive power control has emerged as a suitable framework for surpassing the suboptimal performance yielded by local control. Unfortunately, most decentralized methods proposed in the literature impose stringent computational processing and communication network requirements which may lead to practical infeasibility. Taking this issue into account, two novel decentralized VC methods are proposed which yield

adequate reactive power support while maintaining relatively simple implementation requirements when compared to similar approaches in the literature. Both methods are based on partitioning the grid into voltage control zones (VCZ), each of which is controlled by an associated zone coordinator (ZC). In Chapter 6, a method that employs coordination between ZC by means of specialized controllers based on the solution of a Cooperative Partially Observable Markov Decision Process (C-POMDP) model is proposed. On the other hand, very scarce computational, communication and hardware resources are assumed in Chapter 7, wherein a method with independent ZC operation and direct compatibility with standard PV inverter droop controllers is developed. At last, Chapter 8 proposes a hybrid approach which incorporates the main advantages yielded by the methods from Chapters 6 and 7 (i.e., cooperation and droop compatibility) and further balances out the voltage regulation objective with reduction of active power losses throughout the grid.

Chapter 6

With the aim of avoiding the aforementioned issue of high communication and computational processing requirements, a few heuristic methods for decentralized VC have been proposed in the recent literature. However, this type of approach remains relatively unexplored despite its advantage of providing closed-form reactive power setpoint (RPS) control laws and thereby not depending on real-time optimization. Even more notably, the probabilistic framework of Markov Decision Processes has been scarcely considered for performing VC by means of PV reactive power support, being mostly used for battery scheduling in microgrids. As an attempt of filling such research gaps, a heuristic decentralized VC method based on the C-POMDP model is proposed. It consists in associating a Markov agent to each grid VCZ and specifying model probabilistic and reward parameters in a heuristic manner that adequately represents the VC implications of each agent incrementing or decrementing its zone RPS. Given the heuristic model, it is then solved offline via a Nash equilibrium-based algorithm and yields closed-form RPS policies for all VCZ. The proposed approach is validated via simulations based on the IEEE 123-bus test feeder, with random irradiance profiles, load curves and allocation of PV generators along the grid being considered. Obtained results show the proposed method outperforms other recent decentralized VC heuristics in the literature.

Chapter 7

Despite the favorable performance attained by the heuristic method proposed in Chapter 6, it could be argued that some practical implementation difficulties may still stem from it, namely the requirement of specialized RPS controllers for implementing agent policies, an upper-level network for enabling the cooperation between VCZ and knowledge of voltage magnitudes in all grid nodes. Taking this into account and under the motivation of achieving decentralized VC with minimal implementation requirements, a method that

does not require VCZ coordination, is directly compatible with standard PV inverter droop controllers and only requires two voltage measurements per VCZ is proposed. The method consists in selecting two pilot nodes per VCZ which best represent, in a statistical sense, maximum and minimum zone voltage magnitudes. Then, in each VCZ, the pilot nodes are used as reference for droop control of the subsumed PV inverters. A single binary decision by each ZC is required, namely which of the pilot node voltages is fed to the PV controllers. This is decided by comparing the upper and lower voltage limit violations by the maximum and minimum voltage nodes, respectively; the one which presents the greatest violation has its voltage broadcasted by the ZC to the PV inverters. Performance of the proposed method is compared (also via simulations on the IEEE 123-bus feeder) to those of local and decentralized single pilot node droop controls. The results show that, despite its simplicity, the proposed method yields significant VC performance improvements.

Chapter 8

The decentralized methods proposed in the two previous Chapters were shown to provide superior performance to similar VC approaches in the literature. However, both methods and those to which they were compared only consider voltage regulation as an objective, whereas it can be argued that achieving an adequate compromise with active power loss reduction is equally important. In this sense, a method is presented which combines the cooperative MDP approach from Chapter 6 with a selection law for switching between voltage control and loss reduction. More precisely, it outputs, for each PV inverter, either the RPS yielded by the MDP solution or the RPS computed by means of a well-known loss minimization heuristic. Furthermore, instead of considering an arbitrary RPS controller as in Chapter 6, the droop control scheme proposed in Chapter 7 is incorporated into the MDP policy to achieve a more realistic, yet with fewer implementation requirements, reactive power controller. Comparison to similar (yet local) switching law and weight-based methods is carried out, whose results demonstrate the proposed approach yields superior performance.

A Note Regarding Implementation

It is of interest to emphasize that all simulations carried out in this work have been implemented from the ground up in the MATLAB and Simulink (R2017a) environments. In this sense, the construction of a substantial software basis for future research is a relevant product of this Thesis.

Graphical Scheme of the Thesis

For the sake of clarity and further comprehension, a graphical scheme of the organization of this thesis is given in the figure below.

Scheme of thesis organization.

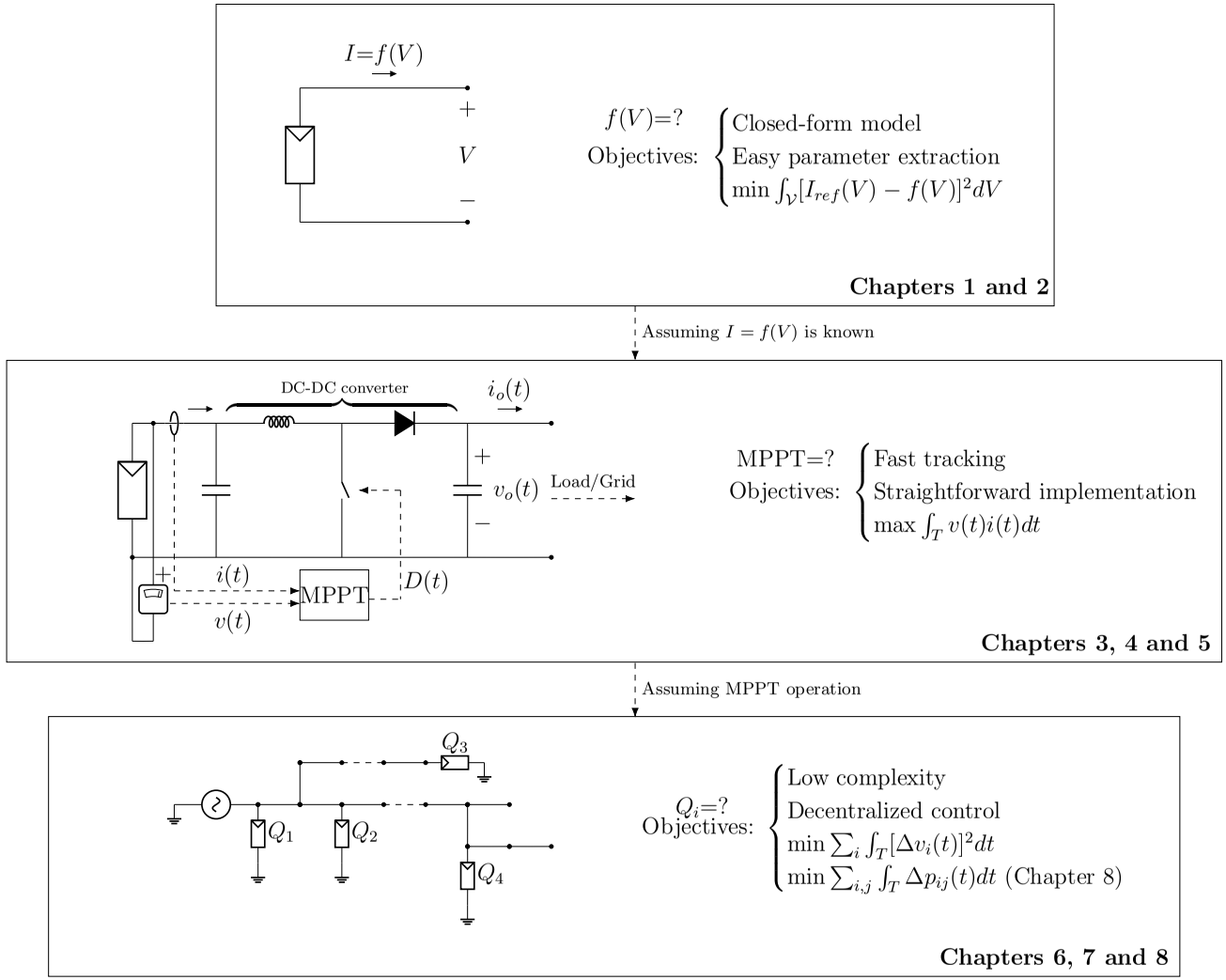

Source: The author.

Introdução Geral

A combinação de crescentes preocupações na sociedade com relação à sustentabilidade energética, redução dos custos para implementação de meios alternativos para geração de energia elétrica e incentivos econômicos, muitas vezes oferecidos por governos àqueles que tomam a iniciativa em utilizar tais tecnologias, culminou no rápido aproveitamento de recursos energéticos renováveis para geração de potência. Sistemas fotovoltaicos (FV), em particular, foram integrados massivamente à matriz energética mundial em função de sua incomparável modularidade e custos continuamente decrescentes de fabricação dos painéis FV. Além de grandes plantas FV conectadas aos sistemas de potência nacionais a nível de transmissão, a modularidade dos painéis FV permitiu a bem-sucedida implementação de sistemas FV em escalas menores, os quais consistem em unidades FV de propriedade dos consumidores conectadas diretamente às redes de distribuição (geração distribuída *grid-tied*) e arranjos FV *off-grid* para suprimento completamente autônomo de energia.

Precisamente em função da supramencionada modularidade de sistemas FV, sua análise e projeto é uma tarefa complexa que deve ser abordada a partir de pontos de vista significativamente distintos. De fato, um entendimento minucioso da geração FV só pode ser alcançado se atenção adequada for dada ao amplo espectro de análise que se inicia nas características elétricas da célula FV e finda no controle conjunto de múltiplos painéis FV *grid-tied* em cenários de geração distribuída. O objetivo desta tese é prover contribuições significativas à análise e projeto de sistemas FV em três escalas de implementação de maior interesse, as quais podem ser convenientemente denominadas como modelagem de células FV, controle local de geração FV e regulação de tensão em sistemas de potência com geração FV distribuída. Nesse sentido, os Capítulos desta tese são divididos em três partes, em cada uma das quais um dos supramencionados escopos de análise é considerado. No que segue, é realizada uma descrição concisa de cada Parte, Capítulo e suas respectivas contribuições ao estudo de sistemas FV.

Parte I

A modelagem de características corrente-tensão (I-V) de células FV é abordada nesta Parte. Reconhece-se que o amplamente utilizado modelo I-V de um diodo, apesar de sua precisão, traz alguns inconvenientes em termos de tratabilidade matemática e extração de parâmetros pelo fato de não ser um modelo explícito. Tomando isto em consideração, um modelo I-V de forma fechada com excelente tratabilidade é desenvolvido cujos parâmetros podem ser determinados de maneira simples, seja analiticamente (Capítulo 1) ou via otimização de baixa complexidade (Capítulo 2).

Capítulo 1

Um novo modelo de característica I-V é proposto, sendo este baseado em duas curvas quadráticas referidas a sistemas de coordenadas ortogonais e que se interceptam no ponto de máxima potência da célula FV. Sua principal vantagem reside no fato de ser um modelo de forma fechada, ou seja, no qual a corrente é expressada diretamente como função da tensão. Dados os pontos de operação notáveis disponibilizados no *datasheet* da célula FV (circuito aberto, curto-circuito e máxima potência), a estrutura matemática simples propiciada pelos segmentos quadráticos do modelo proposto permite a derivação de equações analíticas para o cálculo de seus parâmetros. A título de validação, o modelo proposto é aplicado a três células solares distintas e tem seu desempenho comparado àqueles propiciados por três modelos de forma fechada já consolidados na literatura. Os resultados obtidos mostram que o modelo proposto pode prover desempenho melhor ou comparável ao do modelo que é usualmente considerado o mais preciso na literatura. Por fim, é demonstrado que o modelo proposto possui a característica única de permitir o cálculo analítico dos pontos de operação da célula FV em termos da carga alimentada. Simulações com condições dinâmicas de irradiância e temperatura demonstram que este cálculo provê valores para a potência de saída com forte correspondência relativamente àqueles obtidos com o modelo de um diodo.

Capítulo 2

Um método alternativo de extração dos parâmetros do modelo I-V quadrático, proposto no Capítulo anterior, é desenvolvido com o objetivo de melhorar sua precisão. Propõe-se um ponto de operação notável que, após ser utilizado em substituição a um dos pontos notáveis, permite expressar todos os parâmetros do modelo em função de um único parâmetro auxiliar. Este parâmetro, por sua vez, pertence a um subconjunto do intervalo unitário. Por fim, o valor ótimo do parâmetro auxiliar é obtido por meio de um algoritmo de otimização a uma variável e de complexidade linear denominado *compass search*. Esta estratégia contorna as principais dificuldades associadas à otimização multivariável requerida para extração dos parâmetros do modelo de um diodo, quais sejam: a implementação de algoritmos complexos, pois o *compass search* é um dos mais simples procedimentos de otimização, e domínios amplos de busca multidimensional, já que a otimização utilizada é a uma variável e restrita a um intervalo estreito. Para validar o novo método para extração de parâmetros, seu desempenho é comparado ao do método analítico deduzido no Capítulo 1. Os resultados obtidos mostram que o método proposto pode prover expressivas reduções de erro, em contrapartida a um pequeno tempo de execução.

Parte II

O controle local de sistemas FV *grid-tied* e *off-grid* para garantir o adequado suprimento de potência a sua cargas é o tema desta Parte. Mais especificamente, o problema de realização do rastreamento do ponto de máxima potência (RPMP) sob condições ambientes (irradiância e temperatura) variáveis é abordado. Em geral, os algoritmos RPMP legados possuem implementações simples, mas padecem de rastreamento lento. Por outro lado, algoritmos modernos são mais eficientes mas, frequentemente, requerem implementações complexas e elevada capacidade de processamento. Tomando tais fatos como motivação, um novo algoritmo RPMP para sistemas *grid-tied* que hibridiza dois métodos RPMP legados é proposto, o qual provê elevada eficiência enquanto mantém requisitos simples de implementação (Capítulo 3). Subsequentemente, um algoritmo RPMP analítico projetado para um tipo emergente de sistema *off-grid* (geradores FV de tensão variável) é proposto (Capítulo 4), o qual possui desempenho superior e implementação computacional ainda mais simples do que a do clássico método *Perturb & Observe* (P&O). O algoritmo analítico proposto é, por fim, generalizado para sistemas trifásicos com harmônicos na corrente de saída (Capítulo 5).

Capítulo 3

Um novo algoritmo RPMP para sistemas FV *grid-tied* de dois estágios é proposto, sendo este um híbrido de P&O com uma versão modificada do método Tensão Fracionária de Circuito Aberto (TFCA). Em condições estacionárias, o P&O é utilizado com um pequeno passo de perturbação para que se obtenha rastreamento preciso. Sensores de irradiância e temperatura detectam variações rápidas nas condições ambientes e ativam o TFCA modificado, o qual utiliza os valores medidos para estimar a nova tensão do ponto de máxima potência (TPMP). Por fim, o conhecimento da tensão do barramento de corrente contínua (CC) aproximadamente constante em sistemas de dois estágios é utilizado para converter a TPMP estimada em uma estimativa do ciclo de trabalho do conversor CC-CC. Este último passo é particularmente importante, pois permite o controle direto do ciclo de trabalho (CDCT), portanto não requerendo um controlador proporcional-integral e evitando as oscilações causadas por tal controlador quando utilizado para RPMP via controle por referência de tensão. O método proposto é de simples implementação, visto que combina dois algoritmos RPMP legados bem conhecidos. Ademais, sua eficiência é elevada em função do rápido rastreamento provido pelo TFCA e da redução de perdas por oscilação devido ao uso do CDCT. Sua validação é realizada, de início, através de simulações cujos resultados mostram seu desempenho superior com relação ao P&O e a um algoritmo híbrido semelhante que não emprega CDCT. Por fim, a efetividade do método proposto é confirmada por meio de um experimento simples em pequena escala.

Capítulo 4

Além de ser aplicável a sistemas *grid-tied* de dois estágios, o algoritmo MPPT desenvolvido no Capítulo 3 pode também ser utilizado em sistemas FV *off-grid* com baterias, visto também satisfazerem a suposição de tensão aproximadamente constante no barramento CC. Notavelmente, topologias FV *off-grid* que não utilizam baterias têm sido utilizadas com mais frequência recentemente, principalmente na aplicação de sistemas fotovoltaicos para aquecimento de água (SFAA). Uma característica pouco usual desta implementação é o fato da mesma constituir um sistema FV de tensão variável (SFTV), que é, portanto, incompatível com o método RPMP desenvolvido no Capítulo 3. Levando isso em consideração, um algoritmo RPMP específico para SFTVs é proposto, o qual se utiliza das características elétricas específicas do SFTV para obter elevada eficiência e rastreamento analítico. O algoritmo proposto é baseado em uma expressão derivada para estimação da impedância de entrada DC do inversor do sistema FV. Ademais, os sensores de tensão e corrente empregados na maioria dos métodos RPMP são substituídos por sensores de temperatura e irradiância, cujas medidas são utilizadas para estimar a resistência de máxima potência do painel FV. De posse de ambas estimativas de impedância, o ciclo de trabalho do ponto de máxima potência (CTPMP) é calculado via solução analítica da equação da razão de transformação do conversor DC-DC. Esta estratégia demanda uma implementação ainda mais simples do que a requerida pelo P&O, visto ser completamente analítica (i.e., não utiliza *hill climbing*) e não requerer a especificação de um parâmetro de perturbação. Ademais, provê rastreamento rápido devido ao cálculo quase instantâneo do CTPMP após mudanças nas condições ambientes. Simulações são realizadas com vistas a validar o algoritmo proposto; os resultados obtidos demonstram que sua performance é superior à do P&O, com a significativa vantagem de ser insensível ao tempo de amostragem.

Capítulo 5

Duas generalizações do método RPMP analítico desenvolvido no Capítulo anterior são propostas. Ao obter a impedância de entrada DC do inversor no Capítulo 4, considerou-se um SFTV monofásico cuja corrente de saída foi assumida senoidal. Apesar desta suposição ser frequentemente satisfeita na prática devido aos filtros de saída do inversor, considerar o efeito dos harmônicos é interessante pelo fato de cargas resistivas para aquecimento não imporem requisitos estritos para qualidade de energia, de modo que SFAA podem ser implementados com pequenos (ou até mesmo sem) filtros de saída. Nesse sentido, a primeira generalização consiste em relaxar a suposição de corrente senoidal e obter uma expressão mais precisa que incorpora o efeito dos harmônicos de corrente na impedância de entrada DC. Subsequentemente, uma segunda generalização é obtida em que, além de serem considerados os harmônicos de corrente, a impedância de entrada DC é calculada para um STFV trifásico a quatro fios com cargas desbalanceadas. Ambas

generalizações são validadas via simulações, cujos resultados mostram que a generalização monofásica melhora significativamente a performance do método RPMP do Capítulo 4 para cargas com pequeno ângulo de potência e que a generalização trifásica também supera e possui implementação mais simples do que o método P&O.

Parte III

O controle de geradores FV integrados massivamente à rede de distribuição por meio de sistemas *grid-tied* é considerada. Em particular, o foco desta Parte é o importante problema do controle de tensão (CT) via suporte de potência reativa fornecido pelos sistemas FV. Sabe-se que a utilização de controle *droop* local em cada inversor FV é uma estratégia que, embora simples, não considera adequadamente o perfil de tensão global da rede de distribuição. Nesse contexto, o controle descentralizado de potência reativa emergiu como um *framework* que possibilita superar o desempenho subótimo do controle local. Infelizmente, a maioria dos métodos descentralizados propostos na literatura impõe requisitos severos quanto ao processamento computacional e rede de comunicação necessários para sua execução, o que pode levar à sua inviabilidade em situações práticas. Levando em conta esse fato, dois novos métodos para CT descentralizado são propostos, os quais provêem suporte de reativos adequado enquanto mantêm requisitos de implementação relativamente simples quando comparados a métodos similares na literatura. Ambos métodos são baseados no particionamento da rede de distribuição em zonas de controle de tensão (ZCT), cada uma das quais é controlada por um coordenador de zona (CZ) associado. No Capítulo 6, um método que emprega a coordenação entre CZ por meio de controladores especializados baseados na solução de um Processo de Decisão de Markov Parcialmente Observável Cooperativo (PDMPO-C) é proposto. Por outro lado, assume-se escassez de recursos computacionais, de comunicação e de *hardware* no Capítulo 7, propondo-se um método em que as CZ operam independentemente e que possui compatibilidade direta com os controladores *droop* usuais dos inversores FV. Por fim, o Capítulo 8 propõe uma abordagem híbrida que incorpora as principais vantagens providas pelos métodos dos Capítulos 6 e 7 (i.e., cooperação e compatibilidade com controle *droop*) e busca balancear o objetivo de regulação de tensão com a redução das perdas de potência ativa na rede.

Capítulo 6

Visando evitar o problema de requisitos severos relativos a processamento computacional e comunicação, alguns métodos heurísticos para CT descentralizado já foram propostos na literatura recente. Todavia, este tipo de método permanece relativamente pouco explorado, apesar de sua vantajosa propriedade de prover leis em forma fechada para controle do ponto de ajuste da potência reativa (PAPR) e, portanto, não depender de otimização em tempo real. Ainda mais notavelmente, o *framework* probabilístico dos

Processos de Decisão de Markov foi pouco considerado para realização de CT por meio do suporte de potência reativa por unidades FV, sendo usado principalmente no gerenciamento de baterias em *microgrids*. Como uma tentativa de preencher esta lacuna de pesquisa, um método de CT heurístico e descentralizado baseado no modelo PMDPO-C é proposto. O método consiste em associar um agente Markov a cada ZCT da rede e especificar os parâmetros probabilísticos e de recompensa do modelo heuristicamente, atribuindo-se valores que representam adequadamente as implicações sobre o CT devido às decisões de cada agente quanto ao aumento ou redução do PAPR de sua ZCT. Dada a especificação do modelo heurístico, sua solução é obtida *offline* por meio de um algoritmo baseado em equilíbrio de Nash, obtendo-se políticas para controle de PAPR em forma fechada a serem seguidas por cada ZCT. O método proposto é validado através de simulações baseadas no alimentador IEEE de 123 barras, nas quais considera-se a aleatoriedade dos perfis de irradiância, curvas de carga e alocação de geradores FV ao longo da rede. Os resultados obtidos mostram que o método proposto possui desempenho superior a outras heurísticas de CT propostas recentemente na literatura.

Capítulo 7

Apesar do desempenho favorável alcançado pelo método heurístico proposto no Capítulo 6, é possível argumentar que persistiriam algumas dificuldades relativas à sua implementação prática, as quais derivariam da necessidade de: controladores de PAPR especializados para implementação das políticas de agente, uma camada superior na rede de comunicação para cooperação entre ZCT e o conhecimento das magnitudes de tensão em todos os nós da rede. Dada esta consideração e sob a motivação de realizar CT descentralizado com requisitos mínimos de implementação, é proposto um novo método que não requer coordenação de ZCT, é diretamente compatível com controladores *droop* usualmente utilizados em inversores FV e requer apenas duas medidas de tensão por ZCT. O método consiste em selecionar dois nós piloto por ZCT que melhor representam, em sentido estatístico, as magnitudes de tensão máxima e mínima da zona. Então, em cada ZCT, os nós piloto são utilizados como referência para o controle *droop* dos inversores FV subordinados. Apenas uma decisão binária deve ser realizada por cada CZ, qual seja: identificar qual das tensões dos nós piloto será repassada aos controladores FV. Isto é feito comparando-se as violações dos limites superior e inferior de tensão pelos nós representativos de máxima e mínima tensão, respectivamente; aquele que apresentar a maior violação tem sua tensão transmitida pelo CZ aos inversores FV. O desempenho do método proposto é comparado, também via simulações, no alimentador IEEE de 123 barras àqueles dos controles *droop* local e descentralizado com nó piloto único. Os resultados demonstram que, apesar de sua simplicidade, o método proposto provê significativa melhoria no desempenho de CT.

Capítulo 8

Demonstrou-se que os métodos descentralizados propostos nos dois Capítulos anteriores provêem desempenhos superiores a estratégias de CT similares existentes na literatura. Todavia, ambos métodos e aqueles aos quais foram comparados consideram apenas a regulação de tensão como objetivo, sendo possível argumentar-se que a obtenção de um equilíbrio adequado com a redução das perdas de potência ativa é igualmente importante. Nesse sentido, é apresentado um método que combina a estratégia de MDP cooperativo do Capítulo 6 com uma lei de seleção para chaveamento entre controle de tensão e redução de perdas. Mais precisamente, sua saída, para cada inversor FV, é ora o PAPR dado pela solução MDP, ora o PAPR calculado por meio de uma bem conhecida heurística para minimização de perdas. Ademais, em vez de considerar um controlador de PAPR arbitrário como no Capítulo 6, o controle *droop* proposto no Capítulo 7 é incorporado à política MDP, de modo a obter-se um controlador de potência reativa mais realista e, simultaneamente, com menores requisitos de implementação. É realizada uma comparação com métodos similares baseados tanto em leis de chaveamento quanto de ponderação (porém de natureza local); os resultados obtidos demonstram que o método proposto provê desempenho significativamente superior.

Uma Nota Relativa à Implementação

É importante enfatizar que todas as simulações realizadas neste trabalho foram implementadas, desde suas concepções básicas, nos ambientes MATLAB e Simulink (R2017a). Nesse sentido, a construção de uma base substancial de *software* para uso em pesquisas futuras é um produto relevante desta Tese.

Esquema Gráfico da Tese

Com vistas a proporcionar maior clareza e compreensão, um esquema gráfico da organização da presente tese é dado na figura abaixo.

Esquema de organização da tese.

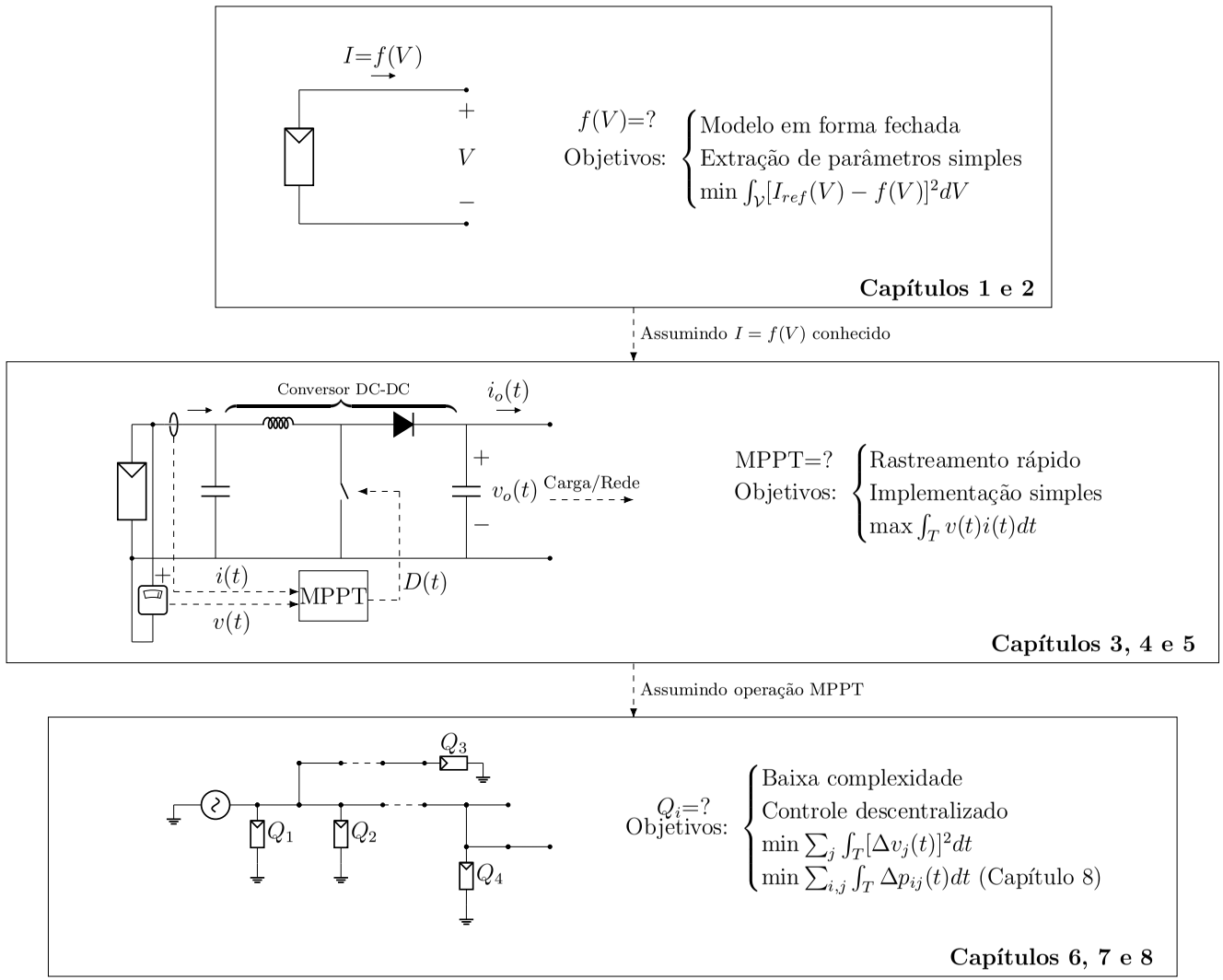

Fonte: O autor.

Part I

PV Cell Modeling

1 Explicit Two-Piece Quadratic Model for I-V Characteristics of Solar PV Cells

1.1 Introduction

A standard approach for modeling solar cells is employing the one-diode model (ODM) equivalent circuit [1]. Despite its high accuracy and association of physical phenomena to its parameters, this approach entails two difficulties which are undesirable for practical calculations: a highly nonlinear and implicit current-voltage (I-V) characteristic equation and the need of using it for estimating five model parameters (photogenerated current I_{ph}, reverse saturation current I_o, ideality factor m, series resistance R_s and shunt resistance R_{sh}). This is further complicated by the fact that it is deemed desirable that only data pertaining to three notable I-V characteristic points (open circuit, short circuit and maximum power) be used in estimation [2]. Several approaches exist for carrying out parameter estimation [3–9], which proceed either via optimization [3, 4], approximation [5, 6] or by employing additional data [7–9]. In practice, such approaches imply the disadvantages of processing time, precision loss and additional measurements, respectively.

To circumvent such difficulties and enable more practical and straightforward computations, explicit I-V models have been proposed [10–18]. In general, these approaches consist in specifying an equation $I = g(V)$ and fitting its parameters by using the solar cell notable points, thus avoiding the implicit nature of the one-diode model I-V characteristic. The models given in [10, 11] rely on curve fitting to multiple sample points, which violates the requirement of only using the notable points. In a similar manner, usage of additional slope data is required by [12]. It has been shown in [2] that the remaining models (i.e., those given in [13–18]) can be determined by using solely the notable points.

An assessment of models [13–18] is carried out in [2], with each model being tested for solar cells of different technologies. It is reported that the model by Karmalkar and Haneefa [16] is, in general, the one with best performance. Significant exceptions apply: for legacy silicon solar cells, whose fill factors are relatively low, the model by Pindado and Cubas [17] achieves better performance. Furthermore, the method by Akbaba and Alattawi [18], whose performance is usually the worst, approaches that of [16] for composite polymer cells (very low fill factor). In this sense, it has been established that the performances of explicit models vary with cell fill factor and may suffer appreciable degradation for specific ranges of such parameter.

In this Chapter, a novel explicit I-V model which can be determined solely from notable point data is proposed and compared to [16–18]. The obtained results suggest it has

superior flexibility, in that it achieves best or second-to-best performance for all considered fill factors. Furthermore, it is also shown that it has the unique and advantageous feature of enabling explicit computations of cell operating points.

1.2 Proposed Model

Let the open circuit voltage, short circuit current, maximum power point voltage and maximum power point current be denoted, respectively, by V_{oc}, I_{sc}, V_{mp} and I_{mp}. The I-V characteristic of a solar cell is roughly approximated by a non-ideal current source for $V \in [0, V_{mp}]$, which implies that a model $V = g_V(I)$ is easier to fit since current varies in a narrow interval. For analogous reasons, a model $I = g_I(V)$ is adequate for $V \in [V_{mp}, V_{oc}]$. To ensure that the model is explicit in the range $V \in [0, V_{mp}]$, $g_V(I)$ must be invertible.

Taking the above into account, the proposed model is based on two quadratic curves referred to inverse orthogonal coordinate systems in complementary voltage ranges:

$$I(V) = \underbrace{[aV^2 + bV + c]}_{g_I(V)} u(V - V_{mp}) + \underbrace{\left[\frac{-e - \sqrt{e^2 - 4d(f - V)}}{2d}\right]}_{h_I(V) = [g_V(I)]^{-1}} u(V_{mp} - V) \tag{1.1}$$

where $V \in [0, V_{oc}]$, $g_V(I) = dI^2 + eI + f$, $u(\cdot)$ is the unit step and a, b, c, d, e, f are the model parameters. It will later be made clear why, among the two possible inverses of $g_V(I)$, the one with negative square root term is selected as $h_I(V)$.

Proposition 1: Assuming the I-V characteristic of a solar cell is described by Equation 1.1, the corresponding model parameters can be computed as:

$$a = \frac{I_{mp}}{(V_{oc} - V_{mp})^2} \cdot \left(\frac{V_{oc}}{V_{mp}} - 2\right) \tag{1.2}$$

$$b = -\frac{2V_{mp}I_{mp}}{(V_{oc} - V_{mp})^2} \cdot \left(\frac{V_{oc}}{V_{mp}} - 2\right) - \frac{I_{mp}}{V_{mp}} \tag{1.3}$$

$$c = \frac{I_{mp}V_{oc}}{V_{mp}} - \frac{V_{oc}I_{mp}(V_{oc} - 2V_{mp})^2}{V_{mp}(V_{oc} - V_{mp})^2} \tag{1.4}$$

$$d = -\frac{V_{mp}(2I_{mp} - I_{sc})}{I_{mp}(I_{mp} - I_{sc})^2} \tag{1.5}$$

$$e = \frac{2V_{mp}(2I_{mp} - I_{sc})}{(I_{mp} - I_{sc})^2} - \frac{V_{mp}}{I_{mp}} \tag{1.6}$$

$$f = \frac{V_{mp}I_{sc}(2I_{sc} - 3I_{mp})}{(I_{mp} - I_{sc})^2} \tag{1.7}$$

Proof: Five equations on the model parameters can be obtained by invoking conditions pertaining to the notable points, namely $g_V(I_{sc}) = 0$, $g_I(V_{oc}) = 0$, $g_I(V_{mp}) = I_{mp}$, $g_V(I_{mp}) = V_{mp}$ and $\partial_V g_I(V_{mp}) = -I_{mp}/V_{mp}$, where ∂_x denotes derivative with respect to x. A sixth equation can be obtained by enforcing equality of the derivatives of $g_I(V)$ and $[g_V(I)]^{-1}$ at $V = V_{mp}$ so that continuity is enforced. From orthogonality considerations, it is seen that this condition is given by $\partial_V g_I(V_{mp}) \cdot \partial_I g_V(I_{mp}) = 1$. Such equations constitute a nonlinear system on a, b, c, d, e, f and are given as follows:

$$aV_{oc}^2 + bV_{oc} + c = 0 \tag{1.8}$$

$$aV_{mp}^2 + bV_{mp} + c = I_{mp} \tag{1.9}$$

$$2aV_{mp} + b = -I_{mp}/V_{mp} \tag{1.10}$$

$$dI_{sc}^2 + eI_{sc} + f = 0 \tag{1.11}$$

$$dI_{mp}^2 + eI_{mp} + f = V_{mp} \tag{1.12}$$

$$2eI_{mp} + f = 1/(2aV_{mp} + b) \tag{1.13}$$

Despite its nonlinearity, the above system can be solved in a straightforward manner. First, solve Equations 1.8-1.10, which constitute a third order linear system, to obtain a, b and c. Then, substituting a and b in Equation 1.13, it is seen that Equations 1.11-1.13 become a third order linear system which is then solved for obtaining d, e and f. ■

Corollary 1: Among the two possible inverses of $g_V(I)$, only the negative sign one, namely $h_I(V)$, is physically meaningful.

Proof: First, assuming that $h_I(V)$ has been selected as the inverse and recalling that it is required that $\partial_V I(V) < 0$ for all $V \in [0, V_{oc}]$, it is seen from Equation 1.1 that, for $V \leq V_{mp}$, $\partial_V I(V) < 0$ iff $\partial_V h_I(V) < 0$. Computing such derivative, the expression $\partial_V h_I(V) = -1/\sqrt{e^2 - 4d(f - V)}$ is obtained, which satisfies $\partial_V I(V) < 0$ for all V. If the positive sign inverse had been selected, the corresponding derivative would always be greater than zero. Hence, the condition $\partial_V I(V) < 0$ would not be satisfied and the positive sign inverse is not physically meaningful, whereas $h_I(V)$ is valid in this sense. ■

1.3 Performance Evaluation

In order to validate the proposed model, it is compared to the ones from [16–18] for three solar cells of different manufacturing technologies, namely organic composite

polymer [19], legacy polycrystalline silicon [20] and thin-film triple junction with germanium substrate [21]. Such cells have fill factors equal to, respectively, 0.442, 0.709 and 0.833.

Evaluation of model performance is carried out as follows. An ODM characteristic $I_{\text{odm}}(V)$ is computed with the optimized ODM parameter values from [2]. Then, explicit model parameters are computed via notable point data and a corresponding characteristic $I(V)$ is obtained for each model. In all cases, current values are evaluated for voltage increments of $\delta V = 1$ μV. The characteristics are then used for computing normalized absolute error (NAE) curves $\xi(V)$ and normalized root mean square errors (NRMSE) [2]:

$$\xi(V) = \frac{1}{I_{sc}} \cdot |I_{\text{odm}}(V) - I(V)| \tag{1.14}$$

$$\text{NRMSE} = \sqrt{\frac{1}{N+1} \sum_{i=0}^{N} \left[\xi(i \cdot \delta V)\right]^2} \tag{1.15}$$

where $N = V_{oc}/\delta V$ is the number of I-V sample intervals. Finally, the absolute error curve $\zeta(V)$ of the derivative $\partial_V I(V)$ and its associated mean square error (RMSE) are also computed for each obtained characteristic; such computations are analogous to Equations 1.14 and 1.15, with the exception that a normalization factor is not used.

Obtained results are depicted in Figures 1-3. It should first be noted that the performances of models [16–18] conform to the analysis from [2]. In particular, it is seen that the model by Karmalkar and Haneefa [16] is more well-balanced when compared to [17, 18], since it does not suffer severe performance degradations for any solar cell.

The performance of the proposed model suggests it is a competitive approach, since it surpasses Karmalkar and Haneefa [16], both in terms of NRMSE and current derivative RMSE, for the polymer and silicon solar cells. Furthermore, it has second-best performance for the triple junction cell. Coupled with the fact that Equation 1.1 has an even more manageable form than the power law model proposed in [16], such results indicate that the proposed model is a strong candidate for usage in practical solar cell computations.

It should be noted that the ODM was employed as an error reference due to its high accuracy and wide practical usage. Also, a more thorough error assessment is enabled by using the ODM to generate a reference curve using small δV. In any case, to further corroborate this procedure, it must be ensured that $I_{\text{odm}}(V)$ is, in fact, an adequate reference against which the obtained $I(V)$ can be compared. To this effect, the aforementioned NRMSE computations are repeated with the ODM characteristic substituted by 20 equally-spaced points sampled graphically from the experimental solar cell I-V characteristics [19–21]; corresponding NRMSE values are given in Table 1.

The results displayed in Table 1 follow the same trend as those obtained by using $I_{\text{odm}}(V)$ as reference, which indicates that the considered cells have I-V characteristics

Figure 1 – Results obtained for the composite polymer solar cell.

Explanatory note: The subfigures correspond to plots of (a) current, (b) normalized absolute error of current and (c) absolute error of current derivative as functions of output voltage. The thinner "reference" curve is that yielded by application of the ODM. Presented values of RMSE and NMRSE are in the same units as their corresponding vertical axes.

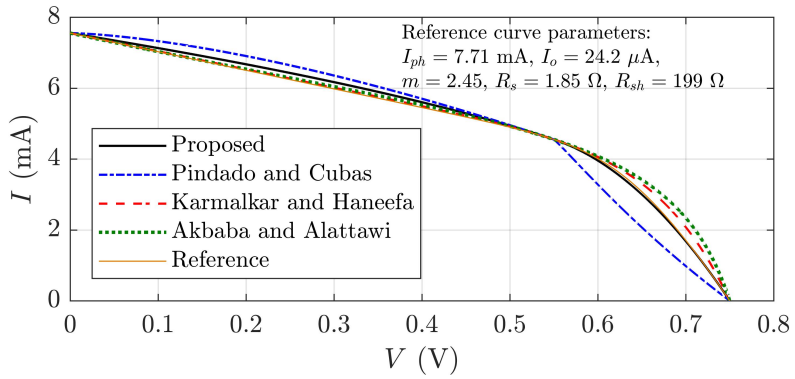

(a) Plots of I-V characteristics.

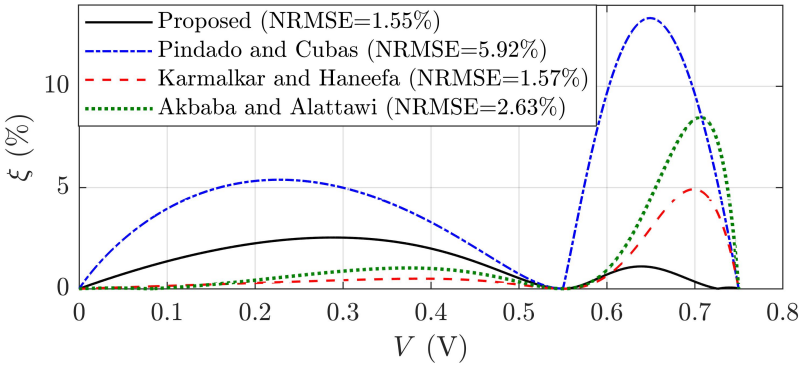

(b) Plots of current NRMSE.

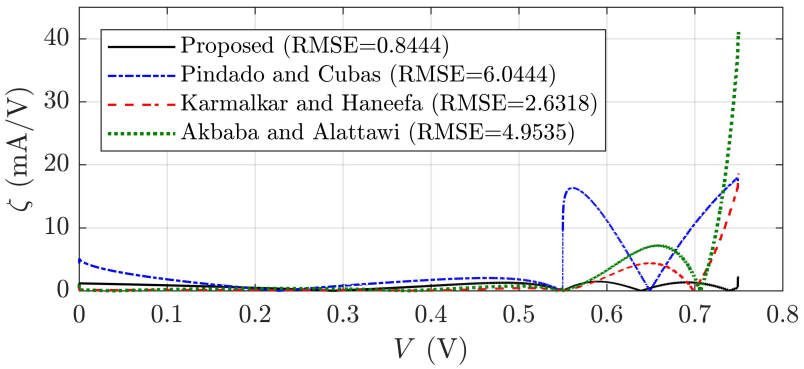

(c) Plots of current derivative RMSE.

Source: The author.

Figure 2 – Results obtained for the legacy silicon solar cell.

Explanatory note: The subfigures correspond to plots of (a) current, (b) normalized absolute error of current and (c) absolute error of current derivative as functions of output voltage. The thinner "reference" curve is that yielded by application of the ODM. Presented values of RMSE and NMRSE are in the same units as their corresponding vertical axes.

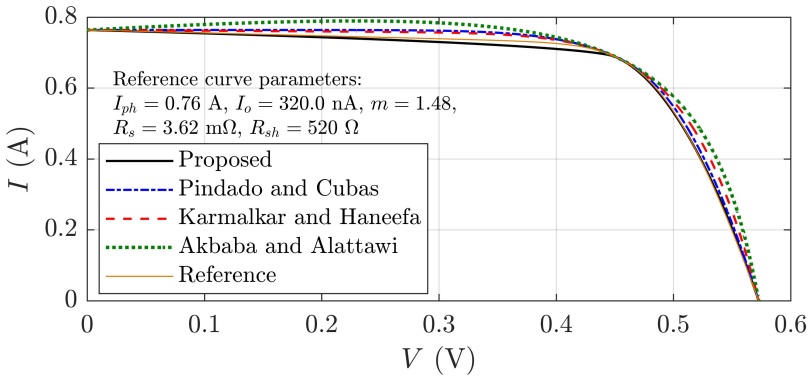

(a) Plots of I-V characteristics.

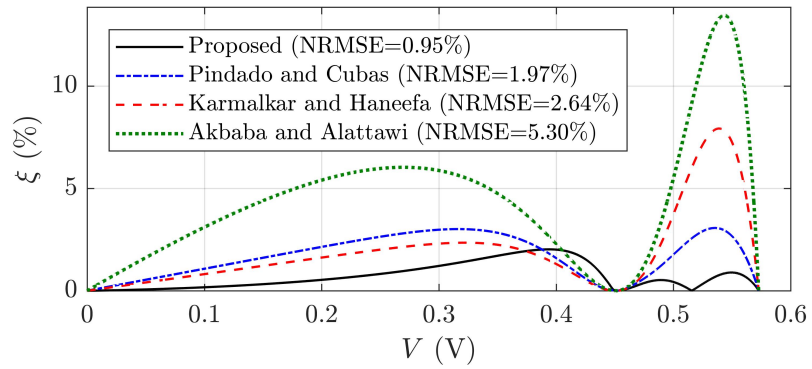

(b) Plots of current NRMSE.

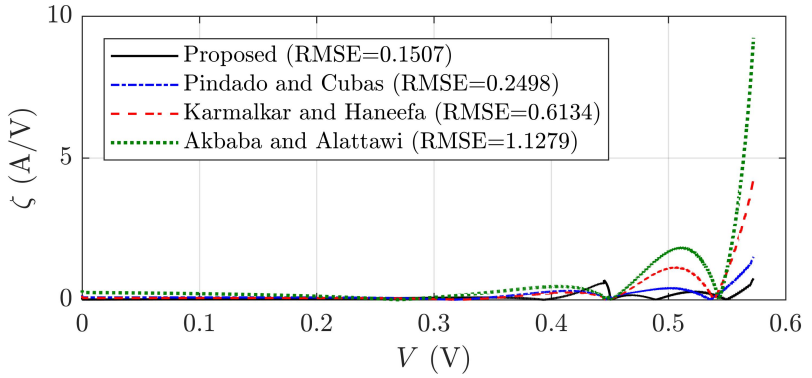

(c) Plots of current derivative RMSE.

Source: The author.

Figure 3 – Results obtained for the triple junction solar cell.

Explanatory note: The subfigures correspond to plots of (a) current, (b) normalized absolute error of current and (c) absolute error of current derivative as functions of output voltage. The thinner "reference" curve is that yielded by application of the ODM. Presented values of RMSE and NMRSE are in the same units as their corresponding vertical axes.

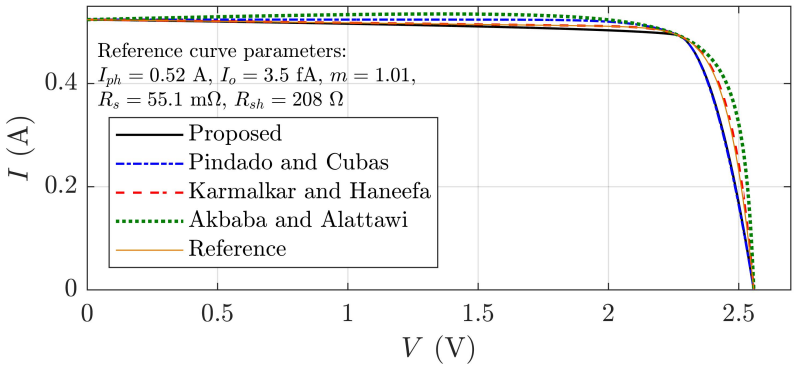

(a) Plots of I-V characteristics.

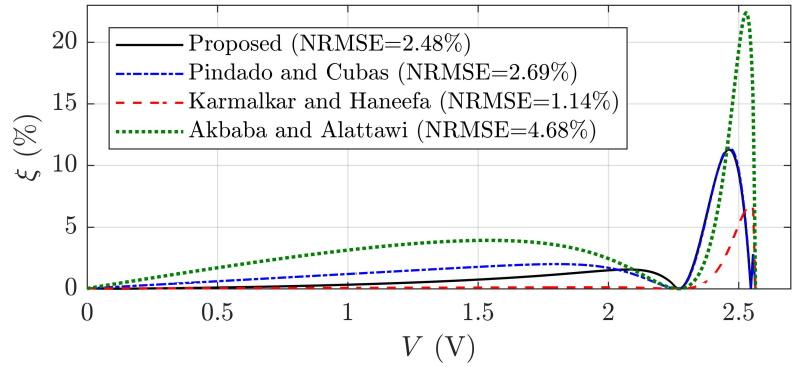

(b) Plots of current NRMSE.

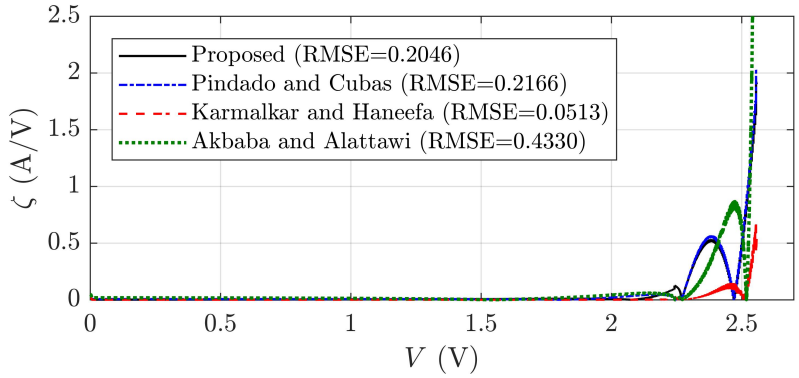

(c) Plots of current derivative RMSE.

Source: The author.

Table 1 – NRMSE with respect to samples of experimental I-V characteristics

Solar Cell	**NRMSE (%)**			
	Proposed	**[16]**	**[17]**	**[18]**
Composite polymer	1.53	1.54	5.81	2.60
Legacy silicon	0.93	2.58	1.93	5.19
Triple junction	2.53	0.77	2.73	3.87

Source: The author.

which are modelled precisely by the ODM. More importantly, the low NRMSE values attained with the proposed method confirm that it was capable of approximating not only the ODM, but the experimental solar cell I-V characteristics as well.

In accordance with the above analysis, it is fair to note that the proposed model is expected to incur in greater error for I-V curves which greatly deviate from the ODM, such as S-shaped characteristics of organic PV cells [22]. However, such increase in error would also occur in the ODM itself (with respect to the real I-V curve) and in the remaining explicit models, which were also designed for approximating ODM-type curves.

1.4 Explicit Operating Point Computation

In what follows, it is shown that the proposed model enables explicit computation of solar cell operating points in terms of load and ambient conditions. The model parameters a, b, c, d, e, f are functions of V_{oc}, V_{mp}, I_{sc} and I_{mp}, which are themselves functions of irradiance and temperature. In particular, $I_{sc}(S,T)$ and $V_{oc}(S,T)$ are given by [23, 24]:

$$I_{sc}(S,T) = I_{sc}(S_o,T_o)\cdot\frac{S}{S_o}\left[1+\alpha_I(T-T_o)\right] \tag{1.16}$$

$$V_{oc}(S,T) = N_s m V_t \ln\left(\frac{S}{S_o}\right) + V_{oc}(S_o,T_o)\cdot\left[1+\alpha_V(T-T_o)\right] \tag{1.17}$$

where $V_t = kq/T$ denotes thermal voltage, in which k is the Boltzmann constant and q is the elementary charge [1], T_o and S_o are nominal temperature and irradiance, α_I and α_V are the short circuit current and open circuit voltage temperature coefficients, m is the ideality factor and N_s is the number of elementary series-connected cells. Since m is an ODM parameter and is unknown in this case, $m = 1$ is henceforth assumed. This is a usual and accurate procedure, since the term containing m in Equation 1.17 is small [24].

It is known that, for any S and T, the ratios $K_V = V_{mp}/V_{oc}$ and $K_I = I_{mp}/I_{sc}$ are approximately constant [25]. Hence, maximum power conductance $G_{mp}(S,T)$ is given by:

$$G_{mp}(S,T) = \frac{I_{mp}(S,T)}{V_{mp}(S,T)} \approx K\cdot\frac{I_{sc}(S,T)}{V_{oc}(S,T)} \tag{1.18}$$

where $K = K_I/K_V$ can be computed from the solar cell notable points.

Proposition 2: Let R be a load connected to the output terminals of a solar cell at given S and T. Assuming the I-V characteristic is given by Equation 1.1, the operating point $\boldsymbol{X} = (V, I)$ can be computed as follows:

$$V = \left[\frac{1 - bR - \sqrt{(1-bR)^2 - 4ac}}{2aR}\right] u(G_{mp} - 1/R) + R\left[\frac{R - e - \sqrt{(R-e)^2 - 4df}}{2d}\right] u(1/R - G_{mp}) \tag{1.19}$$

and $I = V/R$, where $G_{mp} = G_{mp}(S, T)$.

Proof: If $G_{mp}(S,T) \leq 1/R$, then $V \leq V_{mp}$ and curve $h_I(V)$ contains $\boldsymbol{X}$, whereas $g_I(V)$ contains $\boldsymbol{X}$ for $G_{mp}(S,T) \geq 1/R$. In the first case, $\boldsymbol{X}$ is computed by solving $g_V(V/R) = V$, which yields the second term in Equation 1.19. Similarly, for the case $G_{mp}(S,T) \geq 1/R$, $\boldsymbol{X}$ is computed by solving $g_I(V) = V/R$, from which the first term is obtained. The signs of square root terms in Equation 1.19 derive from **Corollary 1**. ■

Hence, the proposed model can be used to carry out entirely analytical computation of the cell operating point, which is highly desirable for simulation purposes. Note that the explicit computation of operating points is not straightforward and requires numerical procedures when using the other explicit models considered in Section 1.3. In fact, for such models, enforcement of the condition $I(V) = V/R$ results either in fractional-power [16,17] or cubic [18] polynomial equations in V.

1.5 Application Example

To illustrate the above-derived explicit operating point computation, a simulation of the triple junction solar cell subjected to varying ambient conditions is considered. Given a resistive load R fed by the cell, an irradiance profile $S(t)$ and a temperature profile $T(t)$, the simulation objective is computing the output power waveform $P(t) = V(t)I(t)$.

The triple junction cell parameters required for computing Equations 1.2-1.7 and 1.16-1.18 are given in its datasheet [21]. In particular, note that its maximum power rating is $P_{mp} = 1.126$ W at $S_o = 1350$ W/m^2 and $T_o = 28$°C. Furthermore, its associated maximum power conductance is $G_{mp} = 0.22$ S. The adopted $S(t)$ is a real 24-hour irradiance profile with one minute time resolution, which was measured at the School of Electrical, Mechanical and Computer Engineering of the Federal University of Goiás on January 1st, 2021. Identical considerations apply to $T(t)$, which was measured on the same day and location as $S(t)$ [26]. The waveforms $S(t)$ and $T(t)$ are depicted in Figure 4. Three

Figure 4 – Considered irradiance and temperature profiles.

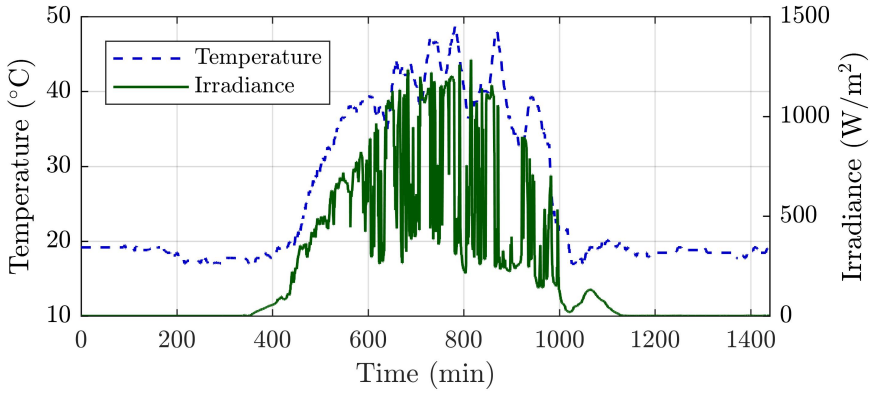

Source: The author.

different loads are considered for simulation: an approximately matched load ($R = 5\ \Omega$) and two strongly mismatched loads, one of them towards short circuit ($R = 1\ \Omega$) and the other towards open circuit ($R = 25\ \Omega$) operation of the solar cell.

In Figures 5-7, the output power curves yielded by Equation 1.19 and the optimal ODM [2] are presented, together with corresponding RMSE (with the ODM taken as reference) in miliwatts. The $P(t)$ plots confirm the high accuracy of the proposed model, which was able to closely reproduce the solar cell dynamics for real ambient conditions. It should be noted that RMSE is larger for the matched load case because the output power itself is greater. In any case, it is seen from Figures 5-7 that all simulations yielded RMSE values which are two orders of magnitude below $\max_t P(t)$.

Different loads were considered to provide a more reliable validation of the model. The short circuit load drives the solar cell towards the $V < V_{mp}$ region, in which case $h_I(V)$ is predominantly active in Equation 1.1. For analogous reasons, $g_I(V)$ dominates Equation 1.1 for the open circuit load. Finally, the matched load makes the model switch between the two quadratic curves in terms of the ambient conditions. Hence, the considered simulation cases adequately contemplate the full solar cell operating range $V \in [0, V_{oc}]$.

To further clarify the usefulness of explicit operating point computation by means of Equation 1.19, consider simulation of dynamic ambient conditions with the ODM. Since ODM is implicit, operating point computation at each iteration requires terminal voltage feedback to a numerical solver, whose output is then used to drive a controlled current source model [27]. This approach establishes a voltage algebraic loop, since the cell output voltage at a given iteration is computed as a function of its value at the previous iteration. Hence, aside from increased processing time due to numerical computations, the simulation can be subject to convergence errors [28] due to unstable interactions between the algebraic loop and system dynamics. On the other hand, the closed form of Equation 1.19 entirely avoids the voltage loop problem during simulation, thereby inhibiting convergence errors.

Figure 5 – Plots of output power obtained by applying the proposed method and the one-diode model for the approximately matched load.

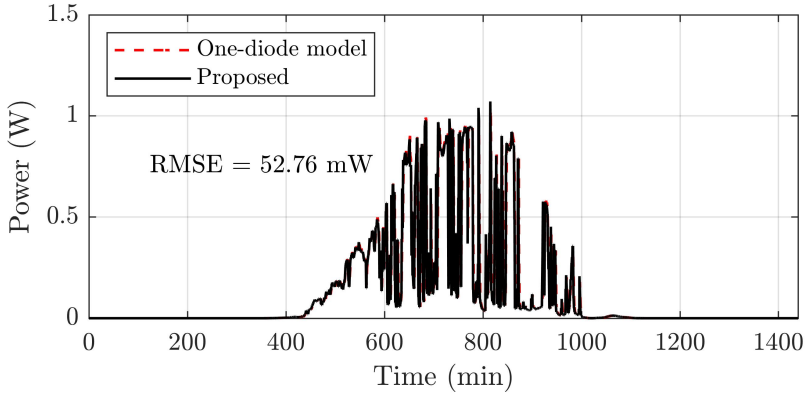

Source: The author.

Figure 6 – Plots of output power obtained by applying the proposed method and the one-diode model for the mismatched open circuit load.

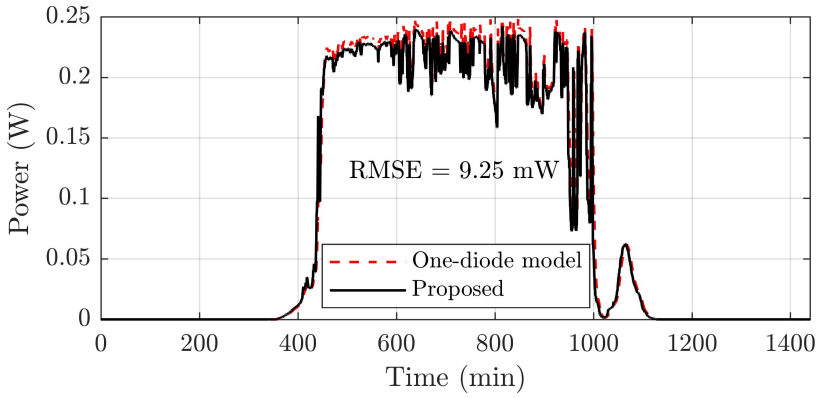

Source: The author.

Figure 7 – Plots of output power obtained by applying the proposed method and the one-diode model for the mismatched short circuit load.

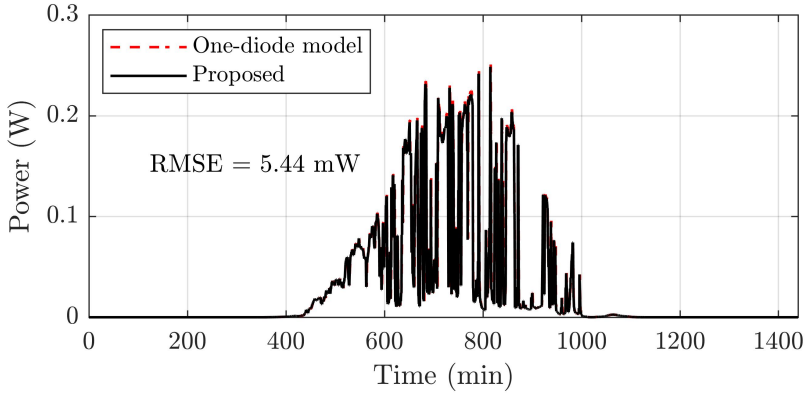

Source: The author.

Coupled with convenient analytical and explicit computation of solar cell operating points, the above-described results suggest the proposed method is an excellent tool for carrying out practical simulations of photovoltaic power generation.

1.6 Conclusion

A novel explicit I-V model for solar cells has been proposed, which consists of two quadratic curves in inverse orthogonal coordinate systems and joined at the maximum power point. Comparison against the most relevant explicit models in the literature showed that it has superior flexibility in fitting a variety of solar cell I-V characteristics. It was also shown that it has the unique feature of enabling the explicit and accurate computation of cell operating points, which is a major advantage when simulating photovoltaic generation.

2 Enhancing the Quadratic Solar Cell Model via Low Complexity Direct Search

2.1 Introduction

Usage of the ODM for the modeling of solar cell I-V characteristics has become a staple approach due to its advantages of high accuracy and physically meaningful model parameters [1, 23]. In particular, the latter feature makes it an indispensable tool for calculations during the practical design of solar cells [29].

Despite its usefulness, some criticisms to the ODM have emerged in the literature with regard to its application in higher-level (i.e., not cell design) circuit analysis. It has been argued that, in such scenarios, the modeling priority lies in obtaining explicit I-V models whose parameters can be extracted either analytically or via trivial optimization procedures, regardless of whether such parameters provide any direct physical meaning [2]. It is well-known that such requirements are not satisfied by the ODM, since it is an implicit model [i.e., $I = g(V, I)$] and the extraction of its parameters is far from straightforward. A confirmation of this latter fact is given by the sheer number of existing methods for ODM parameter extraction, each of which establishes a different compromise between accuracy of the I-V curve fitting and required computational processing [30].

To provide some brief context on existing ODM parameter extraction procedures, attention is directed to the two dominant general approaches. One of them consists in making use of simplifying approximations to compute all parameters in terms of three so-called remarkable operating points (open circuit, short circuit and maximum power); methods of this type [5–9] are less accurate but very fast due to being analytical. The other general approach is using multivariable optimization to compute ODM parameters via minimization of root mean square error (RMSE) of the predicted I-V curve with respect to the empirically sampled characteristic; such methods [3, 4, 31–41] have high accuracy, but require larger execution times due to the relatively wide five-dimensional variable domain that must be explored during optimization [42].

A third, albeit less common, type of parameter extraction approach is described as follows. First, the remarkable points are used to express some ODM parameters as functions of the remaining ones, which are treated as free parameters. Then, a low-dimensional direct search is carried out over the free parameters to minimize RMSE with respect to the empirical I-V curve. Such methods [27, 43, 44] are more accurate than the analytical ones (due to RMSE minimization) and faster than the optimization-based ones (due to usage of low-dimensional direct search), which leads to an adequate compromise between accuracy

and computational burden. At last, an added advantage is that direct search is trivial to implement. As will soon be explained, such benefits of this general approach to parameter extraction are the motivation behind the contribution proposed in this Chapter.

2.1.1 The Explicit Two-Piece Quadratic Model

Based on the aforementioned criticisms to the ODM, a number of explicit I-V models have been proposed in the literature [13–18] to avoid its disadvantages. Such models have equations of form $I = g(V)$ whose parameters can be computed analytically from the remarkable points. In [2], a comprehensive assessment of the models from [13–18] was carried out. Despite concluding that the power law model [16] performs better in most cases, it was found out that all models presented significantly worsened performances for specific solar cell fill factor (FF) ranges. Taking this problem into account, the explicit two-piece quadratic model (ETPQM) was proposed in Chapter 1, which was shown to always perform better or comparably to the power law model, yet with more consistency over a wide FF range.

For better understanding, briefly recall the ETPQM equation and its analytical parameter extraction from Chapter 1. The I-V equation of ETPQM is:

$$I(V) = \underbrace{[aV^2 + bV + c]}_{g_I(V)}\, u(V - V_{mp}) + \underbrace{\left[\frac{-e - \sqrt{e^2 - 4d(f - V)}}{2d}\right]}_{h_I(V) = [g_V(I)]^{-1}} u(V_{mp} - V) \qquad (2.1)$$

where $V \in [0, V_{oc}]$, $g_V(I) = dI^2 + eI + f$, $u(\cdot)$ is the unit step and a, b, c, d, e and f are the model parameters, which can be extracted analytically via Equations 1.2-1.7.

2.1.2 Proposed Contribution

Recall from the previous discussion on ODM parameter extraction that the fully analytical methods are less accurate since they only consider the I-V curve remarkable points and, as a consequence, do not minimize RMSE with respect to a sampled I-V characteristic. It is clear that identical considerations apply to the ETPQM parameter extraction given by Equations 1.2-1.7 and, as a consequence, it is expected that computing a, b, c, d, e and f via RMSE minimization will improve the accuracy of Equation 2.1.

However, using multivariable optimization would lead to possibly even greater execution time than in the ODM case, since it would imply dealing with a six-dimensional optimization whose variables (a, b, c, d, e and f) bring the additional difficulty of not having reasonably well-known domain bounds. Hence, the remaining alternative for improving ETPQM accuracy with small execution time is to devise a low-complexity search-based parameter extraction method, similarly to those proposed in [27, 43, 44] for the ODM.

The above discussion leads precisely to the contribution presented in this Chapter. A search-based method for extracting the ETPQM parameters is proposed which enhances model accuracy when compared to the original explicit equations. It consists in using a new I-V point condition that allows expressing all model parameters as functions of an auxiliary parameter which belongs to a subset of the unit interval. Hence, the ETPQM parameters are extracted via one-dimensional direct search, whose complexity is further reduced due to the narrow domain to which the auxiliary parameter belongs.

In brief, the approach proposed in this Chapter is advantageous in that it further enhances accuracy of the ETPQM equation proposed in Chapter 1 with a minor trade-off, namely the short execution time (which will be shown to lie in the milisecond range) required for executing a single-variable search in a small domain.

2.2 Low-Complexity Search-Based ETPQM Parameter Extraction

The proposed parameter extraction method is derived in what follows. A scheme of Equation 2.1 is given in Figure 8, where the unused parts of curves $g_I(V)$ and $g_V(I)$ are drawn as dashed lines and the conditions pertaining to remarkable points are indicated by arrows. In the analytical parameter extraction method obtained in Chapter 1, the following conditions were used to compute a, b, c, d, e and f:

- $g_V(I_{sc}) = 0$ (short circuit current);
- $g_I(V_{oc}) = 0$ (open circuit voltage);
- $g_I(V_{mp}) = I_{mp}$ (maximum power current);
- $g_V(I_{mp}) = V_{mp}$ (maximum power voltage);
- $\partial_V g_I(V_{mp}) \cdot \partial_I g_V(I_{mp}) = 1$ (orthogonality);
- $\partial_V g_I(V_{mp}) = -\frac{I_{mp}}{V_{mp}}$ (current derivative at maximum power);

In particular, the condition $\partial_V g_I(V_{mp}) = -\frac{I_{mp}}{V_{mp}}$ is less strict than the remaining ones. It only enforces a current derivate value, whereas the other conditions interpolate the remarkable points and ensure that Equation 2.1 is differentiable at V_{mp}. Hence, it is proposed that this condition be substituted by $g_I(\gamma V_{oc}) = 0$, as indicated in Figure 8, where γ is the so-called auxiliary parameter. In what follows, it is shown in **Lemma 1** that γ necessarily belongs to a subset of interval $[0, 1]$.

Lemma 1: The parameter $\gamma \in [0, 1]$. Moreover, if $V_{mp} \geq \frac{V_{oc}}{2}$, then it also true that $\gamma \in \Gamma = [0, \gamma_{\max}]$, where $\gamma_{\max} = 2V_{mp}/V_{oc} - 1$.

Figure 8 – Scheme of the quadratic model. The condition marked with one asterisk is used in the original analytical method, whereas the proposed approach substitutes it by the one marked with two asterisks.

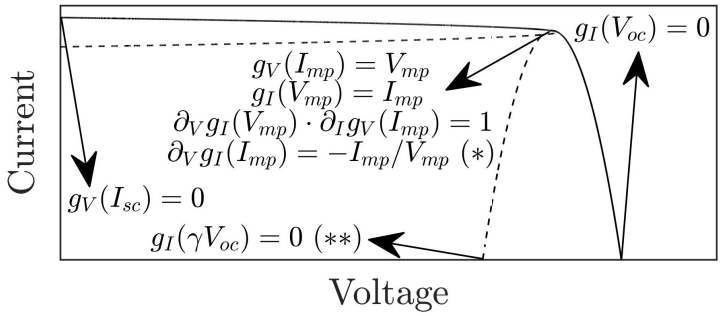

Source: The author.

Proof: First, let $V_{mp} \geq \frac{V_{oc}}{2}$. From physical considerations, $\partial_V I < 0$ must be satisfied for all $V \in [0, V_{oc}]$. It is seen from Figure 8 that this requirement is satisfied if and only if $V_{mp} - \gamma V_{oc} \geq V_{oc} - V_{mp}$, otherwise the intercept of $g_I(V)$ and $h_I(V)$ at V_{mp} would be such that $\partial_V g_I(V_{mp}) > 0$, which is not allowable. Hence, the maximum value of γ is obtained by enforcing equality, from which $\gamma_{\max} = 2V_{mp}/V_{oc} - 1$ is obtained. For $V_{mp} < \frac{V_{oc}}{2}$, it is seen from Equation 1.2 that $g_I(V)$ is a convex parabola and $\partial_V g_I(V_{mp}) < 0$ is thus satisfied for any value of γ. Now, since the parabola is: (i) convex, (ii) passes through (V_{mp}, I_{mp}) and (iii) has V_{oc} as its rightmost intercept at the V-axis, it is necessary that $\gamma < 1$. ■

Since $V_{mp} > \frac{V_{oc}}{2}$ for usual cells, it is seen that **Lemma 1** further reduces the already narrow domain of parameter γ. We now proceed to deriving **Proposition 3**, in which the ETPQM parameters are expressed as functions of γ.

Proposition 3: Assuming the I-V quadratic model given in Equation 2.1, its associated parameters can be computed as:

$$a = K \cdot (I_{mp} - I_{sc}) \tag{2.2}$$

$$b = -K \cdot (1 + \gamma)(I_{mp} - I_{sc})V_{oc} \tag{2.3}$$

$$c = K \cdot \gamma(I_{mp} - I_{sc})V_{oc}^2 \tag{2.4}$$

$$d = K - V_{mp}(I_{mp} - I_{sc})^{-2} \tag{2.5}$$

$$e = 2V_{mp}I_{mp}(I_{mp} - I_{sc})^{-2} - K \cdot (I_{mp} + I_{sc}) \tag{2.6}$$

$$f = K \cdot I_{mp}I_{sc} + V_{mp}I_{sc}(I_{sc} - 2I_{mp})(I_{mp} - I_{sc})^{-2} \tag{2.7}$$

where $K = -\frac{I_{mp}}{(I_{mp}-I_{sc})(V_{mp}^2-(1+\gamma)V_{oc}V_{mp}+\gamma V_{oc}^2)}$.

Proof: By enforcing the remarkable point conditions to Equation 2.1 with the derivative condition substituted by $g_I(\gamma V_{oc}) = 0$, a system on a, b, c, d, e and f is obtained:

$$aV_{oc}^2 + bV_{oc} + c = 0 \tag{2.8}$$

$$a\gamma^2 V_{oc}^2 + b\gamma V_{oc} + c = 0 \tag{2.9}$$

$$aV_{mp}^2 + bV_{mp} + c = I_{mp} \tag{2.10}$$

$$dI_{sc}^2 + eI_{sc} + f = 0 \tag{2.11}$$

$$dI_{mp}^2 + eI_{mp} + f = V_{mp} \tag{2.12}$$

$$2dI_{mp} + e = 1/(2aV_{mp} + b) \tag{2.13}$$

The nonlinearity of Equation 2.13 does not prevent the computation of a solution. To achieve this, first solve Equations 2.8-2.10, which constitute a linear system on a, b and c. Then, manipulate the obtained expressions algebrically to arrive at Equations 2.2-2.4. Substituting a and b into Equation 2.13, it is seen that Equations 2.11-2.13 become a linear system on d, e, f, which is then solved for obtaining Equations 2.5-2.7. ■

In this sense, all parameters in Equation 2.1 have been expressed as functions of γ via Equations 2.2-2.7. It remains to determine the optimal γ^* value, which is defined as the one that minimizes NRMSE with respect to an empirically sampled I-V characteristic $I_{\text{ref}}(V)$. The current NAE and NMRSE, which are henceforth denoted by ξ and Ξ, are:

$$\xi(V) = \frac{1}{I_{sc}} \cdot |I(V) - I_{\text{ref}}(V)| \tag{2.14}$$

$$\Xi = \left[\frac{1}{N_v}\sum_{i=1}^{N_v} \xi^2(V_i)\right]^{1/2} \tag{2.15}$$

where V_i, $i = 1, 2, \ldots, N_v$, is the i-th sample of the empirical I-V curve. Note that, since I_{sc} is a constant, the minimization of NRMSE is equivalent to that of RMSE.

Remark 2.1: Note that, unlike in Chapter 1, the direct approach of computing NAE and NRMSE with reference to empirical I-V characteristics is considered. Aside from being more representative of a practical scenario, this is also done because solar cells that are *not* well-modeled by the ODM shall be considered.

Hence, the ETPQM parameter extraction has been reduced to solving the single-variable optimization $\gamma^* = \text{argmin}_{\gamma\in\Gamma}\,\Xi$. Since Γ is a narrow interval (as established by **Lemma 1**), it is simply proposed that it be discretized according to an increment $\Delta\gamma$ and optimization be carried out via direct search over $\mathcal{G} = \{i \cdot \Delta\gamma \mid i = 0, 1, \ldots, N_\gamma\}$, where $N_\gamma = \gamma_{\max}/\Delta\gamma$. In other words, Ξ is evaluated for every $\gamma \in \mathcal{G}$ and γ^* is selected as the value that minimizes Ξ.

Remark 2.2: The proposed optimization uses the simplest possible implementation of direct search, which consists in searching Γ by means of fixed steps $\Delta\gamma$. This implementation is named *compass search* by some authors [45].

2.3 Required Number of Operations

Consider the number of operations required by the proposed method, where the evaluation of NRMSE via Equations 2.14 and 2.15 is counted as the basic elementary operation. Since the method evaluates Ξ for all $\gamma \in \mathcal{G}$ and $\gamma_{\max} = \sup\mathcal{G}$, it is clear that the total number of operations is $1 + \frac{\gamma_{\max}}{\Delta\gamma}$, which has the favorable property of being linear in $\frac{1}{\Delta\gamma}$. Since $\gamma_{\max} \leq 1$, the number of operations is clearly bounded.

Furthermore, the proposed method has an easily tunable trade-off between accuracy and processing time. For instance, if a premium is put on fast execution time, this can be obtained by increasing $\Delta\gamma$, which reduces the number of computations linearly at the expense of model accuracy due to a coarser search of Γ being carried out.

For the sake of comparison, consider the required number of operations in the low-complexity search-based ODM parameter extraction methods from [27, 43, 44]. In [27], a single-variable search is carried out over the ODM series resistance R_s according to an increment ΔR_s; this implies linearity with respect to $\frac{1}{\Delta R_s}$, but bounds on R_s are cell-dependent and cannot be defined in a general manner. In [43], a search over the ODM ideality factor m is carried out with increment Δm and is followed by a search over R_s. Hence, the number of operations is linear with respect to $\frac{1}{\Delta R_s}$ and $\frac{1}{\Delta m}$. Since it is known that $m \in [1, 2]$ is a reasonable search interval, this amounts to an expected $1 + \frac{1}{\Delta m}$ additional operations compared to [27]. On the other hand, a two-dimensional search over R_s and m is carried out in [44]. As a consequence, the number of operations is no longer linear on the increment reciprocals. Instead, it is proportional to $\frac{1}{\Delta R_s \Delta m}$, which may lead to much larger execution times for small values of ΔR_s or Δm.

It is thus seen, from this brief comparison, that the method proposed in this Chapter compares favorably to [27, 43, 44] with regard to the number of required operations, since it not only is linear with respect to a single variable but, even more importantly, has general, tight and well-defined bounds on its variable γ.

2.4 Validation of the Proposed Method

The ETPQM itself has already been validated in Chapter 1 against other explicit I-V models from the literature. Hence, focus is given to comparing the proposed ETPQM parameter extraction method with the analytical procedure given by Equations 1.2-1.7 and with the ODM-based search methods from [27, 43, 44].

2.4.1 Methodology

Validation is carried out by applying each method to five solar cells. The selected cells have distinct manufacturing technologies and very different FF values to provide a more robust assessment. The considered solar cells are as follows:

- Monocrystalline silicon, $FF = 0.773$ [46];
- Polycrystalline silicon, $FF = 0.709$ [20];
- Thin-film with germanium substrate, $FF = 0.833$ [21];
- Organic (composite polymer), $FF = 0.442$ [19];
- Organic with titanium oxide layer, $FF = 0.147$ [47].

For computing NRMSE, $N_v = 50$ points with approximately equal spacing were sampled graphically from the empirical I-V characteristics reported in [19–21, 46, 47]. As additional metrics for evaluating model accuracy, the NAEs and NRMSEs of output power $P = VI$ and current derivative $\partial_V I$ are also considered. Such metrics are defined as:

$$\psi(V) = \frac{1}{P_{mp}} \cdot |P(V) - P_{\text{ref}}(V)| \tag{2.16}$$

$$\Psi = \left[\frac{1}{N_v} \sum_{i=1}^{N_v} \psi^2(V_i) \right]^{1/2} \tag{2.17}$$

$$\zeta(V) = \frac{1}{|\partial_V I_{\text{ref,m}}|} \cdot |\partial_V I(V) - \partial_V I_{\text{ref}}(V)| \tag{2.18}$$

$$Z = \left[\frac{1}{N_v} \sum_{i=1}^{N_v} \zeta^2(V_i) \right]^{1/2} \tag{2.19}$$

where ψ and Ψ are power NAE and NRMSE, ζ and Z are current derivative NAE and NRMSE, $P_{mp} = V_{mp} I_{mp}$ is the cell nominal maximum power and $\partial_V I_{\text{ref,m}}$ is the maximum current derivative (in absolute value) computed for the empirical curve.

We consider an increment $\Delta\gamma = 0.1\%$ for carrying out direct search with the proposed method. For the ODM-based methods, $\Delta m = 0.001$ is used for the ideality

factor with search bounds $m \in [1, 2]$. On the other hand, recalling that R_s is strongly cell-dependent, the following reasonable guesses are used. For the solar cells with currents in the miliampere range, $\Delta R_s = 1\ \Omega$ and $R_s \in [0, 100]\ \Omega$, whereas for those whose currents are in the ampere range, $\Delta R_s = 1$ mΩ and $R_s \in [0, 100]$ mΩ.

2.4.2 Results

The obtained results are given in Figures 9 to 13 and Tables 2 to 6. For each solar cell, the following information is presented in the figures: (i) sample points drawn from the empirical I-V characteristic; (ii) $I(V)$, $P(V)$, $\xi(V)$, $\psi(V)$ and $\zeta(V)$ plots obtained with each parameter extraction method; and (iii) the optimization trajectory $\Xi(\gamma)$ yielded by the proposed method. The following data are displayed in the tables for each solar cell: (i) values of Ξ, Ψ and Z for each method; (ii) execution time of each method, in miliseconds and rounded up to the nearest integer (i.e., $\lceil T \rceil$, where T is execution time); and (iii) whether each method provided an adequate fit of the maximum power point (MPP).

Remark 2.3: Implementation and execution of all considered methods was carried out in MATLAB R2017a on a laptop equipped with an Intel quad-core 2.7 GHz processor and 8 GB of RAM. The processing times were measured by using the *tic/toc* commands.

Remark 2.4: We define the MPP fit as adequate if the estimated P-V curve has its maximum at a voltage value within a $\pm 1\%$ range of the solar cell nominal V_{mp}.

In what follows, the results obtained for each of the considered solar cells are briefly described. Then, a discussion on the most relevant aspects of such results is carried out.

Table 2 – Performance metrics of each method for the monocrystalline cell

Method	Ξ (%)	Z (%)	Ψ (%)	$\lceil T \rceil$ (ms)	MPP fit
Villalva et al. [27]	1.3282	2.1146	1.5844	2567	Adequate
Vieira and Corrêa [43]	0.4523	0.4514	0.5244	2801	Adequate
Rhouma et al. [44]	0.2757	0.3932	0.2961	24434	Adequate
Analytical method (Ch. 1)	2.1539	3.1778	2.3508	1	Adequate
Proposed method	1.6136	2.1847	1.5306	7	Adequate

Source: The author.

Table 3 – Performance metrics of each method for the polycrystalline cell

Method	Ξ (%)	Z (%)	Ψ (%)	$\lceil T \rceil$ (ms)	MPP fit
Villalva et al. [27]	0.3804	1.2902	0.4009	2362	Adequate
Vieira and Corrêa [43]	0.3804	1.2902	0.4009	2593	Adequate
Rhouma et al. [44]	0.2439	0.4018	0.2224	25581	Adequate
Analytical method (Ch. 1)	0.9337	1.5386	0.8505	1	Adequate
Proposed method	0.9330	1.4992	0.8451	6	Adequate

Source: The author.

Figure 9 – Obtained results for the monocrystalline solar cell.

Explanatory note: The results are comprised of plots of (a) the current NRMSE optimization trajectory of the proposed method and the current NRMSE values yielded by the other considered methods, (b) I-V characteristics, (c) P-V characteristics, (d) current NAE curves, (e) power NAE curves and (f) current derivative NAE curves. The plotted curves are identified as follows: Villalva et al. [27] (thin solid line, magenta), Vieira and Corrêa [43] (alternating traced line, blue), Rhouma et al. [44], analytical method (traced line, red), proposed method (solid line, black) and empirical I-V samples (gray round markers, only in I-V and P-V plots). Numerical values of current NRMSE, current derivative NRMSE, power NRMSE and execution time are given in Table 1.

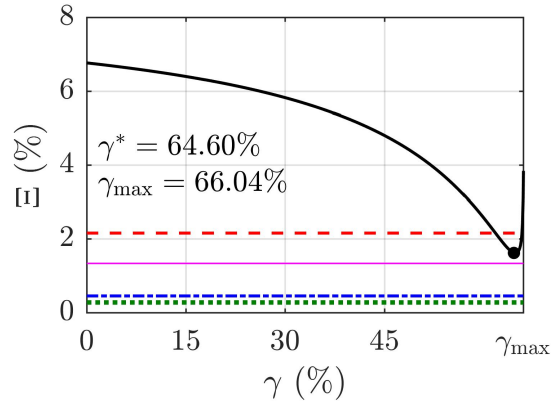

(a) Illustration of optimization trajectory.

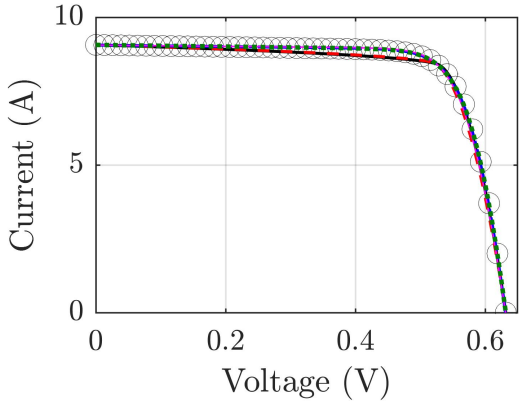

(b) Current-voltage plots.

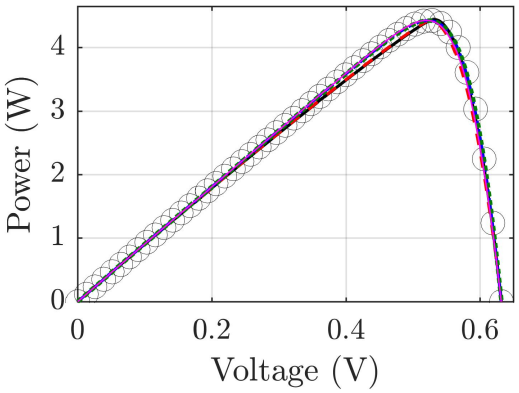

(c) Power-voltage plots.

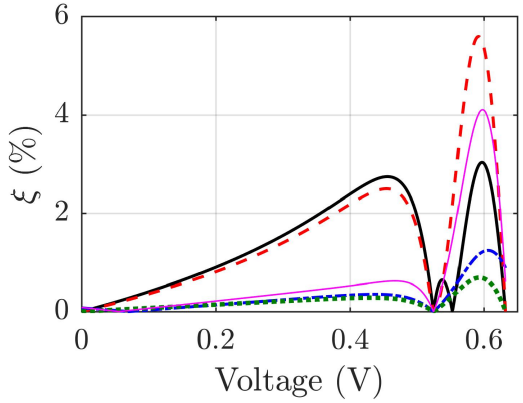

(d) Current NAE plots.

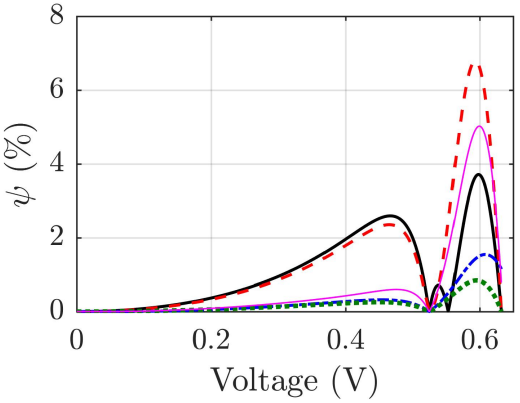

(e) Power NAE plots.

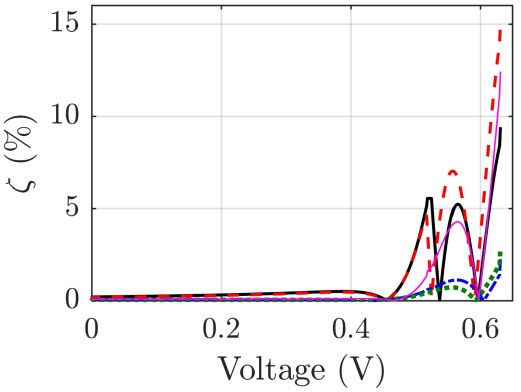

(f) Current derivative NAE plots.

Source: The author.

Figure 10 – Obtained results for the polycrystalline solar cell.

Explanatory note: The results are comprised of plots of (a) the current NRMSE optimization trajectory of the proposed method and the current NRMSE values yielded by the other considered methods, (b) I-V characteristics, (c) P-V characteristics, (d) current NAE curves, (e) power NAE curves and (f) current derivative NAE curves. The plotted curves are identified as follows: Villalva et al. [27] (thin solid line, magenta), Vieira and Corrêa [43] (alternating traced line, blue), Rhouma et al. [44], analytical method (traced line, red), proposed method (solid line, black) and empirical I-V samples (gray round markers, only in I-V and P-V plots). Numerical values of current NRMSE, current derivative NRMSE, power NRMSE and execution time are given in Table 2.

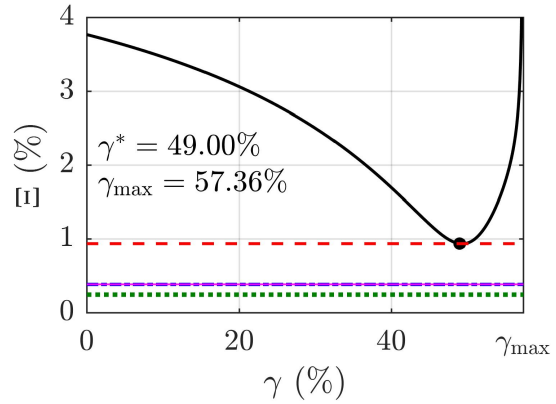

(a) Illustration of optimization trajectory.

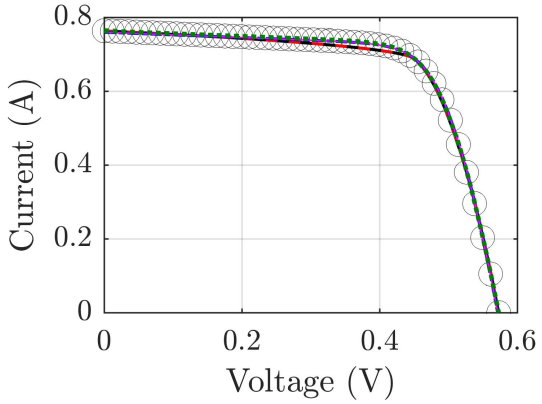

(b) Current-voltage plots.

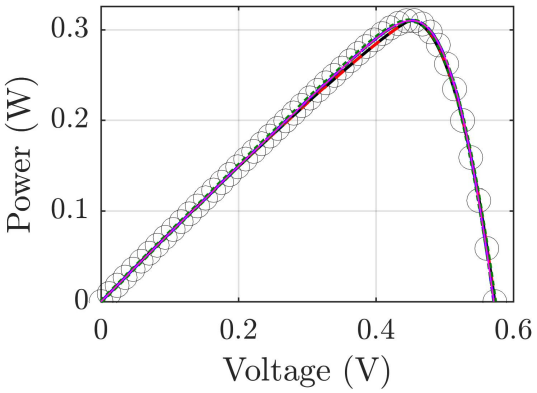

(c) Power-voltage plots.

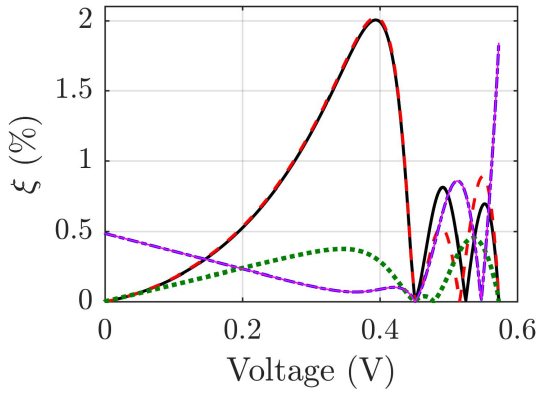

(d) Current NAE plots.

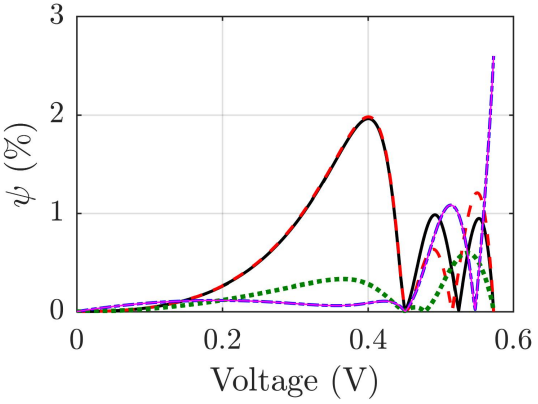

(e) Power NAE plots.

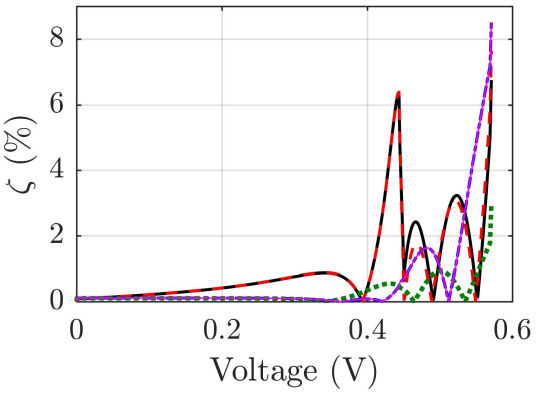

(f) Current derivative NAE plots.

Source: The author.

Figure 11 – Obtained results for the thin-film solar cell.

Explanatory note: The results are comprised of plots of (a) the current NRMSE optimization trajectory of the proposed method and the current NRMSE values yielded by the other considered methods, (b) I-V characteristics, (c) P-V characteristics, (d) current NAE curves, (e) power NAE curves and (f) current derivative NAE curves. The plotted curves are identified as follows: Villalva et al. [27] (thin solid line, magenta), Vieira and Corrêa [43] (alternating traced line, blue), Rhouma et al. [44], analytical method (traced line, red), proposed method (solid line, black) and empirical I-V samples (gray round markers, only in I-V and P-V plots). Numerical values of current NRMSE, current derivative NRMSE, power NRMSE and execution time are given in Table 3.

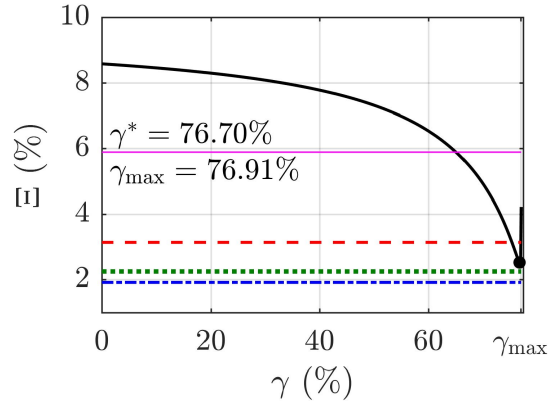

(a) Illustration of optimization trajectory.

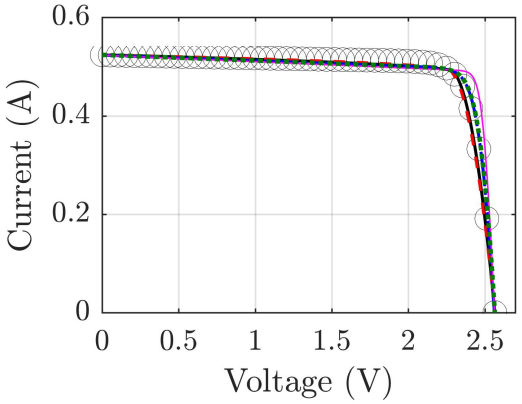

(b) Current-voltage plots.

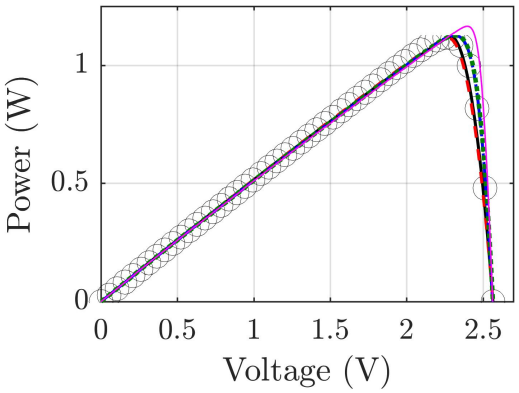

(c) Power-voltage plots.

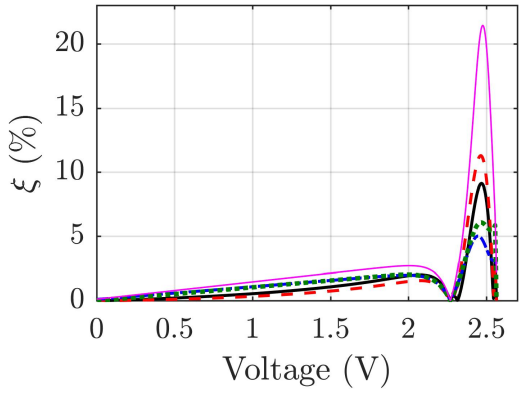

(d) Current NAE plots.

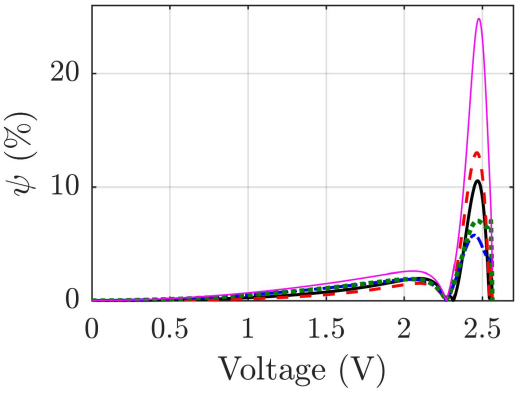

(e) Power NAE plots.

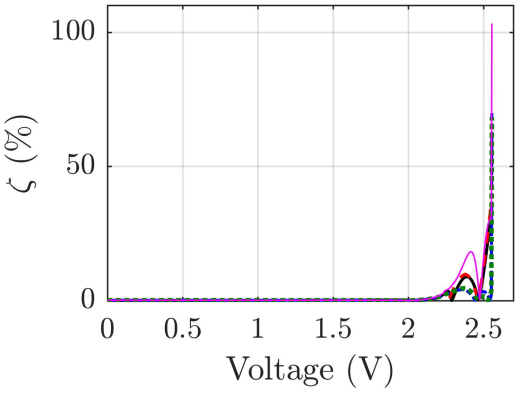

(f) Current derivative NAE plots.

Source: The author.

Figure 12 – Obtained results for the organic solar cell.

Explanatory note: The results are comprised of plots of (a) the current NRMSE optimization trajectory of the proposed method and the current NRMSE values yielded by the other considered methods, (b) I-V characteristics, (c) P-V characteristics, (d) current NAE curves, (e) power NAE curves and (f) current derivative NAE curves. The plotted curves are identified as follows: Villalva et al. [27] (thin solid line, magenta), Vieira and Corrêa [43] (alternating traced line, blue), Rhouma et al. [44], analytical method (traced line, red), proposed method (solid line, black) and empirical I-V samples (gray round markers, only in I-V and P-V plots). Numerical values of current NRMSE, current derivative NRMSE, power NRMSE and execution time are given in Table 4.

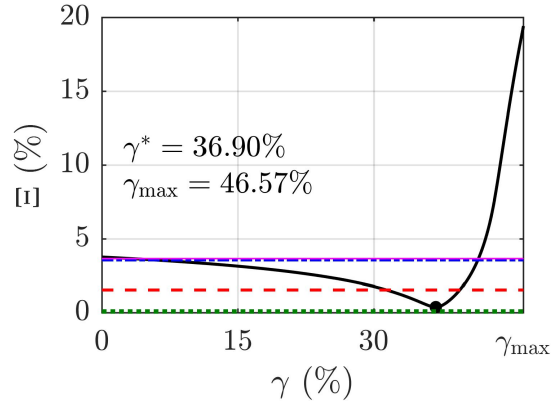

(a) Illustration of optimization trajectory.

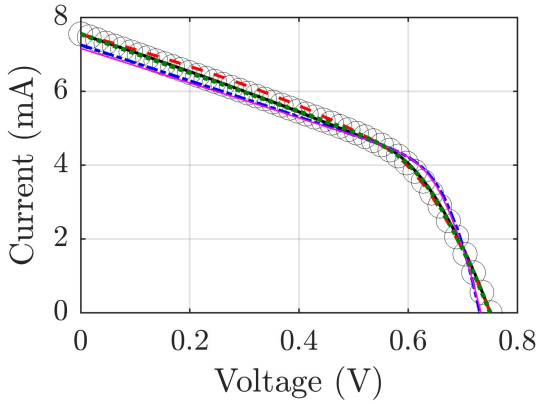

(b) Current-voltage plots.

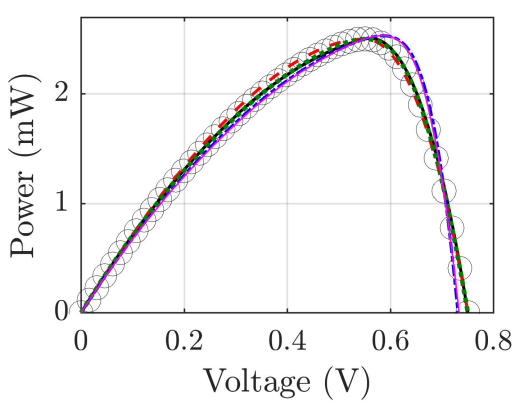

(c) Power-voltage plots.

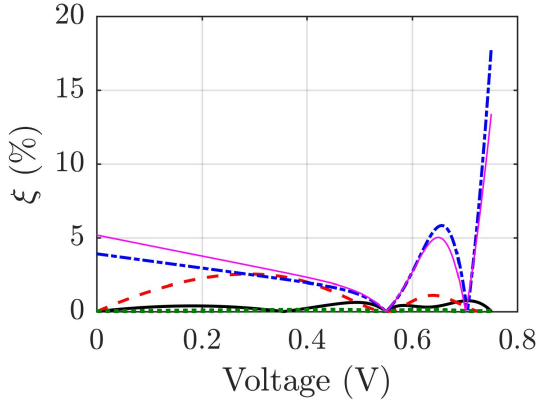

(d) Current NAE plots.

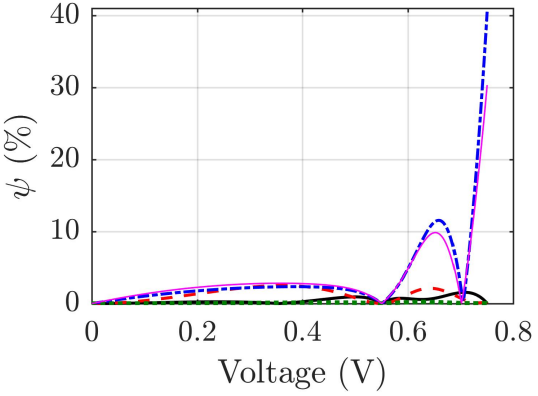

(e) Power NAE plots.

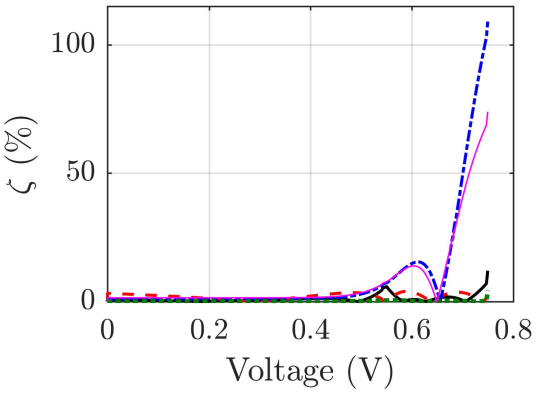

(f) Current derivative NAE plots.

Source: The author.

Figure 13 – Obtained results for the organic solar cell with titanium oxide layer.

Explanatory note: The results are comprised of plots of (a) the current NRMSE optimization trajectory of the proposed method and the current NRMSE values yielded by the other considered methods, (b) I-V characteristics, (c) P-V characteristics, (d) current NAE curves, (e) power NAE curves and (f) current derivative NAE curves. The plotted curves are identified as follows: Villalva et al. [27] (thin solid line, magenta), Vieira and Corrêa [43] (alternating traced line, blue), Rhouma et al. [44], analytical method (traced line, red), proposed method (solid line, black) and empirical I-V samples (gray round markers, only in I-V and P-V plots). Numerical values of current NRMSE, current derivative NRMSE, power NRMSE and execution time are given in Table 5.

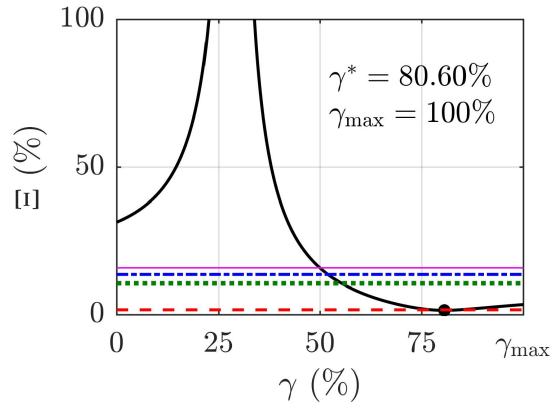

(a) Illustration of optimization trajectory.

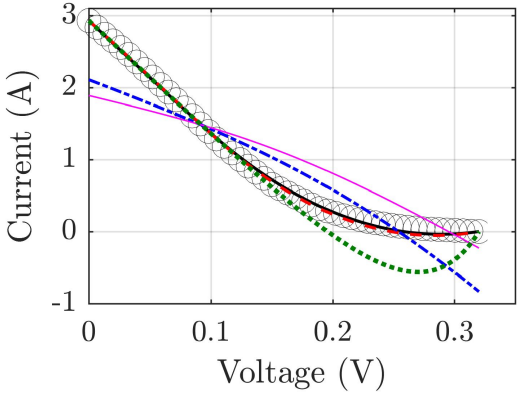

(b) Current-voltage plots.

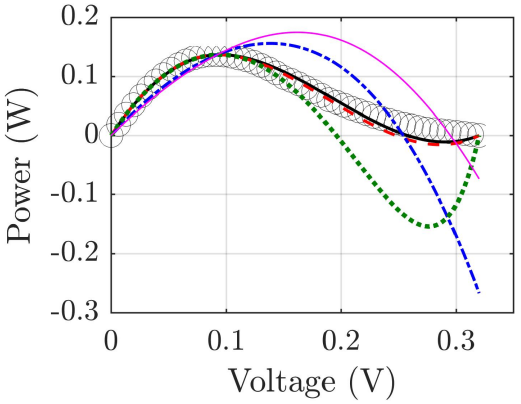

(c) Power-voltage plots.

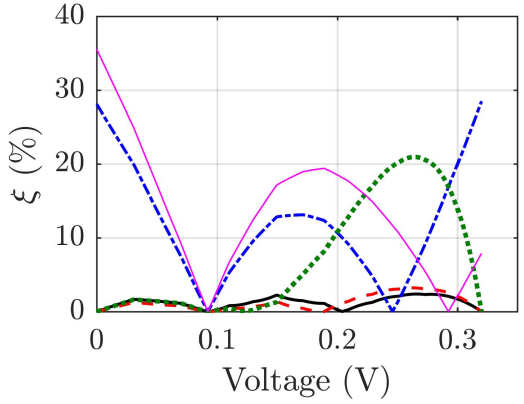

(d) Current NAE plots.

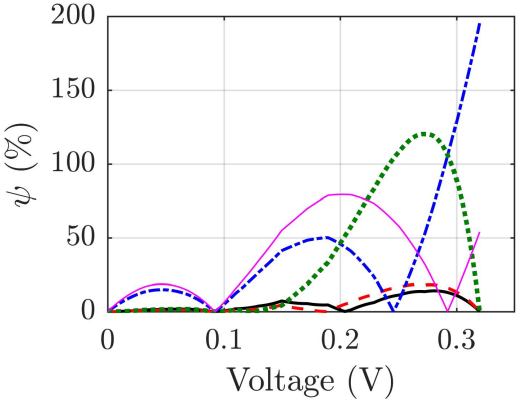

(e) Power NAE plots.

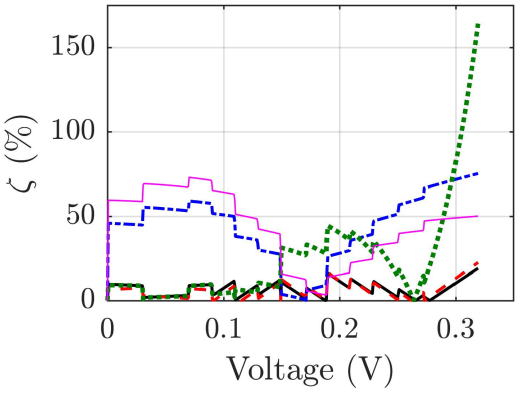

(f) Current derivative NAE plots.

Source: The author.

Table 4 – Performance metrics of each method for the thin-film cell

Method	Ξ (%)	Z (%)	Ψ (%)	$\lceil T \rceil$ (ms)	MPP fit
Villalva et al. [27]	5.8901	8.0035	6.6581	2140	Inadequate
Vieira and Corrêa [43]	1.9132	3.2788	1.9650	2413	Inadequate
Rhouma et al. [44]	2.2474	3.2488	2.4043	26920	Inadequate
Analytical method (Ch. 1)	3.1384	5.4482	3.5614	1	Adequate
Proposed method	2.5225	4.9260	2.8139	7	Adequate

Source: The author.

Table 5 – Performance metrics of each method for the organic cell

Method	Ξ (%)	Z (%)	Ψ (%)	$\lceil T \rceil$ (ms)	MPP fit
Villalva et al. [27]	3.6479	14.5882	5.1198	2542	Inadequate
Vieira and Corrêa [43]	3.5578	19.2682	6.0517	2825	Inadequate
Rhouma et al. [44]	0.0726	0.3390	0.1049	25463	Adequate
Analytical method (Ch. 1)	1.5329	2.3690	1.5012	1	Adequate
Proposed method	0.3713	1.5679	0.5813	4	Adequate

Source: The author.

Table 6 – Performance metrics of each method for titanium oxide layer organic cell

Method	Ξ (%)	Z (%)	Ψ (%)	$\lceil T \rceil$ (ms)	MPP fit
Villalva et al. [27]	15.7854	48.4370	45.6812	2874	Inadequate
Vieira and Corrêa [43]	13.5468	48.4555	55.3319	3232	Inadequate
Rhouma et al. [44]	10.5515	38.4997	57.6145	27474	Adequate
Analytical method (Ch. 1)	1.6057	7.7751	8.5024	1	Adequate
Proposed method	1.4296	7.8788	6.5699	13	Adequate

Source: The author.

2.4.2.1 Monocrystalline Cell

As depicted in Figure 9 and Table 2, all methods were able to provide high-quality fits to the empirical I-V curve. The worst-performing method was the analytical ETPQM parameter extraction, which still yielded a small $\Xi \approx 2\%$. Using the proposed method, a relative NRMSE improvement of 25.08% was obtained with respect to the analytical method, which made the proposed method very closely approach the one by Villalva et al. [27] in terms of accuracy. Together with the polycrystalline cell, this is one of the cases in which the proposed method, despite yielding low NRMSE, did not surpass the accuracy of any ODM-based method; the reason for this will be discussed in Section 2.4.2.6. The proposed method required much smaller execution time: compared to the fastest ODM-based method, a 99.73% time reduction was achieved. Furthermore, only an additional 6 ms were required in comparison to the analytical method.

2.4.2.2 Polycrystalline Cell

The results presented in Figure 10 and Table 3 are similar to those for the monocrystalline cell: all methods yielded precise fits, with the worst-peforming one being, once more, the analytical method with $\Xi \approx 1\%$. The main difference in this case is that the relative NRMSE improvement by the proposed method, with respect to the analytical one, was quite modest at 0.07%. Once again, the proposed method was comparatively very fast and yielded a 99.75% time reduction with respect to the fastest ODM-based method.

2.4.2.3 Thin-film Cell

From Figure 11 and Table 4, it is seen that the proposed method yielded significantly superior performance to the ODM method of Villalva et al. [27] and reduced NRMSE of the analytical method by 19.62%. Furthermore, its accuracy closely approached that of the best-performing ODM-based methods. Notably, only the proposed and analytical methods were able to adequately fit the MPP, whereas the remaining ones yielded P-V curves with considerable V_{mp} error. With regard to execution time, the proposed method yielded a 99.67% reduction compared to the fastest ODM method.

2.4.2.4 Organic Cell

The results in Figure 12 and Table 5 show that the proposed method attained greater accuracy than two ODM-based methods, namely those of Villalva et al. [27] and of Vieira and Corrêa [43]. It nearly equalled the performance of the ODM method of Rhouma et al. [44], yielding a very small NRMSE of $\Xi = 0.58\%$. Compared to its analytical counterpart, the proposed method yielded a large relative NRMSE improvement of 75.78%. We also note that, among the search-based methods, only the proposed method and that of Rhouma et al. [44] fitted the MPP adequately. As in previous cases, the proposed method sharply reduced execution time (by 99.84%) with respect to the fastest ODM method.

2.4.2.5 Organic Cell With Titanium Oxide Layer

Some organic cells (such as the one with a titanium oxide layer considered here) may have severe bottlenecks in charge transport, which gives rise to physical phenomena that cause the I-V characteristic to be S-shaped and have very low FF [48]. This is *not* taken into account by the ODM, which thus perform poorly [22]. Since it is not known how the ETPQM and the proposed parameter extraction method would perform in this case, it must be properly assessed and compared to the ODM-based methods.

The obtained results, which are presented in Figure 13 and Table 6, clearly show that the ETPQM is, indeed, able to fit the S-shaped characteristic much better than the ODM. In fact, the I-V curves yielded by the ODM-based methods are very innacurate, in

that they have large negative-sign currents and NRMSEs above 10%. Contrastingly, the ETQPM yields $\Xi < 2\%$ both for the analytical and proposed method. As was the case for the other solar cells, the proposed method improves upon the analytical NRMSE; in this case, a relative improvement of 10.97% was obtained. At last, the proposed method saved 99.55% execution time compared to the ODM-based method with smallest execution time.

Despite the much better performance of ETPQM and the proposed method for the S-shaped characteristic, the author intends to research, in future work, further improvements specifically for S-shaped curves. In particular, the proposed method still yielded negative currents (albeit in much smaller degree than the ODM-based methods) near V_{oc}, which is not physically realistic. We thus conjecture that, in future work, some modification can be made to Equation 2.1 so that the model itself better fits S-shaped characteristics.

2.4.2.6 Discussion

The proposed parameter extraction method consistently achieved its main objective for all solar cells, namely improving upon the NRMSE yielded by Equations 1.2-1.7 with small execution time. The relative improvement with respect to analytical parameter extraction was modest in some cases but large in others, ranging from 0.07% to 75.78%.

For all non-silicon solar cells, the proposed method has surpassed at least one of the ODM-based methods and, more importantly, closely approached (and in one case surpassed) the best-performing ODM method in terms of accuracy. This confirms our initial hypothesis (see Section 2.1.2) that, in general, the ETPQM is a high-performing explicit I-V model which could be further enhanced via optimization.

It is simple to explain why all the ODM-based methods performed better for the silicon cells: the monocrystalline and polycrystralline technologies are the ones which most closely conform to the modeling assumptions of the ODM. Hence, it naturally provides an excellent fit to their empirical I-V characteristics. In any case, it is emphasized that the proposed method also yielded good performance for the silicon solar cells, with $\Xi < 2\%$.

Also compared to the ODM-based methods, it is clear that the proposed method yields much smaller execution times, which has a twofold cause. First, as was established in **Lemma 1**, the optimization variable γ is constrained to the narrow interval $\Gamma \subset [0, 1]$. Hence, it is ensured that a small number of operations will be required for completing the direct search; this is not true for methods [27, 43, 44], since R_s does not have general (i.e, applicable to any solar cell) and well-defined search bounds. Second, during NRMSE evaluation of the ODM-based methods, each $I(V_i)$ in Equation 2.14 must be obtained by evaluating the Lambert W function to solve the implicit ODM [2]. Hence, aside from using more operations, the ODM methods have a time-consuming fundamental operation.

It is interesting to note that $\gamma_{\max}$ bears some influence on execution time of the

proposed method. The results clearly show that larger $\gamma_{\max}$ imply greater execution time, which is entirely consistent with the analysis carried out in Section 2.3, where we established a required number of operations equal to $1 + \frac{\gamma_{\max}}{\Delta\gamma}$. The organic cell with titanium oxide layer represents the worst-case scenario of $\gamma_{\max} = 1$ [see Figure 13(a)], which, as per **Lemma 1**, happens because $V_{mp} < \frac{V_{oc}}{2}$. However, even in this case, the proposed method required 13 ms, which is at least two orders of magnitude below the execution times of the ODM-based methods against which it was compared.

At last, an important feature of the proposed method is that it avoided the problem of inadequate MPP fit that occurred at least once for each ODM-based method, which is explained as follows. Despite all ODM-based methods using the condition $I(V_{mp}) = I_{mp}$ in their formulations, none of them imposes the condition $\partial_V I(V_{mp}) = -\frac{I_{mp}}{V_{mp}}$, which is responsible for ensuring that $I(V)$ has its maximum exactly at (V_{mp}, I_{mp}). Hence, it is possible for the predicted curve to pass through (V_{mp}, I_{mp}) but not have its maximum at this point. Such considerations are also true for the proposed method (since it does not use the derivative condition), but it compensates for this by fitting (V_{mp}, I_{mp}) *close to the maxima of two orthogonal parabolas* (as seen from Figure 8), which makes the predicted I-V curve closely approximate the maximum condition $\partial_V I(V_{mp}) = -\frac{I_{mp}}{V_{mp}}$.

All of the foregoing discussion shows that, if ETPQM is used for modeling, it is worthwhile to apply the proposed parameter extraction method if empirical I-V samples are available for NRMSE computations. In fact, it consistently reduces NRMSE with respect to the analytical method from Chapter 1 and requires negligible processing time. However, if the empirical I-V samples are unavailable, the analytical method remains as a simpler but less accurate alternative.

2.5 Conclusion

A low-complexity search-based parameter extraction method for the ETPQM solar cell I-V characteristic model has been proposed. Its validation was carried out via accuracy and execution time comparisons against the analytical ETPQM parameter extraction and other low-complexity search-based methods from the literature applicable to the ODM. The results proved that the proposed method consistently reduces NRMSE with respect to the analytical method with a very mild execution time trade-off. Furthermore, it is faster than the ODM-based methods and, depending on the considered solar cell, is capable of outperforming them. Hence, it is an effective and easily applicable method for ETPQM parameter extraction and its usage is encouraged if a sampled solar cell I-V curve is available for carrying out NRMSE optimization.

Part II

PV System Control

3 Hybrid Sensor-Aided Direct Duty Cycle MPPT for Two-Stage PV Systems

3.1 Introduction

Greater awareness of sustainability in society has led to the rapid adoption of photovoltaic (PV) power generation by electricity consumers [49–51]. Owing to concerns regarding cost and ease of implementation, PV generation is mainly implemented by means of two solutions, namely batteryless grid-tied and battery-equipped off-grid systems [52–55].

Aside from the specification of PV module and inverter with its associated controls, implementation of such PV systems requires a power stage that performs maximum power point tracking (MPPT), which ensures that maximum PV power is extracted for arbitrary ambient conditions [56]. The development of efficient MPPT algorithms is of particular interest for electricity consumers that host distributed generation units, as their main objective is reducing electricity bills via maximization of PV output [50].

Based on whether the MPPT scheme is implemented by means of a dedicated direct current (DC) converter (i.e., a DC-DC switching circuit) or an internal stage of a specialized inverter, the PV system is denoted as two-stage or single-stage, respectively.

Single-stage systems are comparatively recent and yield some advantages due to their lower number of components, namely: reduced cost, fewer dissipation losses and higher reliability [57]. On the other hand, such systems have poorer MPPT performance and are susceptible to hot spotting [58], which may worsen performance even further [59]. In fact, a comparison from [60] has shown that a single-stage system *without* hot spotting has overall losses similar to those of a two-stage system. Furthermore, two-stage systems yield superior DC bus voltage regulation [61, 62].

In this work, it is assumed that a premium is put on MPPT performance, for which reason solely two-stage systems are considered. Also, the aforementioned regulation of DC bus voltage in two-stage systems is an assumption required in this work. For practical two-stage PV applications, economic concerns dictate that the DC converter must be one of the lower-cost topologies, i.e., buck or boost [63]. Hence, it is seen that most room for improvement in performance lies on the design of effective MPPT algorithms [64].

The requirement of high MPPT efficiency has led to the development of various complex algorithms which use optimization and soft computing techniques [65] for enhancing efficiency when compared to simpler approaches, which are henceforth denoted as *legacy* algorithms [66]. In any case, it is noteworthy that legacy algorithms remain

dominant in practice due to their simpler and much less demanding implementations [67]. In fact, the high processing times and complex hardware required by soft computing algorithms may be too restrictive for practical MPPT applications [64].

In this context, the Perturb & Observe (P&O) algorithm is the most used legacy MPPT method due to its ease of implementation and precise tracking. For a brief comparison, first recall that the other most relevant legacy algorithms are Fractional Open Circuit Voltage (FOCV), Fractional Short Circuit Current (FSCC), Incremental Conductance (INC) and Incremental Resistance (INR) [66, 68]. Despite the very fast response times of FOCV and FSCC, these methods yield inexact MPPT and are therefore inneficient. On the other hand, INC and INR provide precise tracking and perform either equally or slightly better than P&O [69], at the cost of more complex implementations. Hence, P&O has a superior trade-off between efficiency and complexity [70].

The major drawback of P&O is its slow tracking speed, which reduces efficiency when rapid changes in irradiance or temperature occur [64]. Additional performance degradation occurs due to wrong perturbation sign decisions caused by sudden increases in maximum power (drift) [71]. Taking such disadvantages into account, yet considering the convenience of using a simple algorithm such as P&O, it is reasonable to inquire if P&O can somehow be modified so that its tracking speed and efficiency are improved while maintaining a straightforward implementation.

As a matter of fact, this problem is an active research topic [72], for which many contributions have been proposed in the literature. In what follows, a concise review is given of such state-of-the-art P&O-based algorithms. For more general surveys of MPPT algorithms (including those not based on P&O), the reader is referred to [64–66, 73].

3.1.1 Related Works

Due to the great variety of P&O-based MPPT methods which currently exist in the literature, a systematic review of such algorithms can be benefitted by partitioning them into broad classes, each of which encompasses a general type of approach to improving P&O efficiency. Taking this into account and carrying out a survey of the recent literature, it is found out that a convenient grouping into three classes can be made, namely the classes of methods that are (a) adaptive modifications of P&O [67, 74–91]; (b) hybridizations of soft computing algorithms with P&O [92–105]; and (c) hybridizations of P&O with other legacy algorithms [106–108].

Aside from classifying the existing methods according to *how* they improve P&O, it is also relevant to consider whether each method is capable of tracking the global MPP under *partial shading* (PS) conditions and its associated *computational complexity*. With regard to this latter aspect, it is instructive to classify the methods based on whether

Table 7 – Literature review of P&O-based MPPT methods

Ref.	Type	O(1)	PS	Description
[74, 75]	AD	Yes	No	Additional decision layer based on sign of load resistance perturbation [74] or current perturbation [75] is used to avoid P&O drift after rapid changes in ambient conditions.
[76, 77]	AD	Yes	No	Improve on [74,75] by doubling the next perturbation step after drift avoidance, thereby increasing tracking speed.
[78]	AD	Yes	No	A smaller secondary perturbation step is used to increase symmetry of P&O oscillations around the maximum power point (MPP), thereby reducing efficiency losses.
[79]	AD	Yes	Yes	Each maximum power point voltage (MPPV) reached by P&O is stored. Then, voltages of individual modules in the PV array are monitored and the system attempts to track the previous MPP when partial shading is detected.
[67]	AD	Yes	No	The range of PV output voltage is divided into four segments, to each of which different P&O step sizes are assigned to enhance tracking speed.
[80, 81]	AD	Yes	No	Step size is dinamically adjusted in terms of output power [80] or output voltage [81]. When the system is further away from the MPP, perturbations are increased.
[82]	AD	Yes	No	Step size is adjusted proportionally to derivative of current with respect to duty cycle. Then, sampling frequency is changed to accomodate the new settling time.
[83]	AD	Yes	No	Merges the drift avoidance technique from [75] with an adaptive step size, which is taken as proportional to the derivative of output power with respect to PV voltage.
[84–87]	AD	Yes	No	A power envelope is used to determine if the system is in steady-state or dynamic conditions. If power perturbation violates the envelope thresholds, step size is changed accordingly to increase tracking speed during transients or reduce oscillations at steady-state. Generalizes well to INC [85, 86] and hill-climbing [87] algorithms.
[88]	AD	Yes	No	Adapts the envelope approach from [84–87] to voltage reference-based (i.e., non-DDCC) implementations.
[89]	AD	Yes	No	Step size is adapted as a function of conductance (i.e., the current-voltage ratio) and its measured perturbation. Furthermore, the PV voltage search range is bounded so that proximity to MPP is always ensured.
[90]	AD	Yes	Yes	The step size adaptation method from [89] is generalized to PS scenarios. A voltage scanning mechanism is used for finding the global MPP, whose fast tracking performance is ensured by voltage search range bounding.
[91]	AD	Yes	Yes	Fixed-step P&O is coupled with a voltage scanning method for tracking global MPP. The PV curve is divided into three voltage ranges associated to different duty cycle lower and upper bounds which are used to enhance scanning speed.

Literature review of P&O-based MPPT methods (cont.)

Ref.	Type	O(1)	PS	Description
[92–94]	SH	No	Yes	A sliding mode controller is used to dynamically adjust step size. To determine optimal controller gains and track global MPP, particle swarm [92], shuffled frog leaping [93] and krill herd [94] optimization algorithms are used.
[95, 96]	SH	No	No	An adaptive step size is computed by a fuzzy controller whose decision variable(s) is/are taken either as the derivative of output power with respect to voltage [95] or as output power and previous step size [96].
[97]	SH	No	No	The usual P&O perturbation sign computation is carried out and supplied as input to a fuzzy controller, which outputs a final perturbation step magnitude.
[98, 99]	SH	No	No	The basic flowchart rules of P&O are fuzzified and then implemented as a fuzzy controller, thereby not requiring a crisp perturbation input as in [97].
[100]	SH	No	No	An adaptive step size is computed by passing the measured output power error through a linear controller whose parameters are tuned by means of a genetic algorithm.
[101–103]	SH	No	Yes	Fixed-step P&O is used during steady-state, whereas grey wolf [101], ant colony [102] or bee colony [103] optimization takes over after rapid changes in ambient conditions to speed up tracking and ensure a global optimum.
[104, 105]	SH	No	Yes	When a sudden decrease in power occurs, the butterfly particle swarm [104] or modified firefly [105] optimization algorithm overtakes P&O and estimates the duty cycle [104] or MPPV reference [105] for tracking the global MPP.
[106]	LH	Yes	No	Standard P&O is used, with short circuit current being sampled periodically and used to estimate the maximum power point current (MPPC). If the difference between this estimate and output current is sufficiently large, FSCC is used to rapidly track the new MPPC.
[107]	LH	Yes	No	Analogous to [106], but an irradiance sensor is used to detect large irradiance changes and trigger FSCC, thereby eliminating losses due to periodic short-circuiting.
[108]	LH	Yes	No	A temperature sensor monitors for abrupt temperature changes. When this happens, P&O is interrupted and FOCV is used to quickly estimate the MPPV reference.
Prop.	**LH**	**Yes**	**Yes**	Hybridization of P&O with a modified version of FOCV that uses irradiance and temperature sensors to compute duty cycle directly (which reduces losses due to MPPT controller oscillations) and track PS conditions.

Source: The author.

their optimization routines have O(1) computational complexity, as is the case for P&O, or impose additional processing burden due to the usage of more complex optimization algorithms. Such consideration is of critical importance for practical applications, since the optimization algorithm must be iterated after each sampling of PV output power.

A literature review of recent P&O-based methods was carried out according to the aforementioned criteria and is presented in Table 7. Considering that descriptions of all methods are given in Table 7, focus is directed to more general comments in what follows.

The approaches based on *adaptive P&O modifications* (termed as *adaptive - AD* in Table 7) consist in either introducing additional decision layers to the P&O flowchart [67,74–79] or adjusting P&O step size dinamically [80–88] to improve tracking efficiency. The former strategy is simpler due to not using adaptation, yet affords modest improvements to tracking speed. Contrastingly, the latter approach can significantly increase tracking speed, but may be harder to implement since tuning adaptation rates is not trivial.

Some particularly effective adaptive methods use the concept of power envelope [84–88], which defines upper and lower bounds for measured power perturbation that are used to decide whether the system is in transient or steady-state conditions and adapt duty cycle accordingly, thereby improving both tracking speed and steady-state oscillations. Also noteworthy are the adaptive methods which, despite having O(1) complexity iterations, achieve global MPP tracking during PS conditions by means of memory [79] and voltage scanning [90, 91] mechanisms.

Now, consider the algorithms that belong to the class of *hybridizations of P&O and soft computing techniques* (termed as *soft-hybrid - SH* in Table 7). Such methods consist in either using soft computing to dynamically adjust P&O step size [92–100] or employing standard P&O during steady-state conditions and switching to a soft computing algorithm to track the new MPP after a fast change in ambient conditions is detected [101–105]. Regardless of which strategy is used, the well-known computational burden of soft computing algorithms (in their training, execution or both) implies that O(1) complexity is lost [64]. However, aside from their high processing times, such methods yield high efficiencies and peform well when PS conditions occur.

As seen from the above discussion, the most efficient adaptive and soft-hybrid algorithms may be difficult to implement due to their complexities or high processing times which, coupled with engineering constraints on system implementation costs, may lead to practical infeasibility. Hence, the methods that are *hybridizations of P&O and other legacy algorithms* (termed as *legacy-hybrid - LH* in Table 7) are of great practical interest: they yield significant tracking speed improvements and, since they only use well-known legacy algorithms, are easy to implement and have O(1) complexity iterations [106–108]. It is thus quite noteworthy that such type of algorithm remains relatively unexplored when compared to the adaptive and soft-hybrid approaches.

Such legacy-hybrid methods are now considered in some more detail since they are the focus of this work. The approaches proposed by [106–108] consist in running P&O during steady-state operation and, when an abrupt change in ambient conditions is detected, to use either FSCC [106, 107] or FOCV [108] to quickly track the new MPP. Changes in ambient conditions are tracked via different strategies: periodic sampling of short circuit current [106], an irradiance sensor [107] and a temperature sensor [108].

The main weaknesses of the aforementioned methods consist of their (a) increased steady-state oscillation losses, due to usage of indirect duty cycle control via current/voltage proportional-integral (PI) controller, which is required by FSCC/FOCV; and (b) lack of provisions for tracking the global MPP in PS scenarios. Elimination of such problems, conditioned on maintaining low computational complexity, would give rise to a more efficient legacy-hybrid algorithm.

3.1.2 Proposed MPPT approach

Taking the above discussion into account, this Chapter proposes a new MPPT algorithm for two-stage PV systems that is a P&O and FOCV hybrid with direct duty cycle control (DDCC) and efficient PS tracking. A modified sensor-aided version of FOCV is used to compute duty cycle directly, thereby enabling usage of DDCC. Its main contributions, when compared to similar hybrid methods, are: increased efficiency due to the smaller DDCC steady-state oscillations, hardware simplification due to a PI controller not being required and global MPP tracking during PS.

3.2 Modeling of Two-Stage PV System

This Section covers the modeling of relevant two-stage PV system components, namely: PV module, DC-DC converter driven by DDCC P&O and inverter DC bus.

3.2.1 PV Module

As pointed out in Chapter 1, the ODM is a widely used equivalent circuit model for PV modules due to its adequate balance between precision and complexity [109]. Hence, it is also considered in this Chapter for modeling purposes. The ODM parameters are R_s, R_{sh}, I_{ph}, I_o, m, N_s and N_{sh}, which denote, respectively: cell series resistance, cell shunt resistance, cell photogenerated current, cell saturation current, diode ideality factor, number of series cells per string and number of parallel strings.

The parameters N_s and N_{sh} are determined from module design, whereas the remaining ones must be estimated by means of nominal values given on the module datasheet. Since parameter estimation is not our focus, values from the National Renewable

Energy Laboratory database [110] are considered. The I-V characteristic yielded by the ODM is described by the following implicit equation:

$$I = N_{sh} I_{ph} - \frac{N_{sh} V + N_s R_s I}{N_s R_{sh}} - N_{sh} I_o \left[\exp\left(\frac{N_{sh} V + N_s R_s I}{N_s N_{sh} \cdot m V_t} \right) - 1 \right] \tag{3.1}$$

where $V_t = kq/T$ is cell thermal voltage, in which k is the Boltzmann constant and q is the positive elementary charge [1].

The ODM as given in Equation 3.1 is valid for PV module operation at fixed ambient conditions. For time-varying temperature (T) and irradiance (S), the dependences of model parameters on S and T must be considered as follows [23]:

$$I_o(S,T) = I_o(S_o, T_o) \cdot \left(\frac{T}{T_o} \right)^3 \exp\left[\frac{E_g(T)}{kT} - \frac{E_g^{(o)}}{kT_o} \right] \tag{3.2}$$

$$I_{ph}(S,T) = I_{ph}(S_o, T_o) \cdot \frac{S}{S_o} \left[1 + \alpha_I (T - T_o) \right] \tag{3.3}$$

$$R_{sh}(S,T) = R_{sh}(S_o, T_o) \cdot \frac{S_o}{S} \tag{3.4}$$

where T_o and S_o are nominal temperature and irradiance, α_I is the short circuit current (SCC) temperature coefficient, $E_g^{(o)}$ denotes the semiconductor bandgap energy at T_o and $E_g(T) = E_g^{(o)}[1 - 0.0002677(T - T_o)]$ is the bandgap energy at an arbitrary temperature T. For additional clarity, note that Equation 3.2 expresses how saturation current varies due to the dependence of bandgap energy (exponential term) and of intrinsic carrier concentration (cubic term) on temperature [29]. At last, it should be noted that R_s and m are approximately constant with respect to S and T.

For each (S,T) pair, the I-V characteristic has a MPP with voltage V_{mp} and current I_{mp}. Usually, the MPPV and MPPC dependences on S and T are not given on the PV module datasheet. On the other hand, the dependences of SCC and open circuit voltage (OCV), which are respectively denoted by I_{sc} and V_{oc}, can be computed as [23, 24]:

$$I_{sc}(S,T) = I_{sc}(S_o, T_o) \cdot \frac{S}{S_o} \left[1 + \alpha_I (T - T_o) \right] \tag{3.5}$$

$$V_{oc}(S,T) = N_s m V_t \ln\left(\frac{S}{S_o} \right) + V_{oc}(S_o, T_o) \cdot \left[1 + \alpha_V (T - T_o) \right] \tag{3.6}$$

where α_V is the OCV temperature coefficient. Note that Equations 3.3 and 3.5 express identical dependences on S and T, which is due to the fact that $I_{ph} \approx I_{sc}$ [23]. In what follows, $V_{mp}^{(o)} = V_{mp}(S_o, T_o)$ and analogous notations for magnitudes referred to nominal ambient conditions are used for convenience.

Figure 14 – Boost converter with DDCC P&O.

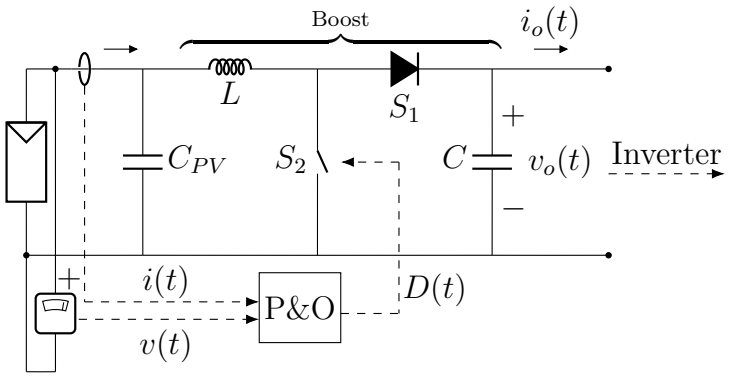

Source: The author.

3.2.2 DC-DC Converter with DDCC P&O

As discussed in Section 3.1, practical budget constraints recommend using low-cost DC-DC converter topologies. Since the boost converter is often employed due to its higher efficiency [111], it is henceforth considered. In Figure 14, the connection of a PV module to the inverter DC bus by means of a boost converter with DDCC P&O is illustrated.

The PV output voltage $v(t)$ and current $i(t)$ are periodically sampled with period T_s by the controller, which then computes output power $p(t) = v(t)i(t)$ and perturbs the duty cycle $D(t)$ according to P&O logic. For DDCC, this operation is described as:

$$D[n+1] = D[n] - \text{sgn}\left\{(p[n+1] - p[n])\,(v[n+1] - v[n])\right\} \cdot \Delta D \tag{3.7}$$

where $y[n] = y(nT_s)$ denotes the n-th sample of waveform $y(t)$, $n \in \mathbb{N}$, the function $\text{sgn}(\cdot)$ is defined as a modified *signum* with $\text{sgn}(0) = +1$ and $\Delta D > 0$ is the duty cycle increment of the DDCC P&O controller.

For the purpose of carrying out MPPT analysis, converter average waveform modeling is considered sufficiently accurate [112] and is henceforth adopted. In this context, the conversion ratio of the boost converter is given, in terms of D, by:

$$M(D) = \frac{V_o}{V} = \frac{I}{I_o} = \frac{1}{1-D} \tag{3.8}$$

in which $V = \bar{v} = \frac{1}{T_{sw}} \int_0^{T_{sw}} v(t)dt$ and similar notations apply to waveforms $v_o(t)$, $i(t)$ and $i_o(t)$ indicated in Figure 14, where T_{sw} designates the boost converter switching period.

Components L and C are functions of the desired inductor current and output voltage ripples, whereas C_{PV} is designed to reduce input voltage oscillations. The following continuous conduction mode relations are satisfied by L and C [113]:

$$L = \frac{DVT_{sw}}{2 \cdot \Delta I_L} \tag{3.9}$$

$$C = \frac{DI_o T_{sw}}{2 \cdot \Delta V_o} \tag{3.10}$$

where ΔI_L and ΔV_o are, respectively, inductor current and output voltage ripples.

Considering that L and C must be specified for MPP at nominal ambient conditions, $V = V_{mp}^{(o)}$ in Equation 3.9. Furthermore, the value of D in Equations 3.9 and 3.10 is that obtained by introducing $V = V_{mp}^{(o)}$ in Equation 3.8. Similarly, $I_o = I_{mp}^{(o)}/M(D)$ is computed from Equation 3.8 via substitution of the obtained D value. Carrying out the described manipulations, the following is obtained:

$$L = \frac{\left(V_o - V_{mp}^{(o)}\right) \cdot V_{mp}^{(o)} T_{sw}}{2V_o \cdot \Delta I_L} \tag{3.11}$$

$$C = \frac{\left(V_o - V_{mp}^{(o)}\right) \cdot V_{mp}^{(o)} I_{mp}^{(o)} T_{sw}}{2V_o^2 \cdot \Delta V_o} \tag{3.12}$$

where the output voltage V_o and ripple parameters are system design choices.

It is known that input voltage ripple is relatively small in boost converters. For this reason, small C_{PV} values (when compared to C) are enough to suppress it [114]. Hence, for the sake of simplicity, it is henceforth assumed that $C_{PV} = C$.

3.2.3 Inverter DC Bus

In two-stage PV systems, MPPT and DC bus voltage control are decoupled: the former is performed by the DC converter, whereas the latter is carried out by the PV inverter. As a consequence, two-stage systems yield, comparatively, much better DC bus voltage regulation [61,62]. In this sense, constant DC bus voltage must *not* be assumed for a single-stage system [115], whereas it is a reasonable assumption when analyzing a two-stage system, provided the low frequency ripple introduced in the DC bus by inverter operation is also taken into account [116–119]. Based on such considerations, it is henceforth assumed that voltage regulation is adequately performed by the PV inverter and the DC bus may thus be modeled as an equivalent voltage source:

$$v_o(t) \approx V_o + \overbrace{\Delta V_o^{lf} \cdot \sin(2\pi f t + \phi)}^{v_o^{lf}(t)} \tag{3.13}$$

where $v_o^{lf}(t)$ is the low frequency ripple waveform with amplitude ΔV_o^{lf}, frequency f and phase ϕ. The DC bus equivalent model is depicted in Figure 15.

This modeling approach has also been used in [120], where experimental MPPT testing for two-stage PV systems is simplified by substituting a grid-tied inverter with the series connection of DC and alternating current (AC) sources. Aside from simplifying

Figure 15 – Equivalent DC bus model for a two-stage PV system.

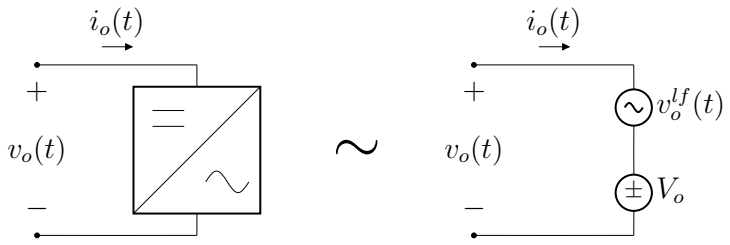

Source: The author.

modeling and implementation, the model is also used in this work so that the ripple amplitude ΔV_o^{lf} for which performance will be evaluated can be selected directly.

Remark 3.1: Using Equation 3.13 implies that high frequency ripple is disregarded in $v_o(t)$. This approximation is valid *solely* at the DC bus, in which ΔV_o is either dominated by ΔV_o^{lf} in a grid-tied system [118] or very small with respect to the battery voltage V_o in an off-grid system. On the other hand, high frequency ripple and its effects on MPPT may not be neglected in $v(t)$ or $i(t)$, for which reason L and C must still be computed according to *nominal* high frequency ripples, i.e., as per Equations 3.11 and 3.12.

Remark 3.2: During numerical simulations, the DC bus model may lead to convergence problems when paralleled with capacitor C. To avoid such issues, a small decoupling resistor $r_d = 1$ mΩ is introduced in series with $v_o^{lf}(t)$ in the simulations from Section 3.4.

3.2.4 MPPT Problem Statement

The objective when using any MPPT algorithm is to maximize power efficiency η via discrete-time control of duty cycle D. Efficiency is computed according to:

$$\eta = \frac{\int_0^{t_f} p(t)dt}{\int_0^{t_f} p_{mp}(t)dt} \tag{3.14}$$

where t_f is the considered time duration and $p_{mp}(t)$ is the maximum PV power at time t; note that the denominator is a constant. Hence, in a general manner, MPPT can be cast as a constrained mathematical optimization problem as follows:

$$\begin{aligned} \underset{D(\tau)}{\text{maximize}} \ & \int_0^{t_f} p(t; D(\tau \leq t), S(\tau \leq t), T(\tau \leq t), \mathcal{S})dt \\ \text{s.t.} \ & \frac{\partial D(\tau)}{\partial \tau} = 0, \ \forall \ \tau \neq nT_s, \ n = 1, 2, 3, \ldots; \\ & 0 \leq D(\tau) \leq 1, \ \forall \ \tau. \end{aligned} \tag{3.15}$$

where $p(t; D(\tau \leq t), S(\tau \leq t), T(\tau \leq t), \mathcal{S})$ denotes that output power at time t depends, in general, on the history of duty cycle, irradiance and temperature values until t and on

the set $\mathcal{S}$ of PV system nominal specifications. The first constraint establishes that D is controlled in discrete time with sample interval T_s, whereas the second one is simply a physical constraint on the value of duty cycle.

Solving the general problem in Equation 3.15 is infeasible in practice, not only due to its complexity but also because it implies that a priori knowledge of $S(t)$ and $T(t)$ would be required, which is physically impossible. Hence, MPPT algorithms actually attempt to solve Equation 3.15 approximately by iterating, at each $t = nT_s$, an optimization algorithm for maximizing $p[n]$ given only $p[n-1]$ and other limited information (e.g., in the case of P&O, $v[n]$ and $v[n-1]$). We emphasize that this discussion corresponds to the great importance attributed to O(1) complexity in Section 3.1.1, since MPPT algorithms must be sufficiently fast to be iterated at *each* sample time.

3.3 Proposed Hybrid MPPT Approach

In this Section, the proposed method is described. It is an hybridization of DDCC P&O and a modified version of FOCV, which leverages DC bus voltage and measurements from irradiance and temperature sensors to estimate the MPP duty cycle value.

3.3.1 Modified FOCV Algorithm

Consider the standard FOCV algorithm. It consists in periodically sampling the OCV and computing an associated estimate of the MPPV as follows [121]:

$$V_{mp} \approx K \cdot V_{oc} \tag{3.16}$$

where K is a proportionality constant between V_{mp} and V_{oc}. The value of K can be easily estimated by means of nominal data, i.e., $K \approx V_{mp}^{(o)}/V_{oc}^{(o)}$. As a general rule, $K \in [0.7, 0.8]$ for usual PV module material technologies [64].

Since it yields an estimate of V_{mp} as output, FOCV requires a voltage reference controller and is thus incompatible with DDCC. Furthermore, the open-circuiting of the PV module required for sampling the OCV reduces MPPT efficiency. To achieve direct estimation of D and eliminate OCV sampling losses, a modified FOCV algorithm, henceforth named Sensor-Aided FOCV (SFOCV), is proposed as follows.

At first, OCV sampling is substituted with irradiance and temperature sensor measurements. Given S and T, the OCV is estimated via Equation 3.6 and subsequently used as input to Equation 3.16, from which V_{mp} is obtained with no sampling loss. Now, recall from Section 3.2.3 that DC bus voltage is assumed to have a constant mean value V_o. Substituting such value and $V = V_{mp}$ in Equation 3.8 and solving for D, a MPP duty

cycle estimate is obtained. The procedure just described is expressed by:

$$D_{mp} \approx 1 - \frac{K \cdot V_{oc}(S,T)}{V_o} \tag{3.17}$$

where $V_{oc}(S,T)$ is computed as in Equation 3.6 and D_{mp} is the estimated maximum power point duty cycle (MPPDC).

3.3.2 Proposed Method: P&O+SFOCV

The proposed MPPT approach is a hybrid of P&O and SFOCV, which is denoted by the acronym P&O+SFOVC. It consists in running P&O while monitoring ambient conditions, with SFOCV being triggered when large relative variations in irradiance $\delta S = (S[n] - S[n-1])/S[n-1]$ or temperature $\delta T = (T[n] - T[n-1])/T[n-1]$ are detected. In brief, SFOCV overrides P&O when $|\delta S| > \beta_S$ or $|\delta T| > \beta_T$, where $\beta_S, \beta_T > 0$ are fixed thresholds for relative irradiance and temperature variations, respectively.

This approach ensures that large transients in ambient conditions, which would be slowly compensated by standard P&O, are rapidly tracked by SFOCV. Hence, fast tracking is achieved with no adaptive parameters, no major computational burden and without sacrificing DDCC. Hence, the disadvantages of P&O-based methods discussed in Section 3.1.1 are avoided. The proposed method is given as pseudocode in **Algorithm 1**.

3.3.2.1 Computational Complexity

Recall from Sections 3.1.1 and 3.2.4 that computational complexity *per iteration* of MPPT algorithms is a metric of utmost importance. Such complexity can be determined

Algorithm 1 P&O+SFOCV

Input: $v[n]$, $i[n]$, $S[n]$, $T[n]$, ΔD, β_S, β_T, $n \in \mathbb{N}^*$.
Output: $D[n]$, $n \in \mathbb{N}^*$.

for $n = 1, 2, \ldots, \infty$ **do**
  $\delta S \leftarrow (S[n] - S[n-1])/S[n-1]$.
  $\delta T \leftarrow (T[n] - T[n-1])/T[n-1]$.
  if $|\delta S| > \beta_S$ or $|\delta T| > \beta_T$ **then**
    Use Equation 3.6 to estimate $V_{oc}(S[n], T[n])$.
    Use Equation 3.17 to estimate D_{mp}.
    $D[n] \leftarrow D_{mp}$.
  else
    Use Equation 3.7 to compute a DDCC P&O iteration.
    $D[n] \leftarrow D[n-1] \pm \Delta D$.
  end if
end for
return $D[n]$, $n \in \mathbb{N}^*$.

Source: The author.

for P&O+SFOCV by means of a simple inspection of **Algorithm 1**.

For each n, the routine of **Algorithm 1** starts off by computing δS and δT. Then, up to two comparisons of such values with their respective thresholds are carried out. At last, either Equations 3.6 and 3.17 are evaluated or Equation 3.7 is computed. Hence, each iteration amounts to a small and *fixed* number of operations (either five or six), which does not depend on any parameter. Hence, it is clear that P&O+SFOCV has O(1) complexity. This constrasts directly with optimization methods, whose complexity per MPPT iteration is proportional to the amount of optimization steps required until a convergence criterion is satisfied. In particular, note that soft computing often requires a very large number of steps which, as an additional problem, strongly depends on the specification of heuristic optimization parameters [64].

3.3.3 Upper Bound on SFOCV Estimation Error

In what follows, upper bounds on the estimation errors of MPPV and MPPDC yielded by SFOCV are derived. Such results are theoretical guarantees that the SFOCV estimates do not deviate arbitrarily from their true values.

Proposition 4: Let the *true* FOCV constant, which is a function of ambient conditions $K = K(S,T)$, belong to domain $\mathcal{K} = [K_o,\ K_o+\Delta K] \subset \mathbb{R}^+$. Denote as $\hat{V}_{mp}(S,T)$ the MPPV estimated via SFOCV. The absolute error $\Delta V_{mp}(S,T) = |V_{mp}(S,T) - \hat{V}_{mp}(S,T)|$ has an upper bound, which is valid for any S and T, given by:

$$\Delta V_{mp}(S,T) \leq V_{oc}(S,T) \cdot \Delta K \tag{3.18}$$

Proof: Let $\hat{K} \in \mathcal{K}$ be the particular value of K selected when computing SFOCV via Equation 3.16. For arbitrary S and T, the true proportionality constant $K(S,T) \in \mathcal{K}$ satisfies, by definition, the relation $V_{mp}(S,T) = K(S,T) \cdot V_{oc}(S,T)$. Hence, SFOCV estimation error can be expressed as:

$$\Delta V_{mp}(S,T) = \left| K(S,T) \cdot V_{oc}(S,T) - \hat{K} \cdot V_{oc}(S,T) \right| \tag{3.19}$$

which is upper-bounded by the particular case $K(S,T) = K_o$ and $\hat{K} = K_o + \Delta K$ (or vice-versa). Substituting in Equation 3.18, the desired upper bound is obtained. ■

Corollary 2: Let $\Delta D_{mp}(S,T) = |D_{mp}(S,T) - \hat{D}_{mp}(S,T)|$ be the MPPDC absolute error yielded by SFOCV. For arbitrary S and T, the following upper bound holds:

$$\Delta D_{mp}(S,T) \leq \frac{V_{oc}(S,T)}{V_o} \cdot \Delta K \tag{3.20}$$

Proof: From Equations 3.16 and 3.18, it is clear that $\Delta D_{mp}(S,T)$ can be expressed as a function of $\Delta V_{mp}(S,T)$. More precisely, $\Delta D_{mp}(S,T) = \Delta V_{mp}(S,T)/V_o$. Using Equation 3.18 and the fact that $V_o > 0$, Equation 3.19 is obtained. ■

It must be noted that the bounds given by **Proposition 4** and **Corollary 2** are loose, since they are obtained by maximizing error with respect to K. However, they are of interest due to their validity for arbitrary ambient conditions, which ensures that estimation error is always bounded. In any case, the obtained bounds may also be used to obtain quick, albeit quite conservative, estimates of maximum error.

To further understand why Equations 3.18 and 3.19 provide loose bounds, let $K(S,T) = \hat{K} + \epsilon(S,T)$, where $\epsilon(S,T)$ is the error of $\hat{K}$, with respect to the true K, for some S and T. Substituting in Equation 3.19, the following is obtained:

$$\Delta V_{mp}(S,T) = |V_{oc}(S,T)| \cdot |\epsilon(S,T)| \tag{3.21}$$

If $\hat{K}$ is an accurate estimate, then $|\epsilon(S,T)| \ll \Delta K$ and error is much smaller than the upper bound in Equation 3.18. It is important to emphasize that Equation 3.21 applies to individual ambient conditions, whereas Equations 3.18 and 3.20 are valid $\forall\ S,\ T$.

3.3.4 Generalization to Partial Shading Scenarios

It is known that P&O may perform poorly during partial shading (PS), since it may track a local MPP instead of the global one [122]. In what follows, a strategy is proposed for obtaining approximate global MPPT with P&O+SFOCV.

At first, note that a trivial, yet costly, approach for attaining global MPPT would be supplying each module of a PV array with its own MPPT-controlled converter. However, a more cost-effective approach often used in PV systems is to employ string-level converters, which provide a reasonable balance between cost and efficiency [57]. Hence, a PV string with N_a modules is considered in this discussion.

Using P&O+SFOCV requires irradiance and temperature sensors for triggering and computing the SFOCV step. For the PS scenario under consideration, it is assumed that all modules in the PV string have irradiance sensors, which yield measurements $S_1 > S_2 > \ldots > S_{N_a}$. On the other hand, temperature measurements T from one module in the string can be used as estimates for the remaining ones.

Let V_{oca} be the OCV of a single module in the PV string. Since OCV is a weak function of S (as per Equation 3.6), the approximation that it is solely a function of temperature is henceforth adopted, i.e., $V_{oca} = V_{oca}(T)$. When PS occurs, it is known that the local MPPVs have approximate values $jK \cdot V_{oca}$, $j = 1, 2, \ldots N_a$ [123]. Hence, for tracking the global MPP, the value of j associated to it must be estimated. As an approximation, the following scheme is proposed: every sensor S_i continuously monitors for irradiance changes. Detection by any sensor indicates PS, thereby triggering SFOCV which is computed as:

$$D_{mp} \approx 1 - \frac{\hat{N}K \cdot V_{oca}(T)}{V_o} \tag{3.22}$$

$$\hat{N} = \underset{m=1,2,\ldots,N_a}{\operatorname{argmax}} \; m \cdot S_m \tag{3.23}$$

where $\hat{N}$ is the proposed estimate of j. To understand Equations 3.22 and 3.23, consider the approximate computation of output power at the local MPPV value $jK \cdot V_{oca}$. At such local MPP, voltage is $jK \cdot V_{oca}$ since the j PV modules with greater irradiance values $(S_1, S_2, \ldots, S_j)$ conduct, whereas the remaining ones $(S_{j+1}, S_{j+2}, \ldots, S_{N_a})$ are shorted by their bypass diodes [124]. Since the conducting modules are in series, the flowing current is limited by the conducting module with lowest irradiance S_j. Hence, considering that MPPC is approximately proportional to irradiance, the flowing current can be estimated as $I_{mp}^{(o)} \cdot S_j/S_o$. By multiplying output voltage and current, the estimated power $jKV_{oca}I_{mp}^{(o)}S_j/S_o$ is obtained, which can be optimized by maximizing the product $j \cdot S_j$, from which Equation 3.23 is obtained. Given $\hat{N}$, the estimated global MPPV is $\hat{N}K \cdot V_{oca}$. Substituting such estimate in Equation 3.8 and manipulating, Equation 3.22 is obtained.

It is fair to note that, if the global MPPV has a neighbouring local optimum with PV power very close to its own, this approach may lead to suboptimal tracking. Efficiency loss will not be large in this case due to closeness of the PV power values. On the other hand, Equation 3.22 ensures that exceedingly suboptimal maxima will not be reached.

3.4 Computer Simulations

In this Section, the proposed method is validated via simulations carried out in Simulink R2017a. At first, the simulation model is described and controller stability analysis is performed. Then, a four-part computer experiment is presented, in which the following evaluations of P&O+SFOCV are carried out: (a) comparison to multiple legacy MPPT algorithms (P&O, FOCV, INC and INR); (b) sensitivity analysis with respect to sample time and DC bus ripple; (c) comparison to a similar hybrid algorithm which uses voltage reference duty cycle control [108]; and (d) performance under partial shading.

3.4.1 Simulation Model

In what follows, the inverter DC bus is simulated via its equivalent model given by Equation 3.13. As discussed in Section 3.2.3, this approach has been preferred so that ripple ΔV_o^{lf} can be directly specified as a simulation parameter. The PV module considered for simulation is the *1Soltech 1STH-215-P* panel, whose datasheet information and ODM parameters are given in Table 8 [110]. The values selected for DC bus equivalent model parameters, boost converter components and MPPT parameters are given in Table 9.

Boost converter circuit components and T_{sw} are specified for nominal ripples $\Delta V_o \approx 70$ mV and $\Delta I_L \approx 20$ mA. Nonideal forward voltage drop and on-resistance are

Table 8 – PV module parameters

Parameter	**Specification**
Nominal conditions	$T_o = 25°\text{C}$ $S_o = 1000\ \text{W/m}^2$
Number of cells	$N_s = 60$ $N_{sh} = 1$
$V_{mp}^{(o)}$	29.0 V
$V_{oc}^{(o)}$	36.3 V
$I_{mp}^{(o)}$	7.35 A
$I_{sc}^{(o)}$	7.84 A
α_V	$-0.361\%/°\text{C}$
α_I	$0.102\%/°\text{C}$
ODM model	$m = 0.98$, $I_o = 292$ pA, $I_{ph} = 7.86$ A, $R_s = 0.39\ \Omega$, $R_{sh} = 313.40\ \Omega$

Source: The author.

Table 9 – Boost converter, DC bus and MPPT parameters

Parameter	**Specification**
C, C_{PV}	250 μF
L	1 mH
S_1	On-resistance: $r_{on} = 1\ \text{m}\Omega$ Forward voltage: $V_{fwd} = 0.7$ V
S_2	MOSFET On-resistance: $r_{on} = 100\ \text{m}\Omega$ Internal diode parameters: same as S_1
DC bus	$V_o = 50$ V, $\Delta V_o^{lf} \in [0, 5]$ (V) $f = 100$ Hz, $\phi = 0°$
MPPT	$T_s \in [1, 5]$ (ms), $T_{sw} = 20\ \mu$s, $K = 0.8$ $\Delta D = 0.01$, $\beta_S = \beta_T = 5\%$

Source: The author.

taken into account for both converter switches, with the active switch assumed to be a MOSFET. The low frequency ripple ΔV_o^{lf} is considered in a range from 0% to 10% of V_o.

Since the idea behind P&O+SFOCV is to achieve fast tracking via SFOCV and use P&O to fine-tune the duty cycle, a small $\Delta D = 0.01$ is used so this can be achieved. Now, since ΔD is small, relatively fast sampling must be used, otherwise P&O would be innefective. Hence, sampling times in a range from 1 ms to 5 ms are considered.

Since small T_s values are employed, triggering of SFOCV for relatively small thresholds is used by setting $\beta_S = \beta_T = 5\%$. Finally, K is estimated by considering PV module operation under nominal ambient conditions, from which $K = 29.0/36.3 \approx 0.8$.

Figure 16 – Averaged linearized model of the PV system.

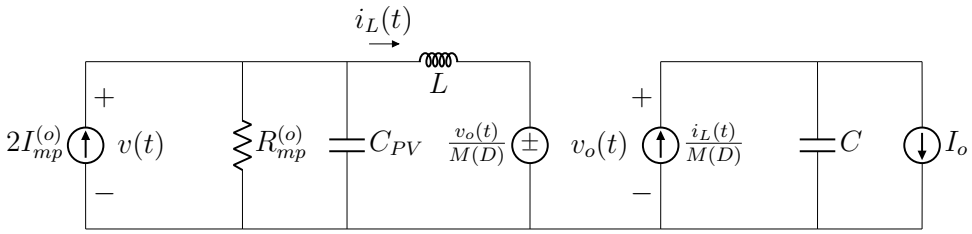

Source: The author.

3.4.2 Controller Stability Analysis

Considering that DDCC acts directly over $D(t)$ in order to control PV panel output voltage $v(t)$, the analysis of controller stability can be carried out by obtaining the voltage to duty cycle small signal transfer function. To achieve this, nominal MPP operation is considered to obtain the linearized averaged circuit model of the PV system in Figure 16.

The linearized PV representation is a Norton equivalent with current $2I_{mp}^{(o)}$ and resistance $R_{mp}^{(o)} = V_{mp}^{(o)}/I_{mp}^{(o)}$. The usual approximation that all output current ripple flows through C is used [125], thereby enabling the load to be modeled as a constant current source I_o corresponding to the quiescent MPP. Working out the state variables associated to each reactive element in the circuit, the following is obtained:

$$C_{PV}\frac{dv}{dt}(t) = 2I_{mp}^{(o)} - \frac{1}{R_{mp}^{(o)}}v(t) - i_L(t) \tag{3.24}$$

$$L\frac{di}{dt}(t) = v(t) - \frac{1}{M(D)}v_o(t) \tag{3.25}$$

$$C\frac{dv_o}{dt}(t) = \frac{1}{M(D)}i_L(t) - I_o \tag{3.26}$$

Let $y(t) = \bar{y} + \tilde{y}(t)$ denote a waveform decomposed in its DC and AC components. In what follows, time dependence of AC terms is omitted for conciseness. By decomposing $v(t)$, $i_L(t)$, $v_o(t)$ and $D(t)$ in Equations 3.24-3.26, eliminating second order AC terms and recalling that $M(D) = 1/(1-D)$, the following small signal equations are obtained:

$$C_{PV}\frac{d\tilde{v}}{dt} = -\frac{1}{R_{mp}^{(o)}}\tilde{v} - \tilde{i}_L \tag{3.27}$$

$$L\frac{d\tilde{i}}{dt} = \tilde{v} - (1-\bar{D})\tilde{v}_o + \bar{v}_o\tilde{D} \tag{3.28}$$

$$C\frac{d\tilde{v}_o}{dt} = (1-\bar{D})\tilde{i}_L - \bar{i}_L\tilde{D} \tag{3.29}$$

Finally, applying the bilateral Laplace transform, which is denoted as $\mathcal{L}[\tilde{y}(t)] = \tilde{y}(s)$, to Equations 3.27-3.29 and manipulating algebrically, the desired transfer function follows:

Figure 17 – Step response yielded by the DDCC MPPT system.

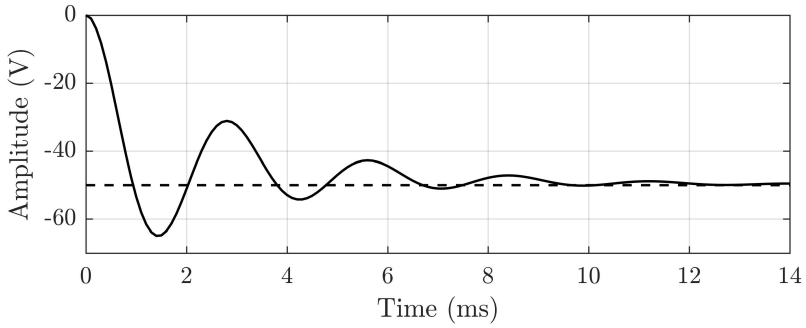

Source: The author.

$$G_{vD}(s) = \frac{\tilde{v}(s)}{\tilde{D}(s)} = A \cdot \frac{s + a_o}{s^3 + b_2 s^2 + b_1 s + b_0} \tag{3.30}$$

$$A = -\frac{\bar{v}_o}{LC_{PV}} \tag{3.31}$$

$$a_o = \frac{(1 - \bar{D})\bar{i}_L}{C\bar{v}_o} \tag{3.32}$$

$$b_2 = \frac{1}{C_{PV} R_{mp}^{(o)}} \tag{3.33}$$

$$b_1 = \frac{(1 - \bar{D})^2}{LC} + \frac{1}{LC_{PV}} \tag{3.34}$$

$$b_0 = \frac{(1 - \bar{D})^2}{LCC_{PV} R_{mp}^{(o)}} \tag{3.35}$$

Introducing the data from Tables 8 and 9 in Equations 3.30-3.35, the zeros, poles and step response of $G_{vD}(s)$ are evaluated. In particular, it should be noted in such computations that $\bar{v}_o = V_o$, $\bar{i}_L = I_{mp}^{(o)}$ and $\bar{D} = 1 - V_{mp}^{(o)}/V_o$.

The transfer function has a zero at $z_1 = -341$ and three poles at $p_{1,2} = -374 \pm j2238$ and $p_3 = -265$. From the fact that $\mathrm{Re}\{z_1\} < 0$ and $\mathrm{Re}\{p_i\} < 0$, $i = 1, 2, 3$, the system is minimum-phase and stable. A plot of the unit step response is given in Figure 17. It has a DC gain of -50, settling time of 11.5 ms, rise time of 635 μs and overshoot of 29.7%.

Finally, it is instructive to consider $z_1 \approx p_3$ and evaluate the damping ratio ξ and natural frequency ω_o of the resulting approximate second-order system. Proceeding as such, $\xi = 0.165$ and $\omega_o = 2270$ rad/s are obtained.

3.4.3 Part 1: Comparison to Widely Used Legacy MPPT Algorithms

As a first effort towards validating P&O+SFOCV, it is imperative to carry out a comparison with the established legacy MPPT algorithms. Hence, the proposed method is compared with P&O, FOCV, INC and INR. In this comparison, focus is given to algorithm responses during start-up (i.e., when the PV system is turned on) and after rapid changes in irradiance and temperature. To this end, a simulation with duration $t_f = 1.5$ s is considered as follows. Initial conditions are $D = 0$, $S = 500$ W/m^2 and $T = 25$°C. At $t = 0.5$ s, irradiance changes to $S = 1000$ W/m^2. Then, a temperature change to $T = 75$°C occurs at $t = 1.0$ s. In this simulation, $T_s = 2$ ms and $\Delta V_o^{lf} = 0$; the effects of varying T_s and ΔV_o^{lf} will be considered later. Results are given in Figure 18, where plots of $p(t)$ and $D(t)$ in different time ranges are given for each method, together with their efficiencies (computed for the full range $0 \leq t \leq t_f$).

Remark 3.3: The original FOCV algorithm is incompatible with DDCC and requires a voltage reference controller. In this simulation, the same PI controller whose design is thoroughly described in Section 3.4.5 is considered. For the sake of simplicity, it is assumed that very fast OCV sampling is available and open-circuiting losses are thus ignored.

Consider, at first, the start-up transient. Since $D(0^-) = 0$, the initial operating point is far from the MPP and, consequently, P&O performance suffers due to slow tracking. In fact, it is seen in Figures 18(a) and 18(b) that its power and duty cycle waveforms are the last ones to reach steady-state. As could be expected, INC and INR provide a small tracking speed improvement, with their $p(t)$ and $D(t)$ waveforms beginning to rise slightly earlier than those of P&O.

The FOCV algorithm reduces tracking time due to its direct MPPV estimation, but its steady-state error introduces some efficiency loss: this is clear from its $D(t)$ plot, which does not converge to the same average duty cycle value of the other methods. It is important to note that FOCV still presents some tracking delay due to the dynamics of its PI controller, which slows down system response. In fact, much faster tracking is obtained with P&O+SFOCV precisely because, at $t = 0$, it uses its DDCC-compatible FOCV computation (i.e., SFOCV) and is not penalized by PI controller delay. This corresponds, in the $D(t)$ plot, to the large jump in duty cycle value near the time origin.

We now discuss the irradiance step at $t = 0.5$ s. Recalling from Equations 3.6 and 3.16 that V_{mp} is a weak function of S, it is clear that performance differences among the considered methods will be less pronounced. However, interesting phenomena still emerge. First, note how PI controller dynamics once more worsen FOCV response: in Figure 18(c), FOCV rise time is the smallest, but this benefit is opposed by a greater settling time caused by its oscillatory response. In Figure 18(d), it is seen that P&O and INC suffer from duty cycle drift after the irradiance transient, which delays their $p(t)$ responses

Figure 18 – Results from Part 1 of the MPPT simulation experiment.

Explanatory note: The results consist of time plots of (a) PV power during start-up, (b) duty cycle during start-up, (c) PV power after irradiance step, (d) duty cycle after irradiance step, (e) PV power after temperature step and (f) duty cycle after temperature step. The plotted curves are identified as follows: P&O (red), P&O+SFOCV (blue), FOCV (green), INC (purple), INR (yellow) and maximum power point (traced line, black). The obtained efficiencies were: P&O (95.14%), P&O+SFOCV (99.26%), FOCV (96.63%), INC (95.39%), INR (95.62%).

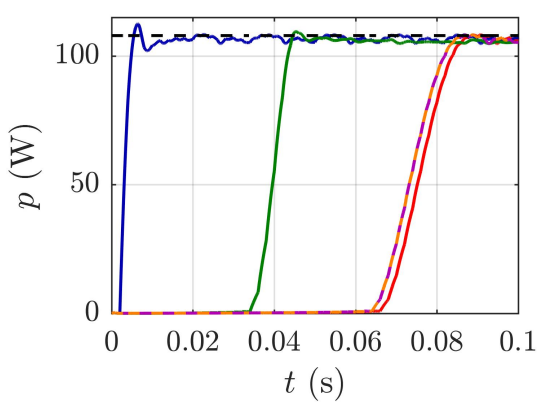

(a) $p(t)$ for $t \in [0, 0.1]$ (s).

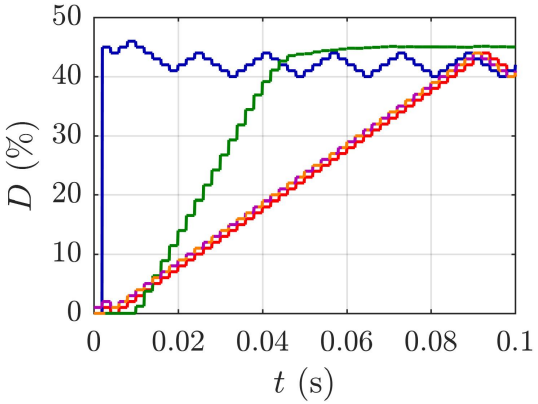

(b) $D(t)$ for $t \in [0, 0.1]$ (s).

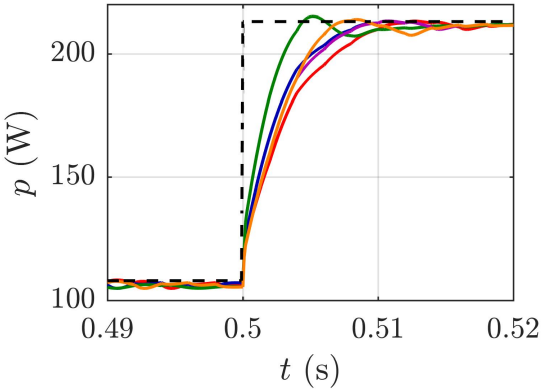

(c) $p(t)$ for $t \in [0.49, 0.52]$ (s).

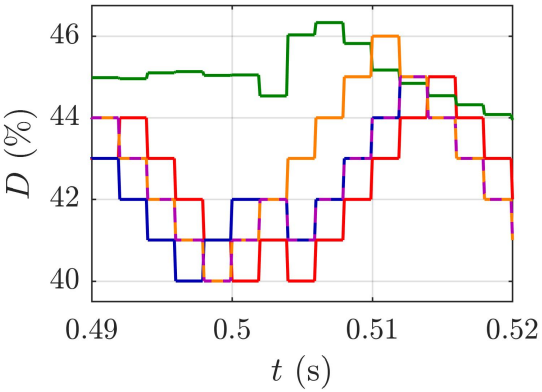

(d) $D(t)$ for $t \in [0.49, 0.52]$ (s).

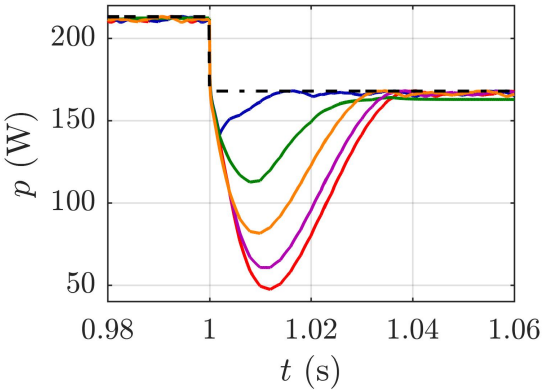

(e) $p(t)$ for $t \in [0.98, 1.06]$ (s).

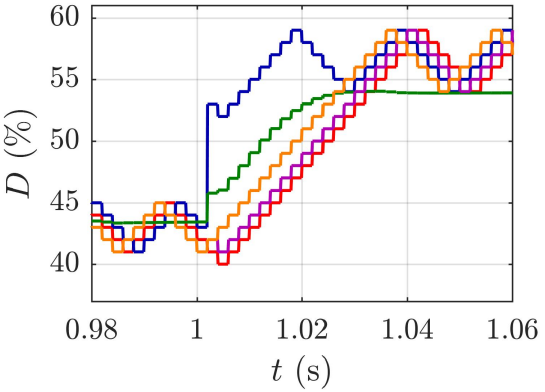

(f) $D(t)$ for $t \in [0.98, 1.06]$ (s).

Source: The author.

with respect to P&O+SFOCV and INR. In particular, the proposed method avoids drift because SFOCV overrides P&O after the irradiance step, thereby not considering the wrong step sign decision taken by P&O.

At last, consider the temperature step at $t = 1.0$ s. The strong dependence of V_{mp} on temperature implies that a large mismatch between operating point and the new MPP occurs, which in turn causes a sharp drop in output power until the new MPP is tracked. From Figure 18(e), it is clear that the $p(t)$ plot of P&O+SFOCV converges much more rapidly to the MPP. This is a direct consequence of SFOCV adjusting duty cycle to a near-optimal value immediately after the temperature transient, as depicted in Figure 18(f). Note that, analogously to the irradiance step, P&O and INC presented the slowest responses due to drifting and FOCV converges with considerable steady-state error.

3.4.4 Part 2: Effects of Sample Time and Ripple

It is important to assess how the performances of P&O and P&O+SFOCV are affected by sample time T_s and low frequency ripple ΔV_o^{lf}. To perform this parametric study, the selected ranges for T_s and ΔV_o^{lf} (given in Table 9) are discretized according to $T_s \in \{0.5 \cdot j,\ j = 1, 2, \ldots, 10\}$ (ms) and $\Delta V_o^{lf} \in \{0.5 \cdot j,\ j = 0, 1, \ldots, 10\}$ (V). At first, the same simulation scenario from Section 3.4.3 is iterated for all T_s and fixed $\Delta V_o^{lf} = 5$ V. Then, the simulation is iterated for varying ΔV_o^{lf} and fixed $T_s = 2$ ms. Obtained results are presented in Figure 19, where η is plotted in terms of T_s and ΔV_o^{lf}. The plots of $p(t)$ obtained for $T_s = 2$ ms and $\Delta V_o/V_o = 10\%$ are also presented for further illustration.

For a fixed and large ripple $\Delta V_o^{lf}/V_o = 10\%$, the results in Figure 19(a) show that P&O+SFOCV is relatively insensitive to sample time, whereas P&O efficiency rapidly decreases for larger T_s. This phenomenon is explained by the fact that ripple acts as noise for P&O, which increases its tracking time even further. This can be visualized in Figure 19(c), where wrong perturbation sign decisions caused by ripple make P&O oscillate during start-up and after the temperature step. Such noise effect can be compensated up to a certain point by faster sampling, which is the cause of η being sensitive to sample time. This issue is eliminated by SFOCV, since it uses V_o to estimate duty cycle and is thus unaffected by ripple. Hence, P&O+SFOCV is much less sensitive to T_s.

Constrastingly, Figure 19(b) shows that, for fixed T_s and increasing ΔV_o^{lf}, efficiency decreases at approximately equal rates for P&O and P&O+SFOCV. It should first be noted that the almost constant difference between the η plots is due to reduction of tracking delay by P&O+SFOCV, which occurs for all ΔV_o^{lf}. Now, the similar η decays are explained by steady-state oscillations around the MPP caused by increasing ripple. Since both algorithms perform equally at steady-state, their efficiencies decrease at equal rates.

To further visualize the severe effect of DC bus voltage ripple on efficiency, it is

Figure 19 – Results from Part 2 of the MPPT simulation experiment.

Explanatory note: The results consist of (a) plots of η as a function of T_s with $\Delta V_o^{lf}/V_o = 10\%$, (b) plots of η as a function of $\Delta V_o^{lf}/V_o$ with $T_s = 2$ ms and (c) time plots of $p(t)$ for $T_s = 2$ ms and $\Delta V_o^{lf}/V_o = 10\%$. The plotted curves are identified as follows: P&O (traced line, red, square markers), P&O+SFOCV (solid line, black, round markers) and maximum power point (thick traced line, black).

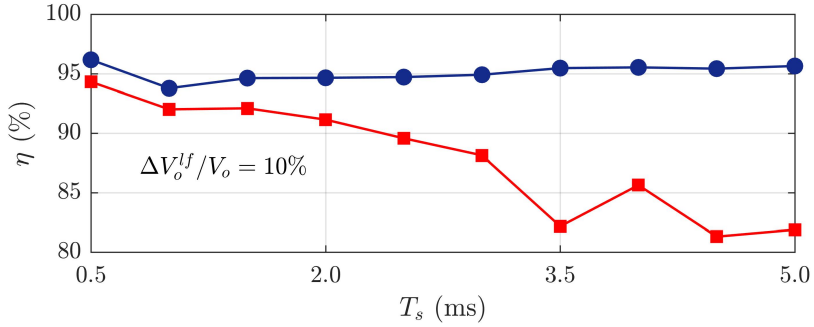

(a) Efficiency as a function of sample time.

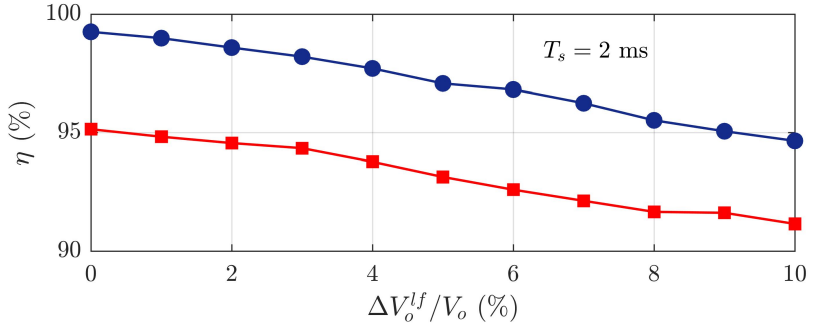

(b) Efficiency as a function of DC bus voltage ripple.

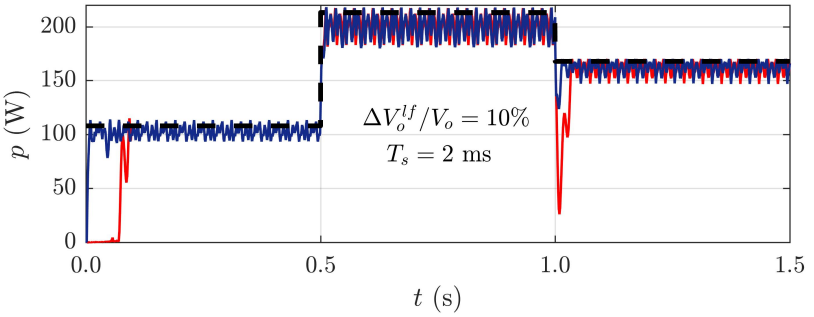

(c) Time plots of PV power for $T_s = 2$ ms and $\Delta V_o^{lf}/V_o = 10\%$.

Source: The author.

of interest to compare the obtained $p(t)$ plots with those from Figure 18(a), in which $\Delta V_o^{lf} = 0$. The output power ripple is negligible in the latter case, whereas it reached up to $\approx 8.67\%$ amplitude for $\Delta V_o^{lf}/V_o = 10\%$.

3.4.5 Part 3: Comparison to a Similar Algorithm

To validate the benefits of DDCC yielded by P&O+SFOCV, comparison to a similar non-DDCC method devised by Moradi and Reisi [108] is carried out. This MPPT algorithm is a hybrid of P&O and FOCV, which uses a temperature sensor to detect large changes in T and estimate the new MPPV via FOCV (i.e., by applying Equations 3.6 and 3.14). The influence of S on MPPV is not considered in [108], since an irradiance sensor is not used. Duty cycle control is then carried out by feeding the estimated MPPV reference to a PI voltage controller.

To achieve a meaningful comparison between both methods, a PI controller whose closed-loop settling time is similar to that of the DDCC system must be used. Hence, consider at first controller specification and a brief stability analysis. In what follows, let $G_c(s) = K_P[1 + T_I^{-1}s]$ denote the PI controller and $\tilde{D}(s) = G_c(s)[\tilde{v}_{ref}(s) - \tilde{v}(s)]$, where $\tilde{v}_{ref}(s)$ is the small-signal reference voltage. Hence, the closed-loop transfer function is:

$$G_{vv_{ref}}(s) = \frac{\tilde{v}(s)}{\tilde{v}_{ref}(s)} = \frac{G_c(s)G_{vD}(s)}{1 + G_c(s)G_{vD}(s)} \tag{3.36}$$

In order to specify the constants K_P and T_I, the Ziegler-Nichols method is applied, followed by manual tuning. The criterion used during tuning was to obtain a settling time similar to that of DDCC while maintaining gain and phase margins of, at least, 3 dB and 40°, respectively. Obtained controller parameters are $K_P = 0.0090$ and $T_I = 0.0015$, which yield a gain margin of 25.8 dB at 6.49 krad/s and a phase margin of 40° at 2.82 krad/s. The Bode plots and unit step response of transfer function $G_{vv_{ref}}(s)$ are given in Figure 20. The system has a settling time of 12.7 ms, rise time of 5800 μs and 27.6% undershoot. Hence, for similar settling time and overshoot/undershoot, DDCC has better rise time.

Comparison between the methods is carried out on a simulation scenario identical to that of Section 3.4.3 so that start-up, temperature and irradiance responses can be assessed. Two different cases are considered, namely ripple-free operation and $\Delta V_o^{lf}/V_o = 10\%$. For fairness, a P&O reference voltage disturbance $\Delta V_{ref} = -V_o \cdot \Delta D$ is used with [108], which, for constant V_o, is equivalent to the DDCC disturbance ΔD. All remaining parameters of [108] are identical to those given in Table 9 for P&O+SFOCV. Results are given in Figure 21, where plots of $p(t)$ and computed efficiency values are presented.

The obtained $p(t)$ plots show that voltage reference PI control introduces significant oscillation in MPPT when compared to DDCC, which agrees with the experimental findings from [70]. It is thus seen that, by enabling usage of DDCC, the P&O+SFOCV algorithm

Figure 20 – Stability plots for the non-DDCC MPPT system.

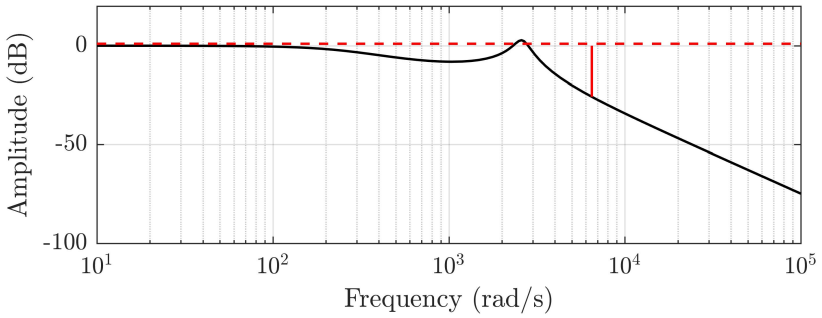

(a) Bode magnitude plot.

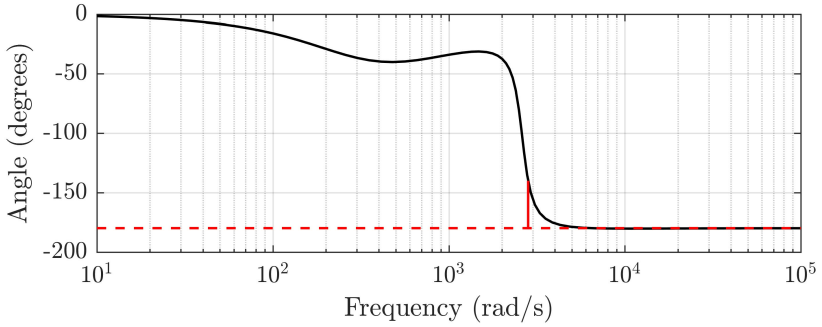

(b) Bode phase plot.

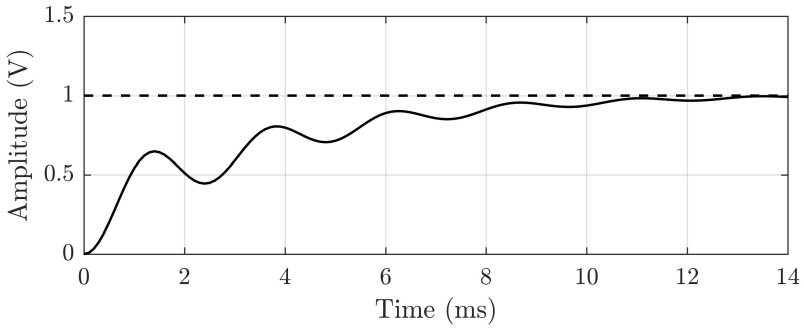

(c) Unit step response plot.

Source: The author.

Figure 21 – Results from Part 3 of the MPPT simulation experiment.

Explanatory note: The results consist of $p(t)$ plots for (a) ripple-free operation and (b) 10% ripple. The plotted curves are identified as follows: method of Moradi and Reisi [108] (solid line, red), P&O+SFOCV (solid line, black) and maximum power point (thick traced line, black). Efficiencies of P&O+SFOCV and [108] were, respectively: 99.26% and 97.36% (no ripple), 94.65% and 90.75% (10% ripple).

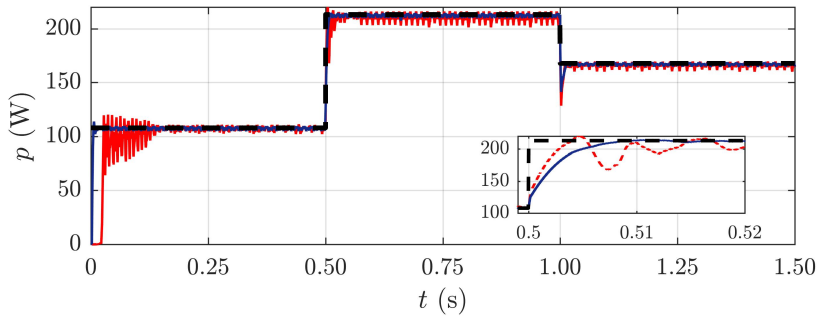

(a) Time plots of PV power for $\Delta V_o^{lf} = 0$.

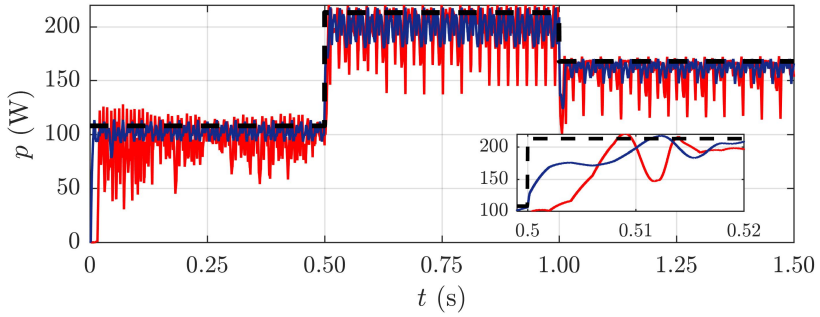

(b) Time plots of PV power for $\Delta V_o^{lf}/V_o = 10\%$.

Source: The author.

sharply reduces oscillation-related efficiency losses when compared to an equivalent method based on voltage reference control. This advantage is even more apparent in the $\Delta V_o^{lf} \neq 0$ case, where the combination of ripple and PI oscillations lead to considerable losses when using voltage reference control for MPPT.

At last, since [108] does *not* trigger FOCV after large irradiance changes, the P&O drift due to increase in output power at $t = 0.5$ s is not prevented. This is further illustrated in the details of Figure 21, where the $p(t)$ waveforms yielded by voltage reference control have larger settling times, when compared to P&O+SFOCV, after the irradiance step.

3.4.6 Part 4: Performance Under Partial Shading

To evaluate the generalization of P&O+SFOCV to PS (i.e., as in Equations 3.22 and 3.23), it is compared to P&O and the method by Moradi and Reisi [108]. For fairness in comparison, [108] is also generalized in a similar manner: it is assumed that irradiance sensors are available at each module and are used to estimate the MPPV via Equation

3.23. However, since [108] uses voltage reference control, duty cycle is *not* estimated with Equation 3.22. Instead, the estimated MPPV is fed to the PI controller.

The considered scenario is a two-module string ($N_a = 2$) subjected to PS. Simulation is carried out as follows. A constant temperature $T = 25°\text{C}$ is assumed throughout the simulation and initial duty cycle is $D = 0$. One module has constant $S_1 = 1000$ W/m^2, whereas the other one starts at $S_2 = 100$ W/m^2, increases to $S_2 = 1000$ W/m^2 at $t = \frac{1}{3}$ s and decreases to $S_2 = 300$ W/m^2 at $t = \frac{2}{3}$ s. Then, the simulation is terminated at time $t_f = 1$ s. In order to focus only on the effects of partial shading, $\Delta V_o^{lf} = 0$ is used.

Since the unshaded MPPV is approximately doubled with respect to a one-module system, $V_o = 100$ V is adopted. To avoid the consequent doubling of settling time, C_{PV} is reduced in half. Results are given in Figure 22, where P-V curves of the two-module string and obtained p-v trajectories are depicted. Associated $p(t)$ plots are also presented.

Let us first describe the p-v trajectory of P&O depicted in Figure 22(a). At $t = 0^-$, the system is at $(v, p) = (0, 0)$. Then, it progresses towards open-circuit operation since V_o is larger than V_{oc} and duty cycle is still near $D = 0$ due to slow P&O tracking. After reaching $(v, p) = (V_{oc}, 0)$, P&O tracks the suboptimal MPP in the $S_2 = 100$ W/m^2 characteristic and keeps oscillating around it; the larger oscillations correspond to the transient prior to duty cycle stabilization. Then, after the first irradiance step, P&O tracks the unique MPP in the $S_2 = 1000$ W/m^2 characteristic. Finally, after the second step, a suboptimal MPP in the $S_2 = 300$ W/m^2 curve is tracked. It is thus seen that P&O was only able to track the global MPP when it was unique. In all remaining cases (i.e., those with PS), a suboptimal MPP was obtained.

For the particular type of PV system (i.e., two-stage) under consideration, such suboptimal behaviour of P&O can be explained as follows. When a change in irradiance occurs, the PV string voltage does not change rapidly due to the constant DC bus voltage. Hence, P&O tends to continue tracking the present MPPV, regardless of it being a local or global optimum. This is particularly clear in the transition from $S_2 = 1000$ W/m^2 to $S_2 = 100$ W/m^2 in Figure 22(a): the global MPP is actually approached, but P&O ends up bringing the system to its prior (and now suboptimal) MPPV.

In a quite constrating manner, Figure 22(b) shows that the proposed generalization of P&O+SFOCV to PS scenarios adequately tracks the global MPP after both irradiance steps, which resulted in an efficiency increase of 27.61% with respect to P&O. The p-v trajectory is described in what follows. As in the P&O case, the system starts by progressing towards $(v, p) = (V_{oc}, 0)$. However, due to the fast tracking of P&O+SFOCV, it moves towards the optimal MPP in the $S_2 = 100$ W/m^2 curve before actually reaching the open circuit point. Again, the larger oscillations around the MPP correspond to the duty cycle stabilization transient. After the first irradiance step, the unique MPP for $S_2 = 1000$ W/m^2 is tracked. Then, after the second step, the global optimum of the

Figure 22 – Results from Part 4 of the MPPT simulation experiment.

Explanatory note: The results consist of: (a) plot of the p-v trajectory yielded by P&O, (b) plot of the p-v trajectory yielded by P&O+SFOCV and (c) time plots of PV power. Efficiencies obtained with P&O+SFOCV, the method by Moradi and Reisi [108] and P&O were 97.98%, 90.47% and 70.37%.

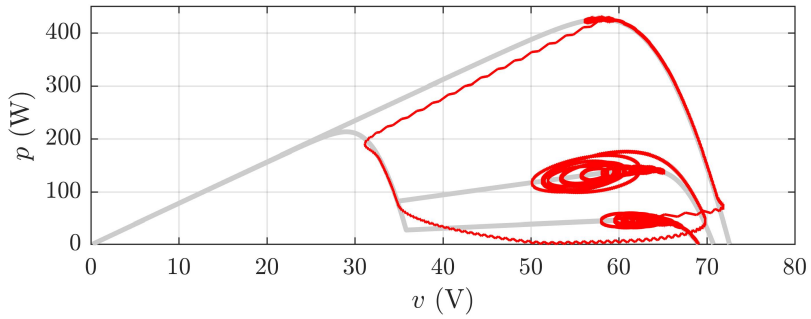

(a) Plot of p-v trajectory for P&O.

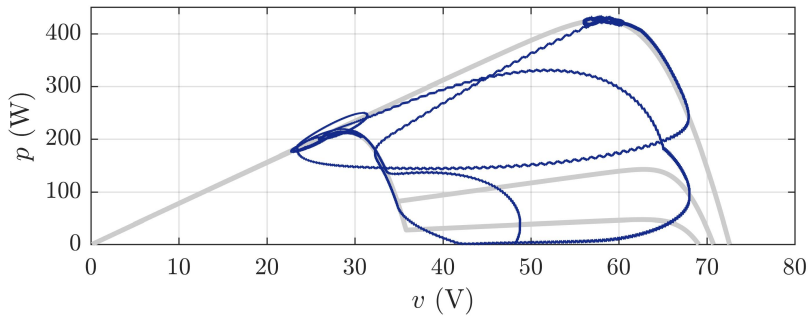

(b) Plot of p-v trajectory for P&O+SFOCV.

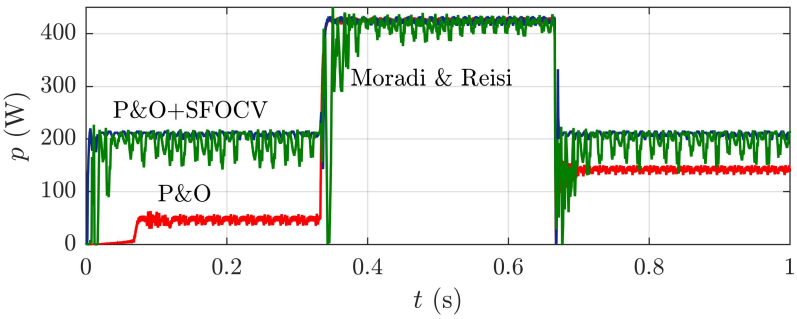

(c) Time plots of PV power.

Source: The author.

$S_2 = 300$ W/m^2 characteristic is reached. Hence, the proposed method effectively avoided the aforementioned tendency of P&O to keep tracking the same MPVV, thereby driving the PV panel to its global MPP during PS.

The p-v trajectory yielded by [108] has been omitted since it is very similar to that of P&O+SFOCV, albeit with much larger oscillations around the power maxima. In any case, it is seen from Figure 22(c) that, coupled with irradiance sensors and Equation 3.23, method [108] is also able to track the global MPP. However, it is clear from Figure 22(c) that [108] results in significant efficiency degradation due to oscillations caused by the PI controller, which led to a 7.51% efficiency loss with respect to P&O+SFOCV. It is particularly interesting to observe that the PI oscillations are much more severe than those in Section 3.4.5, which is explained by the large changes in the PI voltage reference when $\hat{N}$ increases or decreases.

It is straightforward to see that, for the considered $N_a = 2$ and $S_1 = 1000$ W/m^2, the estimate from Equation 3.23 implies a decision threshold $S_2 = 500$ W/m^2 for selecting $\hat{N} = 1$ or $\hat{N} = 2$. It was verified via manual testing that the true threshold is ≈ 457 W/m^2. Hence, the *worst-case* suboptimal tracking would occur for $S_2 = 499$ W/m^2, for which an 8.3% efficiency loss was computed. This analysis confirms the discussion from Section 3.3.4, in which it was established that Equation 3.23 may be suboptimal only for a small subset of PS cases whose associated losses are not exceedingly large.

3.5 Experimental Validation

As a practical validation of P&O+SFOCV, a small-scale experiment is carried out with a low-power prototype of the two-stage PV system depicted in Figures 14 and 15. The prototype consists of a PV cell, a low-power boost converter whose duty cycle is controlled via a microcontroller and, as in [120], a series connection of DC and AC sources for emulating the DC bus. A scheme of the prototype is presented in Figure 23, which is escribed in greater detail in what follows.

The considered PV cell is the 3 W model *CanadianSolar CS6MB-3P*, whose nominal parameters are $V_{mp}^{(o)} = 5.5$ V, $V_{oc}^{(o)} = 6.8$ V, $I_{mp}^{(o)} = 0.55$ A and $I_{sc}^{(o)} = 0.59$ A at nominal conditions $S_o = 1000$ W/m^2 and $T_o = 25$°C. For measuring PV output voltage and current, a *MAX471* sensor was used. Sensing of temperature was carried out with an *HDC1080* sensor, whereas a photodiode *OPT101* was approximately callibrated against high-accuracy measurements from the EMC weather station [26] and used to estimate irradiance. The *ATmega328* microcontroller is used and supplies pulse-width modulation at 50 kHz ($T_{sw} = 20$ μs). Selected switching elements were a *IRF630* MOSFET and a *1N5408* rectifier diode. The component values of the boost converter are given in Figure 23 and were approximately specified so that $\Delta V_o/V_o = 1\%$ and $\Delta I_L/I_L = 10\%$. A series

Figure 23 – Depiction of the experimental setup.

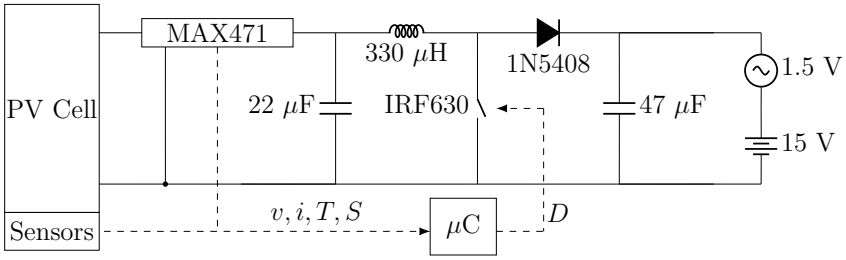

(a) Graphical scheme.

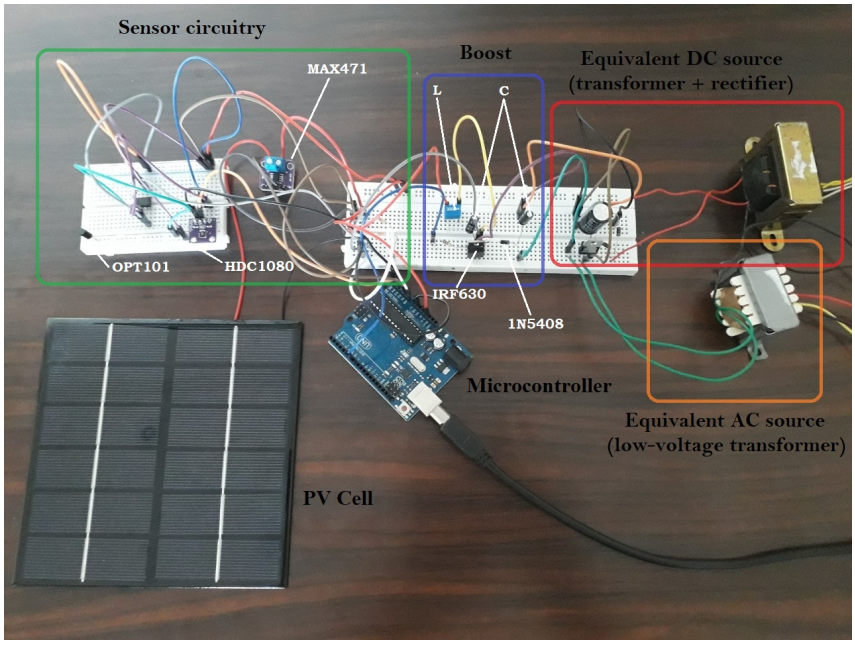

(b) Low-power prototype built with breadboards and jumper wires.

Source: The author.

connection of 15 Vdc and 1.5 Vac (@ 60 Hz) sources is used to emulate a DC bus with 10% ripple. Finally, $T_s = 2$ ms and other MPPT parameters are equal to those in Table 9.

An experiment was carried out as follows: the prototype was exposed to sunlight from 06:00 to 18:00 (local time) and the PV output power was registered by means of a data logger on a minute-by-minute basis. The irradiance and temperature measurements were then used together with the measured PV output power to estimate efficiency as:

$$\eta \approx \frac{\sum_{i=360}^{i=1080} p[i]}{\sum_{i=360}^{i=1080} \underbrace{FF \cdot V_{oc}(S[i], T[i]) \cdot I_{sc}(S[i], T[i])}_{\hat{p}_{mp}[i]}} \tag{3.37}$$

where $FF = V_{mp}^{(o)} I_{mp}^{(o)} / V_{oc}^{(o)} I_{sc}^{(o)}$ is the cell fill factor, $\hat{p}_{mp}[i]$ is the estimated PV maximum power and the values of $V_{oc}(S, T)$ and $I_{sc}(S, T)$ are computed via Equations 3.5 and 3.6. The notation $y[i]$ in Equation 3.37 denotes a sample of $y(t)$ at the i-th minute of the day.

The estimated efficiency computed for P&O+SFOCV was 93.41%. Obtained plots

Figure 24 – Results from the practical experiment.

Explanatory note: The results consist of time plots of (a) S and T at the weather station and (b) PV output power and estimated maximum power. The efficiency computed for P&O+SFOCV was 93.41%.

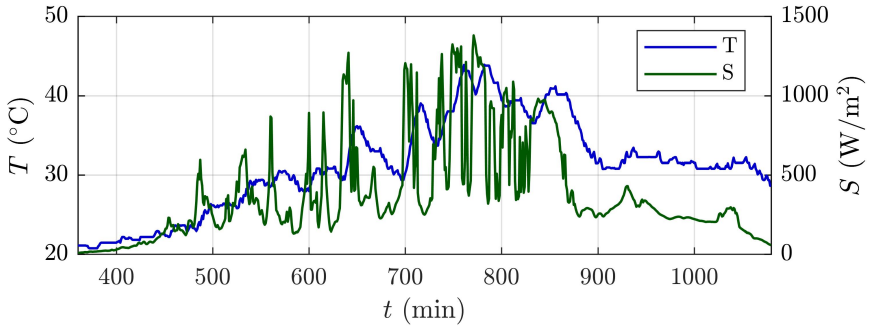

(a) Irradiance and temperature profiles.

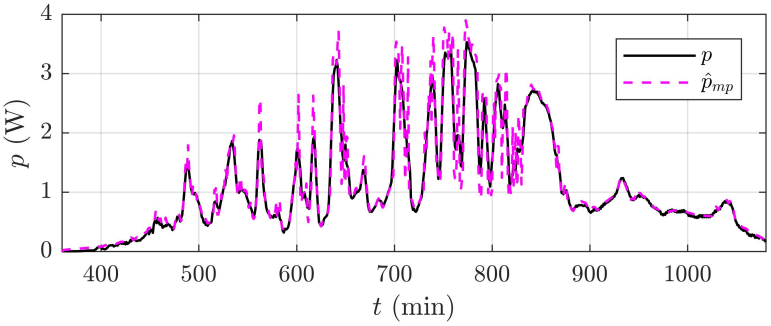

(b) Plots of PV power and estimated maximum power.

Source: The author.

of $p[i]$ and $\hat{p}_{mp}[i]$ are given in Figure 24, together with the irradiance and temperature profiles measured by the weather station. Note that, since $\hat{p}_{mp}[i]$ is an estimate, it is possible for $p[i] > \hat{p}_{mp}[i]$ to occur, which indeed happens for brief intervals of time as seen in Figure 24(b). This does not make Equation 3.37 inconsistent, since it estimates efficiency by means of an energy (and *not* power) ratio.

For the sake of comparison and further validation, the same experiment was repeated in the following day using the standard P&O algorithm. We omit the corresponding irradiance, temperature and power plots due to their similarity with those presented in Figure 24. An estimated P&O efficiency of 91.80% was obtained by using Equation 3.37.

It is seen that the estimated efficiencies of P&O+SFOCV and P&O agree with those computed in the 10% DC bus ripple simulation considered in Section 3.4.4, whose values are, respectively, 94.65% and 91.17%. The efficiency values obtained in the practical experiment present some deviation from those computed via simulation due to multiple factors, i.e.: noise, minute-by-minute sampling used to compute Equation 3.37 and different ambient condition dynamics. In any case, the approximate match with the obtained experimental results corroborates the simulations carried out in Section 3.4.

3.6 Conclusion

A novel hybrid MPPT approach specialized to two-stage PV systems has been proposed. Its main innovations are usage of sensor-aided FOCV for tracking changes in ambient conditions and of DDCC for reducing power oscillations in comparison to other hybrid methods. Validation of the proposed method was first carried out via simulation, whose results show that it (a) consistently outperforms P&O in uniform irradiance conditions, with an efficiency increase ranging from $\sim 2\%$ to $\sim 15\%$ depending on sample time and DC bus ripple; (b) provides a simple approximation to global MPPT in partial shading scenarios, which enabled it to surpass P&O efficiency by more than 27%; and (c) reduces oscillation losses when compared to a similar high-efficiency hybrid of P&O and FOCV, thereby surpassing its efficiency by up to $\sim 7\%$. Then, a practical experiment in which the proposed algorithm was applied to a PV cell exposed to sunlight for 12 hours was carried out. The obtained MPPT efficiency was in agreement with previous simulation results, corroborating the simulations and theoretical analysis. The proposed approach boasts of simple implementation since it does not require a PI controller and uses well-known legacy MPPT algorithms, thereby not requiring the use of adaptive parameters or large processing times, as is the case with most hybrid MPPT algorithms.

3.7 Acknowledgement

The author thanks Mr. Gilberto Lopes Filho for his assistance and for the equipment which were used for setting up the prototype used in the practical experiment.

4 Analytical MPPT for PV Water Heating Based on Inverter Input Impedance

4.1 Introduction

The increase in ecological and economic awareness of electricity consumers has caused the rapid adoption of power generation by means of distributed energy resources. In particular, PV generation is favoured by smaller consumers due to its modularity and ease of implementation [49–51]. Usual PV systems are implemented via one among two solutions, namely grid-tied (GT) and battery-equipped off-grid (BEOG) topologies [52–55].

A recent trend in PV generation that deviates from the aforementioned solutions is that of the photovoltaic water heating system (PWHS), which consists of a *batteryless off-grid* PV array dedicated to feeding a resistive element that heats a water reservoir [126]. It is known that water heating represents a large fraction of worldwide power demand, for which reason various solar water heating technologies have been devised over time [127]. In particular, photovoltaic-thermal (PV-T) systems have seen appreciable development and are deemed particularly attractive due to their simultaneous yield of electrical and heat outputs [128]. However, PV-T systems are relatively complex and costly to install, which, coupled with the simplicity and decreasing cost of PV modules, makes the PWHS a competitive approach for sustainable water heating. In fact, feasibility analyses carried out in [129, 130] have shown that the PWHS can yield smaller payback times than PV-T systems. The typical implementation of a PWHS is illustrated in Figure 25, where a water reservoir with dual heating element is used to enable grid demand when irradiance is low.

For all aforementioned types of PV system, a MPPT function must be performed by the electronic converters to ensure optimal PV power extraction for arbitrary loading

Figure 25 – Illustrative scheme of a photovoltaic water heating system with a dual heating element water reservoir. The PWHS block designates the cascade arrangement of PV array, DC converter and inverter.

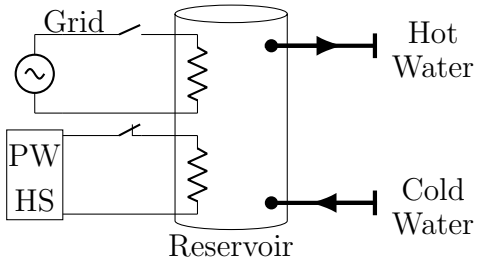

Source: The author.

and ambient conditions [56]. In particular, the off-grid system and its MPPT control structure are often implemented in a two-stage topology due to its superior MPPT performance [58–60]. The PV array is connected to a DC converter, whose output feeds the DC bus of an inverter, which then powers off-grid AC loads. In this context, the inverter terminals correspond to an equivalent load which must be matched to the PV array. Hence, the zero-frequency input response yielded by the DC bus determines the load characteristic perceived from the PV array terminals [131].

Aside from carrying out MPPT, both BEOG and GT systems also perform DC bus voltage regulation [116–119], which is required for adequate battery and grid connection, respectively. Hence, the DC bus load characteristics of such systems are, approximately, of constant voltage type. On the other hand, the PWHS is highly unusual in that inverter voltage operates in an open loop, with DC bus voltage being, thereby, *not* regulated. Furthermore, a constant impedance load (i.e., the heating element) is fed by the inverter. Hence, from the MPPT viewpoint, the PWHS presents a passive, impedance-type and nonlinear (due to inverter harmonics) load to the array.

In general, MPPT algorithms do not take into account the characteristics of loads connected to the PV array. From a viewpoint of generality, this is desirable since MPPT can be used with arbitrary load types. However, it is reasonable to inquire if considering load-specific MPPT methods may yield greater efficiency or simpler implementation for a given load type. Such considerations are the main motivation behind this Chapter, in which a PWHS-specific MPPT algorithm is proposed and has its performance assessed.

4.1.1 Previous Works on MPPT for PWHS

We now briefly review the existing MPPT schemes proposed for PWHS; it is interesting to note that such PWHS-specific approaches are relatively scarce in the literature and are all presented in patent documents [132–135]. The reader interested in extensive surveys of MPPT algorithms not specifically designed for PWHS is pointed to the survey carried out in Section 3.1.1 and to the review papers [64–66, 68].

In [132], the DC converter is controlled by means of a hill-climbing algorithm for carrying out MPPT. The specific algorithm is not disclosed by the authors, but a commercial PWHS implemented according to [132] has a nominal efficiency of 96% [136], from which it can be inferred that Perturb & Observe (P&O) was probably used [71]. It is worth noting that P&O has the problem of high sensitivity of efficiency with respect to sample time, which can complicate practical implementation.

Instead of hill-climbing MPPT, the constant voltage (CV) method is used in [133] to control the DC converter. Despite its simpler computations compared to P&O, a problem of CV is its greater steady-state error [64], which makes it less efficient. Also, it requires a

proportional-integral (PI) voltage controller, which increases implementation cost.

In [134], a variable resistance heater (VRH) is used for performing MPPT; the heating element resistance is switched between two possible values as a function of measured irradiance. This approach has the advantage of not requiring a DC converter, but it is a very rough MPPT approximation which may result in exceedingly low tracking efficiency.

Similarly, a VRH-based approach is also proposed in [135]. The main difference with respect to [134] is that a heating element with more than two resistance values is assumed. However, as pointed out by [129], it remains an approximate MPPT strategy and also implies an undesirably bulky and complex heating load.

4.1.2 Proposed Contribution

The above discussion shows that MPPT strategies for PWHS are quite scarce in the literature, with the existing approaches suffering from significant performance and implementation problems. Taking this as motivation, this work aims at proposing a novel MPPT method for PWHS that avoids the aforementioned difficulties associated to previous methods. Its innovation lies in using an expression deduced for inverter input impedance in combination with measurements from irradiance and temperature sensors, which enables analytical tracking to be performed. The proposed method is shown to have low implementation complexity and, as demonstrated by the experimental results, yields high efficiency and insensitivity to sample time.

4.2 Photovoltaic Water Heating System

The PWHS is comprised of PV module, DC-DC converter with MPPT control and inverter with associated heating load. For the DC conversion stage, a boost topology is assumed. Since modeling of the PV module and MPPT-controlled boost converter have already been described in Section 3.2, only computation of the boost converter reactive components and inverter modeling are considered in what follows.

4.2.1 Computation of DC-DC Converter Components

As discussed in Section 3.2.2, components L and C are functions of desired inductor current and converter output voltage ripples, respectively, whereas C_{PV} is designed to reduce PV voltage oscillations. The inductor and output capacitor can be designed via the continuous conduction mode relations, which are repeated for clarity [113]:

$$L = \frac{DVT_{sw}}{2 \cdot \Delta I_L} \tag{4.1}$$

$$C = \frac{DI_oT_{sw}}{2 \cdot \Delta V_o} \tag{4.2}$$

where ΔI_L and ΔV_o are, respectively, the inductor current and output voltage ripples.

Since L and C must be computed for MPP operation at nominal ambient conditions, $V = V_{mp}^{(o)}$ in Equation 4.1. Assuming a passive load R_o, the value of D in Equations 4.1 and 4.2 is obtained by matching the MPP resistance $R_{mp}^{(o)} \triangleq V_{mp}^{(o)}/I_{mp}^{(o)}$ to R_o. This is done by enforcing $M^2(D) = R_o/R_{mp}^{(o)}$ [113], from which $D = 1 - (R_{mp}^{(o)}/R_o)^{1/2}$ is obtained. The value of I_o in Equation 4.2 is computed by substituting $I = I_{mp}^{(o)}$ and the obtained value of D in Equation 3.8. Working out the described substitutions, it follows that:

$$L = \frac{V_{mp}^{(o)}T_{sw}\left[1 - \sqrt{\frac{V_{mp}^{(o)}}{R_oI_{mp}^{(o)}}}\right]}{2 \cdot \Delta I_L} \tag{4.3}$$

$$C = \frac{I_{mp}^{(o)}T_{sw}\left[\sqrt{\frac{V_{mp}^{(o)}}{R_oI_{mp}^{(o)}}} - \frac{V_{mp}^{(o)}}{R_oI_{mp}^{(o)}}\right]}{2 \cdot \Delta V_o} \tag{4.4}$$

where the value of load resistance R_o is discussed in Section 4.3.1 and the nominal ripple parameters are converter design choices.

Recall from Section 3.2.2 that small values of C_{PV} are sufficient for suppressing PV voltage ripple [114, 137]. Hence, as before, it is assumed that $C_{PV} = C$ for simplicity.

4.2.2 Inverter With Water Heating Load

A single-phase bipolar PWM full-bridge inverter with output and PWM switching frequencies f_c and f_{swi}, respectively, is considered. Since the PWHS inverter does not perform voltage regulation (see Section 4.1), constant amplitude modulation m_a is assumed. Also, PWM undermodulation (i.e., $m_a \leq 1$) is assumed to avoid degeneration to square-wave modulation [125]. As depicted in Figure 26, the inverter feeds an impedance load

Figure 26 – Single-phase inverter with heating load.

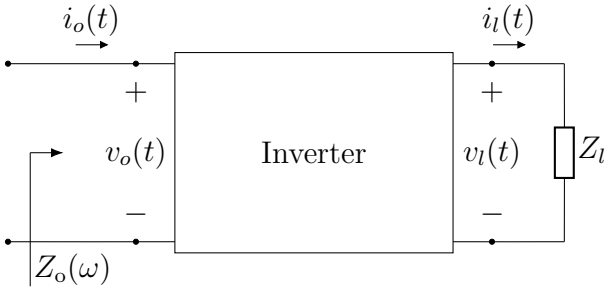

Source: The author.

$Z_l = |Z_l|\angle\theta_l$ ($@f_c$), which is an equivalent of the water heating load R_l and the inverter output filter. Since heaters do not require high power quality [132], a simple output inductor L_l is assumed for filtering current harmonics. Hence, $Z_l(\omega) = R_l + j\omega L_l$, where ω denotes angular frequency. For a DC input $v_o(t) = V_o$, the inverter output voltage is [137]:

$$v_l(t) = V_l\sqrt{2} \cdot \left[\sum_{k\in\mathcal{H}} c_k \sin(k\omega_c t)\right] \tag{4.5}$$

where $\omega_c = 2\pi f_c$, V_l is the root mean square (RMS) value of the fundamental component of $v_l(t)$, $\mathcal{H}$ is the set of voltage harmonic orders and c_k is the fixed ratio of the k-th harmonic RMS value with respect to V_l (in particular, $c_1 = 1$). For bipolar PWM, the set $\mathcal{H} = \{a \cdot m_f \pm b; a, b \in \mathbb{N}^*\}$, where $m_f = f_{swi}/f_c$ is the frequency modulation index.

Note that computing $i_l(t)$ is trivial and can be carried out at each harmonic frequency by using $Z_l(\omega)$ and Equation 4.5, whereas the inverter input current $i_o(t)$ is not straightforward to obtain. Estimation of $i_o(t)$ is crucial for the MPPT approach proposed in this work and will be further considered in Section 4.3.1.

As depicted in Figure 26, the inverter input impedance $Z_o(\omega) = \hat{V}_o(\omega)/\hat{I}_o(\omega)$ is defined for later use, where $\hat{V}_o(\omega)$ is the phasor associated to a single-frequency input $v_o(t) = V_o\sqrt{2} \cdot \sin(\omega t)$ and $\hat{I}_o(\omega)$ is the phasor of the $i_o(t)$ component at input frequency.

4.3 Proposed MPPT Approach for PWHS

In this Section, an analytical MPPT approach for PWHS is proposed. An expression for estimating DC ($\omega = 0$) input impedance of the PWHS inverter is first derived. Next, it is used as basis for formulating the proposed MPPT method.

4.3.1 Estimation of Inverter Input Impedance

Recall from the discussion in Section 4.1 that, since the PWHS inverter does not have a DC bus connected to batteries or AC terminals tied to the grid, voltage regulation must be relegated so that MPPT can be performed. Hence, as anticipated in Section 4.1, the inverter presents a nonlinear impedance-type equivalent load to the PV array.

Now, let a single-frequency input voltage $v_o(t)$ with corresponding phasor $\hat{V}_o(\omega)$ feed the inverter. Aside from nonlinearity yielding a response $i_o(t)$ with harmonic content, it may also be the case that $Z_o(\omega)$ is a function of $\hat{V}_o(\omega)$ itself. In what follows, it is established in **Proposition 5** that this is *not* the case for DC input impedance $R_o \triangleq Z_o(0)$, which is shown to be a constant. Hence, it will be proved that, at zero frequency, the inverter and its associated heating load can be represented as an equivalent resistive load.

Proposition 5: Let $Z_l = |Z_l|\angle\theta_l$ be an AC load connected to the output of a single-phase full-bridge PWM inverter. The DC input impedance R_o of this system is:

$$R_o = \frac{2|Z_l|}{m_a^2 \cos\theta_l} \tag{4.6}$$

Proof: Let $v_o(t) = V_o$. To compute R_o, the input current DC component, namely I_o, is required. Now, consider the computation of instantaneous power at the inverter DC and AC ports. If Z_l is not exceedingly reactive (i.e., $|\theta_l|$ is not very close to 90°), conservation of instantaneous power is approximately valid between the two ports [138]:

$$V_o i_o(t) = v_l(t) i_l(t) \tag{4.7}$$

Since f_{swi} is assumed large, all output current harmonics will be filtered even for small $|\theta_l|$. Hence, it can be safely assumed that $i_l(t) = I_l\sqrt{2}\sin(\omega_c t - \theta_l)$, where I_l is the RMS value of load current. Hence, the following is obtained from Equation 4.7:

$$i_o(t) = \frac{2V_l I_l}{V_o}\sin(\omega_c t - \theta_l) \times \left[\sum_{k\in\mathcal{H}} c_k \sin(k\omega_c t)\right] \tag{4.8}$$

which, when further developed, yields:

$$i_o(t) = \underbrace{\frac{V_l I_l}{V_o}\cos\theta_l}_{I_o} - \underbrace{\frac{V_l I_l}{V_o}\cos(2\omega_c t - \theta_l)}_{i_o^{(2)}(t)} + \underbrace{\frac{2V_l I_l}{V_o}\sum_{k\in\mathcal{H}-\{1\}} c_k \sin(k\omega_c t)\sin(\omega_c t - \theta_l)}_{i_o^*(t)} \tag{4.9}$$

where $i_o^{(2)}(t)$ is a component at double nominal frequency associated to single-phase power oscillation at the inverter AC port and $i_o^*(t)$ is the sum of high frequency components associated to PWM switching. Using the expression for I_o from Equation 4.9 and recalling that $V_l = \frac{1}{\sqrt{2}} m_a V_o$ for bipolar PWM [125], it follows that:

$$R_o = \frac{V_o}{I_o} = \frac{V_o^2}{V_l I_l \cos\theta_l} = \frac{|Z_l| V_o^2}{V_l^2 \cos\theta_l} \Rightarrow R_o = \frac{2|Z_l|}{m_a^2 \cos\theta_l} \tag{4.10}$$

and the proof is thus complete. ■

The assumptions used in **Proposition 5** are satisfied in practice by the PWHS, since the output inductor ensures filtering of $i_l(t)$ and does not dominate load impedance at nominal frequency. In other words, $i_l(t)$ is approximately sinusoidal and $Z_l(\omega_c) = R_l + j\omega_c L_l$ satisfies $|\theta_l| \ll 90°$, with instantaneous power conservation being thus valid.

As a means of further discussing the validity of instantaneous power conservation, a comparison between values of R_o computed by means of simulation and by using Equation 4.6 for varying $|\theta_l|$ is carried out in Section 4.5.

4.3.2 Proposed Method: PWHS-MPPT

It has been established in **Proposition 5** that the PWHS inverter and associated heating load can be represented by an equivalent resistance R_o. The proposed analytical MPPT method, which is named PWHS-MPPT, consists in using irradiance and temperature sensors to estimate the PV array MPP resistance $R_{mp}(S,T) \triangleq V_{mp}(S,T)/I_{mp}(S,T)$ and subsequently computing the D value that matches it to R_o. More precisely, PWHS-MPPT iterates the following steps at each multiple of the selected sample time T_s:

1. Sample S and T from sensors;
2. Use sampled values to estimate $R_{mp}(S,T)$;
3. Solve $M^2(D) = R_o/R_{mp}(S,T)$ analytically for D, where R_o is the equivalent load resistance computed from Equation 4.6.

It remains to establish an approach for computing $R_{mp}(S,T)$. An approximate closed-form expression is derived in **Proposition 6**.

Proposition 6: The value of $R_{mp}(S,T)$ can be computed as:

$$R_{mp}(S,T) = K \cdot \frac{N_s m V_t \ln\left(\frac{S}{S_o}\right) + V_{oc}^{(o)} \cdot [1 + \alpha_V (T - T_o)]}{I_{sc}^{(o)} \cdot \frac{S}{S_o} [1 + \alpha_I (T - T_o)]} \tag{4.11}$$

where $K = V_{mp}^{(o)} I_{sc}^{(o)} / V_{oc}^{(o)} I_{mp}^{(o)}$.

Proof: For any S and T, $K_V = V_{mp}/V_{oc}$ and $K_I = I_{mp}/I_{sc}$ are approximately constant [25]. Hence, from the definition of R_{mp}, it is clear that:

$$R_{mp}(S,T) = \frac{V_{mp}(S,T)}{I_{mp}(S,T)} = K \cdot \frac{V_{oc}(S,T)}{I_{sc}(S,T)} \tag{4.12}$$

where $K = K_V/K_I$ and K_V, K_I can be estimated from datasheet values as $K_V = V_{mp}^{(o)}/V_{oc}^{(o)}$ and $K_I = I_{mp}^{(o)}/I_{sc}^{(o)}$. Combining Equations 3.5, 3.6 and 4.12, the proof is complete. ■

To illustrate the proposed method, it is expressed in block diagram form in Figure 27, where the sets $\mathcal{X}_o = \{m_a, Z_l\}$ and $\mathcal{X}_{mp} = \{m, N_s, S_o, T_o, K, \alpha_V, \alpha_I, V_{oc}^{(o)}, I_{sc}^{(o)}\}$ contain nominal data for computing R_o and $R_{mp}(S,T)$, respectively.

4.3.3 Implementation Requirements

From the description of PWHS-MPPT in Section 4.3.2, its implementation requires (a) nominal PV module and heating load data; (b) specification of sample time T_s; and (c) two sensors. The nominal data are readily available and, as a consequence, their acquisition does not constitute an implementation disadvantage. In particular, note that if

Figure 27 – Block diagram of PWHS-MPPT, where $M^{-1}(D)$ is the conversion ratio inverse. Sets $\mathcal{X}_{mp}$ and $\mathcal{X}_o$ contain nominal PV module and load data.

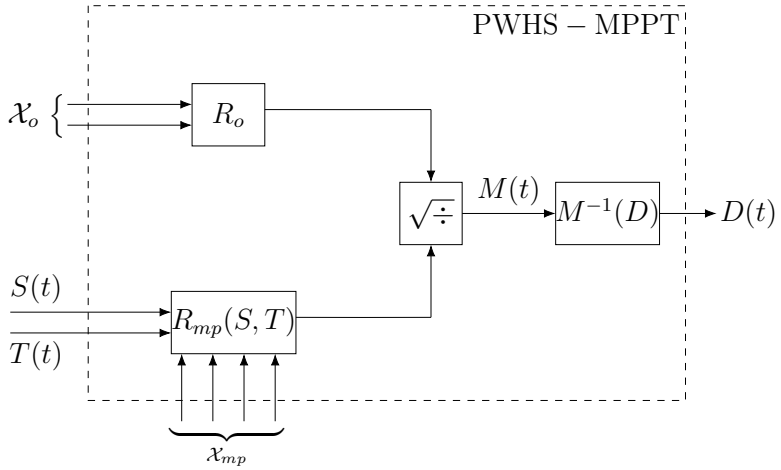

Source: The author.

the ODM parameter m is not known, $m \approx 1$ can be safely adopted in Equation 4.11 since the term which contains m is very small [24]. Now, consider comparing the remaining requirements with those of P&O, whose wide adoption is due to it being the simplest hill-climbing MPPT method. Two parameters must be specified for implementing P&O (T_s and ΔD), whereas PWHS-MPPT only requires T_s. On the other hand, both methods require two sensors. More precisely, voltage and current sensors are used by P&O, whereas PWHS-MPPT employs irradiance and temperature sensors. Coupled with the fact that P&O is an iterative procedure and PWHS-MPPT is entirely analytical, such considerations show that PWHS-MPPT has an even *simpler* computational implementation than P&O.

4.4 Computer Simulations

In this Section, PWHS-MPPT is validated via computer simulations, in which it is compared to other MPPT algorithms proposed for PWHS. First, the considered simulation model is described. Subsequently, the four-part computer experiment is presented. All simulations have been implemented in Simulink R2017a.

4.4.1 Simulation Model

The PV module adopted for simulation is once more the *1Soltech 1STH-215-P* model, whose nominal data are given in Table 8 of Chapter 3. An array with $N_{sha} = 3$ parallel strings with $N_{sa} = 3$ modules each (i.e., a 3×3 array) is considered, for which 1918.35 W peak power at 87 V and 22.05A is obtained at rated ambient conditions.

The boost converter components and switching period have been selected to yield ripple values of $\Delta V_o \approx 180$ mV and $\Delta I_L \approx 125$ mA. A range for MPPT sampling time from

50 μs to 1500 μs is considered. When P&O is used, a small duty cycle increment $\Delta D = 0.01$ is used since the possible sampling times are small. An output frequency $f_c = 60$ Hz is adopted for the PWM inverter, for which amplitude and frequency modulations of $m_a = 1$ and $m_f = 29$, respectively, are considered. An AC load $Z_l(\omega_c) = 25\angle 5°\ \Omega$ is adopted, which corresponds to a heating load of 1928.63 W at 220 Vac and an output filter inductor $L_l \approx 5.8$ mH. Such data on the MPPT-controlled boost converter and inverter are summarized in Table 10, where converter switches (see Figure 14) are also specified.

Table 10 – Boost converter and PWM inverter parameters

Parameter	**Specification**
C, C_{PV}	1 mF
L	5 mH
S_1	On-resistance: $r_{\text{on}} = 1$ mΩ Forward voltage: $V_{\text{fwd}} = 0.7$ V
S_2	MOSFET On-resistance: $r_{\text{on}} = 100$ mΩ Internal diode parameters: same as S_1
MPPT	$T_{\text{s}} \in [50, 1500]$ (μs), $T_{\text{sw}} = 20$ μs $\Delta D = 0.01$ (P&O only)
Inverter	$m_a = 1$, $m_f = 29$, $f_c = 60$ Hz $Z_l = 25\angle 5°\ \Omega$ (@f_c) Full-bridge switches: same as S_2

Source: The author.

4.4.2 Part 1: Comparison to Other Methods

As a first validation step, the performance of PWHS-MPPT is compared to those yielded by the P&O [132], CV [133] and VRH [134] algorithms. In particular, VRH is considered in its version with two possible load resistance values, which functions by doubling the nominal value of R_l when $S < 500$ W/m^2. Also, parameters of the PI controller required in CV are obtained with the Ziegler-Nichols method [71]. For each algorithm, a simulation scenario with $\tau = 1$ s duration is carried out in which irradiance begins at $S = 300$ W/m^2, switches to $S = 1000$ W/m^2 at $t = \frac{1}{3}$ s and, at last, changes to $S = 700$ W/m^2 at $t = \frac{2}{3}$ s. A sample time $T_s = 1000$ μs is used and a constant temperature $T = 25$°C is assumed throughout the experiment.

Obtained results are shown in Figure 28, where computed efficiencies and time plots of $p(t)$, $D(t)$, $v(t)$ and $V_l(t)$ are presented for each considered MPPT method. For clarity, recall that $V_l(t)$ denotes the RMS value associated to the fundamental component of $v_l(t)$. The MPPT efficiency is computed according to Equation 3.34.

As could be expected, the results show that VRH is the least competitive MPPT approach. It is seen to be very inneficient when the PV array is not subject to nominal

Figure 28 – Results for the MPPT algorithm comparison from Part 1.

Explanatory note: The results consist of time plots of (a) $p(t)$, (b) $D(t)$, (c) $v(t)$ and $V_l(t)$. The "MPP" line is the plot of $p_{mp}(t)$. Efficiencies yielded by PWHS-MPPT, P&O, CV and VRH were, respectively, 96.33%, 95.54%, 95.15% and 85.21%. Note that VRH does not use duty cycle control and therefore has no associated $D(t)$ curve.

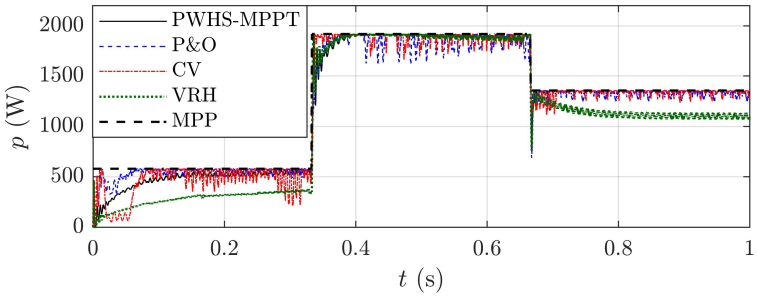

(a) Plots of output power.

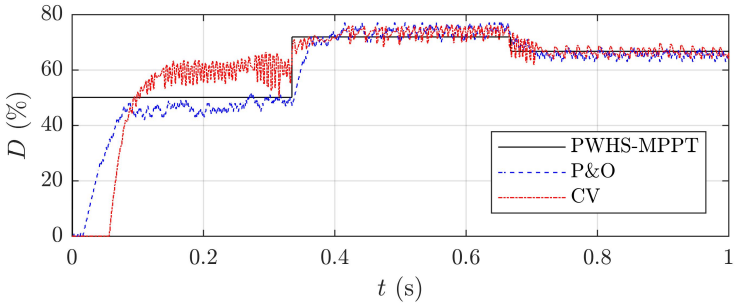

(b) Plots of converter duty cycle.

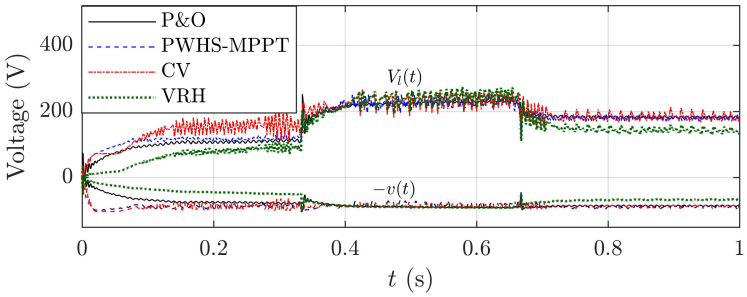

(c) Plots of PV and inverter output voltages.

Source: The author.

conditions, i.e., when $S \neq 1000$ W/m^2. This is explained by the fact that perfect source-load matching occurs with VRH only in two cases, namely nominal irradiance and $S = 500$ W/m^2, which is the threshold used by VRH for doubling load resistance. For all other irradiance values, steady-state error and, as a consequence, efficiency losses occur.

The CV algorithm has its efficiency reduced by two inherent problems, namely steady-state error and PI controller oscillations. The first issue is clearly seen from the $D(t)$ plots, which show that mismatch occurs with respect to the optimal duty cycle. Such

error is caused by the fact that V_{mp} has a slight dependence on S, whereas CV attempts to maintain PV voltage at the nominal value $V_{mp}^{(o)}$. Hence, a large error occurs for $t < \frac{1}{3}$ s since irradiance is far off the nominal S_o. The oscillation issue occurs due to interactions between DC converter and PI controller dynamics: the converter PWM switchings excite the PI response and thereby increase system oscillations, which further reduces efficiency.

Contrastingly to VRH and CV, both P&O and PWHS-MPPT are seen to have negligible steady-state error and small oscillations. Consequently, such algorithms yielded the highest efficiency values. Despite the small oscillations of P&O, it is quite notable that it still oscillates significantly when compared to PWHS-MPPT. Since both algorithms presented similar tracking speeds, it is clear that the very small oscillations yielded by PWHS-MPPT are the cause of its superior efficiency. Due to its importance, this phenomenon is discussed in greater detail in the simulation experiment from Section 4.4.3.

Since it was demonstrated by the obtained results that PWHS-MPPT and P&O are, among the consider algorithms, the best-performing ones, Sections 4.4.3 to 4.4.5 shall focus on comparing both methods in more detailed simulations.

4.4.3 Part 2: Dynamic Ambient Conditions

In this Section, PWHS-MPPT is compared to P&O for scenarios with periodic random-amplitude step variations in irradiance and temperature. Such step-like waveforms are considered for S and T due to being more demanding for the MPPT algorithms, since response speed becomes critical to achieving high efficiency.

A sample time $T_s = 1000$ μs is adopted for both algorithms; the effect of varying sample time on MPPT performance will be considered later in Section 4.4.4. At first, a dynamic irradiance simulation with a 30 s duration and constant temperature $T = 25°\text{C}$ is considered. It is carried out according to the following procedure:

1. Set initial conditions $D = 0$ and $T = 25°\text{C}$ at $t = 0^-$;
2. At $t \in \{0.2 \cdot j,\ j = 0, 1, \ldots, 150\}$, set S to a value randomly drawn, according to a uniform distribution, from $\mathcal{S} = \{100 \cdot j,\ j = 0, 1, \ldots, 10\}$ (W/m^2);
3. Terminate at $t = 30$ s and compute MPPT efficiency.

An analogous procedure is then carried out in a dynamic temperature simulation, in which $S = 1000$ W/m^2 and T is drawn from set $\mathcal{T} = \{10 \cdot j,\ j = 0, 1, \ldots, 10\}$ (°C).

Obtained results are presented in Figures 29 and 30, where computed MPPT efficiencies and time plots of $p(t)$, $D(t)$, $v(t)$ and $V_l(t)$ are presented, respectively, for the dynamic irradiance and temperature simulations.

Figure 29 – Results for dynamic S simulation of Part 2.

Explanatory note: The results consist of partial time plots ($14.9 \leq t \leq 20.1$) of (a) $p(t)$, (b) $D(t)$, (c) $v(t)$ and $V_l(t)$. The "MPP" traced line is the plot of maximum power $p_{mp}(t)$. Efficiencies yielded by PWHS-MPPT and P&O were, respectively, 94.45% and 93.86%.

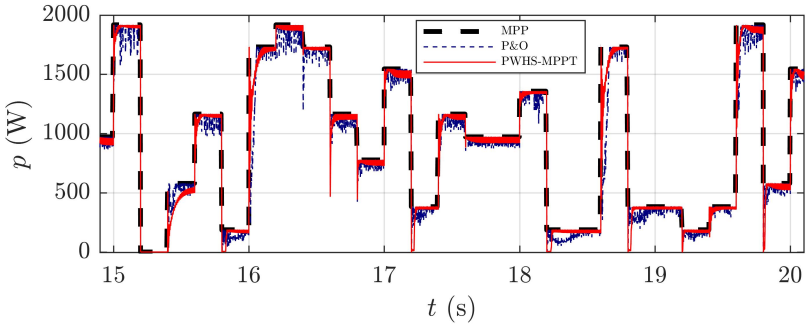

(a) Plots of output power.

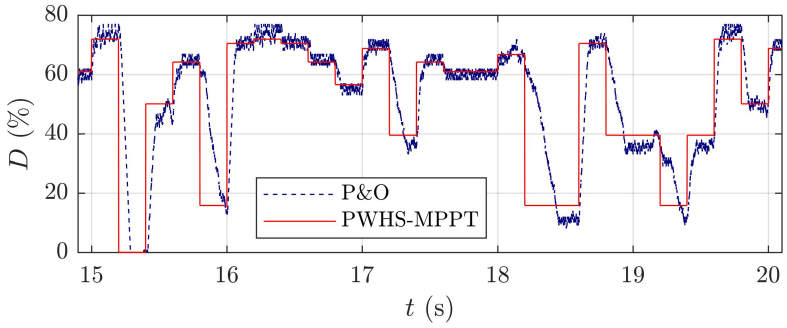

(b) Plots of converter duty cycle.

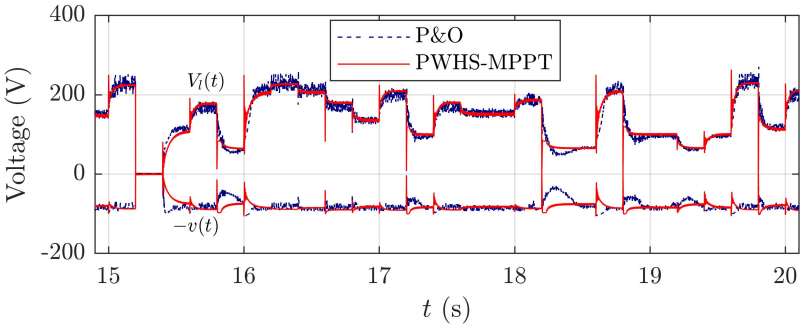

(c) Plots of PV and inverter output voltages.

Source: The author.

Figure 30 – Results for dynamic T simulation of Part 2.

Explanatory note: The results consist of partial time plots ($14.9 \leq t \leq 20.1$) of (a) $p(t)$, (b) $D(t)$, (c) $v(t)$ and $V_l(t)$. The "MPP" traced line is the plot of maximum power $p_{mp}(t)$. Efficiencies yielded by PWHS-MPPT and P&O were, respectively, 97.30% and 96.40%.

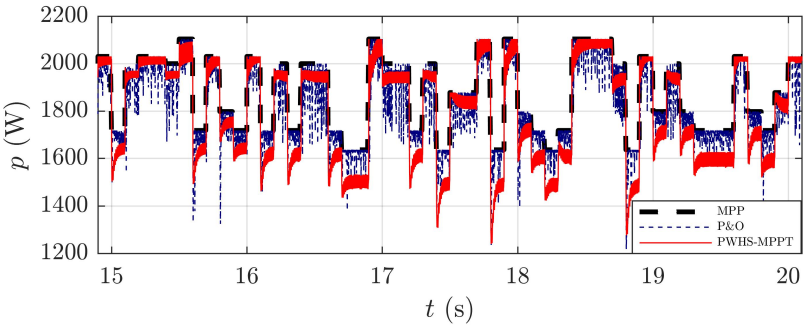

(a) Plots of output power.

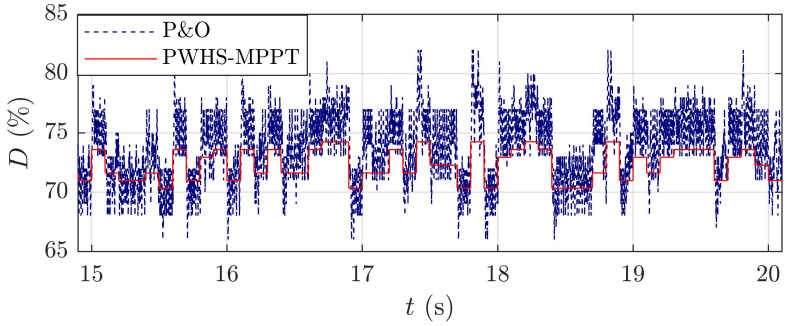

(b) Plots of converter duty cycle.

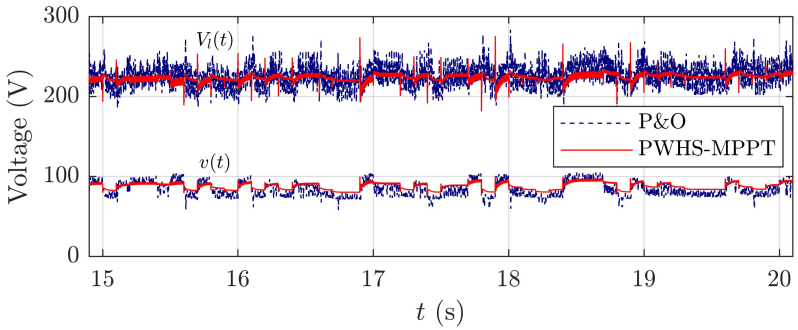

(c) Plots of PV and inverter output voltages.

Source: The author.

As anticipated in the previous experiment, this comparison against P&O makes it particularly clear that a prominent feature of PWHS-MPPT is its very small steady-state oscillation. This is explained by the fact that, during steady-state, PWHS-MPPT yields constant duty cycle, whereas P&O oscillates around the maximum power point. Hence, only the very small oscillations associated to boost converter ripple affect PWHS-MPPT peformance and steady-state efficiency is improved as a consequence. This is corroborated by the plots of $v(t)$ and $V_l(t)$ in Figures 29 and 30, where the P&O voltage waveforms present significant oscillation when compared to PWHS-MPPT.

It is fair to note that some steady-state loss is introduced by PWHS-MPPT due to duty cycle estimation error. However, the $p(t)$ plots in Figures 29 and 30 show that such loss is, in general, negligible. A single exception applies: from Figure 30, it is seen that larger losses happen for smaller $p(t)$ values, which correspond to temperatures close to $T = 100°\text{C}$. This indicates that Equation 4.11 is less accurate for larger T. Fortunately, such loss increase happens for smaller $p_{mp}(t)$ whose associated T are uncommon in practice.

In any case, even with the aforementioned losses due to estimation error in the dynamic T simulation, PWHS-MPPT still performed better than P&O. In fact, as indicated in Figures 29 and 30, the proposed method yielded higher efficiency both for the dynamic irradiance (0.59% improvement) and temperature (0.90% improvement) simulations.

Aside from reduced steady-state oscillation, the good performance of PWHS-MPPT can also be attributed to its very fast tracking, which is clear from the $D(t)$ plots in Figures 29 and 30, where the PWHS-MPPT duty cycle anticipates the trend followed by the $D(t)$ waveform yielded by P&O. This is explained by the fact that PWHS-MPPT computes duty cycle analytically, whereas P&O depends on a iterative perturbation routine. Hence, the proposed method compensates for varying S and T in a nearly instantaneous manner.

At last, it is interesting to note that the absence of voltage regulation in PWHS is especially clear in the dynamic S case, where the AC port voltage $V_l(t)$ varies in a wide range due to the large variations of $R_{mp}(S, T)$, which is a strong function of S. In any case, $V_l(t)$ does not severely exceed the rated 220 V load voltage, since $P_{mp}^{(o)}$ was approximately matched to the nominal heating load power (see Section 4.4.1).

4.4.4 Part 3: Effect of Sampling Time

The performance of P&O has a strong dependence on sample time T_s. Furthermore, tuning T_s for a selected ΔD or vice-versa is nontrivial and dependent on the overall system (i.e., PV array, DC converter and load) dynamic response [120]. This is a significant disadvantage of the P&O algorithm, since it requires significant time to be spent on trial-and-error parameter tuning [71], which may not be allowable in practical circumstances.

In this context, an advantage of PWHS-MPPT is that it only requires specification

of one parameter, namely T_s. However, the sensitivity of PWHS-MPPT with respect to such parameter must still be assessed and compared to that of P&O. To this end, both methods are simulated for varying $T_s \in [50, 1500]$ (μs), with this interval being discretized in increments of 50 μs. Recall that, for P&O, a fixed $\Delta D = 0.01$ is assumed.

For each MPPT method and value of T_s, a simulation with 1 s timespan is carried out which consists of a transition from complete shading to nominal irradiance, at nominal temperature. The considered simulation is described by the following steps:

1. At $t = 0^-$, set $D = 0$, $S = 0$ W/m^2, and $T = 25$°C;
2. At $t = 0.5$ s, set $S = 1000$ W/m^2.
3. Terminate at $t = 1$ s and compute MPPT efficiency.

Obtained results are displayed in Figure 31, where efficiency is plotted as a function of T_s for each MPPT method, together with $p(t)$ and $D(t)$ plots for selected T_s values.

The $\eta(T_s)$ plots in Figure 31 show that PWHS-MPPT is much less sensitive to sample time than P&O, which is explained as follows. Each perturbation induced by P&O excites a transient response in the circuit, which implies that the tracking efficiency depends on the complex interaction between successive and superposed transients. This phenomenon results in the existence, for a given ΔD, of an optimal T_s, whereas other values of sample time worsen efficiency. On the other hand, for each change in S or T, PWHS-MPPT causes a single electrical transient. Hence, complex superpositions do not occur and T_s becomes much less critical in determining tracking efficiency.

Insensitivity of PWHS-MPPT to T_s is a major advantage, since it does not require fine-tuning of sample time in order to achieve adequate performance. The exact opposite is true for P&O: extensive trial-and-error is required to determine an optimal-efficiency T_s. The plots of $p(t)$ and $D(t)$ for $T_s = 50$ μs and $T_s = 1500$ μs in Figure 31 further illustrate the difficulty of selecting T_s for P&O: a high sample time leads to excessive tracking delay, whereas small T_s causes drift due to the noise effect of output power ripple [71].

It is fair to note that a single value $T_s = 250$ μs was obtained for which P&O efficiency slightly surpassed that of PWHS-MPPT; the $p(t)$ and $D(t)$ plots of P&O with $T_s = 250$ μs are depicted in Figure 31. This confirms the prior discussion that P&O requires much fine-tuning to attain optimal efficiency. Furthermore, it can be inferred that, in practical circumstances where a value of T_s would be selected without very extensive testing, PWHS-MPPT would perform better than P&O with very high probability. At last, by averaging over all T_s, it is concluded that PWHS-MPPT yielded an average efficiency improvement of 7.55% with respect to P&O.

Figure 31 – Results for varying T_s simulation of Part 3.

Explanatory note: The results consist of consist of (a) plot of efficiency in terms of T_s and time plots of (b) $p(t)$ and (c) $D(t)$ for selected values of sample time (50 μs, 250 μs and 1500 μs).

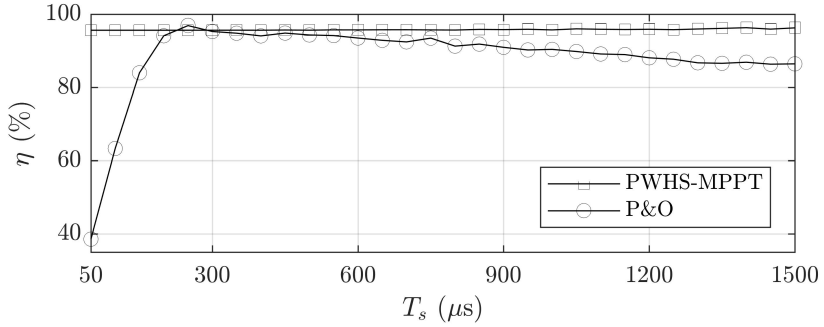

(a) Plots of efficiency in terms of sample time.

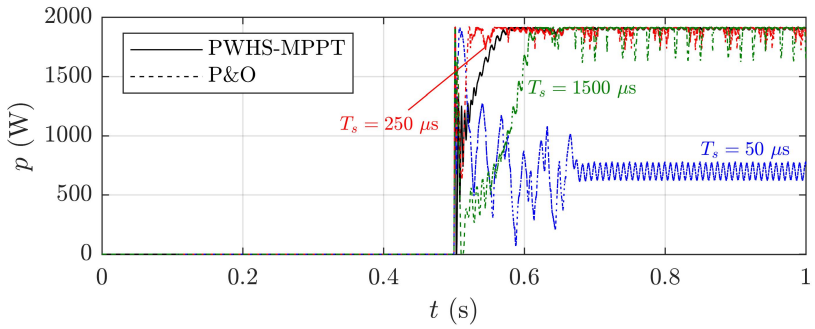

(b) Plots of output power.

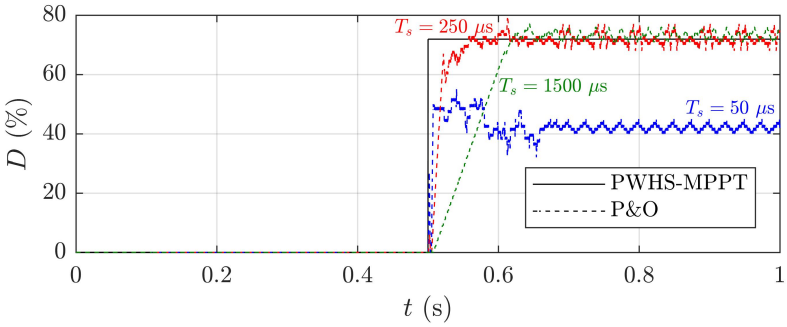

(c) Plots of converter duty cycle.

Source: The author.

4.4.5 Part 4: Effect of Heating Load Mismatch

The PWHS-MPPT algorithm is based on the assumption that heating load R_l is known and constant, which enables using Equation 4.6 to obtain the inverter input impedance. In this sense, the resulting efficiency loss if a mismatch occurs between the real heating load and the value assumed for Z_l when estimating R_o must be assessed.

To perform such analysis, a simulation is carried out in which the real load R_l remains fixed (as given in Table 10) and a value $\tilde{R}_l = R_l + \Delta R_l$ is used for computing Equation 4.6, with the load error ΔR_l being varied in the interval $[-R_l/2, R_l/2]$ at increments of $R_l/400$. The simulation scenario is the same as that of Section 4.4.4, namely a 1 s simulation at nominal temperature, with a step transition from complete shading to nominal irradiance at $t = 0.5$ s. The results are given in Figure 32, where a plot of efficiency *versus* ΔR_l is displayed, together with $p(t)$ plots associated to different η values.

It is seen that constant η values are obtained for different ranges of ΔR_l. This phenomenon is explained by boost converter dynamics: small variations in $\tilde{R}_l$ are masked by power ripple, for which reason the system progresses as if no variation occurred at all. On the other hand, when a certain $\tilde{R}_l$ variation threshold is surpassed which makes it distinguishible from ripple, the dynamics change and cause a corresponding variation in efficiency. This is advantageous for PWHS-MPPT, since it establishes a margin inside of which mismatch does not cause efficiency loss. In fact, the results in Figure 32 show that optimal efficiency was obtained in the relatively wide range $\Delta R_l \in [-0.12 \cdot R_l, 0.25 \cdot R_l]$, i.e., a 37% error margin for no efficiency loss was obtained.

The $p(t)$ plots corresponding to each constant-η in Figure 32 show that worst losses occur when R_l is severely underestimated. This is explained by comparing the nominal maximum power point resistance $R_{mp}(S_o, T_o) \approx 3.95\ \Omega$, with the correct DC input impedance value $R_o \approx 50.2\ \Omega$ computed via Equation 4.6. Since $R_o \gg R_{mp}^{(o)}$, the optimal duty cycle $D \approx 0.72$ is relatively high. Hence, greater matching errors occur when D tends to zero rather than to unity. But $D \to 0$ precisely when R_l is subestimated, i.e., when $\Delta R_l < 0$. For the same reason, the optimal η margin is narrower for $\Delta R_l < 0$.

Most importantly, the wide ΔR_l margin for which optimal efficiency was obtained demonstrates that PWHS-MPPT is robust with regard to estimation error. In this sense, it is concluded that, in practice, subtle changes in R_l which may happen over time are not likely to significantly impact PWHS-MPPT performance.

4.5 Estimation Accuracy

To assess the accuracy of Equation 4.6, a simulation experiment is carried out as follows. An inverter with load Z_l is directly fed by a constant voltage $V_o = 100$ V and the

Figure 32 – Results for heating load mismatch simulation of Part 4.

Explanatory note: The results consist of (a) plot of η as a function of ΔR_l and (b) time plots of $p(t)$ for each of the obtained constant-η intervals.

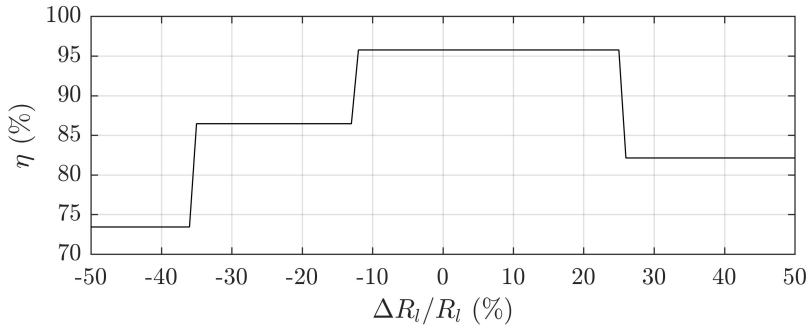

(a) Plot of efficiency in terms of load mismatch.

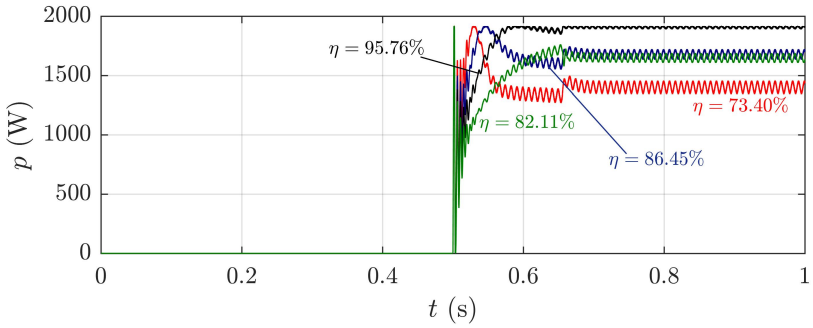

(b) Plots of output power.

Source: The author.

input DC current I_o is recorded, thus enabling the computation of R_o. For this simulation, $m_a = 1$, $m_f = 25$, $f_c = 60$ Hz and $|Z_l| = 1\ \Omega$ are considered. The simulation is iterated for $\theta_l = 0°, 1°, \ldots, 89°$ and the obtained DC input impedance values R_o^{sim} are compared to those computed from Equation 4.6, denoted as R_o^{est}, by means of the relative error:

$$e(\theta_l) = \frac{|R_o^{sim}(\theta_l) - R_o^{est}(\theta_l)|}{R_o^{sim}(\theta_l)} \tag{4.13}$$

The results are plotted in Figure 33 and corroborate the analysis carried out in Section 4.3.1 with respect to the validity of Equation 4.6. The estimation error is relatively low for ranges other than the neighborhood of $|\theta_l| = 90°$, in which it rapidly diverges due to violation of the instantaneous power conservation assumption. It is also noteworthy that error increases for very small power angles, which is explained by violation of the current harmonic filtering assumption used when deriving **Proposition 5**. This is not a major drawback, since the inverter output filter (and, in practice, system inductances) ensure that, despite having a small value, θ_l does not approach zero very tightly.

Figure 33 – Plot of input impedance estimation error against θ_l.

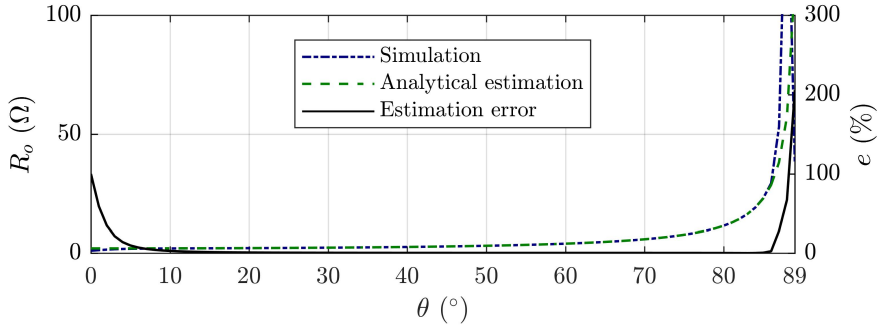

Source: The author.

4.6 Conclusion

A novel high-efficiency and analytical MPPT algorithm for PV water heating systems has been proposed. Its main innovation consists in using measurements of irradiance and temperature sensors, coupled with an estimate of inverter input impedance, to achieve analytical computation of the duty cycle for driving the PV array to its maximum power point. The proposed method was validated via computer simulations, in which it was compared to P&O. Obtained results show that it: has negligible steady-state power oscillations; provides very fast transient response; is insensitive to sample time; is robust with respect to load mismatch; and consistently outperforms P&O. The proposed approach has implementation requirements even simpler than those of P&O, which makes it very attractive for deployment on PV water heating systems.

5 Generalizing the Analytical Input Impedance Estimation MPPT Approach

5.1 Introduction

In the previous Chapter, an analytical expression for estimating the input impedance of single-phase inverters feeding passive impedance-type loads was established, together with an analytical MPPT scheme applicable when such system is fed by a PV array, which corresponds to the scenario of an emerging PV application, namely that of variable-voltage PWHS. It was shown that the proposed MPPT approach has interesting practical features, namely: (a) even simpler implementation and fewer parameters than P&O, which is already considered the simplest hill-climbing approach [68]; (b) high efficiency and robustness with respect to sample time; and (c) no steady-state output power oscillations.

The aforementioned method, which is denoted by the acronym PWHS-MPPT, computes MPPT duty cycle by analytically matching PV array resistance to the inverter input impedance. To achieve this, a closed-form expression derived by the author for estimating the inverter input impedance is used. Two assumptions with respect the load power angle θ_l were used for deriving such expression, namely that it is sufficiently small so that instantaneous power conservation is approximately valid and sufficiently large so that output current can be assumed as sinusoidal. Such assumptions cause divergence for $\theta_l \rightarrow 90^\circ$ and large errors for small θ_l values (particularly in the neighborhood of $\theta_l = 0^\circ$ as shown in Section 4.5). The first problem is of relatively minor importance, since a practical scenario implies small power angles. On the other hand, even if the inverter output filter may often ensure a sufficiently high θ_l in practice, the second issue hampers precision if it is desired to take into account a very small filter or perhaps even a filterless inverter.

In this sense, the objective of this Chapter is improving the input impedance estimate derived previously for small load power angles. This is achieved by relaxing the sinusoidal output current assumption, which enables the derivation of a new generalized closed-form expression for estimating inverter input impedance. By employing it in the analytical MPPT scheme devised in Chapter 4, large efficiency improvements are obtained for small power angles. Subsequently, the improved input impedance estimation and analytical MPPT are once more generalized for three-phase systems with unbalanced loads, harmonics and partial shading; such generalization will be compared to three-phase P&O.

Remark 5.1: Despite PWHS being the main systems to which the proposed MPPT technique is applicable, any variable-voltage photovoltaic system (VPS) can be considered. In this sense, it is henceforth denoted as *analytical input impedance estimation* (AIIE).

5.2 Single-Phase Harmonics Generalization

Modeling of the single-phase VPS has been described in Chapter 4. Hence, derivation of the generalized input impedance estimation is considered directly.

5.2.1 Improved Input Impedance Estimation

In what follows, the improved closed-form expression for input impedance estimation is given by **Proposition 7**. As was the case in Chapter 4, the obtained equation for R_o is constant with respect to input DC voltage. Hence, despite inverter nonlinearity and load reactive power consumption, it is ensured that the inverter-load association can be represented by an equivalent resistive load from the MPPT viewpoint.

Proposition 7: Let $Y_{lk} = |Y_{lk}|\angle -\theta_{lk}$ be the admittance of an AC load, which is connected to the output of a single-phase full-bridge PWM inverter, at frequency $k \cdot f_c$, where $k \in \mathcal{H}$. The DC input impedance R_o of this system is given by:

$$R_o = \frac{2}{m_a^2 \cdot \sum_{k\in\mathcal{H}} c_k^2 |Y_{lk}| \cos\theta_{lk}} \tag{5.1}$$

Proof: Let V_o be the DC input voltage. To compute $R_o = V_o/I_o$, the DC component of input current I_o must be obtained. As in Chapter 4, instantaneous power conservation between the DC and AC ports is assumed as approximately valid and thus:

$$V_o i_o(t) = v_l(t) i_l(t) \tag{5.2}$$

where $i_l(t)$, unlike in Chapter 4, is *not* assumed as sinusoidal.

Using Equations 4.5 and 5.1, the following is obtained:

$$i_o(t) = \frac{2V_l^2}{V_o}\left[\sum_{k_1\in\mathcal{H}} c_{k_1}\sin(k_1\omega_c t)\right] \times \left[\sum_{k_2\in\mathcal{H}} |Y_{lk_2}| c_{k_2}\sin(k_2\omega_c t - \theta_{lk_2})\right] \tag{5.3}$$

which can be developed as follows:

$$i_o(t) = \overbrace{\frac{V_l^2}{V_o}\sum_{k\in\mathcal{H}} |Y_{lk}| c_k^2\cos(\theta_{lk})}^{I_o} + \overbrace{\frac{2V_l^2}{V_o}\sum_{k_1\in\mathcal{H}}\sum_{\substack{k_2\in\mathcal{H}\\ k_2\neq k_1}} q_{k_1k_2}\sin(k_1\omega_c t)\sin(k_2\omega_c t - \theta_{lk_2})}^{\tilde{i}_o(t)} \tag{5.4}$$

where $q_{k_1k_2} = |Y_{lk_2}| c_{k_1} c_{k_2}$ and $\tilde{i}_o(t)$ is the AC component of current $i_o(t)$.

Taking I_o in Equation 5.4 and using the fact that $V_l = m_a V_o/\sqrt{2}$ in bipolar PWM [125], it is straightforward to apply $R_o = V_o/I_o$ and obtain Equation 5.1. ■

At last, note that $\mathcal{H}$ has infinite elements, for which reason the sum in Equation 5.1 must be truncated when computing R_o in practice. It is known that, for the usual case

of $m_a \leq 1$ and $m_f \gg 1$, the dominant bipolar PWM harmonic orders $a \cdot m_f \pm b$ correspond to $a \in \{1, 2, 3, 4\}$ and $b \in \{1, 2, \ldots, 7\}$ [125]. Hence, the subset of $\mathcal{H}$ corresponding to such values is henceforth adopted when computing Equation 5.1. In this sense, the proposed estimate is a *dominant-harmonic* current approximation, whereas the original estimation from Chapter 4 is a *zero-harmonic* approximation for which $\mathcal{H} = \{1\}$ in Equation 5.1.

5.2.2 Error Assessment

To evaluate the estimation errors of the proposed and original (i.e., that from Chapter 4) approaches, a simulation experiment identical to that of Section 4.5 is carried out. First, the estimates of R_o are computed for $\theta_l = 0°, 1°, \ldots, 89°$. Then, an inverter with load $|Z_l| = 1\ \Omega$ is simulated for all values of θ_l with parameters $V_o = 200$ V, $m_a = 1$, $m_f = 27$ and $f_c = 60$ Hz. At last, estimation error is computed as per Equation 4.13.

Obtained results are given in Figure 34, where the $e(\theta_l)$ curves yielded by both estimation methods are depicted. As could be expected, the error curves converge towards each other for increasing θ_l due to current harmonics being filtered and the zero-harmonic assumption $\mathcal{H} = \{1\}$ becoming increasingly valid. Furthermore, divergence in the vicinity of $\theta_l = 90°$ occurs in both cases due to violation of instantaneous power conservation.

More importantly, it is seen that relative error is reduced very significantly for small load power angles. The original approach results in a sharp increase of error as θ_l approaches zero and reaches $e(0) \approx 100\%$, whereas the proposed method yields very small error at small θ_l. This corroborates the analysis from Section 5.1, in which the cause of large error as $\theta_l \to 0$ was pointed out as violation of the zero-harmonic assumption. Since the proposed estimation incorporates the harmonics of $i_l(t)$ into input impedance estimation, this violation no longer occurs and error is reduced.

Figure 34 – Input impedance estimation relative error curves.

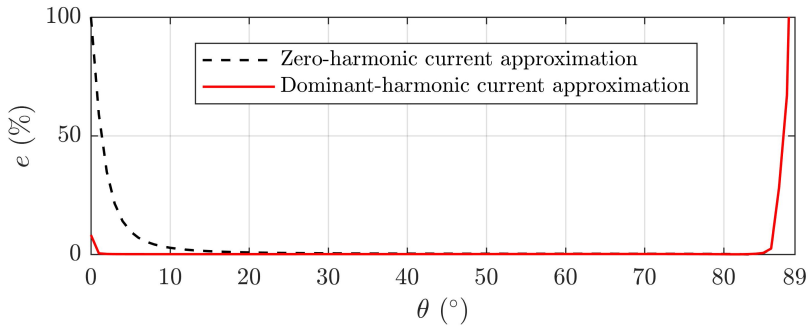

Source: The author.

5.2.3 Efficiency Evaluation

Aside from the assessment of estimation error, it is important to evaluate the implications of Equation 5.1 on the tracking efficiency of AIIE. To this end, the same system considered in Chapter 4 is simulated for varying θ_l and for both impedance estimations incorporated into AIIE. The P&O algorithm is also considered for comparison. Since θ_l varies along iterations, impedance $|Z_l|$ is also varied in order to maintain the rated load active power (see Appendix A). The simulations are carried out in Simulink R2017a.

Simulation is iterated for $\theta_l = i \cdot 0.1°$, $i = 0, 1, \ldots, 100$, and consists in the following scenario. At $t = 0^-$, the initial conditions are $D(0^-) = 0$, $T(0^-) = 25$ °C and $S(0^-) = 0$ W/m^2; the system is at steady-state with zero output. Then, at $t = 0$, an irradiance step increase to $S = 1000$ W/m^2 occurs. The system runs for $t_f = 10$ s, which is sufficiently long to ensure that the transient at $t = 0$ has negligible effect on efficiency computation. A fixed MPPT sample time of $T_s = 1000$ μs is considered. A duty cycle perturbation of $\Delta D = 0.01$ is used for P&O, which was selected via prior trial-and-error testing that yielded such best-performing value. This procedure was adopted to ensure a fair comparison against both implementations of AIIE.

The obtained results are depicted in Figures 35(a)-(f), where efficiency curves $\eta(\theta_l)$ for the MPPT methods are presented together with steady-state time plots of output power $p(t; \theta_l)$ for $\theta_l = 0°, 1°, 2°, 3°$ and a transient time plot for $\theta_l = 0°$.

It is clear from the $\eta(\theta_l)$ plots that the proposed method yields large efficiency improvements for small θ_l. This is a direct consequence of reduced estimation error: the improved R_o estimates of PWHS-MPPT-H make the computation of D_{mp} be more accurate, which in turn drives the PV array closer to its maximum power point. This becomes particularly clear in the $p(t; \theta_l)$ plots: for $\theta_l < 3°$, the estimation error reduction leads to a smaller MPPT steady-state error and thereby increases power efficiency.

On the other hand, the efficiency curves converge for large θ_l, as could expected from previous analysis. It is interesting to note, however, that convergence of the $\eta(\theta_l)$ curves occurs at smaller values of θ_l compared to the $e(\theta_l)$ curves. This phenomenon agrees with simulation results from Chapter 4, where it was shown that sufficiently small variations in $e(\theta_l)$ and, consequently, in the D_{mp} setpoint error, are masked by output power ripple and thereby have negligible effect on MPPT performance.

Now, consider the P&O approach. The $\eta(\theta_l)$ curves show that it is a better alternative than PWHS-MPPT for small θ_l, since the latter method is too inneficient for $\theta_l \to 0°$. In general, it can be said that an advantage of P&O over the other methods is that θ_l is not a parameter inherent to its implementation and, as a consequence, does not significantly affect performance. Hence, adequate usage of both implementations of AIIE depends on sufficiently accurate knowledge of the load angle.

Figure 35 – Evaluation of MPPT efficiency when using P&O, the original and the proposed inverter input impedance estimation approaches.

Explanatory note: The depicted graphs consist of (a) $\eta(\theta_l)$ curves, (b) transient plot of $p(t)$ for $\theta_l = 0°$, and steady-state plots of $p(t)$ for (c) $\theta_l = 0°$, (d) $\theta_l = 1°$, (e) $\theta_l = 2°$ and (f) $\theta_l = 3°$.

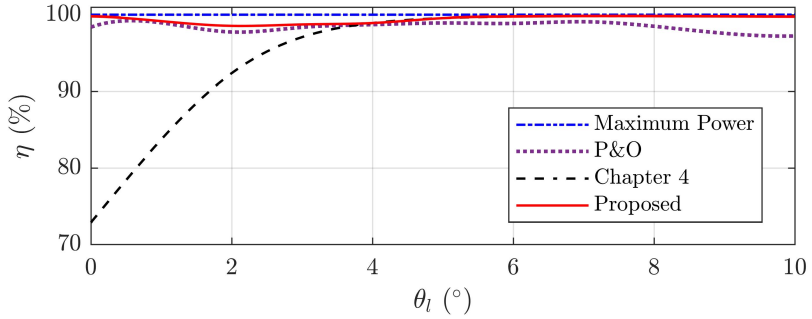

(a) MPPT efficiency curves.

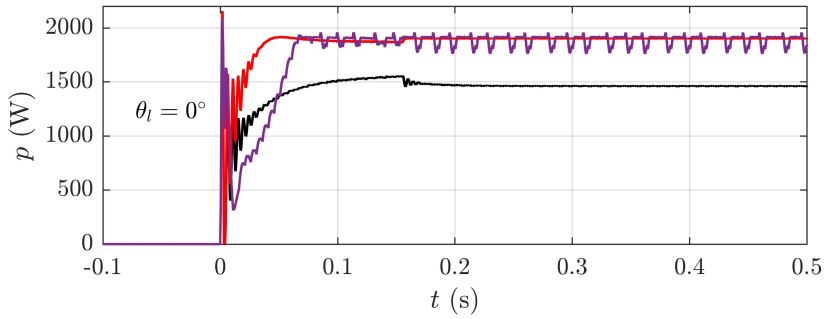

(b) Output power transient for $\theta_l = 0°$.

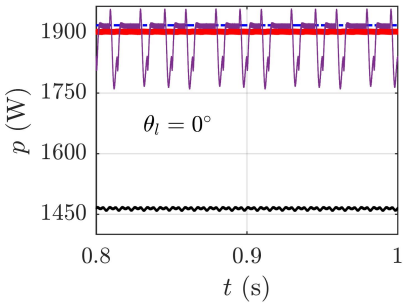

(c) Steady-state power for $\theta_l = 0°$.

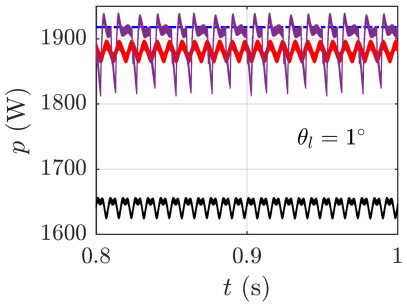

(d) Steady-state power for $\theta_l = 1°$.

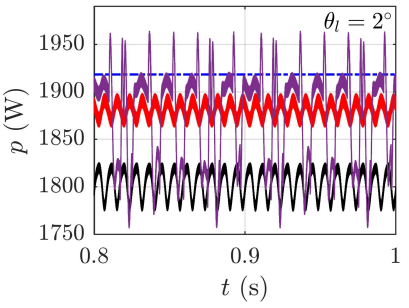

(e) Steady-state power for $\theta_l = 2°$.

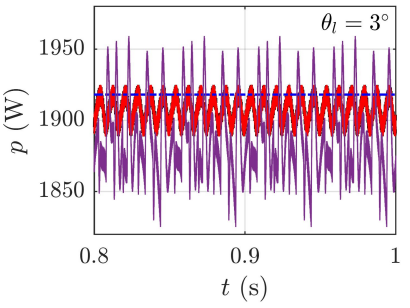

(f) Steady-state power for $\theta_l = 3°$.

Source: The author.

However, it should be recalled that the above advantage of P&O is overshadowed by the difficulty of selecting its optimal ΔD; in practice, extensive trial-and-error (as done in this work) is not allowable and a suboptimal performance must be accepted [71]. Such difficulty does not exist at all with both of the AIIE approaches.

The most important feature of the obtained results is the proposed method yielded superior efficiency for *all values of* θ_l. In particular, its largest efficiency value (99.89%) was obtained for $\theta_l = 0°$, which is the most relevant case in practical PWHS implementations. As previously discussed, the improvement over the original PWHS-MPPT from Chapter 4 is due to steady-state error reduction at small θ_l. On the other hand, it surpassed the efficiency of P&O due to its much *smaller output power ripple*.

In fact, it is seen from the output power plots that P&O may even achieve smaller steady-state errors due to its fine-grained duty cycle search. However, such advantage is not enough to compensate efficiency loss due to the ripple caused by constant duty cycle perturbation. Such problem is eliminated by the proposed method (and, to be fair, also by PWHS-MPPT) since its duty cycle remains *constant* at steady-state.

Both PWHS-MPPT and the proposed method are seen to have yielded faster transient responses compared to P&O. The relatively slow tracking speed of P&O is a known problem caused by errors in the choice of perturbation sign during transients [71], which causes oscillation and tracking delay. The higher-quality transient response of the proposed method with respect to P&O can be attributed precisely to the elimination of such issue, since the new duty cycle value is changed in a single step after the transient occurs. Hence, response time is mainly dependent on the PWHS circuit time constant and not on oscillations inherent to the algorithm.

It is simple to understand why the proposed method yields a very similar transient behavior compared to PWHS-MPPT. Both methods proceed by updating the duty cycle estimate D_{mp}, which is used as the new D setpoint. Hence, in both cases, a *single* duty cycle step is applied to the PWHS circuit. Since the step response is dictated by the circuit time constant, both methods yield similar transients.

5.3 Three-Phase Generalization

The AIIE approach established in Chapter 4 and generalized for current harmonics in Section 5.2 is applicable to VPSs with single-phase inverters. In this Section, the AIIE technique is further generalized to achieve analytical MPPT for three-phase VPSs with possible PS of the PV array. Since polyphase systems have not been considered up to this point, a performance comparison against three-phase P&O shall also be carried out.

Figure 36 – Scheme of the considered three-phase VPS.

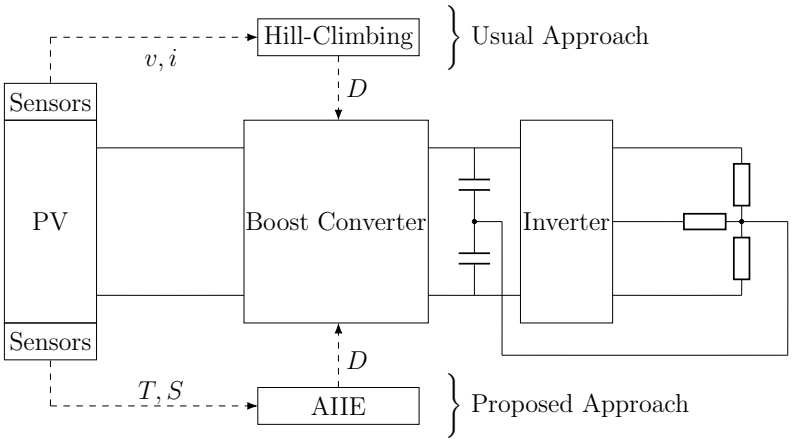

Source: The author.

Figure 37 – Detailed three-phase inverter circuit model.

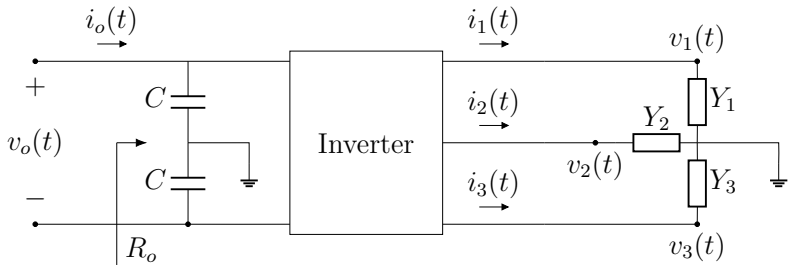

Source: The author.

5.3.1 System Model

The considered three-phase VPS is depicted in Figure 36, where both the usual hill-climbing (P&O) and proposed AIIE approaches for carrying out MPPT are illustrated. Recall that the former consists in sampling PV voltage (v) and current (i) to compute output power and decide, based on such computation, whether the next duty cycle perturbation should be positive ($+\Delta D$) or negative ($-\Delta D$). Differently, AIIE computes an estimate R_o of inverter DC input impedance and matches it to an approximation of the PV maximum power point resistance R_{mp}, whose computation employs temperature (T) and solar irradiance (S) measurements and is carried out according to Equation 4.11. Then, impedance matching is carried out by analytically solving $M^2(D) = R_o/R_{mp}$ [113].

The same modeling of PV array and MPPT-controlled boost converter from Chapter 4 are considered and the reader is referred to such Chapter for details. In what follows, the components required for computation of R_o, i.e., the three-phase inverter and its loads, are elaborated upon. Since usage of unbalanced loads may be desired, a four-wire split-capacitor neutral topology is considered [139], as shown in Figure 36. A more detailed circuit model of the inverter is given in Figure 37, where neutral voltage has been taken as the zero reference for simplifying subsequent computations.

It is assumed that bipolar PWM is used with frequency and amplitude modulations $m_f \gg 1$ and $m_a \leq 1$, so that low-frequency carrier and square-wave effects are avoided [137]. If the input capacitors are sufficiently large so that $v_o(t) \approx V_o$, then:

$$v_r(t) = V_l\sqrt{2} \cdot \sum_{k\in\mathcal{H}} c_k \sin(k\omega_c t - \frac{2\pi}{3}k(r-1)) \tag{5.5}$$

where $r \in \{1,2,3\}$, $V_l = m_a V_o/2\sqrt{2}$ is the root mean square value of the AC voltage fundamental component, $\mathcal{H}$ is the set of non-zero harmonic orders in the spectrum of $v_r(t)$, c_k is the relative amplitude of the k-th harmonic with respect to V_l and $\omega_c = 2\pi f_c$ is the angular frequency of the modulating sinusoidal signal [125]. As in Chapter 4, since voltage regulation is not performed on VPSs, it is assumed that m_a is constant.

The load admittances depicted in Figure 37 are specified for fundamental frequency, i.e., $Y_r = |Y_r|\angle -\theta_r$ $(@f_c)$, $r \in \{1,2,3\}$. For arbitrary $k \in \mathcal{H}$, frequency dependence is denoted as $Y_{rk} = |Y_{rk}|\angle -\theta_{rk}$ $(@kf_c)$. Currents $i_r(t)$ can be easily computed by using Equation 5.5 and the Y_{rk}, whereas $i_o(t)$ and its associated DC component I_o, which is required for DC input impedance estimation, are not trivial to obtain.

5.3.2 Estimating R_o

A closed-form expression for estimating the DC input impedance of the considered three-phase four-wire VPS is now derived in **Proposition 8**.

Proposition 8: Consider a three-phase VPS whose inverter is driven via bipolar PWM. The DC input impedance of this system is:

$$R_o = \frac{8}{m_a^2 \cdot \sum_{k\in\mathcal{H}} c_k^2[|Y_{1k}|\cos\theta_{1k} + |Y_{2k}|\cos\theta_{2k} + |Y_{3k}|\cos\theta_{3k}]} \tag{5.6}$$

Proof: As in Chapters 3 and 4, assume that instantaneous power conservation [138] between the inverter DC and three-phase AC ports is valid (such assumption is increasingly satisfied for smaller load power angles θ_r). Then:

$$V_o i_o(t) = v_1(t)i_1(t) + v_2(t)i_2(t) + v_3(t)i_3(t) \tag{5.7}$$

where $i_r(t) = V_l\sqrt{2} \cdot \sum_{k\in\mathcal{H}} |Y_{rk}|c_k \sin(k\omega_c t - \frac{2\pi}{3}k(r-1) - \theta_{rk})$, which is obtained by using Equation 5.5 and the load admittances. Using such expression for the $i_r(t)$ in Equation 5.7, it follows, after some mathematical development, that:

$$V_o i_o(t) = V_l^2 \sum_{r=1}^{3}\sum_{k\in\mathcal{H}} |Y_{rk}|c_k^2\cos\theta_{rk} + \tilde{p}_{inv}(t) \tag{5.8}$$

$$\tilde{p}_{inv}(t) = 2V_l^2 \sum_{r=1}^{3}\sum_{k_1\in\mathcal{H}}\sum_{\substack{k_2\in\mathcal{H}\\k_2\neq k_1}} q_{rk_1k_2}\sin(k_1\omega_c t - \frac{2\pi}{3}k_1(r-1)) \times \sin(k_2\omega_c t - \frac{2\pi}{3}k_2(r-1) - \theta_{rk_2}) \tag{5.9}$$

where $q_{rk_1k_2} = |Y_{rk_2}|c_{k_1}c_{k_2}$ and $\tilde{p}_{inv}(t)$ is the AC component of inverter output power. Now, let $i_o(t) = I_o + \tilde{i}_o(t)$ and equate the DC components in Equation 5.8 to obtain:

$$I_o = \frac{V_l^2}{V_o} \sum_{r=1}^{3} \sum_{k \in \mathcal{H}} |Y_{rk}| c_k^2 \cos\theta_{rk} \tag{5.10}$$

which yields Equation 5.6 when used with $V_l = m_a V_o/2\sqrt{2}$ and $R_o = V_o/I_o$. ■

As in Section 5.2.1, $|\mathcal{H}| = \infty$ and the harmonic order set must be truncated so that Equation 5.5 can be computed in practice. The same approximation considered in Section 5.2.1 is used, which consists in using the subset of dominant harmonics for bipolar PWM, i.e., $\mathcal{H}' = \{a \cdot m_f \pm b \mid a = 1, 2, 3, 4;\ b = 1, 2, \ldots, 7\}$ [125].

5.3.3 Dealing with Partial Shading

Similarly to the procedure adopted in Section 3.3.4, three-phase AIIE is now extended to PS scenarios by adopting the string-level MPPT framework, which is often favored in practice due to being cost-effective [57]. This approach consists in controlling each string of PV modules in a given array with one DC converter. Hence, a provision is now proposed that makes each string converter avoid local optima during PS.

Consider an M-module PV string whose irradiances are $S_1 > S_2 > \ldots > S_M$. The voltages associated to each candidate MPP can be estimated as $k \cdot V_{mp}$, $k = 1, 2, \ldots M$ [123]. Furthermore, when the string operates at the voltage $k \cdot V_{mp}$, its k modules with greater irradiances conduct $(S_1, S_2, \ldots, S_k)$ and the remaining ones $(S_{k+1}, S_{k+2}, \ldots, S_M)$ are shorted via their bypass diodes [124]. The string current is thus limited by the conducting module with smaller irradiance (S_k) and can be estimated as $I_{mp} \cdot S_k/S_o$. Hence, a reasonable estimate of the output powers at each MPP is $P_k \approx kV_{mp} \cdot I_{mp} \cdot S_k/S_o$.

Taking the above into account, the following approximate approach for global MPP tracking with AIIE is proposed. At each sample time, use all the measured S_k to compute $k^* = \text{argmax}_k\ P_k \approx \text{argmax}_k\ k \cdot S_k$. Then, the estimated global MPP corresponds to k^* series modules and the PV resistance value $k^* \cdot R_{mp}(S_{k^*}, T)$ is fed to the AIIE.

5.3.4 Evaluation of Estimation Error

Since computation of Equation 5.5 depends on the instantaneous power conservation assumption and truncation of $\mathcal{H}$, estimation errors may occur. For this reason, an assessment of precision yielded by the obtained estimate must be performed. To this end, similarly to Section 5.2.2, two simulations of the inverter depicted in Figure 37, with $V_o = 150$ V, $m_a = 1$, $m_f = 33$, $f_c = 60$ Hz and $C = 50$ μF, are carried out as follows.

For both simulations, $Z_1 = 1/Y_1$ has fixed module $|Z_1| = 1\ \Omega$ and varying power angle $\theta_1 \in \{0°, 1°, \ldots, 89°\}$, which is used as a parameter. In the first simulation, load

Figure 38 – Results of estimation error assessment for three-phase VPS.

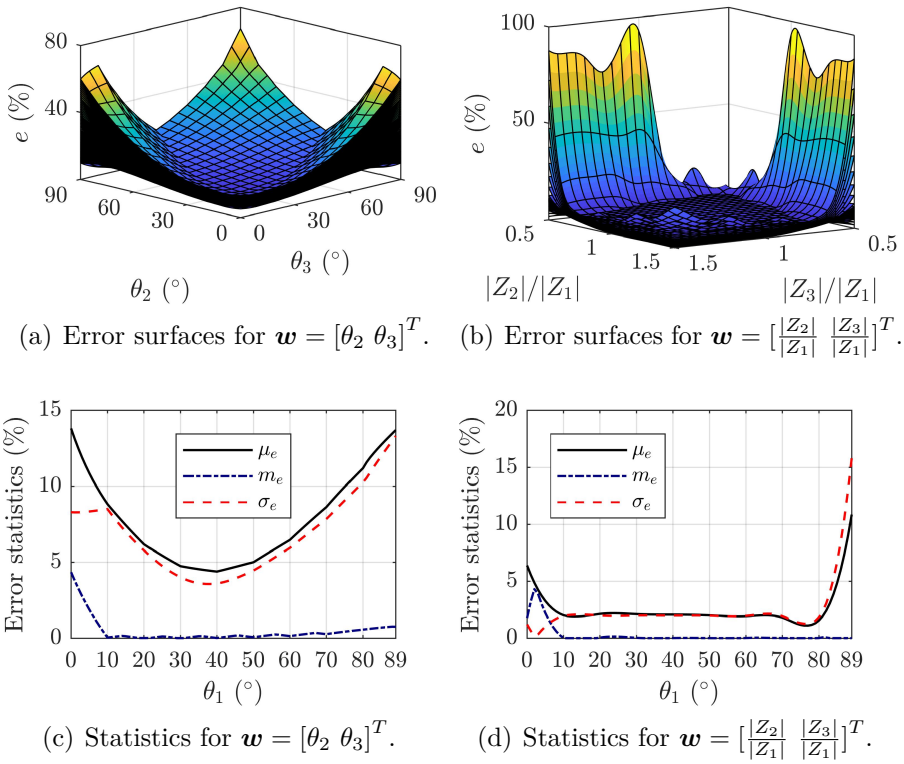

(a) Error surfaces for $\boldsymbol{w} = [\theta_2\ \theta_3]^T$. (b) Error surfaces for $\boldsymbol{w} = [\frac{|Z_2|}{|Z_1|}\ \frac{|Z_3|}{|Z_1|}]^T$.

(c) Statistics for $\boldsymbol{w} = [\theta_2\ \theta_3]^T$. (d) Statistics for $\boldsymbol{w} = [\frac{|Z_2|}{|Z_1|}\ \frac{|Z_3|}{|Z_1|}]^T$.

Source: The author.

impedances are fixed $|Z_2| = |Z_3| = |Z_1|$ and $\theta_2, \theta_3 \in \{0°, 1°, \ldots, 90°\}$, whereas the second simulation considers fixed power angles $\theta_2 = \theta_3 = \theta_1$ and varying impedances $|Z_2|/|Z_1|, |Z_3|/|Z_1| \in \{0.50, 0.55, \ldots, 1.55\}$. Such simulations allow visualizing error both in terms of impedance magnitudes and angles. The estimation error is computed as follows:

$$e(\boldsymbol{w}; \theta_1) = |R_o^{est}(\boldsymbol{w}; \theta_1) - R_o^{sim}(\boldsymbol{w}; \theta_1)| \Big/ R_o^{sim}(\boldsymbol{w}; \theta_1) \tag{5.11}$$

where R_o^{sim} and R_o^{est} are simulated and estimated DC input impedance, respectively, $\boldsymbol{w} = [\theta_2\ \theta_3]^T$ in the first simulation, $\boldsymbol{w} = \frac{1}{|Z_1|}[|Z_2|\ |Z_3|]^T$ in the second simulation and $e(\boldsymbol{w}; \theta_1)$ designates the estimation error for $\boldsymbol{w}$, given θ_1.

Obtained results are given in Figures 38(a)-(d). Error surfaces $e(\boldsymbol{w}; \theta_1)$ are plotted for each θ_1 in Figures 38(a)-(b). Associated statistics (also parametrized by θ_1), namely mean $\mu_e(\theta_1)$, mode $m_e(\theta_1)$ and standard deviation $\sigma_e(\theta_1)$, are presented in Figures 38(c)-(d).

The plots in Figures 38(a)-(b) show that estimation error is small except when any θ_r approaches 90°, which is explained by gross violation of the instantaneous power conservation assumption. In fact, error maxima in Figure 38(a) occur, for any θ_1, when $\theta_2 = 90°$ or $\theta_3 = 90°$. Similarly, the high-error surfaces in Figure 38(b) correspond to $\theta_1 \to 90°$. This is further illustrated by the statistics in Figures 38(c)-(d), where a very small m_e and $\mu_e \approx \sigma_e$ indicate that, aside from large maxima for $\theta_r \to 90°$, error values

Figure 39 – MPPT results for balanced load conditions.

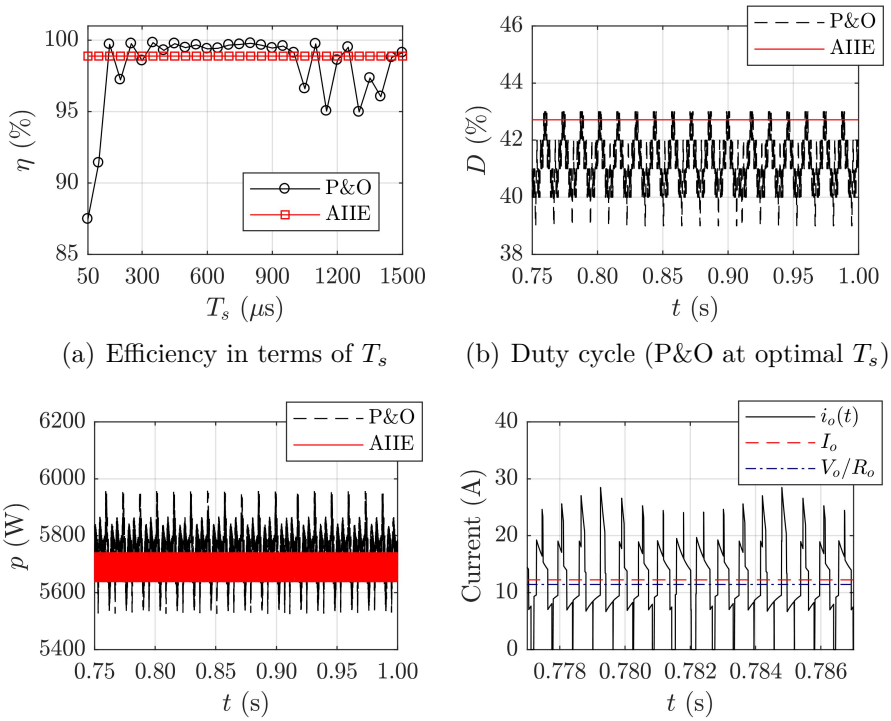

(a) Efficiency in terms of T_s (b) Duty cycle (P&O at optimal T_s).

(c) PV power (P&O at optimal T_s). (d) DC bus current yielded by AIEE.

Source: The author.

are small. Such results are favorable, since practical scenarios imply small θ_r. At last, note that some increase in m_e occurs for very small θ_r. This is explained by the fact that harmonics contribute more significantly in Equation 5.6 when $\theta_r \to 0$, thereby making the truncation of $\mathcal{H}$ cause larger estimation error for very small power angles.

5.3.5 Assessment of Steady-State MPPT Efficiency

In order to further validate the proposed approach, simulations are carried out in Simulink R2017a to compare the MPPT efficiency of a three-phase VPS when using Equation 5.6 incorporated to AIIE with that of P&O. As discussed in Chapter 4, AIIE has even lower computational complexity than P&O, which is therefore used as a benchmark.

The simulated three-phase VPS is as follows. A 9×3 array of *1Soltech 1STH-215-P* PV modules (see Table 8 in Chapter 3) is considered, which amounts to a nominal power $P_N = 5755.05$ W at 261 V and 22.05A for rated ambient conditions. The three-phase inverter switches and boost converter components are specified by Table 10 in Chapter 4. A value of $C = 50$ μF is used for the neutral capacitors. Three arbitrarily selected load conditions are considered: balanced ($P_1 = P_2 = P_3 = P_N/3$, $\theta_1 = \theta_2 = \theta_3 = 0°$), slightly unbalaced ($P_1 = P_N/3$, $P_2 = 4P_N/9$, $P_3 = 2P_N/9$, $\theta_1 = 0°$, $\theta_2 = 5°$, $\theta_3 = 15°$) and very unbalanced ($P_1 = P_N/3$, $P_2 = 5P_N/9$, $P_3 = P_N/9$, $\theta_1 = 0°$, $\theta_2 = 15°$, $\theta_3 = 45°$). For

Figure 40 – MPPT results for slightly unbalanced load conditions.

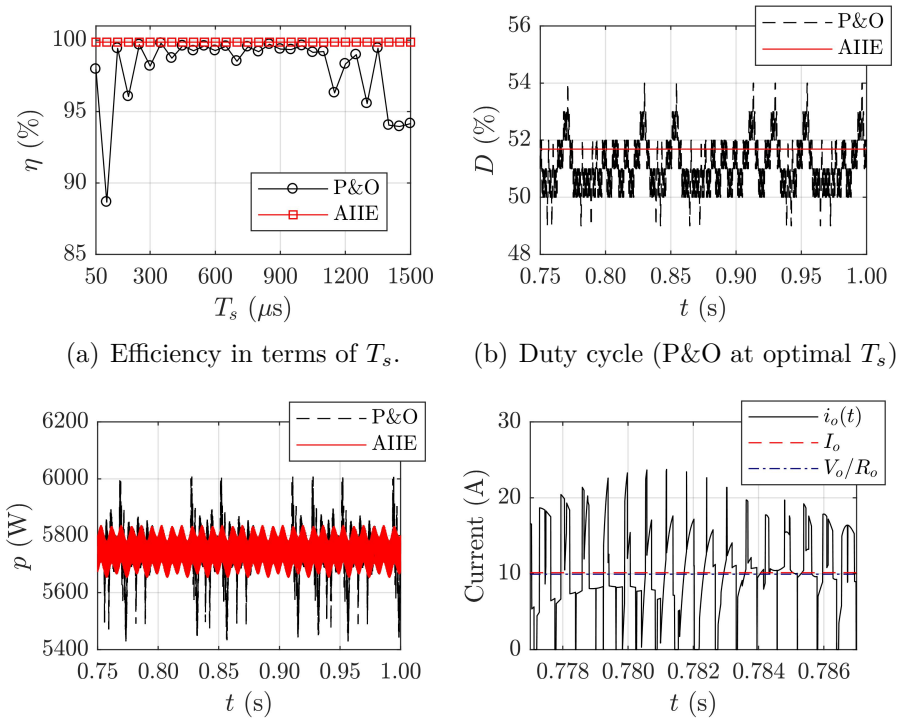

(a) Efficiency in terms of T_s. (b) Duty cycle (P&O at optimal T_s).

(c) PV power (P&O at optimal T_s). (d) DC bus current yielded by AIEE.

Source: The author.

driving the inverter, $m_a = 1$, $m_f = 33$, $f_c = 60$ Hz are used. The boost converter switching frequency is 50 kHz. When P&O is used, a perturbation step $\Delta D = 0.01$ is adopted.

Simulation is carried out according to the following procedure. For each load condition, AIIE and P&O are simulated for a set of sample times $T_s \in [50, 1500]$ (μs), which is discretized in 50 μs increments. The simulated scenario has initial conditions $D(0^-) = 0$, $S(0^-) = 0$ W/m^2 and $T(0^-) = 25$°C. At $t = 0$, irradiance changes to $S = 1000$ W/m^2 and the system is allowed to run until $t_f = 5$ s to ensure steady-state is reached. For each iteration, efficiency is computed according to Equation 3.34.

Obtained results are given in Figures 39(a)-(c), 40(a)-(c) and 41(a)-(c), where efficiency curves $\eta(T_s)$ and steady-state time plots of duty cycle $D(t)$ and PV output power $p(t)$ for optimal T_s are depicted. Also, the DC bus current $i_o(t)$ yielded by AIEE is shown in Figures 39(d), 40(d) and 41(d), together with its mean value I_o and expected mean value obtained by using Equation 5.6 and computing the estimate $I_o = V_o/R_o$, where V_o is the DC component of the $v_o(t)$ waveform obtained during simulation.

It is well-known that practical application of hill-climbing algorithms (and P&O in particular) suffers from non-trivial selection of T_s, given some ΔD, due to complex interactions between system dynamics and sample time [70]. This is seen in the $\eta(T_s)$ plots for P&O, which show that its efficiency is sensitive to sample time. Contrastingly, AIIE

Figure 41 – MPPT results for very unbalanced load conditions.

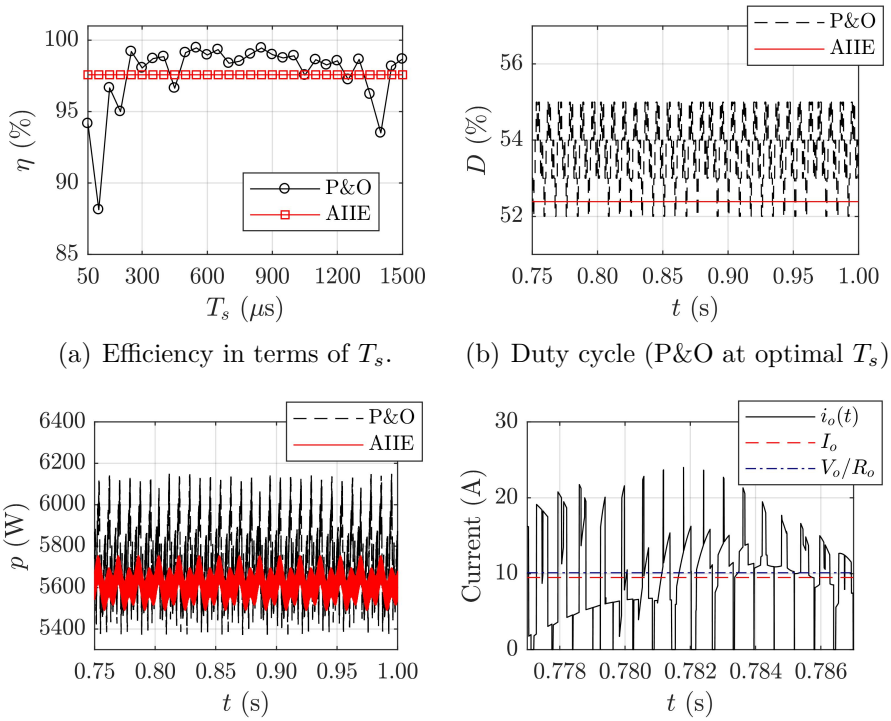

(a) Efficiency in terms of T_s. (b) Duty cycle (P&O at optimal T_s).

(c) PV power (P&O at optimal T_s). (d) DC bus current yielded by AIEE.

Source: The author.

achieves essentially constant efficiency for all T_s, with better or comparable performance with respect to P&O. Furthermore, it must be recalled that AIIE does not require specification of ΔD, thereby further simplifying implementation requirements.

Insensitivity of AIIE to T_s is explained by its analytical duty cycle computation, which avoids hill-climbing steady-state power oscillations. This is particularly clear from the $D(t)$ plots, which show that AIIE duty cycle is constant since S and T do not change, whereas P&O continuosly oscillates around the maximum power point. As a consequence, as seen from the $p(t)$ plots, power oscillations for AIIE are restricted only to those caused by boost converter and inverter PWM switching.

At last, the plots of $i_o(t)$ further validate the accuracy of AIIE. By computing the *real* mean value I_o and comparing it to the *expected* value $I_o = V_o/R_o$, a precise match is obtained. In fact, the largest percent error, which occurred in Figure 41(d), was of 6.65%.

5.3.6 Experimental Assessment of Dynamic PS Performance

To further validate the three-phase generalization, a hardware experiment is carried out. Since a full-scale VPS was not readily available, the processor-in-the-loop (PIL) experimental approach is adopted. In other words, the VPS plant is simulated, but controlled with a *physical* microcontroller into which AIIE is uploaded. Since validation of

Figure 42 – Proposed experimental PIL setup.

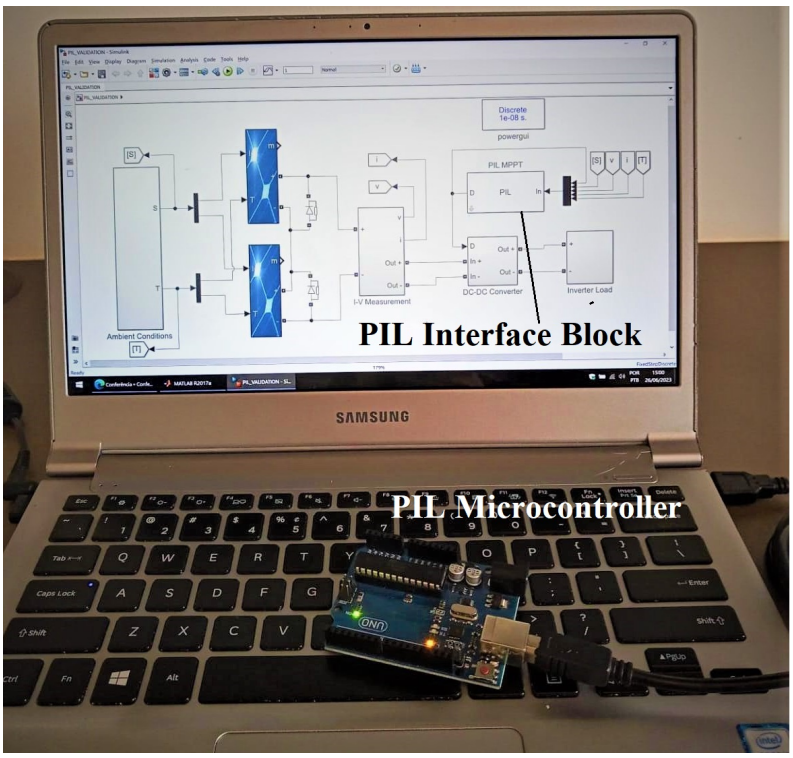

(a) Picture of plant model and PIL microcontroller.

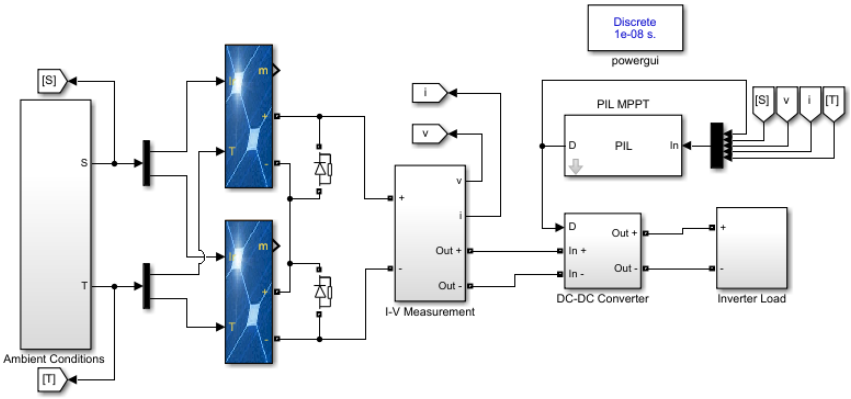

(b) Block diagram of the Simulink plant model.

Source: The author.

MPPT methods is focused on the control hardware (and, of course, the algorithm itself), a PIL-based validation is a reasonable and low-cost approach to prototyping [140, 141].

Since steady-state performance has been evaluated in Section 5.3.5, a dynamic PS scenario is now considered. The VPS plant is run on a laptop with Simulink R2017a at 10 ns time resolution, whereas AIIE is uploaded to an *ATmega328* microcontroller. Laptop-controller bidirectional communication is carried out via their serial ports, with the microcontroller receiving irradiance and temperature samples and trasmitting the computed duty cycle. A depiction of the experimental arrangement is given in Figure 42.

Figure 43 – Experimental PIL results.

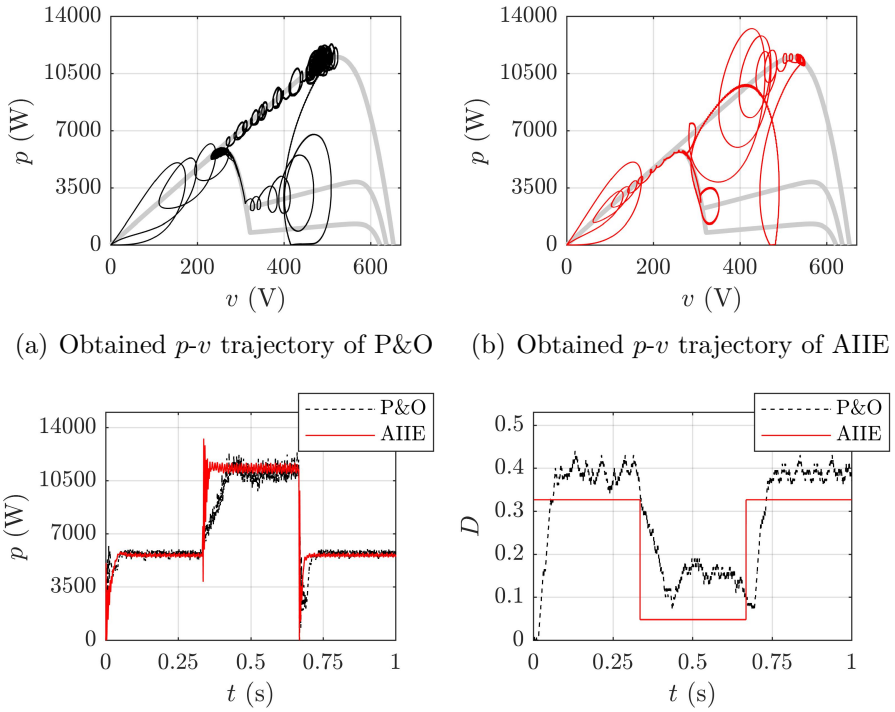

(a) Obtained p-v trajectory of P&O (b) Obtained p-v trajectory of AIIE

(c) Time plots of PV output power (d) Time plots of duty cycle

Source: The author.

A fixed sample time $T_s = 1000$ μs is used for the MPPT algorithms and the very unbalanced load case (see Section 5.3.5) is considered. The remaining VPS plant parameters are identical to those from Section 5.3.5, except that a string of two PV modules ($M = 2$) is now considered. A one second-duration ($\tau = 1$ s) dynamic PS scenario is taken as follows. One of the modules stays at $S = 1000$ W/m^2, whereas the second one begins at $S = 100$ W/m^2, increases to $S = 1000$ W/m^2 at $t = 0.333$ s and finally drops to $S = 300$ W/m^2 at $t = 0.666$ s. Clearly, this scenario enables evaluation of transient and PS performances. The obtained results are shown in Figure 43, where the p-v trajectories yielded by both MPPT algorithms are shown together with the string P-V curves for each shading condition. Time plots of duty cycle and PV output power are also depicted.

Consider the p-v trajectory of P&O in Figure 43(a). It is seen that the system begins at $(v, p) = (0, 0)$ and moves towards the global MPP of the $S = 100$ W/m^2 shading. However, it is very important to note that this is entirely *incidental*: GMPP was tracked merely because it was closer to the starting point. After the change to $S = 1000$ W/m^2, the single MPP is tracked, but a well-known disadvantage becomes apparent: since power has increased, drift occurs [76] and P&O oscillates severely before reaching the MPP. Finally, after $S = 300$ W/m^2, the global MPP is again tracked incidentally: the system oscillated towards smaller voltages after the transient, which enabled tracking of the global MPP.

Similarly, now consider the p-v trajectory of AIIE, which is shown in Figure 43(b). When $S = 100$ W/m^2, the algorithm computes $k^* = 1$ (see Section 5.3.3) and tracks the global MPP. Hence, the PV array could have started at *any* voltage and the global optimum would have likewise been tracked. Now, when $S = 1000$ W/m^2, AIIE computes $k^* = 2$ and rapidly tracks the single MPP; oscillations are small since the proposed method does not incur drifting. At last, the change to $S = 100$ W/m^2 makes AIIE switch back to $k^* = 1$ and, consequently, track the global MPP with no dependence on the system transient behavior (as was the case for P&O).

By analyzing the $p(t)$ plots in Figure 43(c), it becomes clear that AIIE provides a faster transient response. Aside from the elimination of drifting, the other cause for its excellent tracking speed is seen from the $D(t)$ curves in Figure 43(d): since AIIE is analytic, duty cycle is computed in a single step. Hence, response time is not hindered by algorithm-related oscillations and is mainly dependent on the circuit time constant.

At last, Equation 3.34 was used to compute the power efficiencies of each method; the efficiency yielded by P&O was 90.19%, whereas that of AIIE was 95.03%.

5.4 Conclusion

An improved closed-form expression for the analytical estimation of single-phase VPS inverter input impedance was derived. Compared to the estimate from Chapter 4, it takes inverter output current harmonics into account and thereby reduces estimation error for small load power angles significantly. The obtained expression can be substituted for the original input impedance estimate in AIIE for increased efficiency. Simulation results have shown that, by proceeding as such, very expressive efficiency improvements can be obtained at small power angles. Subsequently, input impedance estimation was once more generalized for three-phase VPSs with current harmonics. Evaluation of the three-phase generalization was also carried out via simulation, whose results have shown that it can yield, for a wide range of sample time values, comparable or better efficiency than three-phase P&O with even simpler computational implementation. Furthermore, a pratical experiment has demonstrated its capability of optimal tracking during partial shading scenarios with improved power efficiency.

Part III

PV System Grid Integration

6 Cooperative Markov Decision Process for Voltage Control of Grid-Tied PV Generators

6.1 Introduction

Recall from the introduction of Chapter 3 that the appreciable increase in ecological and economic awareness of utility-connected electricity consumers led to rapid integration of PV generation to the distribution grid [49–51]. Owing to concerns regarding PV system cost, such distributed generation (DG) is predominantly implemented by means of batteryless grid-tied PV inverters installed at consumer units [52–54].

Such scenario has led to new challenges regarding the maintanance of adequate grid operation, among which is that of voltage control (VC) with PV penetration [142,143]. This topic has received expressive attention in recent literature, where a myriad of VC methods formulated under various optimization frameworks has been presented. A common premise of such methods is leveraging existing grid equipment [i.e., voltage regulators (VR) and PV inverters] for achieving VC, thus deferring investments on grid reinforcements [144].

Control of VRs and PV inverters constitute different steps of the overall VC process which yield coarser and finer regulation at relatively slow and fast timescales, respectively [145–147]. This Chapter focuses on PV inverter reactive support, for which reason VRs are not considered. The control of battery-equipped DG systems [148–152], which are typical in microgrids but unusual in distribution, is also out of scope.

A comprehensive survey of VC methods specialized to photovoltaic DG is given in [153]. In what follows, a concise review is carried out of state-of-the-art works which are more closely related to this Chapter, namely those which propose VC schemes based on PV inverter reactive power support.

The *centralized* VC approaches are those in which all PV inverters are subject to dispatch by a single distribution system operator (DSO) [154–156]. An optimal power flow (OPF) problem whose objective function (OF) incorporates power loss and voltage regulation terms is formulated in [154], being iteratively solved by the DSO via cone programming to determine reactive power setpoints (RPSs). In [155], local droop control of PV inverters is adjusted via DSO-computed load flow solutions which are broadcast to the generators. An OPF approach is proposed in [156], where the DSO optimizes, by means of convex programming, a reactive power penalty OF subject to bus voltage constraints. The VC problem is formulated as a Markov decision process (MDP) in [157,158], which is then solved via deep reinforcement learning and policy gradient algorithms, respectively.

Centralized VC may be impracticable implementation-wise, since the infrastructure required for reliable communication between DSO and all subordinate nodes may be unavailable. Such difficulty is avoided by *local* VC methods, which enable VC solely from local measurements [159–162]. The method proposed in [159] uses a gradient-based algorithm to iteratively adjust reactive power at each node in terms of its measured voltage magnitude. Similarly, [160] uses proximal gradient optimization with voltage and a reactive power usage taken as optimization inputs. In [161], an adaptive integral controller with voltage feedback is adopted, with control parameters being dynamically adjusted in terms of PV power for increased response speed and stability. In [162], local controllers iteratively estimate additional reactive power injection for driving bus voltage to a stipulated range.

Despite not requiring communication, local methods imply a different disadvantage: it is not ensured that reasonable control of the global voltage profile is achieved, since each PV inverter only observes local voltage. A compromise between this drawback and the communications-heavy centralized control is achieved by means of *decentralized* [163–165] and *distributed* [166–168] methods. Decentralization consists in partitioning the grid into control zones which are dispatched by zone coordinating agents, whereas distributed methods leverage communication between the PV nodes themselves [153].

In [163], ϵ-decomposition of the load flow sensitivity matrix is used to divide the grid into DG zones. When voltage violation occurs at some node, the zone controller to which the node is subsumed solves a linear program for obtaining the RPSs. Multi-feeder scenarios are analyzed in [164], where the straightforward approach of defining each feeder as a control zone is proposed; each zone reactive power controller then minimizes a voltage deviation OF. An OPF-based approach is given in [165], where the OPF is updated via voltage feedback from selected nodes of each feeder. Then, the OPF output is used as reference for adjusting RPSs of all feeder nodes.

The method in [166] defines gradient-based estimations of the RPSs to be carried out by each DG unit, which take into account the corresponding estimates yielded by neighbouring nodes. In [167], a consensus-based approach is proposed for minimizing a power loss OF with voltage constraints. The PV inverters communicate to their neighbours estimates of their contributions to the grid voltage vector, which are then used for updating reactive power ouput. In [168], the grid is divided in control areas to each of which an OPF is attributed. Then, each OPF is solved distributively by the area PV nodes via the alternating direction method of multipliers (ADMM).

In general, the aforementioned decentralized and distributed VC techniques share the disadvantage of relatively complex implementation due to employment of optimization routines. Furthermore, distributed approaches may suffer from slow convergence [153]. Relatively few *heuristic* methods have been proposed for circumventing such difficulties [169–172]. In [169], a decentralized OPF is solved via particle swarm optimization, whereas

a genetic algorithm is used in [170]. Despite the interesting idea of reducing processing time via heuristic optimization, it is not altogether eliminated as in [171, 172].

The heuristic method from [171] provides a closed-form control law which adjusts RPS proportionately to the derivative of total PV power with respect to local voltages. Since it is model-free, decentralized application to each area of a previously decomposed grid is straightforward. A model-free heuristic is also given in [172]; it consists in maintaining PV nodes on local control mode under regular operation and, when voltage violation is detected at a node, it emits a distress signal and all inverters in its area gradually adjust their RPS towards maximum output. When overvoltage ceases, the RPSs are then readjusted to the previous steady-state reference value. Active power curtailment in critical overvoltage situations is also discussed in [172], but is not henceforth considered.

The results from [171, 172] show that heuristic methods are capable of yielding adequate decentralized VC via simple closed-form control laws, yet this method category remains relatively unexplored. This Chapter contributes a new method of this type based on the cooperative partially observable Markov decision process (C-POMDP) framework. Notably, MDP sees relatively scarce application in VC-related works, with its predominant use being in centralized control as in [157, 158]. Furthermore, to the best of our knowledge, cooperative MDP has been applied solely to microgrids for VC via storage device scheduling [151, 152]. Hence, the approach proposed in this Chapter is a first attempt at applying C-POMDP to VC via inverter reactive support.

A brief description of the proposed method is as follows. A C-POMDP model which describes the distribution grid with DG is a priori unknown, for which reason a direct approach would be using real-time *learning* algorithms for achieving VC. However, C-POMDP learning has very high computational complexity and leads to impracticable processing time for online application. To avoid this bottleneck, a C-POMDP model is heuristically specified and solved via offline *planning* to obtain closed-form VC laws. To ensure coherence of the heuristic model with the underlying power system, the model agents are associated to decentralized control areas defined via clustering of the power system nodes based on the grid sensitivity matrix.

6.2 Problem Description and Statement

In this Section, modeling of load flow in power grids with grid-tied PV generators is first described. Subsequently, the considered VC problem is formulated.

6.2.1 Load Flow Modeling

In a grid with N buses and P phases, let $\boldsymbol{V}$ be the NPx1 vector of voltage magnitudes. It can be expressed as the concatenation of P-phase bus vectors as $\boldsymbol{V} = [\boldsymbol{V_i}]_{N\text{x}1}$,

in which $\boldsymbol{V_i} = [V_i^r]_{P\text{x}1}$, $i \in \mathcal{I} = \{1, 2, ..., N\}$ and the phase index $r \in \Phi = \{\phi_1, \phi_2, ..., \phi_P\}$. Identical notations apply to the bus angle $\boldsymbol{\theta}$, active power $\boldsymbol{P}$ and reactive power $\boldsymbol{Q}$ vectors. The bus power injections can be expressed as [173]:

$$\boldsymbol{P_i} = \boldsymbol{V_i} \odot \sum_{j=1}^{N} \left[\cos \boldsymbol{\theta_{ij}} \odot \boldsymbol{G_{ij}} + \sin \boldsymbol{\theta_{ij}} \odot \boldsymbol{B_{ij}}\right] \boldsymbol{V_j} \tag{6.1}$$

$$\boldsymbol{Q_i} = \boldsymbol{V_i} \odot \sum_{j=1}^{N} \left[\sin \boldsymbol{\theta_{ij}} \odot \boldsymbol{G_{ij}} - \cos \boldsymbol{\theta_{ij}} \odot \boldsymbol{B_{ij}}\right] \boldsymbol{V_j} \tag{6.2}$$

where $\boldsymbol{Y_{ij}} = \boldsymbol{G_{ij}} + j\boldsymbol{B_{ij}}$ is a submatrix of the grid admittance matrix corresponding to buses i and j, $\sin(\cdot)$ and $\cos(\cdot)$ are element-wise operators, $\odot$ denotes the Hadamard product and $\boldsymbol{\theta_{ij}} = \boldsymbol{\theta_i} - \boldsymbol{\theta_j}$. Solving this *steady state* model for a given grid and power injection vectors yields voltage phasors $\dot{\boldsymbol{V}}_{\boldsymbol{i}} = \boldsymbol{V_i} \odot (\cos \boldsymbol{\theta_i} + j \sin \boldsymbol{\theta_i})$.

Since variations of load and PV generation along time must be considered when assessing VC schemes, Equations 6.1 and 6.2 shall be used for carrying out *quasi steady state* simulation. Given a period T larger than typical power grid transient settling times, the steady load flow can be solved for times $t = nT$, $n = 0, 1, \ldots, n_{\mathcal{T}}$, where $n_{\mathcal{T}}$ is the number of time steps, which yields a total simulation time of $\mathcal{T} = n_{\mathcal{T}} T$. A vector $\boldsymbol{x}$ is henceforth denoted as a function of time via the notation $\boldsymbol{x}[n]$.

6.2.2 Time-Varying Load and PV Generation

Let $\mathcal{S}$ be the set of buses with PV generation. The power injections at each $s \in \mathcal{S}$ are computed according to the following equations:

$$\boldsymbol{P_s}[n] = \frac{E_s[n]}{E_o} \cdot \boldsymbol{P_s^{(G_o)}} - \boldsymbol{P_s^{(L_o)}} \odot \tilde{\boldsymbol{P}}_{\boldsymbol{s}}^{(\boldsymbol{L})}[n] \tag{6.3}$$

$$\boldsymbol{Q_s}[n] = \tan \theta_o \cdot \boldsymbol{P_s^{(G_o)}} \odot \boldsymbol{\alpha_s}[n] - \boldsymbol{Q_s^{(L_o)}} \odot \tilde{\boldsymbol{Q}}_{\boldsymbol{s}}^{(\boldsymbol{L})}[n] \tag{6.4}$$

where $\boldsymbol{P_s^{(G_o)}}$ is PV active power at the rated irradiance $E_o = 1$ kW/m^2, $E_s[n]$ is the irradiance profile, $\boldsymbol{P_s^{(L_o)}}$ is installed load power, $\tilde{\boldsymbol{P}}_{\boldsymbol{s}}^{(\boldsymbol{L})}[n]$ is the normalized active power load profile and θ_o is the maximum PV inverter power factor angle. The reactive power vectors $\boldsymbol{Q_s^{(L_o)}}$ and $\tilde{\boldsymbol{Q}}_{\boldsymbol{s}}^{(\boldsymbol{L})}[n]$ are defined analogously to their active power counterparts. Finally, $\boldsymbol{\alpha_s}[n]$ is the RPS vector, whose components satisfy $-1 \leq \alpha_s^r[n] \leq 1$, $r \in \Phi$.

Remark 6.1: In Equation 6.4, PV reactive power is decoupled from generated active power and is solely constrained to not surpassing the rated power factor angle. This implies a rectangular PV inverter capacity curve, which agrees with european standards that require a reactive power reserve for grid-tied PV systems [174].

Prior to simulation, $\tilde{\boldsymbol{P}}_{\boldsymbol{s}}^{(\boldsymbol{L})}[n]$ and $\tilde{\boldsymbol{Q}}_{\boldsymbol{s}}^{(\boldsymbol{L})}[n]$ are sampled randomly (according to a uniform distribution) from a set $\mathcal{PQ} = \{(\tilde{\boldsymbol{P}}^{(\boldsymbol{i})}[n], \tilde{\boldsymbol{Q}}^{(\boldsymbol{i})}[n]) \mid i = 1, 2, \ldots, |\mathcal{PQ}|\}$ of load

profile pairs and associated to s. Similarly, $\mathcal{E} = \{E^{(i)}[n] \mid i = 1, 2, \ldots, |\mathcal{E}|\}$ is also sampled uniformly and the obtained irradiance profile is attributed to bus s.

6.2.3 Randomness of PV Power Allocation

A realistic simulation of distributed PV generation must encompass the randomness of generator positioning in the grid and of nominal power associated to each PV unit. As a straightforward manner of simulating such phenomena, the following procedure is used. First, the total number of PV generators $|\mathcal{S}|$ is selected. Then, the nodes of set $\mathcal{S}$ are selected via repeated sampling an equiprobable categorical distribution [175] with N categories, until a total of $|\mathcal{S}|$ distinct nodes are obtained. This distribution is used to ensure that, at each sampling, every node has equal probability of being selected.

Given $\mathcal{S}$, the components of each $\boldsymbol{P}_{\boldsymbol{s}}^{(\boldsymbol{G_o})}$ are then defined as randomly selected percentages of the corresponding load vector components. The percentage values for each $s \in \mathcal{S}$ are drawn from a uniform distribution, so that no bias towards some specific level of grid PV penetration is introduced. Hence, nominal PV power assigned to $s \in \mathcal{S}$ is:

$$\boldsymbol{P}_{\boldsymbol{s}}^{(\boldsymbol{G_o})} = \boldsymbol{P}_{\boldsymbol{s}}^{(\boldsymbol{L_o})} \odot \boldsymbol{x_s} \tag{6.5}$$

where $x_s^r \sim U(B_1, B_2)$, $r \in \Phi$, $B_1, B_2 \in \mathbb{R}^+$, is a uniformly distributed random variable. Hence, $\boldsymbol{P}_{\boldsymbol{s}}^{(\boldsymbol{G_o})}$ is defined as a percentage of the installed load, which is assumed constant.

Remark 6.2: If a bus i is such that $\boldsymbol{P}_{\boldsymbol{i}}^{(\boldsymbol{L_o})} = \mathbf{0}$, it is excluded from the aforementioned sampling step for determining $\mathcal{S}$. Otherwise, Equation 6.5 would imply $\boldsymbol{P}_{\boldsymbol{i}}^{(\boldsymbol{G_o})} = \mathbf{0}$. Hence, $\mathcal{S} \subset \mathcal{L}$, where $\mathcal{L}$ is the set of buses which have loads in at least one phase. In other words, generation is only considered at prosumer buses.

6.2.4 Statement of the VC problem

Let $\mathcal{N}$ denote the set of all grid buses and consider the utility has established a desired voltage range $[V_l, V_h]$ to which all buses must comply. The associated VC problem can be formulated as the following optimization:

$$\begin{aligned} \underset{\boldsymbol{\alpha_s}[n]}{\text{minimize}} \quad & \mathbb{E}\left[\sum_{n=0}^{n_{\mathcal{T}}} \sum_{k \in \mathcal{N}} \left(\psi(\boldsymbol{V_k}[n] - V_h \mathbf{1}) + \psi(V_l \mathbf{1} - \boldsymbol{V_k}[n])\right)\right] \\ \text{s.t.} \quad & \text{Equations 6.1 and 6.2 (load flow constraints);} \\ & \text{Equations 6.3 and 6.4 (power balance constraints);} \\ & -\mathbf{1} \leq \boldsymbol{\alpha_s}[n] \leq \mathbf{1}, \ s \in \mathcal{S}, \ 0 \leq n \leq n_{\mathcal{T}}. \end{aligned} \tag{6.6}$$

where $\mathbf{1}$ is a P-dimensional vector whose elements are all equal to one and $\psi : \mathbb{R}^P \to \mathbb{R}^+$ is defined as the 2-norm with half-wave rectification, i.e., $\psi(\boldsymbol{x}) = \sqrt{\sum_{i=1}^{P} [\max(x_i, 0)]^2}$.

The expectation $\mathbb{E}[\cdot]$ in Equation 6.6 is referred to the joint distribution of all stochastic processes and random variables, namely: (a) load and irradiance profiles; (b) bus and phase allocation of PV panels; and (c) assigned PV panel nominal powers.

Solution of the optimization problem yields time-varying RPS vectors $\boldsymbol{\alpha_s}[n]$, $s \in \mathcal{S}$, which tend to maintain the power system phase voltages in the desired range $[V_l, V_h]$ along time. This can be seen by the fact that, for any $k \in \mathcal{N}$, its corresponding term from the innermost summation in Equation 6.6 equals zero if voltage magnitude at all phases of $\boldsymbol{V_k}$ belong to $[V_l, V_h]$. On the other hand, voltage violations at k contribute with positive terms proportional to their magnitudes and are thus penalized. Finally, the outer summation penalizes violations which have long durations by summing over time.

6.3 Cooperative Markov Decision Process

In this Section, the general cooperative MDP problem is described, starting from the conditions under which it may be modeled as a C-POMDP and the description of such model. Afterwards, a Nash equilibrium-based algorithm and its application for solving the C-POMDP model are discussed.

6.3.1 Description of the C-POMDP Model

Consider a set of cooperative agents whose goal along a given time horizon is minimizing an objective function by optimizing their actions in a stochastic environment. Provided that agent states and observations can be modeled as Markov processes, this problem is classified as a cooperative MDP.

Furthermore, the C-POMDP model applies if the following additional assumptions are also valid: (a) agents do not have knowledge of the system state, basing their decisions solely on local observations; and (b) each combination of state transition and joint action yields a reward for the team. As will be discussed in Section 6.4, such assumptions are reasonable and may be safely adopted for the voltage control problem.

A finite horizon C-POMDP is a 9-tuple $\mathcal{M} = \langle \mathcal{H}, \mathcal{X}, \mathcal{A}, \Omega, \mathcal{P}, \mathcal{O}, R, n_f, \gamma \rangle$, where:

- $\mathcal{H} = \left\{ h_1, h_2, \ldots, h_{|\mathcal{H}|} \right\}$ is the set of agent indices;
- $\mathcal{X} = \left\{ x_1, x_2, \ldots, x_{|\mathcal{X}|} \right\}$ is the set of system states;
- $\mathcal{A} = \bigtimes_{i=1}^{|\mathcal{H}|} \mathcal{A}_i$ is the set of joint actions, where the action set of some agent i given by $\mathcal{A}_i = \left\{ a_i^{(1)}, a_i^{(2)}, \ldots, a_i^{(|\mathcal{A}_i|)} \right\}$;
- $\Omega = \bigtimes_{i=1}^{|\mathcal{H}|} \Omega_i$ is the set of joint observations, where the observation set of some agent i is given by $\Omega_i = \left\{ o_i^{(1)}, o_i^{(2)}, \ldots, o_i^{(|\Omega_i|)} \right\}$;

- $\mathcal{P} = \{\boldsymbol{P}_a(x'|x)|(x', x) \in \mathcal{X}^2,\ a \in \mathcal{A}\}$ is the set of matrices whose columns comprise the probabilities of transition to states x' conditioned on each x and a fixed joint action a, namely $\mathbb{P}(x[n] = x' \,|\, x[n-1] = x, a[n-1])$;
- $\mathcal{O} = \{\boldsymbol{O}_a(o|x')|(o, x') \in \Omega \times \mathcal{X},\ a \in \mathcal{A}\}$ is the set of matrices whose columns comprise the probabilities of joint observations o conditioned on each x' and a fixed joint action a, i.e. $\mathbb{P}(o[n] = o \,|\, x[n] = x', a[n-1])$. Agent observations are independent, whence $\boldsymbol{O}_a = \odot_{i=1}^{|\mathcal{H}|} \boldsymbol{O}_a^{(i)}$, where $\boldsymbol{O}_a^{(i)}$ is the analogous observation matrix of h_i;
- $R = R(x, a)$, with $(x, a) \in \mathcal{X} \times \mathcal{A}$, is the state-action reward function. The value of $R(x, a) \in \mathbb{R}$ is the immediate reward received by the team when performing joint action a while the current system state is x;
- $n_f \in \mathbb{N}^*$ is the considered time horizon;
- $\gamma \in (0, 1]$ is the discount factor used when summing the reward function over the problem horizon n_f.

Let the action of agent h_i at time n be a function of its local observation history, i.e. $a_i[n] = \pi_i(\bar{o}_i[n])$, with tuple $\bar{o}_i[n] = \langle o_i[1]\ o_i[2]\ \cdots\ o_i[n]\rangle$. Function $\pi_i(\cdot)$ is the policy of agent i, whereas $\pi = \bigtimes_{i=1}^{|\mathcal{N}|} \pi_i$ is termed the joint policy.

The goal in C-POMDP is, given $\mathcal{M}$, to minimize the expected value of the accumulated discounted rewards by finding the optimal joint policy π^*. This is stated as [176]:

$$\pi^* = \underset{\pi}{\operatorname{argmin}}\ \mathbb{E}_\pi \left[\sum_{n=0}^{n_f} \gamma^n R(x[n]; a[n]) \right] \tag{6.7}$$

where $\mathbb{E}_\pi$ is expectation conditioned on joint policy π.

6.3.2 Local Optimum Solution via Nash Equilibrium

Solving C-POMDP planning is a task of double-exponential complexity, but for which approximate techniques may be used for reducing execution time. This is not true in the C-POMDP learning case, for which fast algorithms have not yet been developed [177,178]. Taking this into account, it is henceforth assumed that $\mathcal{M}$ as known and consider the planning approach. Specification of model $\mathcal{M}$ is dealt with in Section 6.4.1.

To achieve planning solutions with reduced processing times, the approximate method of Joint Equilibrium-Based Search for Policies (JESP) is considered in this Chapter [179]. Agent coevolution is the main idea behind JESP, a single iteration of which can be summarized by the following steps:

1. Select $h_i \in \mathcal{H}$ and assume that the remaining agents, i.e. $h_{\neq i}$, have fixed policies;

2. Solve the resulting POMDP (since $\pi_{\neq i}$ is fixed, the problem is no longer decentralized) by optimizing Equation 6.7 with respect to the policy π_i, which is then updated;

3. Use π_i to update the joint policy and return to the first step, unless $\mathcal{H}$ has been exhausted. In this case, terminate the algorithm.

The above-described iteration is repeated until a stopping criterion is satisfied, namely that no π_i is updated during $|\mathcal{H}|$ consecutive iterations of JESP, which indicates convergence to a local optimum [179]. The considered implementation of JESP is given in **Algorithm 2**, where agent selection is carried out via sampling of the $|\mathcal{H}|$-categorical distribution so that all agents have equal chances of selection at each iteration.

The output of JESP is a locally optimal policy which is a Nash equilibrium to a partially observable identical payoff stochastic game [179]. Solving each POMDP during execution of JESP is not trivial, since new transition models $\mathcal{P}'_i$ and $\mathcal{O}'_i$ must first be computed for the currently selected agent h_i.

Such transition models stem from the fact that h_i no longer makes decisions based on its incomplete knowledge of $x[n]$, but must also account for the observation histories of all remaining agents, i.e. $\bar{o}_{j\neq i}$. Hence, the POMDP associated to h_i is solved over an extended state space $\mathcal{Y}_i$ whose elements are, at step n, the tuples $y_i = \langle x, \bar{o}_{\neq i}[n]\rangle$, where $x \in \mathcal{X}$ and $\bar{o}_{\neq i}[n] = \langle \bar{o}_1[n], \bar{o}_2[n], \cdots, \bar{o}_{i-1}[n], \bar{o}_{i+1}[n], \cdots, \bar{o}_{|\mathcal{H}|}[n]\rangle$. At step n, models $\mathcal{P}'_i$ and $\mathcal{O}'_i$ are computed according to [179]:

$$P'_{a_i}(y'_i|y_i) = P_{\langle a_i, \pi_{\neq i}(\bar{o}_{\neq i}[n])\rangle}(x'|x) \times \prod_{j\neq i} O^{(j)}_{\langle a_i, \pi_{\neq i}(\bar{o}_{\neq i}[n])\rangle}(o_j|x') \tag{6.8}$$

$$O'_{a_i}(o|y'_i) = O^{(i)}_{\langle a_i, \pi_{\neq i}(\bar{o}_{\neq i}[n])\rangle}(o_i|x') \tag{6.9}$$

where $P_{\langle\cdot\rangle}(\cdot|\cdot)$ is an element of matrix $\boldsymbol{P}_{\langle\cdot\rangle}$, with the same being true for the remaining analogous notations. Notation o_i designates the observation associated to h_i, as per the factorized representation of $\boldsymbol{O}_a$ described in Section 6.3.1.

It is worthwhile noting that $\boldsymbol{P}_{\langle\cdot\rangle}$ and $\boldsymbol{P}'_{\langle\cdot\rangle}$ are, respectively, indexed by one and $|\mathcal{H}|$-dimensional action tuples. This is intuitively expected, since the updated transition model $\mathcal{P}'$ refers to a single-agent decision process carried out by a given h_i for fixed $\pi_{\neq i}$. Identical considerations are valid for $\mathcal{O}'$ and its associated observation matrices $\boldsymbol{O}'_{\langle\cdot\rangle}$.

Finally, the resulting POMDP for h_i can be solved as a belief MDP [179]. Given an initial belief state $b_i(y_i)$, $y_i \in \mathcal{Y}_i$, the following update is carried out at each time step:

$$b_i(y'_i) = \eta \sum_{y_i \in \mathcal{Y}_i} b_i(y_i) P'_{a_i}(y'_i|y_i) O'_{a_i}(o|y'_i) \tag{6.10}$$

where η is a normalization factor such that $\sum_{y'_i \in \mathcal{Y}'_i} b_i(y'_i) = 1$ and $\mathcal{Y}'_i$ is the extended state space after the belief update.

Algorithm 2 JESP Implementation

Input: $\mathcal{M}$.
Output: π.
1: $c \leftarrow 0$.
2: $\pi \leftarrow$ Random policy.
3: **while** $c \neq |\mathcal{H}|$ **do**
4: $\quad \mathcal{H}' \leftarrow \mathcal{H}$.
5: $\quad$ **for** $i = 0, 1, \ldots, |\mathcal{H}| - 1$ **do**
6: $\quad\quad$ Sample a random integer $j \in [1, |\mathcal{H}| - i]$.
7: $\quad\quad$ $k \leftarrow$ Index of j-th agent in $\mathcal{H}'$.
8: $\quad\quad$ $\mathcal{H}' \leftarrow \mathcal{H}' - \{h_k\}$.
9: $\quad\quad$ Fix policies $\pi_{\neq k}$.
10: $\quad\quad$ Solve resulting POMDP with respect to π_k.
11: $\quad\quad$ **return** π_k.
12: $\quad\quad$ Update $\pi = \bigtimes_{i=1}^{|\mathcal{N}|} \pi_i$.
13: $\quad$ **end for**
14: $\quad$ **if** π has remained constant **then**
15: $\quad\quad$ $c \leftarrow c + 1$.
16: $\quad$ **end if**
17: **end while**
18: **return** π.
Source: The author.

It should be noted that Equation 6.10 is just the standard POMDP belief update, but applied to extended domain $\mathcal{Y}_i$ with models $\mathcal{P}'_i$ and $\mathcal{O}'_i$. For the dynamic programming solution of belief MDP, see [179]; such routine is embedded in line 10 of **Algorithm 2**.

6.4 Proposed Cooperative Voltage Control

In this Section, a method of cooperative and decentralized VC of distributed PV generators is proposed. It consists in constructing a C-POMDP model specialized to the VC problem and whose agents control distinct grid zones. Division of the grid into control zones is carried out with a sensitivity-based clustering algorithm. Then, planning with the C-POMDP model is solved via JESP, yielding closed-form RPS control policies. This enables real-time control, since policy computation is previously carried out offline.

6.4.1 Distributed Reactive Support C-POMDP Model

The proposed model, which is termed as Distributed Reactive Support C-POMDP (DRS-C-POMDP), is now discussed. At first, it is assumed that all nodes of $\mathcal{S}$ have been clustered in $|\mathcal{H}|$ disjoint subsets, denoted by S_i, $i = 1, 2, \ldots, |\mathcal{H}|$. Hence, each $s \in \mathcal{S}_i$ is subsumed under a single agent h_i and the set $\mathcal{H}$ is known. Now, the remaining components

of tuple $\mathcal{M}$ must be specified in order to define the C-POMDP to be solved. The clustering procedure used to obtain $\mathcal{H}$ is considered in Section 6.4.2.

In principle, C-POMDP planning requires knowledge of the joint distribution of all stochastic processes so that $\mathcal{M}$ may be known (as discussed in Section 6.2.1). Since such information is unavailable, it is proposed that the model be specified in a heuristic manner. The selected parameters must adequately represent the VC problem to ensure the attainment of reasonable RPS control policies. In what follows, proposals for specifying each parameter of $\mathcal{M}$ are presented. It must be noted that the model is specified in a per phase manner and may be applied separately to each $r \in \Phi$ (see Section 6.4.2).

6.4.1.1 $\mathcal{X}$

Each $x \in \mathcal{X}$ is an $|\mathcal{H}|$-dimensional tuple whose components are indicators of voltage magnitude status in each cluster $\mathcal{S}_i$, i.e., $x = \langle x^{(1)}\ x^{(2)}\ \cdots\ x^{(|\mathcal{H}|)} \rangle$. It is proposed that, for a given $r \in \Phi$, each $x^{(i)}$ be defined as follows:

$$x^{(i)} = \begin{cases} \texttt{low}, & \text{if } V_l - V^{(-)} > 0 \text{ and } V^{(+)} - V_h < 0 \\ & \text{or } V_l - V^{(-)} > V^{(+)} - V_h > 0 \\ \texttt{normal}, & \text{if } V^{(-)} - V_l \geq 0 \text{ and } V^{(+)} - V_h \leq 0 \\ \texttt{high}, & \text{if } V_h - V^{(+)} < 0 \text{ and } V^{(-)} - V_l > 0 \\ & \text{or } V_h - V^{(+)} < V^{(-)} - V_l < 0 \end{cases} \tag{6.11}$$

where $V^{(-)} = \min_{s \in \mathcal{S}_i} V_s^r$ and $V^{(+)} = \max_{s \in \mathcal{S}_i} V_s^r$. Hence, a `normal` status is assigned to S_i if none of its node voltages deviate from the interval $[V_l, V_h]$. If both types of violations are detected (i.e., under and overvoltage), status assignment is based on maximum deviation magnitude (as indicated in the *or* clauses of Equation 6.11).

6.4.1.2 $\mathcal{A}$

From agent symmetry, all $\mathcal{A}_i$ are identical. The $\mathcal{A}_i$ elements are commands for jointly controlling all α_s^r, $s \in \mathcal{S}_i$. Since evaluation of local inverter controls is not our focus, a simple command structure is adopted with fixed setpoint step $\Delta\alpha$ and commands $\mathcal{A}_i = \{+1, -1, 0\}$, which control the setpoints according to $\alpha_s^r[n] = \alpha_s^r[n-1] + a_s \Delta\alpha$.

6.4.1.3 Ω

From symmetry, all Ω_i are identical. The elements in Ω_i are indicators of voltage status in cluster $\mathcal{S}_i$, identical to those previously defined for the i-th component of each $x \in \mathcal{X}$. In other words, each h_i only observes its *local* voltage status and has an associated observation set $\Omega_i = \{\texttt{low}, \texttt{normal}, \texttt{high}\}$.

6.4.1.4 $\mathcal{P}$

Despite the unavailability of joint distributions, the values attributed to each $P_a(x'|x)$ must reasonably estimate the likelihood of transition $x \to x'$ after joint action a. To achieve this, it is proposed that the probability assignment be carried out according to:

$$P_a(x'|x) \propto \prod_{i=1}^{|\mathcal{H}|} \prod_{j=1}^{|\mathcal{H}|} f_{a_i}(x'_j|x_j) m(i,j) \tag{6.12}$$

where $f_{a_i}(x'_j|x_j)$ and $m(i,j)$ are heuristic functions which measure likelihood of the component transition $x'_j \to x_j$ being induced by the action component a_i and the coupling between states of agents h_i and h_j, respectively.

6.4.1.5 $\mathcal{O}$

Since voltage observation is achieved via actual measurement, it could be thought at first that $\boldsymbol{O}_a$ should be equal to the identity matrix. However, recall that the DRS-C-POMDP model is an approximate representation of the control problem, for which reason observations may not exactly correspond to real states. To incorporate such uncertainty in the model, it is proposed that probabilities be attributed as follows:

$$O_a(x'|x) \propto \prod_{i=1}^{|\mathcal{H}|} g(o_i|x'_i) \tag{6.13}$$

where $g(o_i|x'_i)$ is an heuristic likelihood measure analogous to the previously defined $f_{a_i}(x'_j|x_j)$. Note that $\boldsymbol{O}_a$ is taken as constant with respect to a, since voltage sensing uncertainty is independent from reactive control.

6.4.1.6 R

Each value $R(x,a)$ must measure the desirability of issuing joint action a at state x. In order to enable agent-wise reward attribution, this function is decomposed as follows:

$$R(x,a) = \sum_{i=1}^{|\mathcal{H}|} r(x_i, a_i) \tag{6.14}$$

where $r(x_i, a_i)$ is an agent-level reward function.

6.4.1.7 n_f

The value of this parameter must be kept low enough for avoiding the exponential growth of computational complexity associated to C-POMDP models. However, it must be sufficiently high to effectively capture system randomness in the decision process. Specific considerations on the selection of n_f are given in Section 6.5.2.

6.4.1.8 γ

In finite-horizon problems, convergence problems associated to an unitary discount factor do not exist. For this reason, it is henceforth assumed that $\gamma = 1$ as is customary.

6.4.2 Selecting Agents via Sensitivity-Based Clustering

Computational complexity of exact C-POMDP planning is exponential in $|\mathcal{H}|$ and double-exponential in n_f [176]. Despite yielding local optima, **Algorithm 2** decreases complexity to exponential with respect to both parameters. However, it is empirically known that JESP processing times tend to be much lower than what is suggested by worst-case complexity, provided sufficiently small $|\mathcal{H}|$ and n_f are used [179].

Hence, to enable fast convergence of JESP and obtain the RPS control policies in reasonable time, heuristic modeling of the grid with DG must be carried out with as small values of $|\mathcal{H}|$ and n_f as possible. In what follows, reduction of $|\mathcal{H}|$ is considered; the selection of n_f is dealt with in Section 6.5.2.

At first glance, the VC problem suggests that $|\mathcal{H}|$ should equal the number of grid-tied PV inverters, i.e., $|\mathcal{H}| = |\mathcal{S}|$. However, larger power systems with potentially high $|\mathcal{S}|$ may lead to unacceptable execution times with **Algorithm 2**. To avoid this problem, a decentralized approach is proposed: nodes $s \in \mathcal{S}$ are clustered in disjoint subsets $\mathcal{S} = \bigcup_{i=1}^{M} \mathcal{S}_i$ such that $M < |\mathcal{S}|$, with each $\mathcal{S}_i$ being subject to control by a single $h_i \in \mathcal{H}$. By adopting this approach, a much smaller $|\mathcal{H}| < |\mathcal{S}|$ can be obtained.

Since every $s \in \mathcal{S}_i$ receives identical commands from h_i, the partition of $\mathcal{S}$ must be such that the simultaneous control of multiple PV nodes by each h_i does not exceedingly detract from performance that would be obtained with the trivial partition, namely $\mathcal{S} = \bigcup_{i=1}^{|\mathcal{S}|} \{s^{(i)}\}$. A means of achieving this is ensuring that nodes with high voltage correlation are assigned to the same cluster: with high probability, such nodes are bound to perform better for equal control commands and may thus be aggregated under one h_i.

Since reactive support VC is being considered, voltage correlation must be measured with respect to reactive power injections. Taking this into account, an approach based on electrical distances which measure sensitivity of voltage to reactive injection is adopted [180]. Such distance metric is based on the following sensitivity parameter [181]:

$$\Gamma_{ij}^{rs} = \frac{\partial [V_i^r]^2}{\partial Q_j^s} = 2V_i^r \frac{\partial V_i^r}{\partial Q_j^s} \tag{6.15}$$

where Γ_{ij}^{rs} is the sensitivity of voltage magnitude at phase r of node i to reactive power injection at phase s of node j.

Since $\Gamma_{ij}^{rs} \leq \Gamma_{ij}^{rr}$ is true for any node and phase pair (as shown by **Proposition 9** in Appendix B), it is reasonable to carry out clustering separately in each phase by

considering only Γ_{ij}^{rr} for each $r \in \Phi$. Proceeding as such, potentially different sets of $|\mathcal{H}|$ clusters are obtained for each phase, which are to be controlled independently of each other according to the policies obtained by solving DRS-C-POMDP.

Remark 6.3: Some discussion is due on what requirements are implied by the aforementioned independent phase control. We first note that the PV units may be implemented by means of single or three-phase inverters, since the latter may be used in each $s \in \mathcal{S}$ with PV generation allocated to all phases. Hence, a requirement peculiar to the three-phase case is that the inverter be compatible with unbalanced reactive power injection. Furthermore, general requirements which apply to all PV units are: (a) communication with a zone controller whose processor can receive state data from all its subordinate PV nodes, segregate and process the data pertaining to each phase and broadcast a message to all nodes containing control decisions for each phase; (b) synchronized voltage sampling and state computations for all phases, since the zone controller must receive information on all phases simultaneously; and (c) a communication unit which is capable of concatenating the computed phase states in a message sent to the zone controller.

Remark 6.4: Due to distribution grid phase symmetry, the clusters obtained for each phase may, with high probability, be identical. Despite this fact, independent phase control is still required since undervoltages and/or overvoltages may affect different phases of a given node at distinct times.

The set of derivatives $\partial_{Q_j^r} V_i^r$, $r \in \Phi$, can be computed by inverting an adequate submatrix of the power system Jacobian, namely $\boldsymbol{L} = [\partial_{V_j^s} Q_i^r]_{NP \times NP}$, $i, j = 1, 2, \ldots, N$ and $r, s \in \Phi$. Given the inverse matrix $\boldsymbol{L^{-1}}$, the desired derivative values in Equation 6.15 (i.e., those for $r = s$) are disposed along the diagonals of $P \times P$ submatrices of $\boldsymbol{L^{-1}}$. Electrical distances are then computed for $r \in \Phi$ according to [181]:

$$d_{ij}^r = -\ln\left(\frac{\Gamma_{ij}^{rr}\Gamma_{ji}^{rr}}{\Gamma_{ii}^{rr}\Gamma_{jj}^{rr}}\right) \tag{6.16}$$

For each phase r, the d_{ij}^r represent dissimilarity metrics between nodes. Taking this into account, clustering is carried out over $\mathcal{N}$ by using Equation 6.16 as input to the hierarchical agglomerative clustering (HAC) algorithm [182]. The obtained clustering of $\mathcal{N}$ induces the clusters of $\mathcal{S}$ with the desired property $|\mathcal{H}| \leq |\mathcal{S}|$. Hence, the number $|\mathcal{H}|$ can be selected by adjusting the dissimilarity threshold in the HAC algorithm.

Usage of Equation 7.1 presupposes knowledge of system voltages. To perform offline clustering, the same procedure is adopted as in [181]: a single load flow simulation of the grid is solved for constant loads and no PV generation. Then, obtained voltages are used in Equation 7.1. The proposed clustering approach is summarized in **Algorithm 3**.

Algorithm 3 Sensitivity-Based Clustering

Input: Power system data, $\mathcal{N}$, $\mathcal{S}$, $|\mathcal{H}|$, $r \in \Phi$.
Output: $\mathcal{H}$.
1: $\mathcal{H}' \leftarrow \emptyset$.
2: Solve load flow with fixed load and no PV generation.
3: **return** $\boldsymbol{V}$, $\boldsymbol{L}$.
4: Compute $\boldsymbol{\Gamma} = \boldsymbol{L}^{-1}$.
5: Use Equation 6.16 to compute each d_{ij}^{r}; $i, j = 1, 2, \ldots, N$.
6: **while** $|\mathcal{H}'| \neq |\mathcal{H}|$ **do**
7: Adjust dissimilarity threshold in HAC algorithm.
8: Run the HAC algorithm with the d_{ij}^{r} as input.
9: **return** Clustering over $\mathcal{N}$.
10: Compute the induced clustering over $\mathcal{S}$.
11: **return** $\mathcal{H}'$.
12: **end while**
13: $\mathcal{H} \leftarrow \mathcal{H}'$.
14: **return** $\mathcal{H}$.
Source: The author.

6.4.3 Online Voltage Control

Usage of DRS-C-POMDP does not inhibit online VC, since $\mathcal{M}$ is solved previously to initialization of real-time control. Hence, the *offline* phase of the proposed method consists in solving $\mathcal{M}$ to obtain a joint policy π to be used by the agents for RPS control.

In this sense, the *online* phase consists in updating the agent observation histories and applying the joint policy π at each time step. To summarize the voltage control method proposed in this Section, it is presented as pseudocode in **Algorithm 4**.

6.5 Computer Simulations

In this Section, a three-part computer simulation case study is carried out for validating the proposed VC method. All simulations are implemented in MATLAB R2017a, with the method selected for computing load flow (i.e., line 11 in **Algorithm 4**) being the standard Newton-Raphson algorithm.

6.5.1 Case Study Description

The distribution grid considered in this case study is a modified version of the three-phase IEEE 123-bus test feeder, which has been selected due to its widespread usage in the literature for conducting load flow case studies [183]. Changes made with respect to the original feeder are: (a) system loading is reduced by 50%; (b) constant current and impedance loads are converted to PQ-type with the same rated active and reactive powers; and (c) voltage regulators are removed from their respective lines. Such alterations are

Algorithm 4 DRS-C-POMDP Voltage Control

Input: Power system data, A, B_1, B_2 $n_{\mathcal{T}}$, $|\mathcal{S}|$, $\mathcal{PQ}$, $\mathcal{E}$, $|\mathcal{H}|$.
Output: $\boldsymbol{V}[n]$, π; $n = 1, 2, \ldots, n_{\mathcal{T}}$.

Generate set $\mathcal{S}$ and sample load/irradiance profiles from $\mathcal{PQ}$ and $\mathcal{E}$ to initialize simulation data (as described in Section 6.2).
Run **Algorithm 3** for each $r \in \Phi$.
return $\mathcal{H}$.
Use $\mathcal{H}$ as input to generate the DRS-C-POMDP model.
return $\mathcal{M}$.
{*Begin offline phase*}
Solve $\mathcal{M}$ by running **Algorithm 2**.
return π.
{*Begin online phase*}
for $n = 1, 2, \ldots, n_{\mathcal{T}}$ **do**
    Update $\bar{o}[n]$.
    Adjust $\boldsymbol{\alpha_s}[n]$ according to $\pi(\bar{o}[n])$.
    Solve load flow and update $\boldsymbol{V}[n]$.
end for
return $\boldsymbol{V}[n]$; $n = 1, 2, \ldots, n_{\mathcal{T}}$.

Source: The author.

made so that: (a) the various undervoltage instances that occur in the base feeder are mostly eliminated; (b) load profiles sampled from $\mathcal{PQ}$ may be directly used for modulating all loads; and (c) evaluation of voltage control is carried out with no regulator interference.

Remark 6.5: It should be noted that PQ loads have been considered solely for the convenience of directly modulating nominal loads via the normalized profiles sampled from $\mathcal{PQ}$ (as per Equations 6.3 and 6.4), which does not restrict applicability of the proposed method to other loads. In fact, since the only measurements required by the proposed method are of node *voltages*, its applicability is indifferent to load type.

Remark 6.6: The assumption of no voltage regulators is used to ensure that analysis of VC performance by the PV units is not masked by VR operation. In any case, it appears that the proposed method can, in principle, be seamlessly used to control VR-equipped grids as well. To this effect, consider a grid with VRs to which DRS-C-POMDP would be applied. After a VR tap change, the new voltage profile would be sampled and used for computation of system status via Equation 6.11, with reactive power outputs thus being adjusted as required after the tap change. However, it is fair to mention an issue which may happen due to joint VC by VRs and PV inverter reactive support which is not considered in this work, namely the potential increase of tap switching rate in VRs, which may reduce lifetime. If this problem must be mitigated in particular, specialized optimization methods designed for minimizing VR switching must be considered [145, 147].

Adopted simulation timespan is $\mathcal{T} = 1$ day and 1-minute samples are used (i.e.,

Table 11 – Voltage control simulation input data

Parameter	**Specification**
Power system	IEEE 123-bus feeder, 50% base loading Loads converted to PQ-type, no regulators
$\mathcal{E}$	91 daily profiles, 1 min resolution Measured at EMC-UFG from 01-03/2020
$\mathcal{PQ}$	300 normalized daily profiles, 1 min resolution Generated in *House Load* toolbox
$\mathcal{T}$	1 day
$n_{\mathcal{T}}$	1440 ($T = 1$ sample/min)
$\lvert\mathcal{S}\rvert$	60 generators
θ_o	$\arccos 0.9$
B_1	100%
B_2	150%

Source: The author.

$n_{\mathcal{T}} = 1440$). Dataset $\mathcal{E}$ consists of 91 daily irradiance profiles measured at the rooftop of Block A in the School of Electrical, Mechanical and Computer Engineering of the Federal University of Goiás (EMC-UFG) [26], whereas $\mathcal{PQ}$ is composed of 300 normalized daily load profiles generated with the *House Load* toolbox from [184]. It is assumed that $\tilde{\boldsymbol{Q}}_s^{(\boldsymbol{L})}[\boldsymbol{n}] = \tilde{\boldsymbol{P}}_s^{(\boldsymbol{L})}[\boldsymbol{n}]$ for all $s \in \mathcal{S}$, so that power factors of the original feeder are kept.

The simulation is initialized as follows. First, the random selection of $\mathcal{S}$, nominal PV power and phases with PV generation at each $s \in \mathcal{S}$ are carried out as described in Section 6.2.3. Then, for each $s \in \mathcal{S}$, an irradiance profile is randomly selected from $\mathcal{E}$ via sampling of an $|\mathcal{E}|$-dimensional categorical distribution. Analogously, for each node in $\mathcal{L}$, three normalized load profiles are randomly selected from $\mathcal{PQ}$ via sampling of an $|\mathcal{PQ}|$-dimensional categorical distribution and attributed to each of the node phases. The allocation of PV generators, irradiance profiles and load profiles is redone in each of the parts (Sections 6.5.3 to 6.5.5) of the case study. This simulation approach has been adopted to ensure a more thorough validation of the proposed method, since the practical scenario of distribution grids with DG penetration corresponds to random allocation of grid-connected PV resources and stochastic irradiance/load profiles.

High PV penetration is considered by setting $|\mathcal{S}| = 60$, $B_1 = 1.0$ and $B_2 = 1.5$, with the minimum inverter power factor being assumed as $\cos\theta_o = 0.9$. In Figure 44, illustrations of the IEEE 123-bus feeder topology and the datasets $\mathcal{E}$, $\mathcal{PQ}$ are presented. Furthermore, the simulation input data are summarized in Table 11 for ease of reference.

Remark 6.7: The IEEE 123-bus feeder, despite its nomenclature, actually contains 129 nodes which are *not* numbered sequentially [183]. Henceforth, its nodes are referred to by ordinal numbers $z = 1, 2, \ldots, 129$ computed with reference to their original numbering. Also, system phases are henceforth denoted by $\Phi = \{A, B, C\}$.

Figure 44 – Illustrations of the IEEE 123-bus feeder single-line diagram (with its original node numbering), the irradiance profiles in $\mathcal{E}$ and the normalized load profiles in $\mathcal{PQ}$. Coloured curves are examples of random samples from $\mathcal{E}$ and $\mathcal{PQ}$.

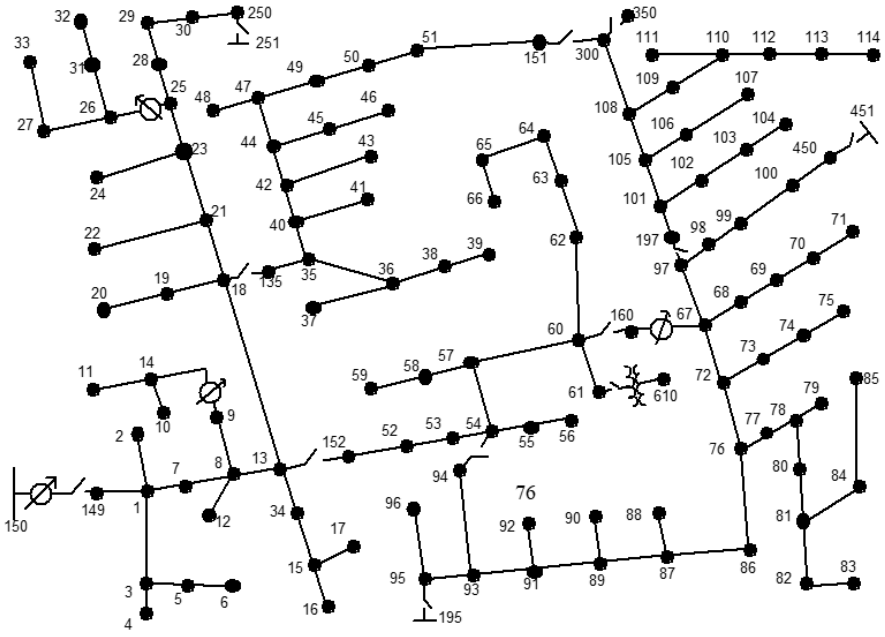

(a) One-line diagram of the 123-bus feeder.

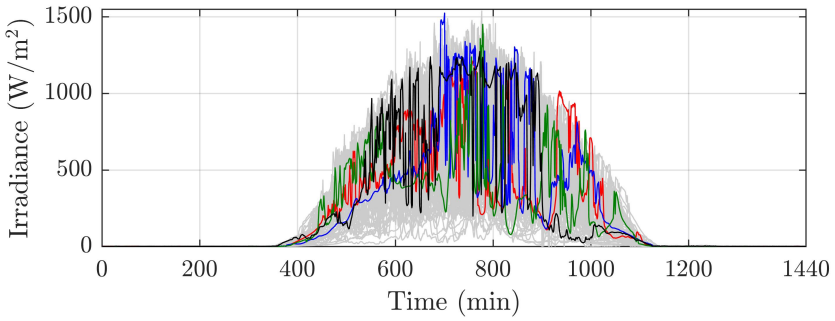

(b) Irradiance profiles.

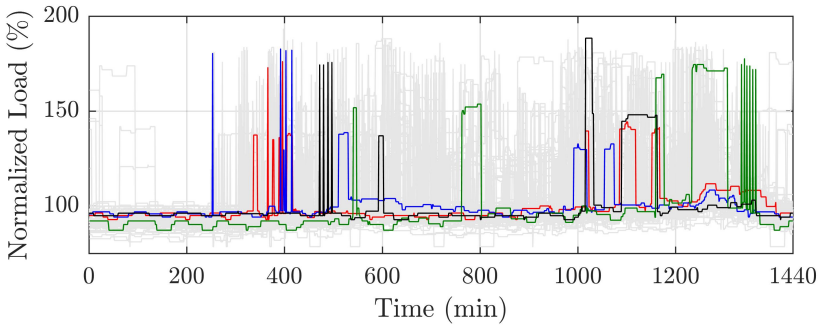

(c) Normalized load profiles.

Source: (a) IEEE [183], (b)-(c) The author.

6.5.2 Design of DRS-C-POMDP Parameters

To enable state computation via Equation 6.11, the minimum and maximum voltage thresholds must be specified. The values $V_l = 0.93$ p.u. and $V_h = 1.05$ p.u. are adopted, as per specifications of the brazilian regulatory agency for the voltage range in which the 123-bus feeder is situated [185]. Given V_l and V_h, $\mathcal{X}$ and Ω are fully specified.

The complete specification of $\mathcal{A}$ depends on setting a value for the reactive setpoint increment $\Delta\alpha$. Since scenarios with high PV penetration (and associated reactive power reserves) are considered, the increment must be sufficiently small to enable gradual adjustments to reactive power injection, for which reason $\Delta\alpha = 0.05$ is adopted.

It remains to specify $\mathcal{P}$, $\mathcal{O}$ and R. This is achieved by giving the values taken by functions $f_{a_i}(x'_j|x_j)$, $g(o_i|x'_i)$, $r(x_i, a_i)$ and $m(i, j)$ for all possible arguments of each function. The designed values are given in matrix form below:

$$f_{+1}(\,\cdot\,|\,\cdot\,) = \begin{bmatrix} 60 & 35 & 5 \\ 5 & 60 & 35 \\ 5 & 15 & 80 \end{bmatrix} \tag{6.17}$$

$$f_{-1}(\,\cdot\,|\,\cdot\,) = \begin{bmatrix} 80 & 15 & 5 \\ 35 & 60 & 5 \\ 5 & 35 & 60 \end{bmatrix} \tag{6.18}$$

$$f_{0}(\,\cdot\,|\,\cdot\,) = \begin{bmatrix} 90 & 10 & 0 \\ 5 & 90 & 5 \\ 0 & 10 & 90 \end{bmatrix} \tag{6.19}$$

$$g(\,\cdot\,|\,\cdot\,) = \begin{bmatrix} 80 & 20 & 0 \\ 10 & 80 & 10 \\ 0 & 20 & 80 \end{bmatrix} \tag{6.20}$$

$$r(\,\cdot\,,\,\cdot\,) = \begin{bmatrix} -300 & -300 & -100 \\ -100 & -300 & -300 \\ -200 & +100 & -200 \end{bmatrix} \tag{6.21}$$

$$m(\,\cdot\,,\,\cdot\,) = \begin{bmatrix} 10 & 3 & 3 \\ 3 & 10 & 3 \\ 3 & 3 & 10 \end{bmatrix} \tag{6.22}$$

where matrix columns and lines in Equations 6.17-6.21 refer, respectively, to first and second arguments, whose domains are defined in Section 6.4.1. For instance, $r(\texttt{normal}, 0) = +100$, $f_{-1}(\texttt{normal}|\texttt{low}) = 15$ and $m(1, 2) = 3$.

When designing the DRS-C-POMDP model, values in Equations 6.17-6.22 were chosen via repeated testing, while taking into consideration the following heuristics:

- Transition and observation probabilities must be higher for neighboring states, yet sufficiently distributed over all states to account for model uncertainty (as discussed in Section 6.4.1.5) and irradiance randomness;
- It is required that $m(i,i) > m(i,j)$, $i \neq j$, since the actions of an agent have greater influence over its state component than the actions of other agents;
- Rewards must take into account desirability of the state with respect to Equation 6.6 and if the selected action tends to make the system remain or leave such state.

Finally, the selected time horizon was $n_f = 5$. This value is considered adequate since VC strongly depends on instantaneous irradiance and load profiles. Hence, an observation history encompassing five one-minute samples is reasonable for taking transients and randomness into account during the decision process.

6.5.3 Part 1: 24-Hour Performance Assessment

To validate the proposed VC method, its performance is compared to that obtained in four scenarios, namely: absence of VC, usage of local VC, usage of the active power derivative heuristic from [171] and usage of the distress signal heuristic from [172]. We justify the selection of [171,172] by the fact that, as discussed in Section 6.1, such methods are heuristic and based on closed-form control laws, which is also the case for the method proposed in this Chapter. Finally, by local VC it is understood that each $s \in \mathcal{S}$ performs status computation Equation 6.11 and acts by taking into account solely its current state (i.e., $|\mathcal{H}| = |\mathcal{S}|$ and $n_f = 1$). For all decentralized methods, $|\mathcal{H}| = 3$ is assumed. The effect of varying $|\mathcal{H}|$ on performance shall be considered in Section 6.5.5.

Aside from the RPS control method, the low-level inverter controls for driving the RPS towards its reference value also affects performance. Since the focus of this Chapter is solely the comparison of high-level controls, the simple low-level RPS control structure described in Section 6.4.1.2 is adopted for all methods. In other words, the RPS control logic of each method is used for taking ternary decisions on whether RPS should be increased, decreased (by the fixed setpoint increment $\Delta\alpha$) or remain constant.

Other than evolution of the objective function given by Equation 6.6 along time, some additional performance metrics are evaluated:

$$\Delta V(z;\phi) = \max_{n} \left[\psi(V_z^{\phi}[n] - V_h) + \psi(V_l - V_z^{\phi}[n])\right] \tag{6.23}$$

$$T_H(z;\phi) = \frac{1}{n_{\mathcal{T}}+1} \sum_{n=0}^{n_{\mathcal{T}}} u\left(V_z^{\phi}[n] - V_h\right) \tag{6.24}$$

$$T_L(z;\phi) = \frac{1}{n_{\mathcal{T}}+1} \sum_{n=0}^{n_{\mathcal{T}}} u\left(V_l - V_z^{\phi}[n]\right) \tag{6.25}$$

Figure 45 – Obtained results for Part 1 of the VC case study.

Explanatory note: The results are comprised of (a) MVV at Phase A, (b) MVV at Phase B, (c) MVV at Phase C, (d) ROT at Phase A, (e) ROT at Phase B, (f) ROT at Phase C, (g) RUT at Phase A, (h) objective function time plots and (i) illustration of the grid clusters. All RUT curves for Phases B and C were identically zero, for which reason they are not shown. The plotted curves are identified as follows: no reactive control (dotted line, green), local control (alternated tracing line, blue), heuristic control [171] (traced line, magenta), heuristic control [172] (thick traced line, red) and proposed control method (solid line, black).

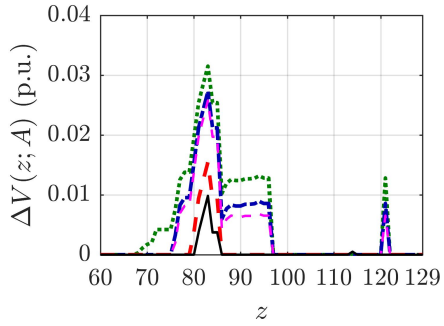

(a) MVV at Phase A.

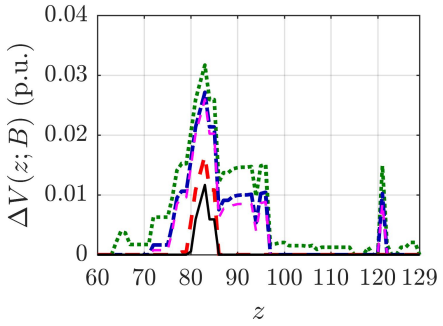

(b) MVV at Phase B.

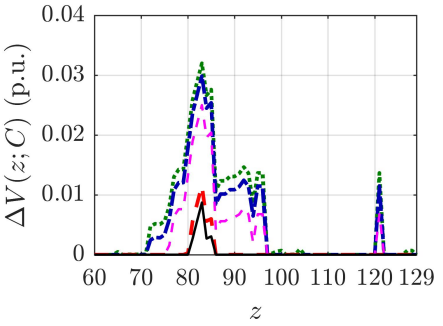

(c) MVV at Phase C.

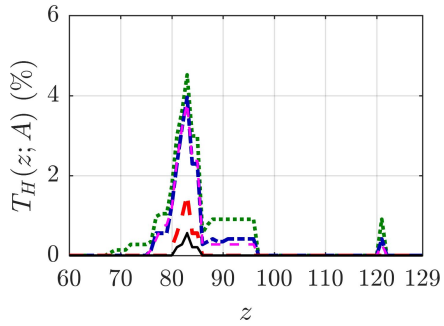

(d) ROT at Phase A.

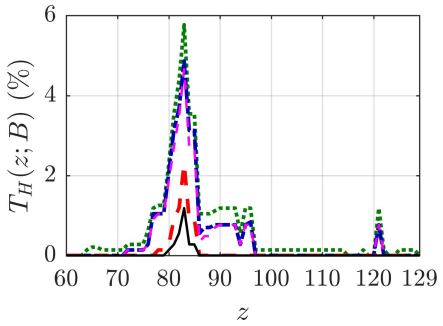

(e) ROT at Phase B.

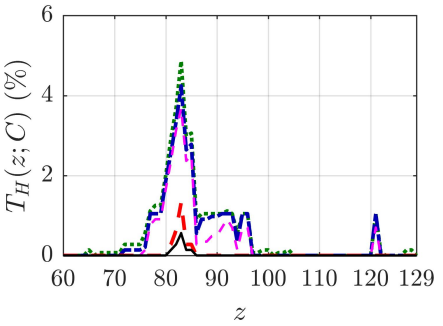

(f) ROT at Phase C.

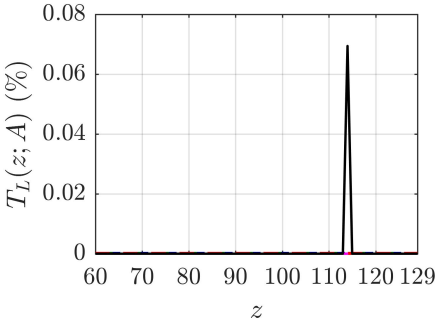

(g) RUT at Phase A.

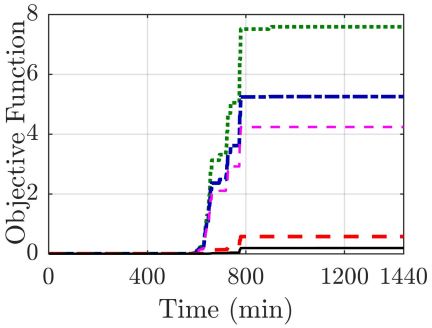

(h) Objective function plots.

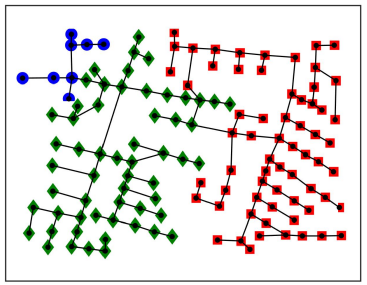

(i) Plot of grid clusters.

Source: The author.

where $u(\cdot)$ is the unit step function and the metrics $\Delta V(z;\phi)$, $T_H(z;\phi)$ and $T_L(z;\phi)$ are, respectively, the maximum voltage violation (MVV), relative overvoltage time (ROT) and relative undervoltage time (RUT) at phase ϕ of node z.

Obtained results are given in Figures 45(a)-(i). As anticipated in *Remark 6.4*, the obtained clustering was identical for each phase due to feeder symmetry; the node clusters subsumed to each of the $|\mathcal{H}| = 3$ control zones are illustrated in Figure 45(i). In general, it is seen that the proposed VC method is the most efficient at avoiding overvoltages caused by excess PV generation. In fact, it yielded the smallest MVV and ROT values for all nodes and phases, as per Figures 45(a)-(f). A small trade-off is verified, in that the proposed method was the only one with non-zero RUT at Phase A. However, such RUT value is very small with respect to obtained ROT and is thus negligible. Superior performance of the proposed approach is also shown by the objective function plots in Figure 45(g), where it achieved about threefold reduction with respect to the second best-performing method.

The results also suggest superiority of decentralized VC in general, since all methods classified as such performed better than local VC. Interestingly, the worse performance of [171] when compared to the proposed method and [172] appears to further corroborate this assertion; since [171] uses total generated PV power and *local* voltages for controlling RPS, it can be considered closer to the local control approach.

6.5.4 Part 2: Voltage Transient Performance

It is important to assess the response of VC methods to impulsive voltage transients. Hence, a simulation scenario in which slack bus ($z = 117$) voltage is abruptly increased from 1 p.u. to 1.03 p.u. at $n = 750$ is considered. A comparison is made between performances attained with each of the methods considered in Section 6.5.3. As in the previous simulation, $|\mathcal{H}| = 3$ clusters are considered. Corresponding results are presented in Figures 46(a)-(d). Aside from objective function plots, ROT and MVV plots for the phase which presented worse overvoltages (Phase B) are given. Finally, a time plot is given of Phase B voltage at the critical node, which is defined as the one that presented greatest MVV when no voltage control was used. All obtained RUT were identically zero.

Figures 46(a) and 46(b) show that the greatest reductions of T_H and ΔV are yielded by the proposed method for all nodes. Such superior performance is corroborated by Figure 46(c), which shows that the proposed approach converges to the smallest objective function value. Interestingly, the heuristic VC from [171] performed worse than local control in this case. Such phenomenon may be attributed to the fact that [171] uses the derivative of total PV power with respect to local voltages: an abrupt change in voltage at approximately constant power may lead [171] to make suboptimal RSP control decisions after the transient. This discussion is supported by the fact that, prior to occurrence of the transient, local VC and [171] have similar performances as seen from the voltage time plots in Figure 46(d).

Figure 46 – Obtained results for Part 2 of the VC case study.

Explanatory note: The results are comprised of (a) ROT at Phase B, (b) MVV at Phase B, (c) objective function time plots and (d) time plots of voltage at Phase B of $z = 83$. The plotted curves are: no reactive control (dotted line, green), local control (alternated tracing line, blue), heuristic control [171] (thin solid line, magenta), heuristic control [172] (thick traced line, red) and proposed method (solid line, black).

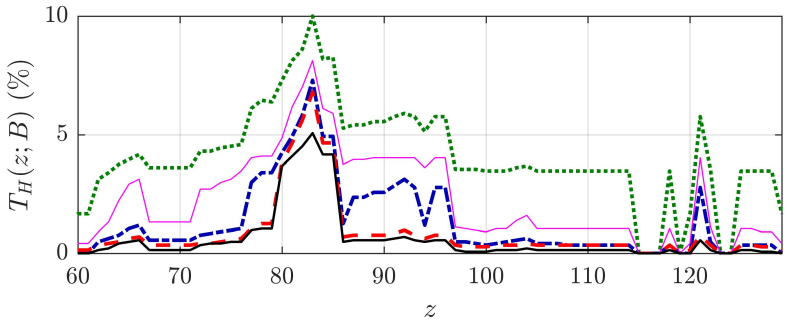

(a) Relative overvoltage times at Phase B.

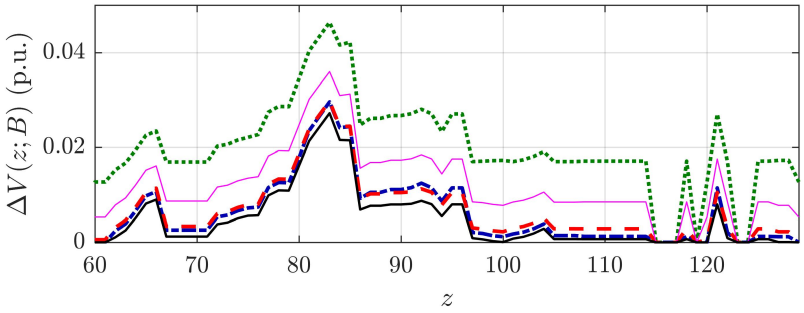

(b) Maximum voltage violations at Phase B.

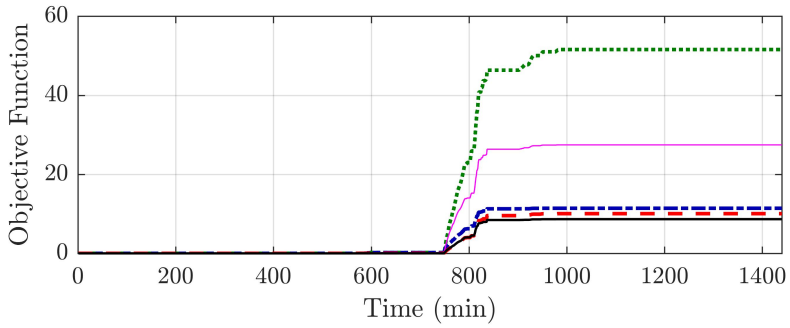

(c) Time plot of objective functions.

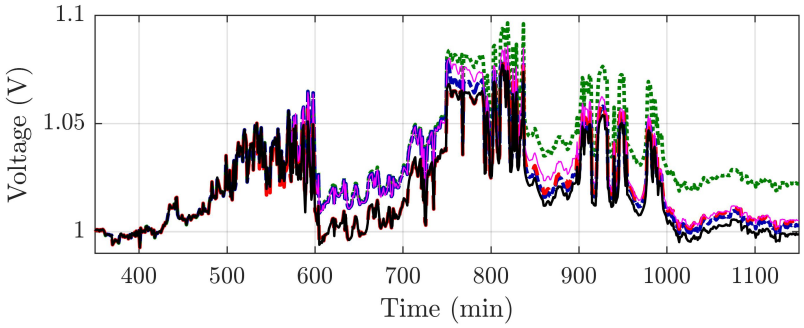

(d) Time plot of voltage at Phase B of critical node ($z = 83$).

Source: The author.

The plots in Figure 46(d) also show that the proposed method provides the most effective dampening of the transient and tends to draw voltages to lower values after its occurrence. Also, even at steady-state ($n < 750$), the proposed method and [172] are seen to perform more conservatively with respect to the upper limit V_h.

Note from Figures 46(a) and 46(b) that greater reductions of ROT and MVV are obtained at non-critical nodes. This is explained by observing Figure 46(d), which shows that the critical node is eventually subjected to large overvoltages which cannot be completely eliminated due to insufficient inverter reactive capacity. In a real distribution grid scenario, such overvoltages would be regulated by means of the joint action of PV inverters and grid VRs, which yield coarser voltage control for eliminating larger overvoltages. As anticipated in *Remark 6.6*, VRs were not considered for simulation to prevent their operation from masking the performances of the considered reactive support methods and thus inhibit their comparison.

The above discussion is supported by the fact that many non-critical nodes benefit from almost complete elimination of overvoltage via application of the proposed method, which shows that reactive support was successfully leveraged to mitigate overvoltages which do not exceed the reactive power capacity of the PV inverters. It is thus concluded that, despite the larger overvoltages which persisted (especially at $z = 83$) due to the combination of high slack bus voltage and absence of VRs, comparison between the performances of each method still indicates that the proposed method yields superior VC both in voltage transient and steady-state scenarios.

6.5.5 Part 3: Effects of Cluster Number

As a last validation effort, it shall be instructive to analyze performance of the proposed method in terms of the adopted number of clusters. To this end, three simulations are carried out in which the proposed method is used with $|\mathcal{H}| \in \{3, 5, 7\}$. The obtained results are presented in Figures 47(a)-(d). For brevity, only plots pertaining to Phase A are shown; entirely analogous results were obtained for the remaining phases.

The ROT curves in Figure 47(a) suggest that increasing the number of clusters further mitigates overvoltages at the critical node and its neighbours, as can be seen at the vicinity of $z = 83$. However, this assertion does not generalize to all nodes. In fact, $|\mathcal{H}| = 3$ has the smallest T_H in the majority of the nodes. On the other hand, Figure 47(b) indicates that higher $|\mathcal{H}|$ dramatically increases the occurrence of undervoltages. As seen from Figure 47(c), such results imply a worsening of the MVV curve for increasing $|\mathcal{H}|$, which is in accordance with the objective function behaviors displayed in Figure 47(d).

Such phenomenon suggests that augmenting the number of clusters increases control instability, which in turn leads to worse performance. This can be further inferred from

Figure 47 – Obtained results for Part 3 of the VC case study.

Explanatory note: The results are comprised of (a) ROT, (b) RUT, (c) MVV at Phase A and (d) objective function plots. The plotted curves are identified as follows: three clusters (dotted line, green), five clusters (alternated tracing line, blue) and seven clusters (solid line, red).

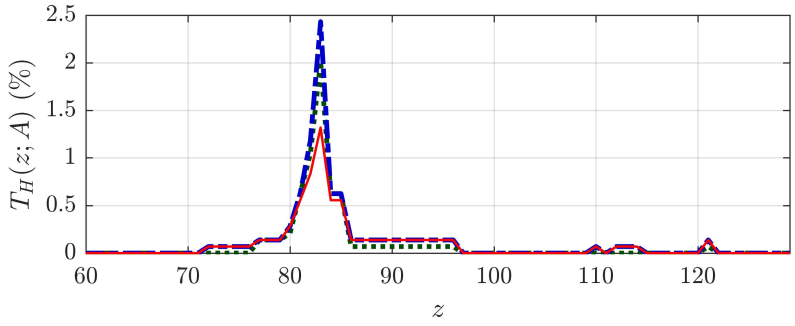

(a) Relative overvoltage times at Phase A.

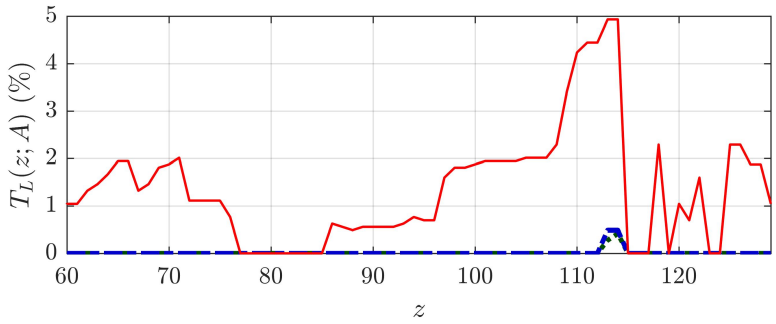

(b) Relative undervoltage times at Phase A.

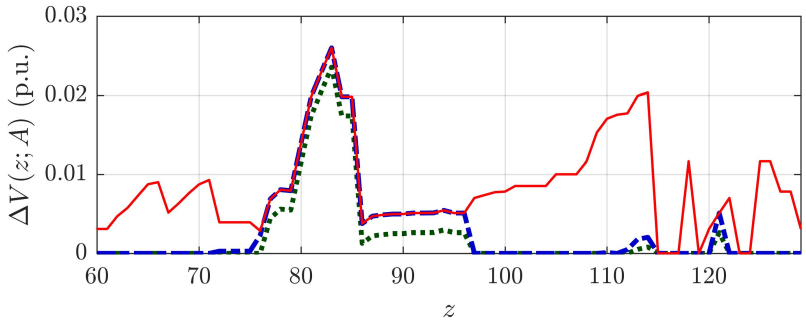

(c) Maximum voltage violations at Phase A.

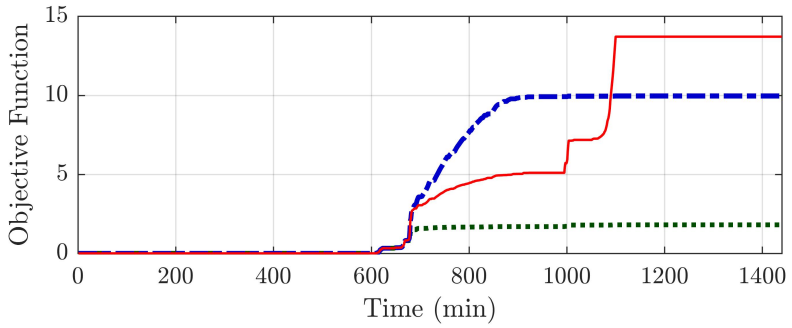

(d) Time plot of objective functions.

Source: The author.

Figure 47(d), where the objective function for $|\mathcal{H}| = 7$ is seen to increase for $n > 1000$, which corresponds to undervoltages caused by the combination of decreased PV generation and voltage overcompensation (via excessive reactive power consumption) triggered by overvoltages during peak PV generation. Hence, at least for the considered IEEE 123-bus feeder, it can be concluded that using fewer clusters yields superior VC.

6.5.6 Comments on Implementation Feasability

Some concluding comments on implementation feasability of the proposed method are now given. As for all decentralized VC approaches, the proposed method requires communication infrastructure which is not common in grids which have not begun or are just starting their transition to the smart grid framework [186]. Hence, implementation could be hindered if the utility is not willing to commit human resouces and investments towards acquiring and adapting communications equipment to the desired VC application [187].

Assuming required communication resources are available, feasability of the proposed method compares favorably against most decentralized methods since, as was discussed in Sections 6.1 and 6.4, it does not require online optimization. Each zone controller can be implemented directly via closed-form control laws, for which reason high processing power is *not* required. Contrariwise, considerable processing may be needed for the OPF-based methods in which optimization problems must be continuously solved for computing RPS. It is also worth noting that even the offline computation of the control laws is not resource-intensive, since the use of JESP with low $|\mathcal{H}|$ and n_f, as pointed out in Sections 6.3 and 6.4, yields fast solving of C-POMDP planning. In fact, it is worth mentioning that the execution of JESP for $|\mathcal{H}| = 7$ in Section 6.5.5 required approximately 7 minutes in a 2.7 GHz quad-core laptop. On the other hand, the $|\mathcal{H}| = 3, 5$ cases took less than one minute of execution time in the same computer.

We also assert that the proposed method may be more reliable than [171, 172] under communication failures. Let some node $s \in \mathcal{S}$ present a failure in its link to the zone controller and consider the implications for each method. Regardless of which node fails, method [171] incurs in error because its control law depends on the sum of all PV output powers. Contrariwise, an error occurs in the proposed method only if the failing node is that with maximum or minimum voltage in its control zone, as seen Equation 6.11.

Now, if the failing node happens to be the node with highest voltage in its zone, the distress signal heuristic from [172] will fail until the second node with highest voltage trespasses V_h, which may happen when the first node is already subject to severe overvoltage. It is also true that the proposed method would not detect overvoltage at the failing node, but it could still compensate the zone RPS correctly since the C-POMDP policy considers agent status probabilistically. For instance, if a previous overvoltage had been properly detected and is still stored in the zone controller *observation history* (whose timespan of

n_f samples), the controller may compensate for overvoltage even if the *current* observation does not indicate overvoltage. Finally, analogous considerations apply for the proposed method if the failing node is undergoing an undervoltage problem. On the other hand, method [172] does not incorporate undervoltage compensation measures at all.

6.6 Conclusion

A novel method for the decentralized voltage control of grid-tied PV generators via inverter reactive power support has been proposed. To this end, a C-POMDP model specialized to the PV voltage control problem, called DRS-C-POMDP, was introduced. To the best of our knowledge, this work is the first attempt at applying cooperative MDP to the decentralized control of inverter reactive support. The main feature of the proposed method is computation of policies by means of an heuristically specified planning problem, which avoids high computational complexity associated to C-POMDP learning and thus enables real-time control via closed-form rules. The proposed method was validated by means of a simulation case study considering the IEEE 123-bus feeder, whose results suggest it has superior performance to other recent heuristic decentralized methods.

7 Double Pilot Node Decentralized Voltage Control for Droop-Type PV Generators

7.1 Introduction

The increase of photovoltaic (PV) penetration in distribution grids has brought new challenges with regard to ensuring adequate power quality during regular operation. In this context, one of the most significant problems is that of regulating the grid voltage profile in the presence of intense PV generation. Despite the high R/X ratio in distribution making voltages less manageable via reactive power control, leveraging the distributed PV inverters for providing ancillary reactive power compensation is still considered a relevant alternative for carrying out voltage control (VC) [188]. Such approach is of particular importance since effective usage of reactive power capabilities of the distributed PV inverters enables the power utility to defer grid reinforcements which would be otherwise required for accomodating the current level of PV penetration [144]. Hence, this topic has received considerable attention in the recent literature, with a wide variety of VC methods based on PV inverter reactive power support being proposed under the different frameworks of local, centralized, distributed and decentralized control [153].

The *local* VC methods [159–162, 189] are those in which each PV inverter reactive power setpoint (RPS) is controlled solely from local voltage measurements. Such a control framework is the simplest since it does not require communication between grid buses that host PV generators. However, it has the major disadvantage of not ensuring reasonable control of the global voltage profile. The classical local-type method is droop reactive power compensation, which is still widely used in practice due to its ease of implementation [189]. On the other hand, modern methods usually carry out real-time optimization at each PV inverter for controlling their associated RPSs individually [159–162].

Contrariwise, *centralized* VC methods [154–157, 190] subject all PV inverters to being dispatched by a central agent, i.e., a distribution system operator (DSO). As a general rule, such methods consist in designing an optimal power flow (OPF) problem in terms of grid voltages and solving it by means of real-time optimization. Since the DSO processes voltage measurements from all generators, centralized control is able to approach close-to-optimal performance. On the other hand, this control framework is disadvantageous in that it requires an elaborate communications infrastructure so that direct transmission between each PV inverter and the DSO can be carried out. Furthermore, sequentially solving OPFs in real time requires high processing capability to be available at the DSO. Such stringent requirements may lead centralized VC to be infeasible in practice.

A compromise between the local and centralized VC methods can be obtained via *distributed* control [166–168]. This VC framework focuses, in general, on alleviating the processing and communication requirements of centralized control by solving OPFs distributively. This is carried out by partitioning the global OPF into smaller subproblems that can be solved locally by the PV inverters, which are only required to communicate with neighboring buses for acquiring the data needed for solving their associated OPFs. Despite its reduction in processing capability requirements, it can be argued that distributed VC may still require a very costly communication infrastructure since a relatively complex mesh network spanning all inverters is required. As a further disadvantage of distributed VC, it is known to be prone to slow convergence of the global OPF [153].

Similarly to distributed VC, the *decentralized* framework [158, 163–165, 169–172, 191–199] can be used to reduce complexity in comparison to centralized methods. The overall strategy of decentralized VC consists in partitioning the grid into voltage control zones (VCZ), wherein PV inverters are controlled by a zone controller (ZC) to which they are connected through a simple star-topology network. In most cases, the ZC use real-time optimization or heuristics for controlling their respective VCZ. Regardless of which approach is used, the processing burden is known to be lower than that of distributed VC and have better convergence properties [153].

7.1.1 Related Works

The above discussion shows that decentralized control is of practical interest since, among the non-local control frameworks, it requires the simplest communication network and offers better convergence. However, it is also clear that most decentralized methods in the literature impose further implementation requirements that increase complexity. To further elaborate on this, a systematic review of recent decentralized VC methods is provided in Table 12, where it is identified whether each method requires real-time optimization (RTO), heuristic control (HC) or zone controller coordination (ZCC).

From Table 12, it is seen that most decentralized methods imply at least one of the following: (a) real-time optimization at each ZC; (b) heuristics-based control at each PV inverter; and (c) ZC cooperation. The resources for implementing such requirements are high-capability processors, programmable controllers and an upper-level ZC network, respectively. In distribution practice, most PV inverters simply use local droop control [189]. Hence, acquiring the aforementioned resources would further increase the cost of transitioning to decentralized VC. In this sense, from an economic viewpoint, it is of interest to eliminate additional requirements and thereby keep investment at the bare minimum, which consists in implementing the star-topology networks in each VCZ.

It is thus clear that the literature on decentralized VC mostly lacks methods that are *directly compatible with the legacy droop compensators used by PV inverters*, which is an

Table 12 – Literature review of decentralized VC methods and their requirements

Ref.	RTO	HC	ZCC	Description
[156]	Yes	Yes	No	The grid is broken down into VCZ via ϵ-decomposition and an optimization problem is attributed to each zone for minimizing squared voltage deviations. Each optimization is solved heuristically by means of a genetic algorithm.
[161]	Yes	Yes	No	A loss minimization problem with voltage constraints is attributed to every grid VCZ, each of which is solved heuristically via particle swarm optimization.
[162]	Yes	No	No	The VCZ are controlled independently via linear programming optimization for minimizing reactive power injection minimization with voltage constraints.
[163]	Yes	No	No	An optimization problem that minimizes the sum of squared voltage deviations is formulated and decomposed into subproblems that are solved at each VCZ.
[167]	Yes	No	Yes	A global optimal power flow (OPF) problem with voltage constraints is considered. The OPF formulation is periodically updated via voltage feedback from selected nodes of each VCZ for optimizing performance.
[168]	Yes	No	Yes	A two-layer approach is used in which intra-VCZ and inter-VCZ optimization problems are solved for achieving fast and slow timescale control, respectively. The adopted formulation minimizes power losses with voltage constraints.
[169]	Yes	No	Yes	An agent-based method is proposed that assigns, to each zone controller, an objective function which accumulates squared voltage deviations and line current magnitudes. Each agent, aided by coordination with the remaining ones, minimizes its objective via gradient-based optimization.
[170]	Yes	No	Yes	An optimal reactive power flow (ORPF) problem with voltage constraints is formulated and solved via duality-based optimization with coordination of grid nodes, each of which acts as a decentralized ZC of its neighboring nodes.
[189]	Yes	No	Yes	An OPF with voltage constraints is solved via dynamic synthesis and setpoint adjustment of inverter controllers, which is carried out via dual subgradient optimization with the aid of coordination between PV inverters and the DSO.
[190]	Yes	No	Yes	The alternating direction method of multipliers is employed to solve an OPF with reactive power constraints and whose objective function is the sum of squared voltage deviations of all grid nodes. To achieve decentralized control, the OPF is divided into subproblems associated to grid VCZ.
[191]	No	Yes	No	The framework of Markov Decision Processes (MDP) is used for carrying out grid VC. A MDP model is specified whose decentralized agents are first trained offline and subsequently applied to real-time control. Each agent is associated to one PV inverter and uses its local voltage to decide on whether its reactive power setpoint should be incremented or decremented.

Literature review of decentralized VC methods and their implementation requirements (cont.)

Ref.	RTO	HC	ZCC	Description
[192]	No	Yes	No	A manual control zone selection is carried out according to the criterion that each VCZ should have a single OLTC. Then, intra-zone control is carried out via heuristic reactive power control equations that take into account PV inverter and OLTC interactions.
[193]	No	Yes	No	A decentralized approach is proposed in which all PV inverters share their voltage deviations and the largest one is used for deciding whether reactive power injection should be employed for voltage regulation or loss reduction. Heuristic equations for each of these functions are given.
[194]	No	Yes	No	During regular system operation, PV inverters are maintained in local control mode. When a voltage violation is detected at any node of a given VCZ, it emits a distress signal and all inverters in its zone increment their reactive power setpoints until the voltage violation is eliminated.
Ch. 6	No	Yes	Yes	An heuristic cooperative MDP model is proposed for carrying out agent-based decentralized VC. The model parameters are attributed according to expected control behavior and it is solved offline via Nash equilibrium. Obtained RPS control policies are then used for real-time control.
[195]	No	No	Yes	Demand response controllers are specified for regulating active and reactive power demands of loads in terms of PV generation. Control decentralization is achieved by means of low bit rate communications between the controllers.
[196]	No	No	Yes	The PV inverters are assumed to have reactive power PI controllers. Intra-VCZ control is carried out so that PV nodes with greater reactive power capacity are dispatched first. At a higher level, VCZ coordination is used to adapt the control zones if grid topology changes occur.
[197]	No	No	No	An electrical distance metric is used to select, in each VCZ, a pilot node that best represents the average zone voltage. Subsequently, *any* reactive power compensation mechanism (including droop control) can be applied to such nodes, which are followed by their subordinate nodes.
Prop.	**No**	**No**	**No**	We generalize the approach from [197] by using two pilot nodes per VCZ, which are statistically selected as those that best represent maximum and minimum zone voltages. The pilot node which incurs greater voltage violation is used for controlling VCZ reactive power injection.

Source: The author.

interesting feature due to enabling easier implementation. A notable exception is the work of Di Fazio et al. [199], where the *pilot node* concept is introduced. It consists in selecting, for each VCZ, a node that best represents the average zone voltage. Then, each VCZ takes its pilot node voltage as the control variable and can be controlled independently (i.e., without coordination) via any VC method, *including* droop compensation.

We note that, despite its ease of implementation, the pilot node approach may lead to inadequate VC performance when the grid is approaching (or already at) overvoltage status. In fact, its response to overvoltages is prone to delay because the pilot nodes always tend to have smaller voltages than the maximum voltage of their respective VCZ.

7.1.2 Contributions

Taking the previous considerations into account, this Chapter contributes a novel decentralized VC method that is optimization-free, does not require VCZ cooperation and outputs a voltage signal that can be fed to standard droop compensators, thereby being directly compatible with legacy PV inverter reactive power controllers. The proposed method uses a new *double pilot node* concept. It generalizes the pilot node approach by selecting *two* nodes per VCZ that best represent *maximum and minimum zone voltages* (instead of average voltage), which significantly improves VC response while maintaining the practicality of pilot node control.

7.2 Modeling and Problem Statement

The exact same problem statement and modeling approach used in Chapter 6 are considered, with the exception that noise in the intra-VCZ communication links is now considered. Hence, for the sake of avoiding repetition, only noise modeling is described in what follows and the reader is referred to Section 6.2 for considerations on power system modeling and the adopted VC problem statement.

7.2.1 Communication Noise

Recall that decentralized VC uses one star-topology network per VCZ for connecting the PV inverters to their associated ZC. In this sense, it is relevant to evaluate VC performance when communication is noisy. The adopted noise model is now described.

Since each ZC must broadcast to all of its subordinate PV inverters, transmission power must be relatively high and noise is thereby ignored for broadcast. On the other hand, it is assumed that the PV inverters employ low-power wireless transmission via direct sequence spread spectrum (DSSS) modulation. For the sake of simplicity, uncoded DSSS with binary phase shift keying (BPSK) carrier modulation and a receiver with coherent

demodulation are assumed. Hence, it is considered that the communication link is designed for a given coherent-BPSK bit error rate (BER) given by $P_b = Q(\sqrt{2E_b/J_o})$, where E_b is energy per bit, $2J_o$ is the equivalent white Gaussian noise power after demodulation of the DSSS signal and $Q(\cdot)$ is the Gaussian Q-function [200].

Now, in order to contemplate the worst-case scenario, it is further assumed that the communication links are subjected to pulse interference due to jamming by a malicious external agent. Hence, the actual BER is $P_b' = 0.083/(E_b/J_o)$ [200], where E_b/J_o is the value obtained from the designed P_b (i.e., the BER value without jamming).

It should be noted that noise has been specified directly in terms of E_b/J_o so that the DSSS modulation spreading factor L_c and the specific narrowband interference characteristics can be abstracted from analysis. In fact, $E_b/J_o = 2L_c \cdot \mathrm{SNR}_{av}$, where SNR_{av} is the narrowband signal-to-interference ratio. Hence, for any L_c and narrowband interference which yield a constant product $L_c \cdot \mathrm{SNR}_{av}$, analysis can be carried out in terms of an equivalent white Gaussian noise power $2J_o$ [200].

7.3 Proposed Method

In this Section, the proposed decentralized VC method is presented. It consists in, at first, using a clustering procedure based on voltage sensitivity data to obtain a previously specified number of VCZ. Then, a straightforward statistical approach is used for selecting a pair of pilot nodes which serve as reference for controlling each VCZ. At last, ZC are proposed which do not require VCZ coordination and whose outputs can be directly used to drive the PV inverter droop compensators.

7.3.1 Selection of VCZ

For decentralized reactive power support, the grid must be partitioned into VCZ according to the correlation between bus voltages with respect to reactive power injections, as has already been discussed in Chapter 6. Hence, the same clustering approach considered in Section 6.4.2 is used for VCZ selection. For clarity, recall the sensitivity metric:

$$\Gamma_{ij}^{rs} = \frac{\partial [V_i^r]^2}{\partial Q_j^s} = 2V_i^r \frac{\partial V_i^r}{\partial Q_j^s} \tag{7.1}$$

where Γ_{ij}^{rs} is the sensitivity of V_i^r with respect to Q_j^s. We further note that it is usual to consider squared voltage magnitudes, as in Equation 7.1, so that sensitivities are consistent with the voltage control objective function, which often involves squared voltages [181], as is the case for the adopted objective function in Equation 6.6.

Let $\mathbf{\Gamma} = [\Gamma_{ij}^{rs}]_{NP \times NP}$, $i, j \in \mathcal{I}$ and $r, s \in \Phi$. In this notation, indices (i, j) precede (r, s) in element ordering. As discussed in Section 6.4.2, to estimate the voltage sensitivities,

it suffices to perform a single load flow simulation (in which PV generation can be disregarded for simplicity) to obtain $\boldsymbol{L} = [\partial_{V_j^s} Q_i^r]_{NP\times NP}$, $i, j \in \mathcal{I}$ and $r, s \in \Phi$. Then, it is straightforward that $\Gamma_{ij}^{rs} = 2V_i^r \gamma_{ij}^{rs}$, where $\boldsymbol{\gamma} = \boldsymbol{L^{-1}}$.

In order to cluster grid buses and generate the VCZ, voltage sensitivities must be converted to a dissimilarity metric. To this effect, as in Chapter 6, the following metric is employed, which is proven in [180] to constitute a distance metric:

$$d_{ij}^{rs} = -\ln\left(\frac{\Gamma_{ij}^{rs}\Gamma_{ji}^{sr}}{\Gamma_{ii}^{rs}\Gamma_{jj}^{rs}}\right) \tag{7.2}$$

where d_{ij}^{rs} is the electrical distance between phase r of bus i and phase s of bus j. We have proved in Appendix B that, due to phase symmetry in power grids, $\Gamma_{ij}^{rr} \leq \Gamma_{ij}^{rs}$ and therefore clustering can be carried out for each phase separately by using Equation 7.2 with $r = s$. Hence, for each $r \in \Phi$, the metrics $d_{ij}^{r} \triangleq d_{ij}^{rr}$ are taken as input to HAC [182]. The outputs of this algorithm are the VCZ computed for some value of dissimilarity threshold. To obtain the desired number of VCZ, such threshold is adjusted while iterating HAC.

Remark 7.1: In practice, phase symmetry ensures that the aforementioned procedure results in identical clustering for all phases. Hence, for simplicity in notation, it is henceforth assumed that VCZ are identical $\forall r \in \Phi$.

7.3.2 Double Pilot Node Selection

Consider that H VCZ have been defined, which are henceforth denoted by $\mathcal{V}_i \subset \mathcal{I}$, $i = 1, 2, \ldots, H$. The VCZ are a partition of $\mathcal{I}$, i.e., $\cup_{i=1}^{M} \mathcal{V}_i = \mathcal{I}$ and $\mathcal{V}_i \cap \mathcal{V}_j = \emptyset$, $i \neq j$. The original pilot node concept proposed in the work by Di Fazio et al. [199] proceeds by selecting, for each $\mathcal{V}_i$, a single bus $\tilde{z}_i \in \mathcal{V}_i$ which, according to some criterion, best represents an *average* of the bus voltages in $\mathcal{V}_i$. Then, voltage measurements at the selected $\tilde{z}_i$, $i = 1, 2, \ldots, H$, are used as inputs to the decentralized VC process.

In a different manner, a *double* pilot node approach is now proposed. For each VCZ, two buses $\{\hat{z}_i, \check{z}_i\} \in \mathcal{V}_i$ shall be selected as VC references. Instead of focusing on average voltages, $\hat{z}_i$ and $\check{z}_i$ are taken as those buses which, in a statistical sense, best represent *maximum* and *minimum* voltages in $\mathcal{V}_i$, respectively.

To select such nodes, a simple Monte Carlo-type statistical approach is adopted. Counters $\hat{c}_i$ and $\check{c}_i$, $i \in \mathcal{I}$, are associated to each grid bus with null starting values. The power grid is simulated L times with random allocation of PV generation and *no* PV reactive support. When a simulation is terminated, the bus in each VCZ which presents the largest (smallest) voltage magnitude has its counter $\hat{c}_j$ ($\check{c}_j$) incremented by one. After

the L iterations are carried out, the pilot nodes are given by:

$$\hat{z}_i = \text{argmax}_{j \in \mathcal{V}_i} \hat{c}_j \tag{7.3}$$

$$\check{z}_i = \text{argmax}_{j \in \mathcal{V}_i} \check{c}_j \tag{7.4}$$

where $i = 1, 2, \ldots, H$.

The above-described double pilot node concept is the main innovation of this Chapter. By monitoring the nodes associated to maximum and minimum zone voltages, each ZC can more rapidly detect and compensate voltage deviations than if only average voltages were being assessed. Clearly, the detection delay of the original pilot node method [199] is due to the fact that average voltage may be a poor representation of a grid zone with significant voltage variance between its nodes.

7.3.3 Optimization and Coordination-Free Droop-Compatible Voltage Control

Given the VCZ and their associated pilot nodes, it remains to specify the VC scheme itself. Now, recall the restrictions imposed in this Chapter: only droop reactive power compensation is available locally at the PV inverters, processing capability for carrying out optimization is unavailable and there is no higher-level coordination between VCZ. Hence, the only available resources are voltage measurements of the pilot nodes and the star networks internal to each VCZ.

We further assume all PV inverter droop compensators use the same reference voltage V_o. The following VC scheme is proposed which complies with the aforementioned restrictions. At each sample time $t = nT$ and for each $r \in \Phi$, the ZC of $\mathcal{V}_i$, $i = 1, 2, \ldots, H$, acquires $V^r_{\hat{z}_i}$ and $V^r_{\check{z}_i}$, i.e., the pilot node voltage measurements. Then, it computes the following voltage deviation metrics:

$$\Delta \hat{V}^r_i = \max\left(V^r_{\hat{z}_i} - V_o, 0\right) \tag{7.5}$$

$$\Delta \check{V}^r_i = \max\left(V_o - V^r_{\check{z}_i}, 0\right) \tag{7.6}$$

where the operator $\max(\cdot, 0)$ is used so that voltages smaller (greater) than V_o are not considered as negative overvoltages (undervoltages). At last, if $\Delta \hat{V}_i \geq \Delta \check{V}_i$, the ZC transmits $V^r_{\hat{z}_i}$ as input to all droop compensators in $\mathcal{V}_i$, whereas $V^r_{\check{z}_i}$ is transmitted otherwise.

Hence, the proposed decentralized VC scheme consists in controlling the RPS vectors $\boldsymbol{\alpha_i}[n]$ in order to modulate reactive power injection at the PV buses as follows:

$$\alpha^r_{\mathcal{V}_i}[n] = \frac{V^r_{\hat{z}_i}[n] - V_o}{V_h - V_o} \cdot u\left(\Delta \hat{V}^r_i[n] - \Delta \check{V}^r_i[n]\right) + \frac{V^r_{\check{z}_i}[n] - V_o}{V_o - V_l} \cdot u\left(\Delta \check{V}^r_i[n] - \Delta \hat{V}^r_i[n]\right) \tag{7.7}$$

where $u(\cdot)$ is the unit step function and $\alpha^r_{\mathcal{V}_i}$ denotes the RPS of phase r at all buses which belong to $\mathcal{V}_i$. For clarity, recall that $\alpha^r_i[n]$ is the component of $\boldsymbol{\alpha_i}[n]$ pertaining to phase r.

Algorithm 5 Double pilot decentralized voltage control

Input: $\mathbf{\Gamma}$, $\mathcal{I}$, H, V_o, V_l, V_h.
Output: $\boldsymbol{\alpha_i}[n]$, $i \in \mathcal{I}$, $n \in \mathbb{N}^*$.

$J, \hat{c}_j, \check{c}_j \leftarrow 0$, $j \in \mathcal{I}$.
$\phi \leftarrow$ Any phase from set Φ.
{*Grid partitioning into VCZ*}
Use $\mathbf{\Gamma}$ to compute the distance metrics d_{ij}^{rs} with (8).
while $J \neq H$ **do**
  Adjust hierarchical clustering dissimilarity threshold.
  Perform hierarchical clustering with the d_{ij}^{rs} as input.
  return $\mathcal{V}_j$, $j = 1, 2, \ldots, J$.
end while
{*Double pilot node selection*}
for $i = 1, 2, \ldots, L$ **do**
  Simulate grid power flow.
  $j \leftarrow \text{argmax}_{k \in \mathcal{I}} V_k^{\phi}$
  $\hat{c}_j \leftarrow \hat{c}_j + 1$
  $j \leftarrow \text{argmin}_{k \in \mathcal{I}} V_k^{\phi}$
  $\check{c}_j \leftarrow \check{c}_j + 1$
end for
Define pilot nodes according to Equations 7.3 and 7.4.
{*Real-time voltage control*}
for $n \in \mathbb{N}^*$ **do**
  for $r \in \Phi$ **do**
    At each ZC, compute $\Delta\hat{V}_i^r$ and $\Delta\check{V}_i^r$ and transmit the voltage associated to the largest of these signals (i.e., either $V_{\hat{z}_i}^r$ or $V_{\check{z}_i}^r$) to all subordinate PV nodes.
    At each of the aforementioned PV nodes, use the received voltage signal as input to the droop reactive power controller of phase r.
  end for
end for
return $\boldsymbol{\alpha_i}[n]$, $i \in \mathcal{I}$, $n \in \mathbb{N}^*$.

Source: The author.

We emphasize that Equation 7.7 is an analytical representation of a two-step control process. First, metrics $\Delta\hat{V}_i^r$ and $\Delta\check{V}_i^r$ are computed and the voltage associated to the largest one is transmitted as the control signal to all PV inverters in $\mathcal{V}_i$. Then, each inverter of the VCZ uses the received signal to adjust its RPS via its droop controller.

From the above discussion, it is clear that the proposed method has autonomous operation of all VCZ, since no ZC coordination is required. Also, compatibility with droop control is ensured by the fact that a voltage magnitude signal is fed to the PV inverters. At last, real-time optimization routines are dispensed with by simply enforcing PV inverters in a given VCZ to use their reactive power capacities in equal proportions, as seen from Equation 7.7. This approximate approach is reasonably accurate due to the fact that buses in the same VCZ hold high correlations between their voltages.

Figure 48 – Control diagram of the proposed VC method for a given phase r.

Explanatory note: In (a), the ZC identifies the relative status between VCZ voltage deviations, which is indicated by the auxiliary binary variable β. Then, as depicted in (b), the droop characteristic of all PV inverters in the VCZ take V_{in} as their input signal, which is the voltage corresponding to the largest deviation ($V^r_{\hat{z}_i}$ or $V^r_{\check{z}_i}$).

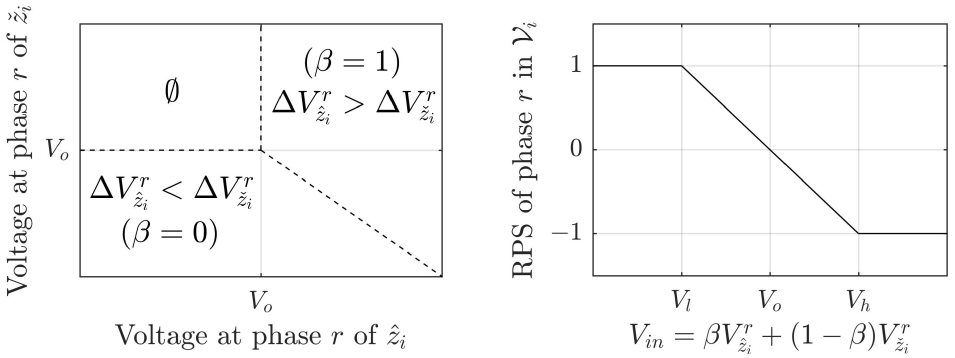

(a) Comparison of voltage deviations. (b) Droop characteristic with input V_{in}.

Source: The author.

It is worth noting that Equation 7.7 implies a droop characteristic without voltage deadbands, i.e., reactive power compensation is carried out for any deviation with respect to V_o. In general, any deadband around V_o could be adopted based on whether a more or less liberal use of PV inverter reactive reserves is desired. Since the focus of this Chapter is a general evaluation of the proposed method without taking into account more detailed design considerations, the droop curve with no deadbands in Equation 7.7 is assumed.

For further illustration, the proposed VC method is presented in pseudocode form in **Algorithm 5** and illustrated by means of a control diagram in Figure 48.

7.4 Simulation Experiments

To validate the proposed VC approach, multiple simulations in the IEEE 123-bus feeder are carried out. First, its performance is compared to those of standard local droop control [189] and decentralized droop control using the pilot node approach from [199]. Then, two performance assessments of the proposed method are carried out in terms of selected VCZ number and communication link noise. At last, a sensitivity analysis with regard to the grid R/X ratio and maximum power angle θ_o (see Section 6.2.2) is carried out. All simulations have been implemented in MATLAB R2017a.

7.4.1 Description of Simulation Parameters

The same data and simulation approach considered in Chapter 6 are used, for which reason the reader is referred to it for detailed discussion. The only exceptions are that, for the sake of not repeating all simulation parameters from Chapter 6, $|\mathcal{S}| = 50$, $\theta_o = \arccos(0.95)$ and a new randomly generated $\mathcal{PQ}$ set with 500 load profiles are now considered. Furthermore, a voltage reference $V_o = 1$ p.u. is used by the droop compensators and $L = 1000$ iterations are used for double pilot node selection. At last, since a simulation in which the grid R/X ratio is varied will be performed, it is worth recalling that the base IEEE 123-bus system has $R/X \approx 0.5$ in most of its branches [201, 202].

Remark 7.2: As in Chapter 6, the on-load tap changing transformers (OLTCs) have been abstracted from analysis since this Chapter focuses solely on evaluation of fast-timescale VC. In future investigations, the author intends to study coordination of the proposed VC approach with the slower timescale required by OLTCs in each VCZ.

7.4.2 Performance metrics

To assess VC performance, the following metrics are considered:

$$F[n] = \sum_{i=0}^{n} \sum_{k \in \mathcal{N}} \left(\psi(\boldsymbol{V_k}[i] - V_h \mathbf{1}) + \psi(V_l \mathbf{1} - \boldsymbol{V_k}[i]) \right) \tag{7.8}$$

$$\Delta V(z, \phi) = \max_{n \leq n_{\mathcal{T}}} \left[\psi(V_z^{\phi}[n] - V_h) + \psi(V_l - V_z^{\phi}[n]) \right] \tag{7.9}$$

$$\Delta \hat{V}(\phi) = \max_{z \in \mathcal{I}} \Delta V(z; \phi) \tag{7.10}$$

$$T_h(z, \phi) = \frac{1}{n_{\mathcal{T}} + 1} \sum_{n=0}^{n_{\mathcal{T}}} \left[u(V_z^{\phi}[n] - V_h) + u(V_l - V_z^{\phi}[n]) \right] \tag{7.11}$$

$$\hat{T}_h(\phi) = \max_{z \in \mathcal{I}} T_h(z; \phi) \tag{7.12}$$

$$\hat{\Xi}(\phi) = \max_{n \leq n_{\mathcal{T}}} \frac{\sum_{z \in \mathcal{I}} \alpha_z^{\phi}[n] P_z^{(G_o, \phi)}}{\sum_{z \in \mathcal{I}} P_z^{(G_o, \phi)}} \tag{7.13}$$

where $F[n]$ is the objective function over time, $\Delta V(z, \phi)$ is the maximum voltage violation (MVV) at phase ϕ of bus z, $\Delta \hat{V}(\phi)$ is the peak MVV at phase ϕ over all buses, $T_h(z, \phi)$ is the relative violation time (RVT) at phase ϕ of bus z, $\hat{T}_h(\phi)$ is the peak RVT at phase ϕ over all buses, $\hat{\Xi}(\phi)$ is the peak reactive capacity usage (PRCU) at phase ϕ and $P_z^{(G_o, \phi)}$ denotes the component of $\boldsymbol{P_s^{(G_o)}}$ relative to phase ϕ.

Remark 7.3: We note that the PRCU metric evaluates the maximum utilization of joint reactive power reserves of all PV inverters at phase ϕ. To obtain Equation 7.13, observe that, at phase ϕ of bus z, the reserve is $\tan\theta_o \cdot P_z^{(G_o, \phi)}$ and injection at time n is given by $\tan\theta_o \cdot \alpha_z^{\phi}[n] P_z^{(G_o, \phi)}$. Hence, dividing the sum of reactive power injections for all $z \in \mathcal{I}$ by the sum of reactive power reserves for all $z \in \mathcal{I}$, the $\tan\theta_o$ factor cancels out and Equation 7.13 is obtained. Clearly, $0\% \leq \hat{\Xi}(\phi) \leq 100\%$.

Figure 49 – Obtained results of the first droop-type VC simulation experiment.

Explanatory note: The results consist of (a) MVV at phase A, (b) MVV at phase B, (c) MVV at phase C, (d) RVT at phase A, (e) RVT at phase B, (f) RVT at phase C, (g) PRCU at each phase, (h) time plots of the objective function and (i) time plots of voltage at phase C of bus $z = 83$. The plotted curves are identified as follows: no VC (dotted line, green), local droop VC (alternated tracing line, red), pilot node droop VC (traced line, blue) and proposed method (solid line, black).

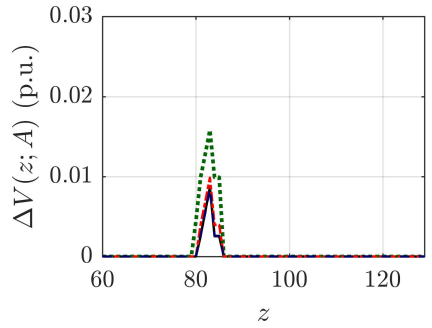

(a) MVV at phase A.

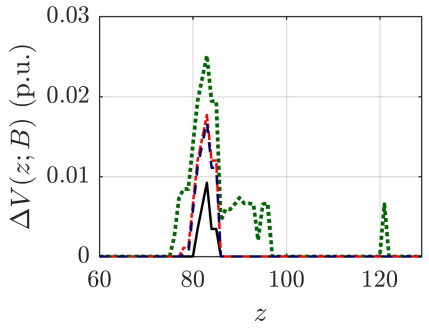

(b) MVV at phase B.

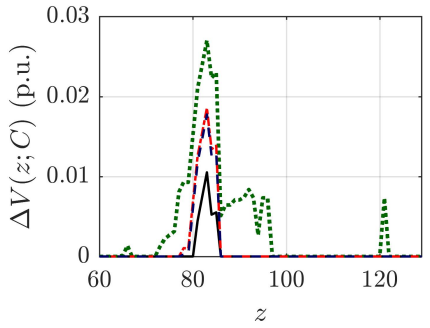

(c) MVV at phase C.

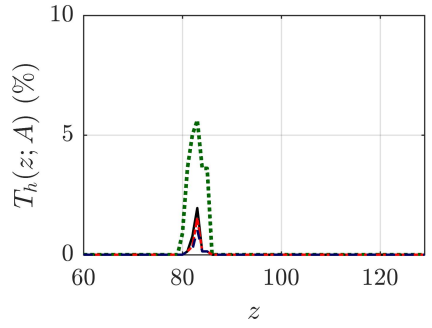

(d) RVT at phase A.

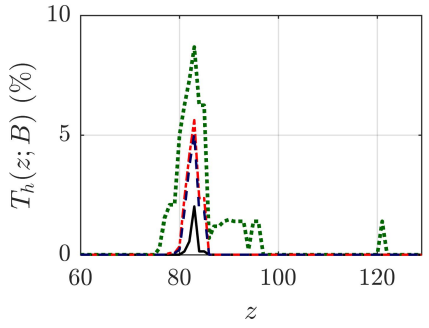

(e) RVT at phase B.

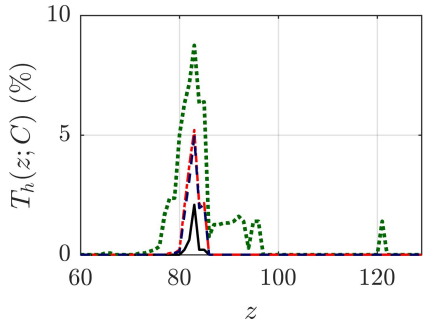

(f) RVT at phase C.

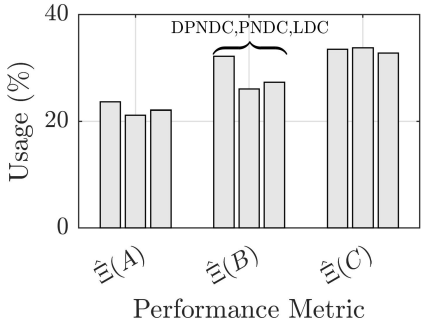

(g) Peak reactive usages.

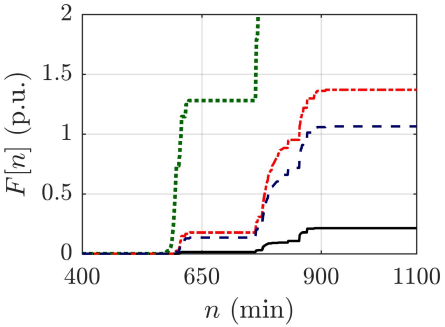

(h) Objective function plots.

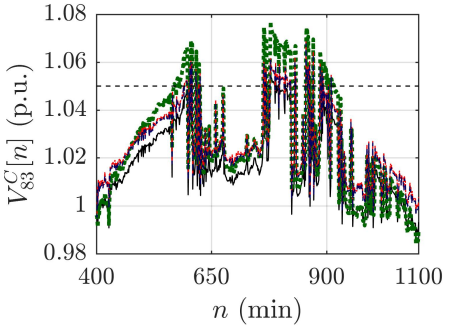

(i) Voltages at $z = 83$, $\phi = \text{C}$.

Source: The author.

7.4.3 Comparison to Other Droop-Based Methods

To validate the double pilot node droop control (DPNDC) proposed in this work, its performance is compared to those yielded by the standard local droop control (LDC) [189] and the pilot node droop control (PNDC) from [199]. The latter method has been selected for the purpose of comparison since, among the recent methods reviewed in Section 7.1, it is the only one that does not impose additional requirements (i.e., it only requires intra-VCZ networks) for achieving decentralized control, just like the proposed method.

In this simulation, $H = 3$ clusters are considered and communication noise is disregarded. Obtained results are given in Figure 49. In general, the results show that the proposed method peforms better than LDC and PNDC. This fact is particularly clear from Figures 49(a)-(f), where DPNDC is seen to yield smaller MVV and RVT for most z.

A single exception applies to the above, namely the slightly higher RVT obtained at phase A for a small number of buses. However, it can be argued that such exception actually results from a more efficient employment of reactive power reserves. In fact, note that phase A is, by far, the one with least severe voltage violations. Correspondingly, the proposed method prioritized the remaining phases, in which large RVT and MVV reductions were attained for *all* buses. This is corroborated by Figure 49(g), which shows that DPNDC injects substantially more (in a proportional sense) reactive power in *both* phases B and C in comparison to the less-critical phase A.

A succint appraisal of the superior performance yielded by the proposed method is also given in Figure 49(h), where the objective function converges to a significantly smaller value for the proposed method, when compared to the remaining ones. Note that, as could be reasonably expected, PNDC is seen to perform better than LDC.

At last, Figure 49(i) presents the time plots of voltage at the worst-performing bus-phase pair, namely $z = 83$ and $\phi = \mathrm{C}$. In particular, it is interesting to note that, when $V_{83}^{C}[n]$ is in the vicinity of V_o, the proposed method tends to follow the uncompensated voltage curve, which is not true for LDC and PNDC. This is further evidence of the more efficient usage of inverter reactive reserves by the proposed method.

7.4.4 Effects of VCZ number

Since H is a preset parameter (whose value is selected by tuning the clustering dissimilarity threshold) of the proposed method, it is important to evaluate its performance in terms of the VCZ number. To achieve this, simulation is carried out for the cases $H = 1, 2, \ldots, 10$. In order to focus solely on the assessment of VC performance as a function of H, absence of communication link noise is also assumed.

The results are presented in Figure 50 and confirm that H has, significant influence over VC performance. As expected, $H = 1$ yields particularly poor voltage regulation since

a single VCZ is unable to accurately represent the entire grid. On the other hand, it is also clear from Figure 50(a) and 50(b) that performance improvement is *not* monotonic with respect to the number of VCZ. In fact, the best results were obtained for $H = 2$.

Such phenomenon can be explained by recalling that LDC corresponds to $H = N$. Hence, as H increases, the system tends to approach LDC performance. It may thus be concluded that H must be sufficiently small so that the obtained VCZ do not approach LDC performance, yet large enough to avoid an innacurate representation of the grid.

Note that $H = 1$ leads to high PRCU despite its poor VC, which shows that inefficient usage of reactive resources occurs. Contrariwise, it is seen that $H = 2$ yields the most balanced PRCU for phases B and C, which, as discussed in Section 7.4.3, suggests a more efficient usage of reactive power compensation. All above discussions are confirmed in Figure 50(c), which shows that, at $z = 83$ and $\phi = \text{C}$, the case $H = 1$ results in long-duration and large overvoltages. On the other hand, the cases $H \geq 2$ perform much better, with $H = 2$ in particular almost suppressing voltage violations.

7.4.5 Effects of Communication Noise

In this experiment, $H = 3$ is considered and focus on assessing the performance yielded by the proposed method when the VCZ communication links are noisy. It is assumed that the measured voltage values are quantized into 8 bits in the range from 0.9 p.u. to 1.1 p.u. for transmission. Since the voltage sampling interval is low (one minute, as per Table 11 in Section 6.5.1), a high bit rate is not required. Considering that data rate is small and low-power transmission via DSSS has been assumed, a carrier frequency of 923 MHz, belonging to the Long Range (LoRa) frequency range, is adopted [203].

Three cases are considered, namely those where the system is designed for $P_b \in \{10^{-6}, 10^{-5}, 10^{-4}\}$, whose required signal-to-noise ratios are $E_b/J_o \in \{10.5, 9.5, 8.5\}$ (dB). Since it is assumed that the system to be jammed by worst-case pulse interference (see Section 7.2.1), the actual BERs for the designed E_b/J_o become $P_b' \in \{0.0079, 0.0087, 0.0098\}$.

Obtained results are presented in Figure 51, where the base noiseless case ($P_b = 0$) is also included. It is particularly clear from Figures 51(a) and 51(b) that the relatively high BER values caused by jamming introduce noticeable performance degradation: despite the PRCU being increased, voltage regulation is worsened as BER increases. This is explained by the fact that noise causes the PV inverters to set their RPSs with error, thereby missing the voltage reference V_o and inducing the system as a whole to overcompensation.

In any case, the proposed method presented relatively robust performance when subjected to a noisy environment: despite the considerable increase in PRCU and MVV due to noise, the RVT remained very close to their noiseless values. In other words, by increasing noise, performance metrics were worsened but did not diverge with respect to

Figure 50 – Obtained results of the second droop-type VC simulation experiment.

Explanatory note: The results consist of (a) peak RVT (left Y-axis), PRCU (left Y-axis) and MVV (right Y-axis), (b) time plots of the objective function and (c) time plots of voltage at phase C of bus $z = 83$, all for varying values of H.

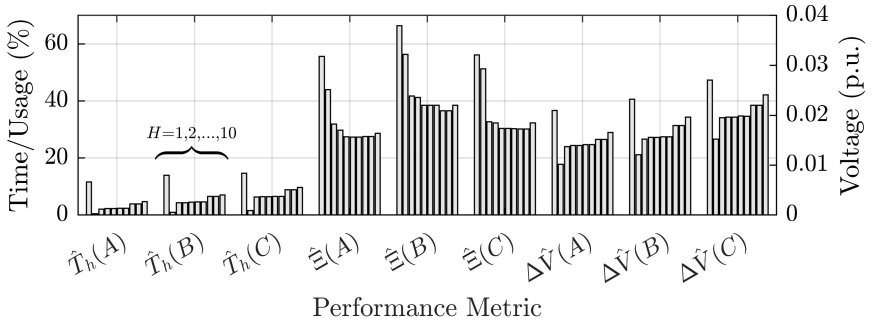

(a) Peak RVT, PRCU and MVV.

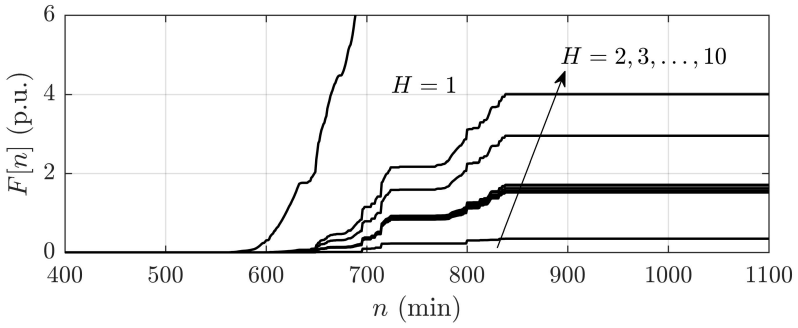

(b) Time plots of the objective function.

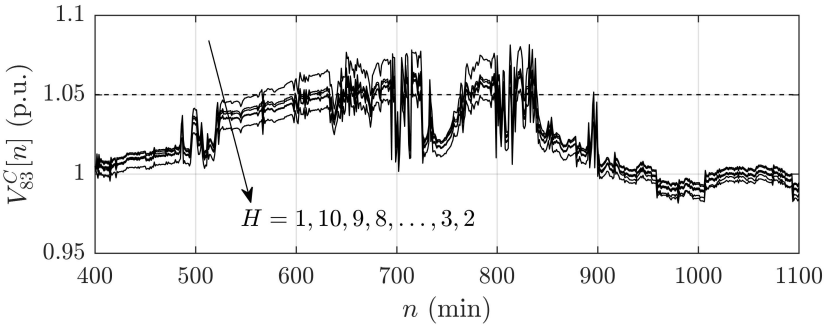

(c) Time plots of voltage at $z = 83$, $\phi = \text{C}$.

Source: The author.

Figure 51 – Obtained results of the third droop-type VC simulation experiment.

Explanatory note: The results consist of (a) peak RVT (left Y-axis), PRCU (left Y-axis) and MVV (right Y-axis), (b) time plots of the objective function and (c) time plots of voltage at phase C of bus $z = 83$, all for varying values of P_b. The plotted curves are identified as follows: $P_b = 0$ (solid line, black), $P_b = 10^{-6}$ (alternating traced line, red), $P_b = 10^{-5}$ (traced line, blue) and $P_b = 10^{-4}$ (thin solid line, magenta).

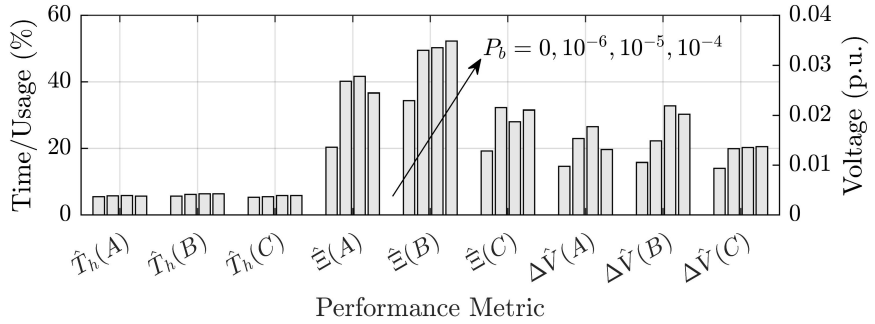

(a) Peak RVT, PRCU and MVV.

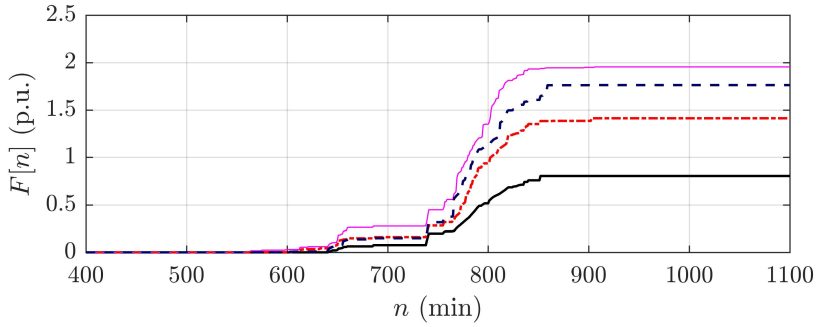

(b) Time plots of the objective function.

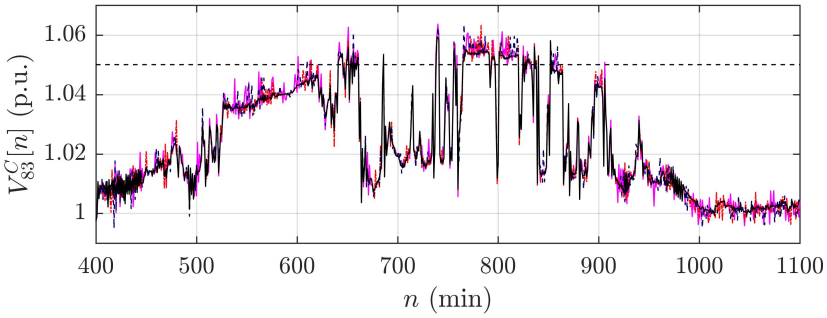

(c) Time plots of voltage at $z = 83$, $\phi = \text{C}$.

Source: The author.

the noiseless case, with voltage violations still being restricted to short time intervals, which is an indicator of robustness to noise. This analysis can be further verified in Figure 51(c), where $V_{83}^{C}[n]$ presents larger oscillations as BER increases, but voltage violations still mostly occur at instants in which the base case ($P_b = 0$) also presents violations.

7.4.6 Sensitivity Analysis With Respect to R/X Ratio and θ_o

As a final effort for validating DPNDC comprehensively, a simulation-based sensitivity analysis is considered of three performance metrics, namely MVV, PRCU and peak RVT [i.e., $\Delta\hat{V}(\phi)$, $\hat{\Xi}(\phi)$ and $\hat{T}_h(\phi)$, $\forall\phi \in \Phi$], in terms of grid R/X ratio and the maximum power angle θ_o. These parameters have been selected due to their relevant influence over the degree of voltage control attainable via reactive power support: the R/X ratio establishes how sensitive the grid voltages are to reactive power injections, whereas θ_o defines the maximum allowable injection by the PV inverters.

The analysis is performed for one parameter at a time. First, a fixed $\theta_o = \arccos(0.95)$ is assumed and simulations are carried out where the R/X ratio of each grid impedance is multiplied by $k = 0.1, 0.2, \ldots, 1.0$ while maintaining its original module. Since $R/X \approx 0.5$ in the base IEEE 123-bus grid, the simulations consider grid R/X ratios ranging from 0.05 to 0.5. Subsequently, $R/X \approx 0.5$ is once more set and simulations are performed for the power angles $\theta_o = \arccos(m)$, $m = 0.90, 0.91, \ldots, 0.99$. In each set of simulations, the same randomly selected PV power, PV allocation and irradiance/load profiles are used for all parameter (i.e., R/X or θ_o) values so that the results are not stochastic. Also, $H = 3$ and assume $P_b = 0$ are used for the sake of simplicity.

Obtained results are illustrated in Figure 52. It is clear that both R/X and θ_o have considerable impact over performance yielded by the proposed method, but with R/X being a dominant parameter. The plots presented in Figure 52(a) are particularly favorable for the proposed method: it is seen to already *eliminate* voltage violations for $R/X \approx 0.3$, which still lies in the distribution grid R/X range. By further decreasing the grid R/X ratio down to transmission-level values ($R/X < 0.1$), the reactive power reserve utilization for eliminating the overvoltages is decreased, as expected.

It is seen from Figure 52(b) that the relatively high ratio $R/X \approx 0.5$ does not allow elimination of voltage violations for $\cos\theta_o \in [0.9, 0.99]$. However, increasing the maximum power angle (i.e., decreasing $\cos\theta_o$) still helps in attenuating voltage violations: in the transition from $\cos\theta_o = 0.99$ to $\cos\theta_o = 0.9$, approximately twofold and threefold decreases were obtained in all $\Delta\hat{V}(\phi)$ and $\hat{T}_h(\phi)$, respectively. At last, note that the plots show that power factor reductions beyond $\cos\theta_o = 0.9$ tend to provide marginal mitigation of voltage violations. This is once again explained by the high R/X ratio, which makes grid voltages also depend strongly on active power injections, whose curtailment is not considered in this work. Hence, it is recommended that a relatively high $\cos\theta_o$ should be used when

Figure 52 – Obtained results of the fourth droop-type VC simulation experiment.

Explanatory note: The results consist of MVV (traced lines, right Y-axis), PRCU (solid lines, left Y-axis) and peak RVT (alternating traced lines, left Y-axis) as functions of (a) grid R/X ratio and (b) maximum power factor angle. The grid phases are identified as follows: phase A (red), phase B (blue) and phase C (green).

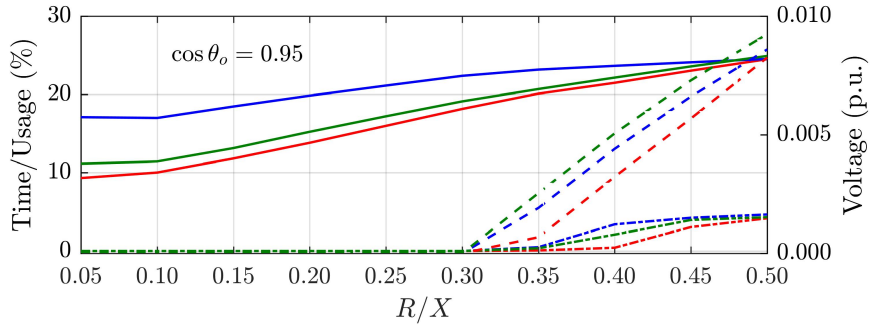

(a) R/X ratio sensitivity analysis.

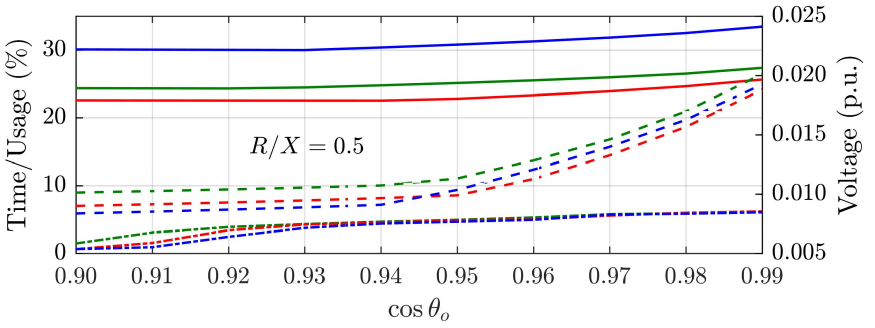

(b) Maximum power angle sensitivity analysis.

Source: The author.

applying the proposed method on distribution grids, otherwise large PV inverter reactive power capacities would be used with no justifiable performance gains.

7.5 Supplementary Evaluation in Worst-Case Power System

The analysis carried out in Section 7.4.6 has shown that the grid R/X ratio is a critical parameter affecting VC performance. In practice, each grid has an overall R/X ratio that is fixed and mostly depends on its nominal voltage. Hence, the simulation procedure of Section 7.4.6 is artificial in the sense that it is not possible to change R/X of a given grid. Taking this into account and considering that good performance has already been verified for smaller values of R/X, it is relevant to provide further evaluation of the proposed method by considering a different grid that has large resistance values.

To this end, a simulation analysis analogous to that of Section 7.4.3 is repeated for the IEEE 13-bus system [204], whose topology is illustrated in Figure 53. It is a

Figure 53 – Illustration of the IEEE 13-bus feeder single-line diagram.

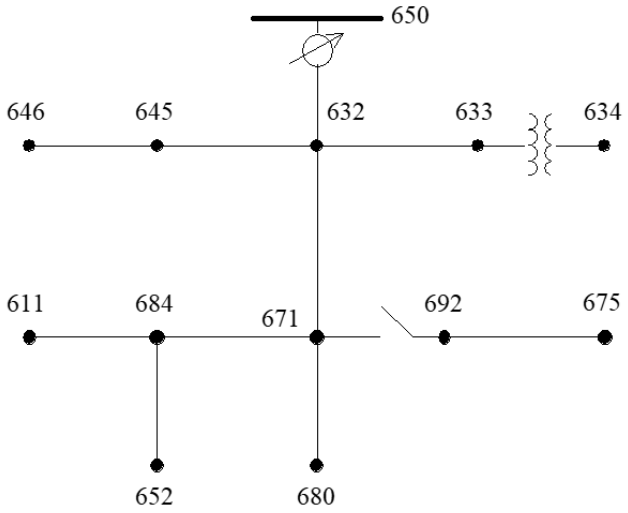

Source: IEEE [204].

4.16 kV system with multiple underground and, consequently, high-resistance distribution lines; in fact, most of its branches have $R/X > 1$. Furthermore, its small size leads to the expectation that performance benefits due to VC decentralization should be less pronounced. Hence, the considered system is representative of a worst-case scenario.

For the sake of simplicity, $\mathcal{S} = \{634, 645, 652, 675\}$ is assumed and $H = 2$ zones are considered. Since branch 632-671 is by far the longest in the grid, the VCZ are intuitively selected as $\mathcal{V}_1 = \{632, 633, 634, 645, 646, 650\}$ and $\mathcal{V}_2 = \mathcal{I} - \mathcal{V}_1$ in this case. All remaining simulation parameters are identical to those considered in Section 7.4.6, except for θ_o. Now, the PV inverters are allowed to reach a much larger power factor angle $\theta_o = 45°$ and therefore be able to inject more reactive power (previously, $\theta_o = \text{acos } 0.95$).

For brevity, obtained MVT and RVT are plotted only for the worst-performing phase ($\phi = A$). As was done in previous Sections for the 123-bus system, such plots are carried out by using the ordinal numbers $z = 1, 2, \ldots, 13$ associated to the original numbering of the grid nodes. A time plot is also given of voltage at the worst-performing pair of node and phase ($z = 10$ and $\phi = A$). Obtained results are depicted in Figure 54.

In general, the results confirm the brief discussion carried out at the beginning of this Section. Despite the greater availability of reactive power reserves (due to larger θ_o), less significant reductions of MVV and RVT (with respect to the no-VC case) are obtained in comparison to the 123-bus system. This is a direct consequence of the high R/X ratio, which attenuates the effect of reactive power injection over system voltages.

Most notably, all VC methods converged to identical performances. This could also be expected from the relatively small size of the grid since, intuitively, the effects of control decentralization are reduced for smaller systems. In any case, such result is

Figure 54 – Results of the worst-case VC evaluation.

Explanatory note: The results consist of (a) MVV and (b) RVT at phase A, (c) time plots of the objective function and (d) time plots of voltage at phase A of bus $z = 10$. The plotted curves are identified as follows: no VC (dotted line, green), local droop VC (alternated tracing line, red), pilot node droop VC (traced line, blue) and proposed method (solid line, black).

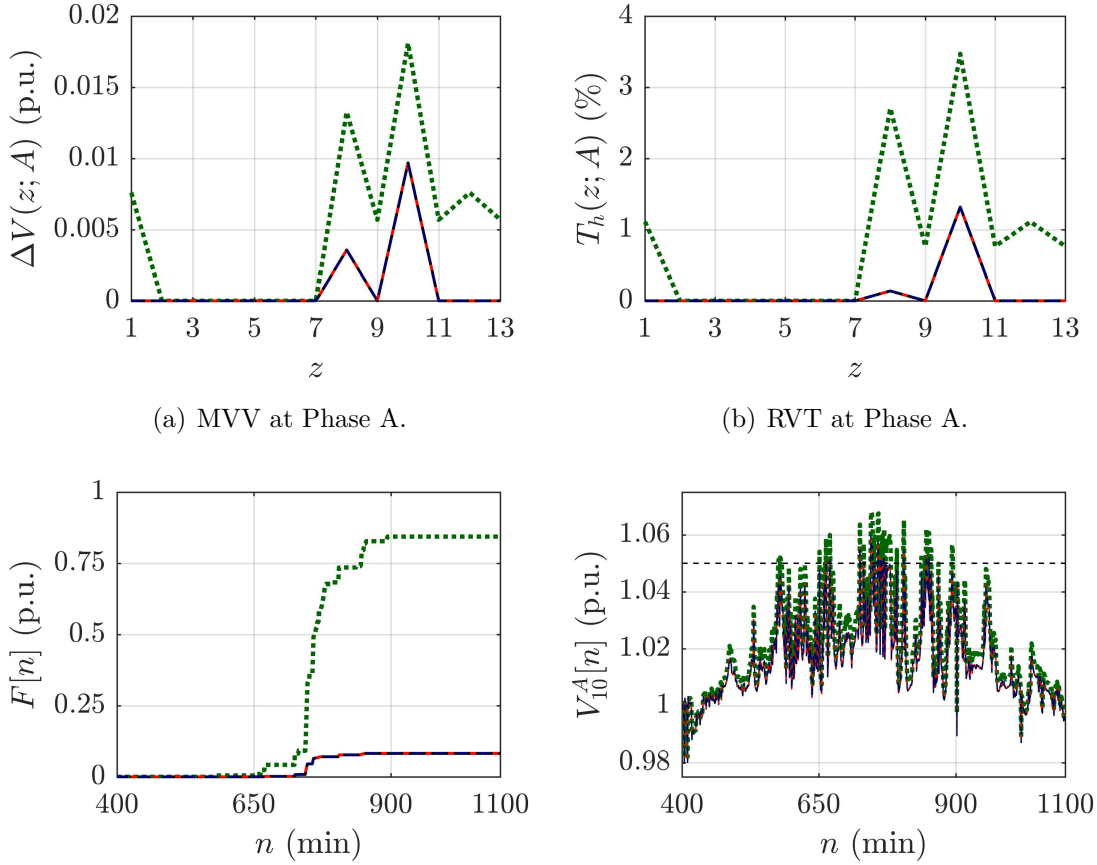

(a) MVV at Phase A.

(b) RVT at Phase A.

(c) Voltage objective function.

(d) Voltage time plot at $z = 10$, ϕ =A.

Source: The author.

important in the sense that it has been shown that a performance *at least* akin to local droop VC can be expected from the proposed method.

At last, the following observation should be made. The obtained results have shown, in general, that the proposed method yields most of its benefits for larger systems and smaller R/X. Fortunately, in practice, resistance tends to decrease with system size (due to larger conductors being used to accomodate greater bulk power). Hence, the proposed VC scheme can be expected to work well in sufficiently large distribution systems.

7.6 Conclusion

A novel decentralized pilot node-based method for carrying out optimization and coordination-free voltage control via reactive power compensation by grid-tied PV generators has been proposed. Its main innovation consists in using two pilot nodes per grid zone, which enhances control response compared to the standard pilot node approach. Furthermore, it is directly compatible with droop control and thereby easy to implement. The proposed method was validated by means of 24-hour simulations based on the IEEE 123-bus system with intense PV penetration. Results have shown that it: (a) yields a 80.1% reduction in the voltage violation objective function compared to the original pilot node method; (b) maintains relative voltage violation time under 2% at all buses and phases, for its optimal cluster number; (c) is robust to communication noise, suffering at most a 12.2% increase in peak voltage violation time for worst-case pulse jamming with high specified BER; and (d) fully eliminates voltage violations for relatively high resistance-to-reactance grid ratios (up to $R/X \approx 0.3$), which further confirms its effectiveness at providing voltage control via PV reactive power support in distribution grids.

8 Hybrid Cooperative MDP Voltage Control and Grid Loss Reduction for PV Generators

8.1 Introduction

Intense photovoltaic (PV) penetration has brought new power quality issues in distribution grids to light. Among such problems, one of the most important is regulation of grid voltages during large PV generation outputs. The high R/X ratio of distribution grids makes them less amenable to voltage control (VC) via reactive power support. However, since PV inverters have the inherent capability of supplying reactive power, it has been generally acknowledged that leveraging them for providing ancillary compensation is an alternative that may not be dispensed with [188]. This approach is even of economic importance for utilities, since it enables them to defer grid improvements required for accomodating current PV penetration levels [144]. Such considerations have led to many VC methods based on PV inverter reactive power support being proposed recently.

The comprehensive literature review carried out in [153] points out that the aforementioned methods differ significantly based on their *general control framework* and the *control objectives* other than voltage regulation per se. In what follows, a brief commentary on such classifications of VC methods is given.

8.1.1 Control Frameworks

With regard to control framework, VC methods can be local, centralized, distributed and decentralized. The *local* techniques control the reactive power setpoint (RPS) of each PV inverter via its measured bus voltage [160–162]. Such approach does not require communication between the PV generators, thereby being the simplest one. However, it does not ensure adequate control of the global voltage profile due to lack of coordination between PV units [205]. To avoid this problem, non-local VC methods must be used.

The *centralized* methods dispatch all PV inverters by means of one distribution system operator (DSO) [155, 156, 190]. In general, this control framework requires solving an optimal power flow (OPF) problem by using real-time numerical optimization. Since all grid voltages are considered in the OPF, near-optimal VC performance can be achieved. On the other hand, a costly communication scheme is required to establish reliable transmission between all PV inverters and the DSO. Furthermore, the task of solving OPFs iteratively in real time imposes the additional requirement of a DSO with large computational processing capability [206]. In practice, such hard-to-accomplish requirements may lead the utility to consider practical implementation infeasible.

An attenuation of the stringent prerequisites of central control can be achieved by carrying out *distributed* VC. This framework partitions a global OPF into subproblems solved locally by the PV inverter processors, which communicate only with their neighbor devices to acquire the data needed for solving their local OPFs [166–168]. Despite its reduction of processing burden, this approach requires complex mesh networks that span all PV inverters. Furthermore, it is susceptible to slow convergence of the global OPF [207].

Another alternative to centralized control is the usage of *decentralized* VC. In this framework, the general strategy is to partition the grid into voltage control zones (VCZ). Then, the PV inverters inside a zone are controlled by a zone controller (ZC) [172, 196, 208]. This approach leads to substantial simplification of communication infrastructure, since one star-topology network can be used per VCZ. Another advantage is that the zone-based control structure makes the design of *optimization-free* methods easier [153], which are valued due to ease of practical implementation.

8.1.2 Control Objectives

Needless to say, all VC methods have regulation of grid voltages as their main objective. It is of interest to note, however, that existing methods differ based on two important aspects, namely: how regulation is posed mathematically and what the additional control objectives (i.e., aside from voltage regulation itself) are [153, 206].

Mathematical *statement* of voltage regulation is carried out either by imposing inequality constraints for bus voltages or by adopting a voltage deviation metric as an objective function to be minimized [206]. The former approach is used in the OPF-based methods, with the objective function being employed to flatten the voltage profile or optimize another performance metric. On the other hand, optimization-free methods must use the latter formulation because complete absence of voltage violations is not *formally* ensured [153] due to optimization not being used; it is only *expected* that grid performance should be enhanced via heuristic control of PV inverter reactive power.

The *complementary objectives* that have been considered in existing works are too numerous to extensively list here. However, the ones most often considered appear to be, as per [153], the minimization of joint PV inverter reactive power injections and of active power losses in the grid. The former objective leads to the freeing of inverter nominal capacities and a consequent avoidance of active power curtailment [209], whereas the latter contributes to enhancement of grid efficiency [210].

Despite the relevance of both aforementioned objectives, a recent update to an important grid code points to greater emphasis in development of loss minimization schemes. The latest revision of EN 50438 (i.e., the european grid code for grid-tied microgeneration) establishes that PV inverters must provide reactive power reserves for VC purposes [174].

Since the provision of reactive power has thus become *mandatory*, even if only in a potential sense (that is, in the form of reactive reserves), it seems to be of greater interest to develop methods that leverage such reserves to achieve power loss minimization.

8.1.3 Related Works

The above discussions show that it is of practical interest to develop VC methods based on PV inverter reactive power support that are: (a) decentralized; (b) optimization-free; and (c) oriented towards the reduction of power losses.

A review of the recent contributions that best correspond to the scope of Chapter (i.e., decentralized VC with loss reduction) is provided in Table 13; optimization approaches have been included both for the sake of completeness and better comparison. The reviewed methods are also classified based on whether communication between ZC is required and on the mechanism used for coordinating voltage regulation and power loss minimization.

From Table 13, it is clear that most decentralized VC methods require real-time optimization or communication between ZC. As anticipated in Section 8.1.1, optimization methods may be considered hard to implement in practice because high-capability and costly processors must be acquired. In a similar manner, inter-ZC communications imply augmented implementation costs for deployment of additional links.

A further difficulty peculiar to some optimization-free methods is the usage of assumptions that may significantly deviate from practical scenarios. The control law proposed in [211] depends on the assumption that system loads are constant (or change very slowly), which is not guaranteed to happen in practice. On the other hand, [212] relies on an *approximate* derivation that voltage regulation necessarily implies the minimization of losses. This has been shown in [214] to not always be true: in high PV penetration scenarios, voltage and loss performances can indeed define a Pareto front.

The optimization-free methods in [171, 213] do not require ZC links and tackle the optimality issue via mechanisms for balancing out the usage of separate voltage regulation and loss reduction control modes. Furthermore, the basic assumption on which such methods are based (i.e., that the grid R/X ratio is approximately constant) is much less stringent than those employed by the aforementioned methods. Comparatively, the strategy of [213] is *not* adaptive and depends on trial-and-error weight selection, whereas [171] only requires the specification of voltage thresholds and carries out adaptation by means of switching between both control modes in terms of measured bus voltages.

8.1.4 Contribution

The prior considerations suggest that a switching-based adaptive framework is of interest for carrying out optimization-free VC with power loss reduction. Under such

Table 13 – Review of recent decentralized VC methods with minimization of power loss via PV reactive support

Ref.	Real-time optimization	Inter-ZC links	Coordination mechanism	Description
[165]	Yes	Yes	Voltage constraints	A loss minimization (LM) OPF is updated via periodic transmission of voltage measurements between VCZs. A linearized solution is obtained via the primal-dual gradient method and used as reference by ZCs.
[191]	Yes	Yes	Voltage constraints	A two-layer approach is used where LM OPFs of intra-VCZ and inter-VCZ scopes are solved for achieving fast and slow timescale VC, respectively. The slow OPF is solved with the alternating direction method of multipliers, whose inputs are obtained via VCZ communications.
[194]	Yes	Yes	Voltage constraints	The setpoint adjustment of the PV inverter controllers is carried out to approximate the solution of a linearized global LM OPF. Such solution is obtained via dual subgradient optimization aided by ZC communications.
[192]	Yes	No	Voltage and current constraints	An agent-based approach is employed, where each ZC uses belief states received from its subordinate nodes and gradient-based optimization to maximize the voltage profile flatness of its VCZ. Additional current constraints are used to indirectly reduce active power losses.
[169]	Yes	No	Voltage constraints	Decoupled LM OPFs are attributed to each VCZ, which are solved (i.e., without inter-ZC transmissions) via particle swarm optimization.
[211]	No	Yes	Reactive power thresholds	Communication between ZC is leveraged, together with a constant-load approximation, for estimating total power loss. Then, a closed-form control law is used at each PV inverter to adjust reactive output in terms of total power loss and bus voltage. Minimum and maximum thresholds are used in order to avoid severe voltage violations.

Review of recent decentralized VC methods with minimization of power loss via PV reactive support (cont.)

Ref.	Real-time optimization	Inter-ZC links	Coordination mechanism	Description
[212]	No	Yes	Assumes objectives are concurrent	Multiple VCZ are defined so that each node acts as a ZC to downstream nodes. After a voltage violation is detected at some node, the downstream PV inverters gradually adjust reactive power injections. No explicit loss reduction is carried out: it is assumed to be a consequence of VC, as suggested by approximate load flow equations.
[213]	No	No	Weighting of control functions	Two heuristic equations, one for voltage regulation and another for loss reduction, are derived analytically. All PV inverters share a preset weighting parameter (in principle determined by the ZC; no specific procedure is proposed) for carrying out a linear combination of both equations, which is then used as the final setpoint solution.
[171]	No	No	Switching between control functions	All nodes report voltages to their associated ZC, which uses the largest deviation for deciding whether voltage regulation or loss reduction should be prioritized. Based on this decision, one of the heuristic equations from [213] is used for computing the inverter setpoints.
Prop.	**No**	**No**	Switching between control functions	A hybrid approach is proposed as follows. A coordination mechanism similar to that from [171] is used. At each PV generator, the ratio between local generation and load is used as a switching variable. If voltage control is selected at a given node, its RPS is set by means of a decentralized policy yielded by a pilot node-compatible C-POMDP algorithm (hybridization of the methods from Chapters 6 and 7). On the other hand, if loss reduction is selected, the heuristic loss equation from [213] is employed to compute the inverter RPS.

Source: The author.

motivation, a novel method based on adaptive switching is introduced in this Chapter.

The proposed method switches PV inverters between voltage regulation and loss reduction modes based on the local ratio between PV generation and load active power consumption. Its control scheme is a hybridization of two approaches: voltage regulation is carried out by means of a modified version of the C-POMDP algorithm developed in Chapter 6, whereas loss reduction is based on the heuristic from [213]. No approximating assumptions are used and communication between ZCs is not required.

8.2 Modeling and Problem Statement

Again, the same modeling approach from Chapter 6 is considered. Hence, for conciseness, only the new problem statement in terms of voltage regulation and power loss reduction is considered in what follows. The reader is referred to Section 6.2 for detailed information on power system modeling.

8.2.1 Problem Statement

Recall from Section 8.1.2 that optimization-free VC does not formally ensure elimination of voltage violations (i.e., mathematical voltage constraints are not enforced). This is even more the case in this Chapter since, as has been explained in Section 6.2, it is considered that PV reactive power output is limited by a maximum allowable power factor angle θ_o. Hence, an appropriate assessment of voltage performance must be carried out via evaluation of a voltage violation objective function.

The considered problem can thus be expressed as a multiobjective minimization of voltage violation and active power loss metrics, which are defined as follows at time n:

$$F_v[n] = \sum_{k=0}^{n} \sum_{i \in \mathcal{I}} [\psi(\boldsymbol{V_i}[k] - V_h \cdot \mathbf{1}) + \psi(V_l \cdot \mathbf{1} - \boldsymbol{V_i}[k])] \tag{8.1}$$

$$F_\ell[n] = \sum_{k=0}^{n} \sum_{r \in \Phi} \sum_{i \in \mathcal{I}} \sum_{j \in \mathcal{I}_i} \ell_{ij}^r[k] \tag{8.2}$$

where V_l is the lower voltage limit, V_h is the upper voltage limit, $\psi(\boldsymbol{x}) = \sqrt{\sum_{i=1}^{P} [\max(x_i, 0)]^2}$ is the Euclidian norm with prior component-wise rectification, the set $\mathcal{I}_i = \mathcal{I} - \{i\}$ and ℓ_{ij}^r is the active power loss at phase r of the branch connecting nodes i and j.

Given Equations 8.1 and 8.2, the VC problem considered in this Chapter is:

$$\begin{aligned} \underset{\boldsymbol{\alpha_s}[n]}{\text{minimize}} \quad & F_v[n_{\mathcal{T}}],\ F_\ell[n_{\mathcal{T}}] \\ \text{s.t.} \quad & \text{Equations 6.1 and 6.2 (load flow constraints);} \\ & \text{Equations 6.3 and 6.4 (power balance constraints);} \\ & -\mathbf{1} \leq \boldsymbol{\alpha_s}[n] \leq \mathbf{1},\ s \in \mathcal{S},\ 0 \leq n \leq n_{\mathcal{T}}. \end{aligned} \tag{8.3}$$

An adequate optimization-free solution of Equation 8.3 yields RPS profiles $\boldsymbol{\alpha_s}[n]$, $s \in \mathcal{S}$, that drive the grid voltages towards the interval $[V_l, V_h]$ and also reduce total power losses over time. In other words, an approximate minimization of both performance metrics $F_v[n_\mathcal{T}]$ and $F_\ell[n_\mathcal{T}]$ must be obtained.

8.3 Proposed Method

The proposed optimization-free VC approach is now presented. For clarity, an outline of the method is given at first. Subsequently, its steps are described in detail.

8.3.1 Outline

A switching-based approach with alternation between voltage regulation and loss reduction modes is proposed. The voltage regulation mode is a modified version of the C-POMDP model introduced in Chapter 6 that takes advantage of the double pilot node concept from Chapter 7, whose solution yields decentralized ZC control policies. On the other hand, the loss reduction mode employs an heuristic for current flow minimization based on load reactive power compensation that has been proposed in [213].

At first, the proposed method must carry out offline processing for: (a) dividing the grid into VCZ; (b) selecting one pair of reference nodes per VCZ; and (c) obtaining the regulation policies by solving the C-POMDP model. Such computations are only made once and, since they are offline, can be carried out prior to controller deployment.

After the aforementioned processing, online VC can be carried out using the switching scheme. It requires the measurement of irradiance at the PV buses and of voltage at the VCZ reference nodes, but all of its computations are analytical.

8.3.2 Preliminary Offline Processing

The steps involved in offline processing are now described.

1. Dividing the grid into VCZ: A clustering-based approach nearly identical to the one from Sections 6.4.2 and 7.3.1 is proposed, for which reason a briefer description is given. As before, the sensitivity-based distance metric is computed as:

$$d_{ij}^{rs} = -\ln\left(\frac{\Gamma_{ij}^{rs}\Gamma_{ji}^{sr}}{\Gamma_{ii}^{rs}\Gamma_{jj}^{rs}}\right) \tag{8.4}$$

where the d_{ij}^{rs} with $r \neq s$ can be ignored since it has been proved in Appendix B that $\Gamma_{ij}^{rr} \leq \Gamma_{ij}^{rs}$ and a single arbitrary phase r can be used for clustering because phase symmetry makes distance ordering be identical $\forall r \in \Phi$ (see Section 7.3.1).

Also in a similar manner to Chapters 6 and 7, the obtained $d_{ij} \triangleq d_{ij}^{rr}$ are used as input to the hierarchical agglomerative clustering (HAC) algorithm, which further requires the desired cluster number H as input. *However,* instead of selecting H arbitrarily as before, the following procedure is adopted. The HAC algorithm is iterated for $1 \leq H \leq 10$ and the *elbow method* heuristic [215] is used to select the number of clusters. That is, the VCZ number H is obtained by qualitatively identifying an elbow point of the within-cluster sum of squares (WCSS) curve, which is computed as follows:

$$\text{WCSS}(H) = \sum_{k=1}^{H} \sum_{i \in \mathcal{H}_k} d_{c_k i}^2 \tag{8.5}$$

where $\mathcal{H}_k \subset \mathcal{I}$ is the k-th VCZ and c_k is its centroid.

2. Selection of VCZ reference nodes: The same Monte Carlo-type procedure of Section 7.3.2 is used for selecting two reference nodes. In other words, L load flow simulations with no reactive support are carried out and the pilot nodes $\hat{z}_i$, $\check{z}_i$ of $\mathcal{H}_i$ are selected as:

$$\hat{z}_i = \text{argmax}_{j \in \mathcal{H}_i} \hat{c}_j \tag{8.6}$$

$$\check{z}_i = \text{argmax}_{j \in \mathcal{H}_i} \check{c}_j \tag{8.7}$$

where $i = 1, 2, \ldots, H$ and the counters $\hat{c}_j$, $\check{c}_j$ are defined in Section 7.3.2.

3. Specifying and solving the C-POMDP model: As anticipated in Section 8.3.1, the proposed C-POMDP model is an improvement of the one considered in Chapter 6. More specifically, it is modified to be compatible with the reference node approach from Chapter 7, which was *not* used in Chapter 6, where voltage measurements at *all* nodes was assumed.

Recall that a C-POMDP model is given by $\mathcal{M} = \langle \mathfrak{h}, \mathcal{X}, \mathcal{A}, \Omega, \mathcal{P}, \mathcal{O}, R, n_f, \gamma \rangle$, where $\mathfrak{h}$ is now used to denote the agent set so as not to cause confusion between the agents $h_i \in \mathfrak{h}$ and their associated voltage control zones $\mathcal{H}_i$ which contain nodes $\hat{z}_i$ and $\check{z}_i$. The proposed improvement with regard to the model from Chapter 6 only involves $\mathfrak{h}$, $\mathcal{X}$, $\mathcal{A}$ and Ω. Hence, for brevity, the reader is referred to Section 6.4.1 for specification of the remaining components of $\mathcal{M}$. The new proposed $\mathfrak{h}$, $\mathcal{X}$, $\mathcal{A}$ and Ω are now described.

a) $\mathfrak{h}$: For the agent set, it is simply proposed that each ZC be one of the C-POMDP agents. More precisely, each $h_i \in \mathfrak{h}$ dictates the actions taken by all PV inverters in $\mathcal{H}_i \subset \mathcal{I}$.

b) $\mathcal{X}$: The elements $x \in \mathcal{X}$ must be status indicators of the voltages in all VCZ. To this end, it is established that x is a PH-dimensional tuple and each of its components furnishes a qualitative indicator of whether a given phase of a VCZ is prone to undervoltages or

overvoltages. In other words, $x = \langle x^{(1,\phi_1)}\ x^{(2,\phi_1)}\ \cdots\ x^{(H,\phi_P)} \rangle$, with each $x^{(i,r)}$ given by:

$$x^{(i,r)} = \begin{cases} \texttt{uv-prone}, & \text{if } V_l - V^r_{\check{z}_i} > 0 \text{ and } V^r_{\hat{z}_i} - V_h < 0 \\ & \text{or } V_l - V^r_{\check{z}_i} > V^r_{\hat{z}_i} - V_h > 0 \\ \texttt{ov-prone}, & \text{if } V_h - V^r_{\hat{z}_i} < 0 \text{ and } V^r_{\check{z}_i} - V_l > 0 \\ & \text{or } V_h - V^r_{\hat{z}_i} < V^r_{\check{z}_i} - V_l < 0 \\ \texttt{normal}, & \text{if } V^r_{\check{z}_i} - V_l \geq 0 \text{ and } V^r_{\hat{z}_i} - V_h \leq 0 \end{cases} \tag{8.8}$$

It is seen that Equation 8.8 classifies a VCZ phase as `normal` if its reference node voltages are inside the interval $[V_l, V_h]$. On the other hand, it is overvoltage-prone (`ov-prone`) if (i) $\hat{z}_i$ has an overvoltage and $\check{z}_i$ does not have an undervoltage or (ii) $\hat{z}_i$ has an overvoltage that surpasses the undervoltage of $\check{z}_i$. Analogous considerations apply to the definition of the undervoltage-prone (`uv-prone`) status.

c) $\mathcal{A}$: The action sets $\mathcal{A}_i, i = 1, 2, \ldots, H$, of the individual ZC are all identically defined as $\mathcal{A}_i = \{0, +1, -1\}^P$, where the power operation is a cartesian product. The r-th element of each $a_j \in \mathcal{A}_i$ refers to actions on phase r of $\mathcal{H}_i$, and its possible values represent the following actions: no reactive power injection (0), reactive power compensation using the high voltage reference node $\hat{z}_i$ (+1) and reactive power compensation using the low voltage reference node $\check{z}_i$ (−1). At last, the joint action set is simply $\mathcal{A} = \bigtimes_{i=1}^{H} \mathcal{A}_i$.

d) Ω: The joint agent observations $o = \langle o_1\ o_2\ \cdots\ o_H \rangle \in \Omega$ are defined according to $o_i = \langle x^{(i,\phi_1)}\ x^{(i,\phi_2)}\ \cdots\ x^{(i,\phi_P)} \rangle$. In other terms, each agent only observes its own voltage status, which ensures that communication between ZC is not required.

The C-POMDP model from Chapter 6 has two limitations. First, computation of voltage status took into account the maximum and minimum voltages at each phase of every VCZ, which makes it a necessity to measure voltages at *all* nodes and compute both $\min_{j \in \mathcal{H}_i} V^r_j$ and $\max_{j \in \mathcal{H}_i} V^r_j$ for every $\mathcal{H}_i$ and r. Also, the a_i of each action set were used for incremental control (e.g., if $a^r_i = -1$, the RPS α^r_i was decreased by some fixed $\Delta\alpha$), which does not leverage reactive power control via the inverter droop curves.

The proposed improvement solves both issues mentioned above. By using previously-determined reference nodes, only *two* node voltages must be monitored per VCZ, thereby significantly improving feasibility. Furthermore, as will be explained in Section 8.3.3, the agent actions are interpreted in a more general sense and used, together with the reference nodes, to manage the droop curves supplied by the PV inverters.

By solving the above model with JESP, the control policies to be used by the ZCs for carrying out voltage regulation (see Section 8.3.3) are obtained.

8.3.3 Voltage Regulation Mode

In what follows, it is assumed that the offline processing described in Section 8.3.2 has been completed. As discussed in Chapter 7, most inverters use linear V-Q droop curves for low-level reactive power control [189]. Hence, it is proposed that the ZC policies and reference nodes be used to leverage the droop curves for voltage regulation.

The proposed voltage regulation mode is now described. It is assumed that all PV inverter droop curves use the same voltage reference V_o. At each sample time n and for each phase $r \in \Phi$, the ZC of each $\mathcal{H}_i$, $i = 1, 2, \ldots, H$, uses the measurements $V^r_{\hat{z}_i}$ and $V^r_{\check{z}_i}$ to compute Equation 8.8 and its latest observation $o_i[n]$. Then, its control action $a_i = \pi_i(\bar{o}_i[n])$ is used to control all PV inverters in $\mathcal{H}_i$ as follows:

$$\alpha^r_{\mathcal{H}_i}[n] = \alpha_{drp}(V^r_{\hat{z}_i}[n]) \cdot \delta(a^r_i - 1) + \alpha_{drp}(V^r_{\check{z}_i}[n]) \cdot \delta(a^r_i + 1) \tag{8.9}$$

$$\alpha_{drp}(V) = \min\left(\max\left(\frac{2(V - V_o)}{V_h - V_l}, -1\right), 1\right) \tag{8.10}$$

where $\alpha^r_{\mathcal{H}_i}[n]$ is the RPS at phase r of all PV buses in $\mathcal{H}_i$, a^r_i is the r-th component of action a_i, $\delta(\cdot)$ is the Kronecker delta and $\alpha_{drp}(V) \in [-1, 1]$ is the inverter droop curve.

In brief, the ZC of each $\mathcal{H}_i$ decides, via its policy π_i, whether to use $V^r_{\hat{z}_i}$ or $V^r_{\check{z}_i}$ as the VC input signal (or not to perform any compensation, if $a^r_i = 0$). Then, the selected voltage is used to adjust the droop RPS of all PV inverters that belong to the VCZ.

8.3.4 Loss Reduction Mode

The heuristic loss reduction scheme originally proposed and validated in [213] is used. It consists in setting each $\alpha^r_i[n]$ so that each PV inverter exactly compensates its load reactive power or uses its full reactive capacity, if the former is not possible. In other words, the control of reactive power injection is carried out as:

$$\alpha^r_i[n] = \min\left(\max\left(\frac{P^{(L_o,r)}_i \cdot \tilde{P}^{(L,r)}_i[n]}{P^{(G_o,r)}_i \cdot \tan\theta_o}, -1\right), 1\right) \tag{8.11}$$

where it should be recalled that $P^{(L_o,r)}_i$ is the r-th component of $\boldsymbol{P}^{(\boldsymbol{L_o})}_{\boldsymbol{i}}$ and analogous definitions apply to the remaining notations in Equation 8.11.

8.3.5 Online Switching-Based VC Scheme

As discussed in Section 8.1.3, the assumption that voltage regulation and loss reduction are concurrent objectives is not *always* true. It has been shown, via extensive simulation experiments in [214], that a Pareto front exists when PV injections become

comparable to load power. This must be considered in modern grids, where high PV penetration may even lead peak generation to surpass the load demand.

In this sense, the VC method in [171] proposes switching between its voltage regulation and loss reduction modes based on the maximum VCZ voltage, which is thus taken as an *indirect* indicator of the current level of PV injections.

It is now proposed that a similar switching approach be used with the control modes proposed in Sections 8.3.3 and 8.3.4. However, instead of using a voltage-based switching threshold as in [171], the measured irradiance at each PV node (which is a *direct* indicator of local generation) is considered, together with a *relative generation threshold* p_{th} used for switching. More precisely, the proposed online VC scheme is given by:

$$\begin{aligned}\alpha_i^r[n] = \alpha_{i,loss}^r[n] \cdot u(p_i^r[n] - p_{th}) \cdot u(1 - p_i^r[n]) \\ + \alpha_{i,regulation}^r[n] \cdot u(p_{th} - p_i^r[n]) \cdot u(p_i^r[n] - 1)\end{aligned} \tag{8.12}$$

$$p_i^r[n] = \frac{P_i^{(G_o,r)} \cdot E_i[n]}{P_i^{(L_o,r)} \cdot \tilde{P}_i^{(L,r)}[n]} \tag{8.13}$$

where $\alpha_{i,regulation}^r[n]$ and $\alpha_{i,loss}^r[n]$ are the voltage regulation and loss minimization control laws given by Equations 8.9 and 8.11, respectively, $u(\cdot)$ is the unit step and $p_i^r[n]$ is the ratio between PV generation and load demand at phase r of bus i.

Equation 8.12 is explained as follows. For small PV generation, F_v and F_ℓ tend to be concurrent objectives [214]. Hence, the voltage regulation mode is employed for $p_i^r[n] < p_{th}$. Contrastingly, a Pareto front exists for high PV generation and both objectives must be balanced out. In this sense, the loss reduction mode is used when $p_i^r[n] \geq p_{th}$ *and* generation is not too large ($p_i^r[n] < 1$). When generation surpasses load demand ($p_i^r[n] \geq 1$), large overvoltages are likely to happen and voltage control mode is used again.

As a straightforward heuristic for threshold selection, it is proposed that $p_{th} = 1/2$ so that both control modes have approximately equal ranges for operation and thus reduce, on average, the risk of poor performance due to suboptimal control mode selections.

It is clear that the proposed VC method does not require inter-ZC links since: (a) the $\mathcal{H}_i$ operate in a decentralized but independent manner during voltage regulation; (b) the loss reduction mode only uses local computations; and (c) the switching scheme is based on local measurements of irradiance and load power.

At last, it must be emphasized that online optimization is not required because partitioning of the grid into VCZ, determination of the reference nodes and execution of JESP for computing the ZC policies are all carried out offline.

For greater comprehension, the proposed method, which is named Voltage Control and Loss Reduction Based Cooperative Partially Observable Markov Decision Process (VLC-POMDP), is given as pseudocode in **Algorithm 6**.

Algorithm 6 VLC-POMDP

Input: Power grid data, L, $\mathcal{M}$, V_o, V_l, V_h, p_{th}, θ_o.
Output: $\alpha_s^r[n]$; $s \in \mathcal{S}$, $r \in \Phi$, $n = 1, 2, 3, \ldots$
{*Offline phase*}
Use power grid data to compute $\mathbf{\Gamma}$.
Use Equation 8.4 to compute the d_{ij} for an arbitrary $r \in \Phi$.
Iterate HAC and compute Equation 8.5 to clusterize the grid.
return H.
Run L load flow simulations and use Equations 8.6, 8.7 to select $\hat{z}_i$, $\check{z}_i$, $i = 1, 2, \ldots, H$.
Generate the C-POMDP model $\mathcal{M}$ with H agents.
return $\mathcal{M}$.
Use JESP to solve $\mathcal{M}$.
return π.
{*Online phase*}
for $n = 1, 2, \ldots$ **do**
    Update agent observations $\bar{o}[n]$.
    Compute the joint action $a = \pi(\bar{o}[n])$.
    Use a and Equations 8.9-8.13 to compute each $\alpha_s^r[n]$.
end for
return $\alpha_s^r[n]$; $s \in \mathcal{S}$, $r \in \Phi$, $n = 1, 2, 3, \ldots$
Source: The author.

8.4 Simulation-Based Validation

To validate the proposed VC method, a three-part simulation experiment is carried out. At first, a performance comparison against the methods from [171, 213] is considered; such approaches were selected for comparison due to their greater similarity to the proposed approach (see Table 13 and Section 8.1.3). Subsequently, performance of the proposed method in terms of p_{th} is evaluated to confirm the effectiveness of the $p_{th} = 1/2$ heuristic. At last, an assessment of VC performance considering different VCZ numbers H is carried out to verify the adequeteness of the adopted elbow method criterion for grid partitioning.

8.4.1 General Simulation Parameters

The exact same system (i.e., the IEEE 123-bus feeder) and simulation parameters used in Chapter 7 are considered. Hence, the reader is referred to Section 7.4.1 for brevity. All simulations were carried out in MATLAB R2017a.

A VCZ number of $H = 4$ was obtained by using the elbow method (see Section 8.3.2). The corresponding WCSS plot and partitioned grid are shown in Figure 55.

Remark 8.1: As in Chapters 6 and 7, the adopted base voltage is simply the nominal system value (i.e., a per phase voltage of $V_{base} = 4.18/\sqrt{3}$ kV). The adopted power base, which is used for computing the losses F_ℓ, is $S_{base} = 5000/3$ kVA per phase.

Figure 55 – Grid partitioning via elbow method clustering.

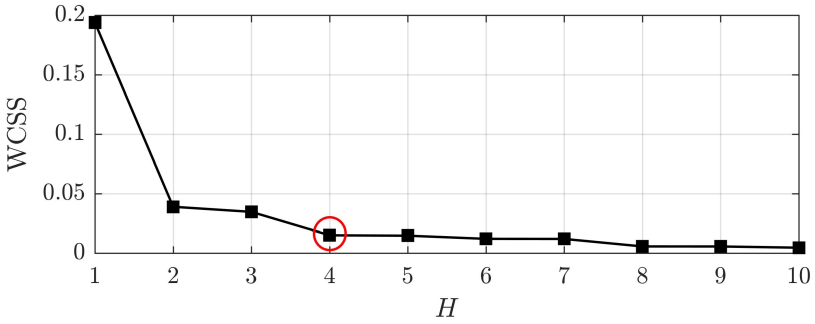

(a) WCSS plot and selection of H.

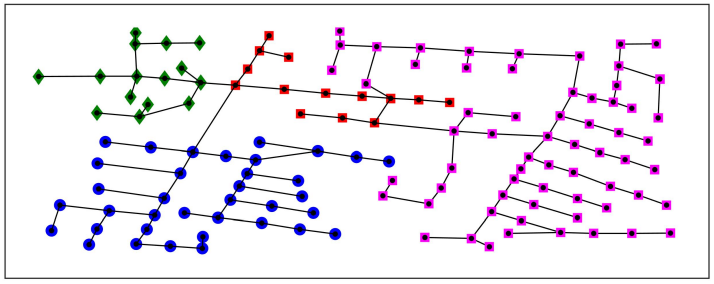

(b) Partition of the grid into VCZ.

Source: The author.

8.4.2 Additional Performance Metrics

Aside from the objective functions given in Equations 8.1 and 8.2, the following metrics shall be evaluated for further detailing the obtained results:

$$\Delta V(z;\phi) = \max_{n \leq n_{\mathcal{T}}} \left[\psi(V_z^{\phi}[n] - V_h) + \psi(V_l - V_z^{\phi}[n]) \right] \tag{8.14}$$

$$T_h(z;\phi) = \sum_{n=0}^{n_{\mathcal{T}}} \left[\frac{u(V_z^{\phi}[n] - V_h) + u(V_l - V_z^{\phi}[n])}{n_{\mathcal{T}} + 1} \right] \tag{8.15}$$

where $\Delta V(z;\phi)$ and $T_h(z;\phi)$ are the maximum voltage violation (MVV) and the relative violation time (RVT) at phase ϕ of bus z, respectively.

8.4.3 Part 1: Comparison to Other VC Methods

Results of the performance comparison against the VC methods of Turitsyn et al. [213] and Yeh et al. [171] are presented in Figure 56 and Table 14. To further enrich the analysis, performances obtained with no VC, local droop control and the original C-POMDP method from Chapter 6 are also considered.

Recall that the method of Turitsyn et al. [213] requires prior specification of a weighting parameter K. To provide a fair assessment, [213] was evaluated for various

Figure 56 – Results in Part 1 of the VC and loss reduction experiments.

Explanatory note: The plotted curves are identified as follows: no VC (traced line, black), local droop (alternating traced line, green), method of Corrêa and Vieira [208] (solid line, yellow), method of Turitsyn et al. [213] (thin alternating traced line, blue), method of Yeh et al. [171] (thin traced line, magenta) and proposed method (thin solid line, red).

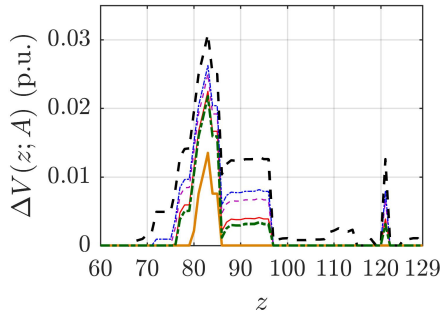

(a) MVV at Phase A.

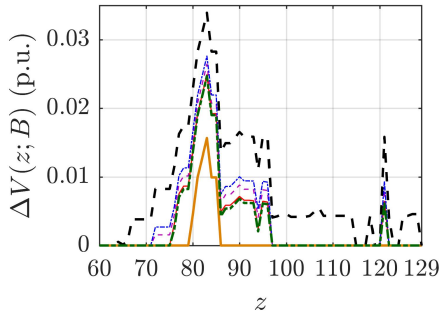

(b) MVV at Phase B.

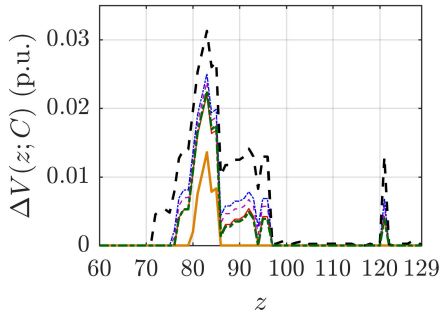

(c) MVV at Phase C.

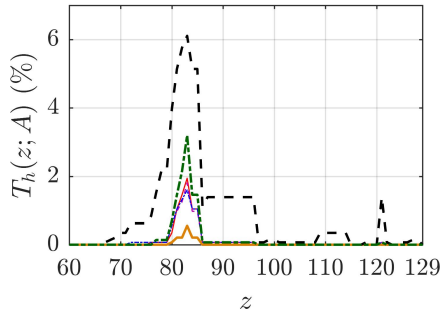

(d) RVT at Phase A.

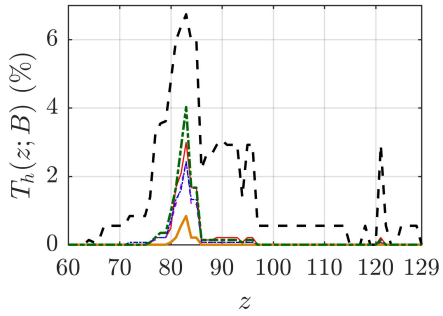

(e) RVT at Phase B.

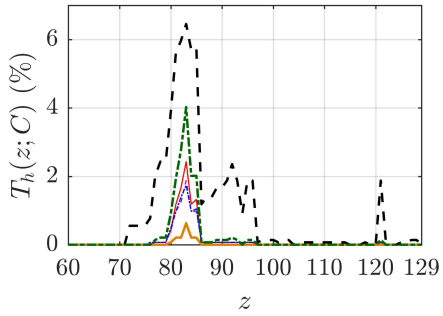

(f) RVT at Phase C.

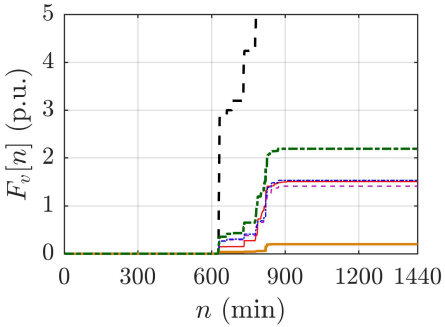

(g) Voltage objective function.

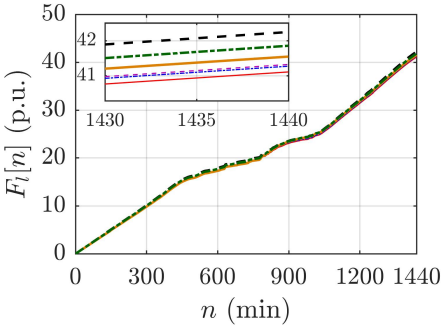

(h) Loss objective function.

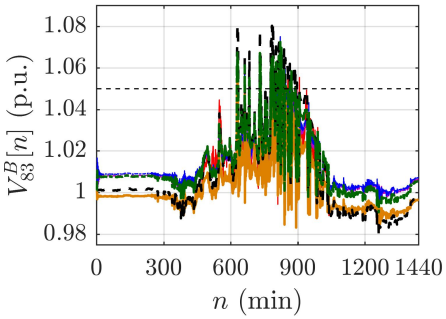

(i) Time plot of voltage at $z = 83$, $\phi = \mathrm{B}$.

Source: The author.

Table 14 – Metrics obtained in Part 1 of VC and loss reduction experiments

Method	**Savings (kWh)**	**Peak MVV (p.u.)**	**Peak RVT (%)**
None	—	0.03392	6.74
Droop	32.5	0.02471	4.03
Chapter 5	34.5	0.01566	0.83
[213]	76.6	0.02762	2.43
[171]	80.8	0.02642	2.44
Proposed	94.2	0.02490	2.99

Source: The author.

weights and $K = 0.95$ was selected, since it yielded the best voltage and loss performances. For the method of Yeh et al. [171], the voltage limits used for switching between control functions are the same ones considered in the proposed method (i.e., V_l and V_h).

In general, the obtained results suggest the proposed method provides superior balance between loss reduction and voltage regulation. Indeed, observing Figures 56(a)-(f) and Table 14 it is seen that, compared to [171, 213], it yields: (a) slight MVV reduction; (b) slight RVT increase; and (c) significant improvement in power savings. Hence, similar voltage regulation was obtained but with additional loss reduction. This is further confirmed by Figures 56(g)-(h), where the $F_v[n]$ plots converge to similar values but the proposed method yields $F_\ell[n_\mathcal{T}]$ reductions (with respect to the value obtained with no VC) that are larger by 22.82% and 16.49% when compared to [171, 213], respectively.

As could be reasonably expected, the proposed method and [171,213] perform much better than local droop control, which yielded higher RVT and much larger losses; this confirms the general acknowledgment that local control does not ensure high-quality VC of the grid as a whole. On the other hand, the original C-POMDP method from Chapter 6 yielded excellent voltage regulation but inferior loss reduction, which is a consequence of it being a VC method devoted exclusively to the voltage regulation task.

At last, the results are further illustrated in Figure 56(i) by the time plot of voltage at the worst-performing pair of node and phase, i.e., $z = 83$ and $\phi = \text{B}$. The $V_{83}^B[n]$ plots show that the proposed method closely follows the voltage regulation of the C-POMDP approach at lower PV generation levels, in which F_v and F_ℓ are concurrent. On the other hand, it allows the grid to operate at higher voltages (and reduced losses), thereby approaching the behavior of [171, 213], when generation increases.

8.4.4 Part 2: Assessment of Generation Threshold

The main parameter of the proposed VC method is the threshold p_{th}, which has been determined by means of a simple heuristic. To further validate the method and ensure the effectiveness of this heuristic, simulations are carried out for $p_{th} \in \{0, 1/4, 1/2, 3/4, 1\}$

and the obtained performances are compared. Results are shown in Figure 57, where MVV and RVT plots are presented only for the worst-performing phase ($\phi = B$) for brevity. A time profile $\ell[n]$ of grid losses is given for further illustration.

For ease of comprehension, consider at first the extreme cases of $p_{th} = 1$ and $p_{th} = 0$. The former corresponds to voltage regulation mode always being used, whereas the latter implies loss reduction mode is always active except when $p_i^r[n] \geq 1$. The results for $p_{th} = 1$ are similar to those reported for C-POMDP in Section 8.4.3; this is expected, since the C-POMDP approach only carries out voltage regulation. The results for $p_{th} = 0$ show that the loss reduction heuristic is suboptimal at low PV generation: it actually increases losses and rises system voltages excessively, as seen from Figures 57(e)-(f).

Now, consider the comparison of $p_{th} = 3/4$ and $p_{th} = 1/4$ to the base heuristic $p_{th} = 1/2$. The former case is more conservative with respect to voltage regulation and, correspondingly, slightly reduces $F_v[n_{\mathcal{T}}]$ with a small increase in losses as trade-off; since the differences are quite small with respect to $p_{th} = 1/2$, it can be argued that both parameter values are equally well-performing. Interestingly, the latter case yields a minute improvement in losses compared to $p_{th} = 1/2$, but has an unnaceptable voltage performance trade-off, resulting in the approximately tenfold increase of $F_v[n_{\mathcal{T}}]$.

The aforementioned results suggest that the proposed $p_{th} = 1/2$ heuristic is reasonable, since it yielded superior balance between both objectives. This can be attributed to the fact that, as discussed in Section 8.3.5, it avoids strongly suboptimal decisions by providing approximately equal ranges for both control modes.

8.4.5 Part 3: Effect of VCZ Number

Since the number of VCZ has been selected by means of an heuristic clustering method, a final validation effort is necessary to ascertain whether the obtained $H = 4$ is indeed satisfactory. To this end, simulations for $H = 1, 2, \ldots, 10$ are considered. The results are presented in Figure 58 where, once more for the sake of briefness, the MVV and RVT plots are only given for the worst-performing phase.

Obtained results show that H has a significant effect on VC performance. It is also noteworthy that many VCZ numbers yield nearly identical performances; for this reason, they are depicted by a single representative plot. It is seen from Figures 58(c)-(d) that, as H increases, voltage regulation worsens and loss reduction improves. Such fact is intuitively understood: for fewer VCZ, buses that are more critical voltage-wise are used as reference nodes by the ZC, which results in conservative use of voltage control mode.

The above is further confirmed by observing Figure 58(e), where it is clear that, for $H = 8 \sim 10$, the grid is allowed to operate at higher voltages and thereby attain further loss reduction during peak PV generation. However, compared to the $H = 3 \sim 7$ case,

Figure 57 – Results in Part 2 of the VC and loss reduction experiments.

Explanatory note: The plotted curves are identified as follows: $p_{th} = 1$ (solid line, yellow), $p_{th} = 3/4$ (alternating traced line, green), $p_{th} = 1/2$ (thin solid line, red), $p_{th} = 1/4$ (thin alternating traced line, blue) and $p_{th} = 0$ (thin traced line, magenta).

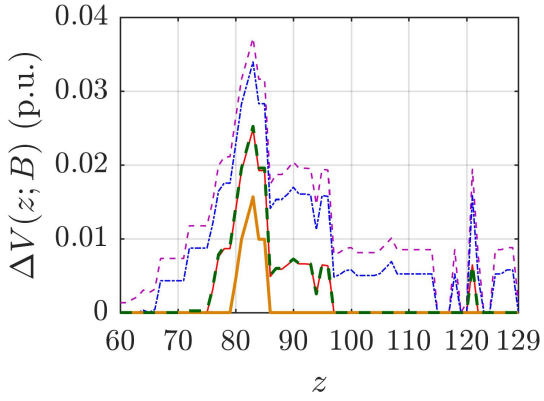

(a) MVV at Phase B.

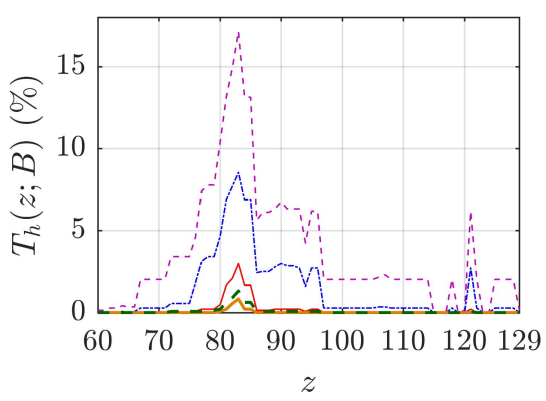

(b) RVT at Phase B.

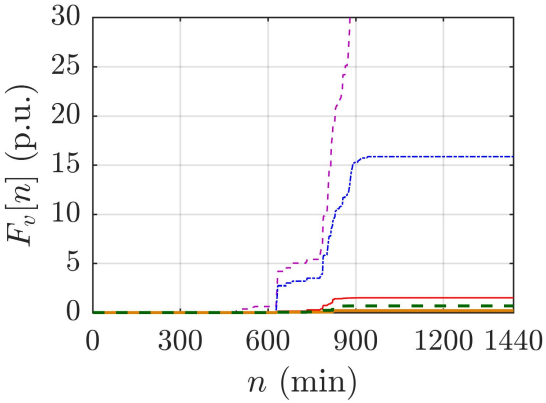

(c) Voltage objective function.

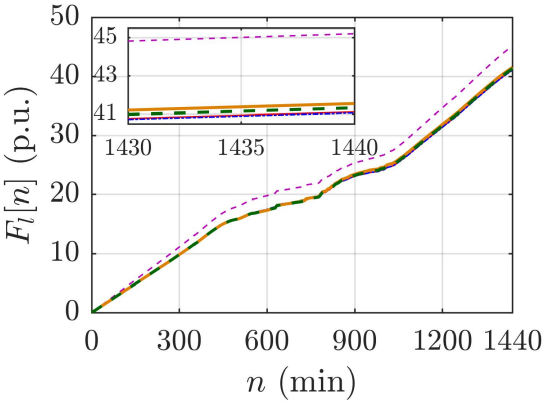

(d) Loss objective function.

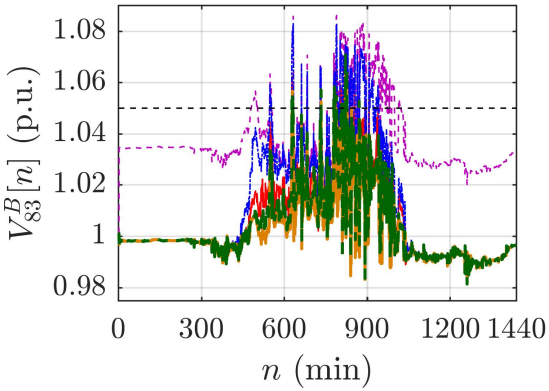

(e) Voltage at $z = 83$, $\phi = \text{B}$.

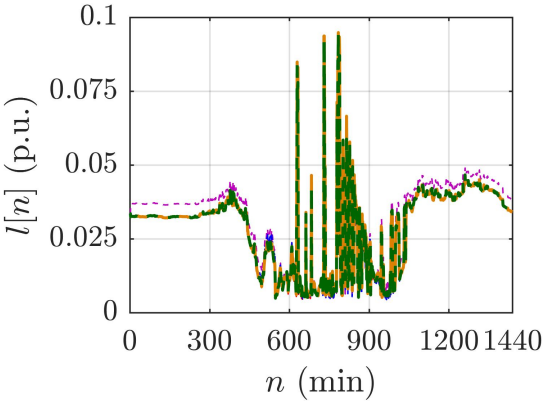

(f) Time profile of grid losses.

Source: The author.

Figure 58 – Results in Part 3 of the VC and loss reduction experiments.

Explanatory note: The plotted curves are identified as follows: $H = 1$ (traced line, red), $H = 2$ (alternating traced line, green), $H = 3 \sim 7$ (solid line, black) and $H = 8 \sim 10$ (traced line, blue).

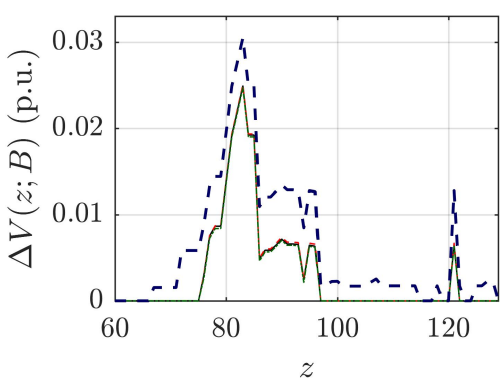

(a) MVV at Phase B.

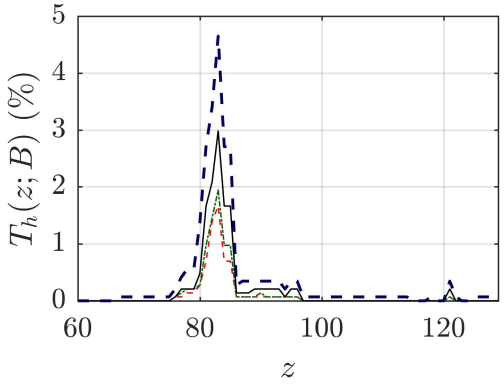

(b) RVT at Phase B.

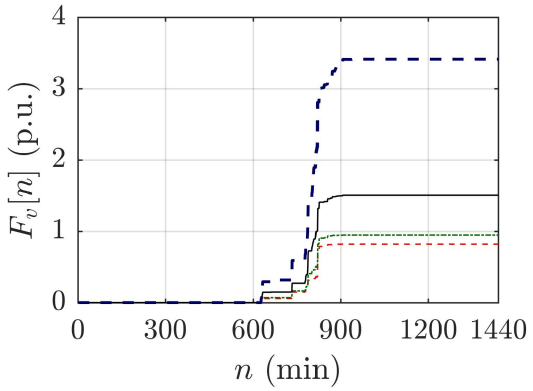

(c) Voltage objective function.

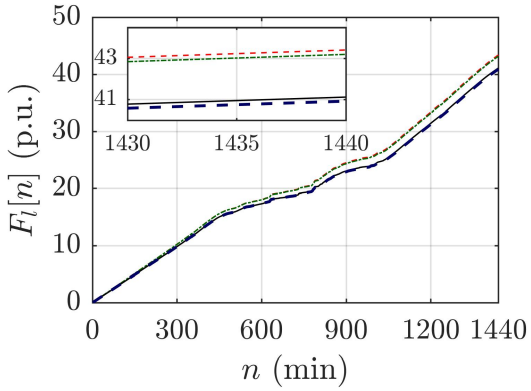

(d) Loss objective function.

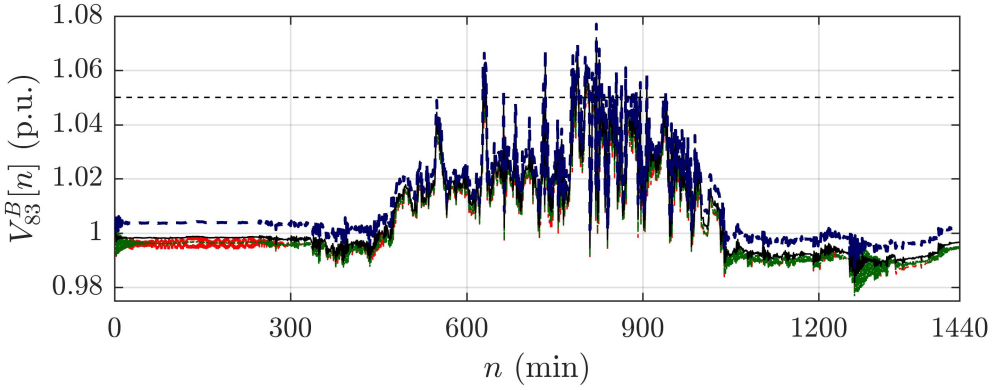

(e) Voltage at $z = 83$, $\phi = \text{B}$.

Source: The author.

the slightly reduced loss does not justify the very worsened voltage regulation, which is illustrated by unfavorable MVV and RVT plots in Figures 58(a)-(b).

It is clear from the results that $H = 3 \sim 7$ (and, as a consequence, $H = 4$ in particular that was obtained via the elbow method) yields a better balance between voltage regulation and loss reduction. Hence, using elbow method-based clustering for partitioning the grid into VCZ has proved to be an effective procedure.

8.5 Energy Savings-Based Payback Analysis

As a final example, it shall be instructive to carry out a simplified economic payback analysis of the proposed method based on the energy savings data computed in the simulation of Section 8.4.3 (see Table 14). It is assumed that, from an economic viewpoint, the local droop control scheme is a baseline case since it is readily available in most PV inverters and commonly used in practice. Hence, payback analysis must be performed by taking into account energy savings with respect to local droop control.

From Table 14, it is seen that the proposed method saves 61.7 kWh daily compared to droop control, which results in 22520.5 kWh yearly savings. It is thus assumed, as a simplification, that a constant yearly cash flow $C = 22520.5 \cdot c_e$ is attained, where the constant c_e is the energy tariff. Now, considering that an investment C_o is directed towards implementing the proposed VC method and taking into account an annual economic depreciation rate r, the payback period T_p (in years) can be computed as follows [216]:

$$T_p = \frac{\ln\left(\frac{C}{C - r \cdot C_o}\right)}{\ln(1 + r)} \tag{8.16}$$

The value of T_p is thus assessed for $C_o \in [1, 3] \times$ R\$ 100,000.00, $r \in [0.1, 3.0]$ % and an assumed tariff of $c_e =$ R\$ 0,671/kWh, which is the current tariff in the state of Goiás, Brazil [217]. Obtained results are presented in Figure 59.

The previously discussed importance of an inexpensive VC implementation (see Sections 8.1.1 and 8.1.3) is further highlighted by the results, which show that attaining a reasonably short payback period mostly depends on C_o. It is also seen that a further advantage of a smaller C_o is a decrease in the payback period margin associated to uncertainty with regard to the depreciation rate. For a more concrete illustration, consider the extreme values of C_o in Figure 59. For the minimum investment, $T_p \in [3.32, 3.54]$ years, whereas $T_p \in [20.06, 30.63]$ years for the maximum value of C_o.

Another useful interpretation can be made of Figure 59. Instead of visualizing T_p as the payback time due to an investment on enhanced energy savings, it can also be pictured as the time taken to recover the capital invested on the enhancement of grid performance and, as a consequence, improvement of customer service. Such interpretation

Figure 59 – Payback period as a function of investment and depreciation rate.

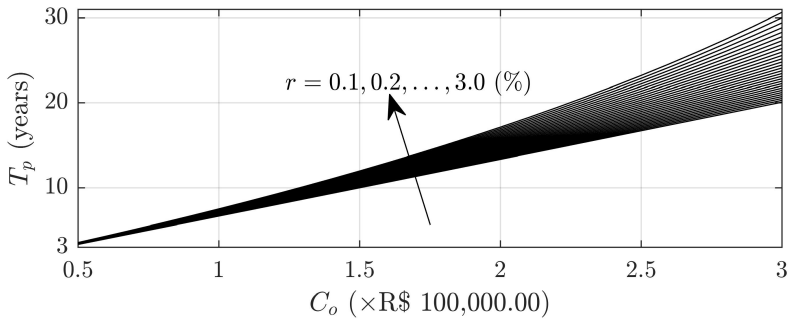

Source: The author.

can be understood by recalling from Section 8.4.3 that, not only does the proposed method improve on losses, it also enhances voltage regulation by reducing the peak RVT in comparison to local droop control. Hence, C_o can also be taken as an investment on performance and improvement of intangible assets (e.g., customer satisfaction) that is eventually covered by power savings after T_p years have passed.

8.6 Conclusion

A hybrid and decentralized method for carrying out optimization-free voltage control with loss reduction by leveraging grid-tied PV inverter reactive power injection has been proposed. Its most relevant innovation consists in using a generation threshold parameter that, coupled with local irradiance measurements, enables the PV inverters to adaptively switch between a Cooperative Markov Decision Process-based voltage regulation mode and a load reactive power compensation-based loss reduction mode. The proposed method was validated via simulation-based experiments considering a 123-bus system with intense PV penetration. Obtained results show that it: (a) outperforms similar methods by yielding comparable voltage regulation with up to 22.82% improvement in power savings; (b) is able to perform well when simple heuristics are used for selecting its parameters; and (c) unlike other decentralized methods, does not require inter-ZC communications or the usage of rougher mathematical approximations.

General Conclusion

This thesis has presented manifold contributions to the engineering of photovoltaic systems, ranging from the small-scale modeling of solar cell electrical characteristics as seen from their output terminals (Part I), passing through the medium-scale problem of maximum power point tracking in photovoltaic generators (Part II), up to large-scale voltage and losses control for distribution grids with distributed generation (Part III). All obtained results have shown that the models and methods proposed in this work resulted in improvements with respect to related state-of-the-art approaches. In what follows, a synthesis of the main achievements relative to each part of this thesis is elaborated.

Part I

The current-voltage characteristic model for solar cells proposed in Chapter 1 is of particular importance for practical applications in which simple-to-use yet sufficiently accurate modeling is required. Such a requirement exists, for instance, when carrying out preliminary circuit design computations. It is widely acknowledged that the standard one-diode model, despite its high accuracy, is somewhat impractical for rapid computations due to its implicit equation and optimization-based parameter extraction. In this sense, explicit models with analytically determinable parameters can be used for performing straightforward computations, albeit with reduced accuracy. The proposed explicit model improves upon the state-of-the-art by yielding consistently accurate modeling over a wide range of solar cell fill factors, which is shown to not be the case for other models in the literature, whose performances worsen for different fill factor values. At last, the model is shown to be the only explicit approach that, aside from yielding closed-form current computations, also enables analytical determination of the solar cell operating point in terms of load resistance. This is a major advantage over previous explicit models, since it allows using analytical equations for simulating solar cells under loading conditions.

Among the two distinctive features of explicit current-voltage characteristic models, namely closed-form computation of current and optimization-free parameter extraction, the former is by far the most important. Hence, if model accuracy is a priority, it is allowable to use optimization for computing model parameters instead of analytical equations. Based on such considerations, a low complexity optimization approach was devised in Chapter 2 for extracting parameters of the previously proposed explicit model. To reduce computational complexity, a virtual notable point condition was introduced which allowed expressing all six model parameters as functions of a single narrow-domain auxiliary parameter, thereby avoiding the higher computational complexity associated to multivariable optimization. In

fact, by using the simple compass search algorithm, the proposed method yields significant accuracy improvements with linear complexity (and correspondingly small execution times). The proposed parameter extraction method is thereby a complementary contribution to the explicit model from Chapter 1, which can be used when greater modeling accuracy is desired and usage of single-variable optimization is permissible.

Part II

A novel high-efficiency maximum power point tracking (MPPT) method applicable to the most common type of photovoltaic system, namely the two-stage converter topology, was developed in Chapter 3. Its main innovation consists in using knowledge of the approximately constant direct current (DC) bus voltage to enhance tracking performance. The method is of significant interest in practical circumstances where an efficient algorithm with simple implementation is desired, which is a requirement not satisfied by algorithms based on soft computing techniques, whose very high efficiencies are overshadowed by their large computational burdens. Since the proposed method is a hybridization of two low complexity legacy algorithms (P&O and FOCV) which are knowingly easy to implement, it is a strong candidate for simple high-efficiency implementations. Simulations and a practical experiment have demonstrated that the proposed method successfully combines the fast response of FOCV with the accurate tracking of P&O. Furthermore, it significantly reduces oscillation losses due to its usage of irradiance and temperature measurements, coupled with the known value of DC bus voltage, to replace proportional-integral voltage control with direct duty cycle control (DDCC). The end result is a competitive method which, despite its straightforward implementation, significantly surpasses P&O and a similar hybrid but non-DDCC algorithm in terms of efficiency.

A type of two-stage photovoltaic system to which the method from Chapter 3 cannot be applied is the photovoltaic water heating system (PWHS), since it is off-grid and does not employ batteries, thereby yielding a variable DC bus voltage. Taking this into account and considering the scarcity of PWHS-specific MPPT methods, a novel method of this type was proposed in Chapter 4. It is unique in that entirely analytical tracking is achieved by using a closed-form equation derived for estimating inverter input impedance, which is then matched to the photovoltaic array maximum power point resistance (whose value is estimated via irradiance and temperature measurements). Aside from having simple implementation requirements which are comparable to those of P&O, simulation results have demonstrated that the proposed method is more efficient than other algorithms previously used in PWHS. Particularly noteworthy features of the proposed method are its very small steady-state oscillations and rapid tracking of ambient conditions, both of which were shown to be direct consequences of its analytical nature. Assuming the availability of low-cost temperature and irradiance sensors, the proposed method could be

easily used for replacing, in a practical PWHS implementation, the less efficient MPPT methods against which it was validated.

Despite its favorable performance, the MPPT method proposed in Chapter 4 has the important limitation of only being applicable to single-phase PWHS. Furthermore, the zero-harmonic load current approximation used for estimating inverter input impedance may cause, for small output filters, significant load mismatch and consequent performance degradation. Both issues were successfully solved in Chapter 5, where generalizations of the method are proposed which consider three-phase systems and incorporate current harmonics into the input impedance estimation. Simulations results demonstrated that the resulting algorithms perform similarly to that from Chapter 4, except that the efficiency reduction due to mismatch at small load impedance angles is avoided. Feasibility requirements are essentially the same as for the zero-harmonic approximation approach, since the only added complexity consists of additional terms in the input impedance equation denominator. Hence, compared to the method proposed in Chapter 4, the approaches presented in Chapter 5 are equally well-suited for practical low complexity implementations.

Part III

The decentralized voltage control method proposed in Chapter 6 is, to the best of our knowledge, the first published attempt at employing the Cooperative Partially Observable Markov Decision Process (C-POMDP) framework for reactive power control of distributed grid-tied photovoltaic generators. This modeling and control framework is often avoided in practice-oriented works due to the double-exponential complexity associated to C-POMDP model learning, which is incompatible with real-time applications. Such difficulty was circumvented in Chapter 6 by specifying an heuristic C-POMDP model corresponding to the voltage control problem and solving it offline with an approximate planning algorithm. This implies a twofold practical advantage: much smaller execution time and, most notably, closed-form control laws which are attributed to the Markov agents prior to the real-time application. By using a voltage sensitivity distance metric, the power grid was clustered into control zones attributed to each agent, which resulted in effective decentralized and cooperative grid voltage control. The obtained simulation results confirmed that the proposed approach yields better-regulated voltage profiles compared to other decentralized heuristic-based methods in the literature.

Despite its effectiveness, it can be argued that the method proposed in Chapter 6 incurs some practical implementation difficulties. In fact, it was discussed that such method requires extensive voltage measurements throughout the grid, special-purpose controllers for implementing agent policies and an upper-level communication network for ensuring cooperation between zone controllers. Taking into account that practical scenarios often imply scarce implementation resources, a different decentralized voltage control

method was proposed in Chapter 7 that is much less resource-intensive. Contrariwise to the previous method, the control zones operate non-cooperatively and special controllers are not required, since the usual inverter droop controller scheme is leveraged for reactive power compensation. To achieve superior voltage regulation than would be possible with strictly local droop control, voltage measurements from only two pilot nodes in each zone were used as upper and lower voltage references for droop control of its associated inverters. The milder implementation requirements just described suggest the proposed method would present better practical feasibility in a smart grid scenario. Validation was carried out via simulation, whose results show that it outperforms local droop control and a recent decentralized method which uses a single pilot node per zone.

Voltage regulation is the only objective considered by the control methods that were proposed in Chapters 6 and 7. It is of interest, however, to simultaneously take into account the problem of active power loss reduction and search for a compromise between both objectives. Since the methods from Chapters 6 and 7 yielded excellent voltage control performances, the idea behind Chapter 8 was adapting them to reduce power loss while maintaining, as much as possible, their favorable voltage regulation properties. To this end, a method was proposed which employs a switching law at each inverter for selecting between the solutions yielded by its associated C-POMDP zone controller and a local heuristic for minimizing active power loss. Furthermore, the original C-POMDP implementation requirements described in Chapter 6 were attenuated by incorporating the double pilot node droop control from Chapter 7 into each C-POMDP voltage control zone. Validation was carried out by comparing the proposed approach via simulation, to similar state-of-the-art methods based on switching and weighting laws for balancing local voltage control and loss reduction. The obtained results have shown that, compared to such local-type methods, the proposed approach yields better performance both with regards to voltage regulation and reduction of the total grid active power loss.

Future Work

Brief pointers to research stemming from each part of this Thesis are as follows:

- Part I: As discussed in Chapter 2, the proposed explicit I-V quadratic model is not adequate for solar cells which significantly deviate from the ODM behavior (e.g., low-FF cells with S-shaped characteristics). A natural step forward consists in developing models which incorporate the analytical advantages of ETPQM and are also able to fit the I-V characteristics of such ill-behaved solar cells.

- Part II: The proposed P&O+SFOCV algorithm is a single possible sensor-aided hibridization between legacy MPPT algorithms. In principle, it is possible to propose analogous approaches which combine a hill-climbing method other than P&O (e.g.,

INC and INR) with a sensor-aided modification of a voltage/current reference-based method other than FOCV (e.g., FSCC); evaluating such possibilities shall be an important extension of the present work. A similar consideration applies to the off-grid MPPT methods that have been proposed: the inverter input impedance equations for analytical load matching have been derived for the most commonly used inverter switching schemes and topologies. It is expected that some generalization, or at least additional results for other relevant inverter schemes, can be obtained.

- Part III: Despite the good voltage regulation and loss reduction performances yielded by the MDP-based methods from Chapters 6 and 8, it must be recognized that the proposed C-POMDP model is specified in a fully heuristic manner. In principle, this is not a major issue: precisely due to the lack of fast-performing algorithms for C-POMDP learning, it is a usual approach in the literature to specify the model heuristically and apply a planning algorithm. However, for the particular application envisaged in this Thesis, it remains to research whether a more structured approach (e.g., via *a priori* Monte Carlo simulation) may be used to help in attributing more consistent values to the model parameters by attenuating reliance on intuition.

Conclusão Geral

Esta tese apresentou várias contribuições à engenharia de sistemas fotovoltaicos, desde a modelagem em pequena escala das características elétricas dos terminais de células solares (Parte I), passando pelo problema em média escala de rastreamento do ponto de máxima potência em geradores fotovoltaicos (Parte II), até o controle em larga escala de tensão e perdas em redes de distribuição com geração distribuída (Parte III). Todos os resultados obtidos demonstram que os modelos e métodos propostos neste trabalho resultam em melhorias com relação a abordagens relacionadas que compõem o estado da arte. No que segue, uma síntese dos principais resultados de cada parte desta tese é dada.

Parte I

O modelo da característica tensão-corrente de células solares proposto no Capítulo 1 é de particular importância para aplicações práticas em que se deseja lançar mão de uma modelagem simples, porém suficientemente precisa. Este requisito ocorre, por exemplo, na realização de cálculos em projeto preliminares de circuitos elétricos. É amplamente reconhecido que o modelo padrão de um diodo, embora detenha elevada acurácia, é pouco prático para cálculos rápidos em função de sua equação implícita e extração de parâmetros baseada em otimização. Nesse sentido, modelos explícitos com parâmetros determináveis analiticamente podem ser utilizados para a realização de cálculos simples, embora com menor acurácia. O modelo explícito proposto é uma melhoria com relação ao estado da arte, provendo modelagem consistentemente precisa para uma ampla faixa de fatores de preenchimento de célula solar, o que não é o caso para outros modelos existentes na literatura, cujos desempenhos apresentam piora para diferentes valores do fator de preenchimento. Por fim, demonstra-se que o modelo é a única abordagem explícita que, além de prover cálculo em forma fechada da corrente, também permite a determinação analítica do ponto de operação da célula solar em função da resistência de carga. Esta é uma grande vantagem com relação a modelos implícitos prévios, pois permite a utilização de equações analíticas na simulação de células solares sob condição de carga.

Dentre as duas características distintivas de modelos explícitos da característica corrente-tensão, quais sejam, o cálculo de corrente em forma fechada e a extração de parâmetros sem emprego de otimização, a primeira é de longe a mais importante. Logo, caso a acurácia do modelo seja prioritária, torna-se permissível substituir a determinação analítica dos parâmetros de modelo por um processo de otimização. Tomando por base tais considerações, uma estratégia para otimização de baixa complexidade computacional foi desenvolvida no Capítulo 2 para extração dos parâmetros do modelo explícito proposto

previamente. Visando redução de complexidade computacional, é introduzida uma condição de ponto notável virtual que permite expressar os seis parâmetros do modelo em função de um único parâmetro auxiliar situado em um domínio estreito, evitando-se a maior complexidade computacional associada à otimização multivariável. Com efeito, utilizando-se o simples algoritmo *compass search*, o método proposto garantiu significativas melhorias de acurácia a custo de uma complexidade linear (e tempos de execução correspondentemente baixos). Nesse sentido, o método para extração de parâmetros proposto é uma contribuição complementar ao modelo explícito do Capítulo 1, podendo ser utilizado caso seja desejada maior acurácia de modelagem e o uso de otimização a uma variável seja permissível.

Parte II

Um novo método de elevada eficiência para rastreamento do ponto de máxima potência (RPMP) aplicável ao tipo mais comum de sistema fotovoltaico, qual seja, a topologia de conversor a dois estágios, foi desenvolvido no Capítulo 3. Sua principal inovação consiste em utilizar o conhecimento da tensão aproximadamente constante do barramento de corrente contínua (CC) para melhorar o desempenho de rastreamento. O método é de significativo interesse para circunstâncias práticas em que se deseja um algoritmo eficiente com implementação simples, requisito este que não é satisfeito por algoritmos baseados em técnicas de computação flexível, cujas eficiências muito elevadas são contrapostas por sua grande demanda de processamento. Sendo o método proposto uma hibridização de dois algoritmos com baixa complexidade (P&O e FOCV) de implementação reconhecidamente acessível, trata-se de um forte candidato para implementações com baixa complexidade e alta eficiência. Foi demonstrado, por meio de simulações e um experimento prático, que o método proposto é bem-sucedido em combinar a rápida resposta do algoritmo FOCV com o rastreamento preciso do algoritmo P&O. Ademais, as perdas por oscilação são significativamente reduzidas devido à utilização de medições de temperatura e irradiância, em combinação com o valor conhecido da tensão do barramento CC, para substituição do controle de tensão proporcional-integral pelo controle direto do ciclo de trabalho (CDCT). O resultado final é um método competitivo que, a despeito de sua implementação simples, supera significativamente, em termos de eficiência, o algoritmo P&O e um método híbrido similar que não se utiliza do mecanismo de CDCT.

Um tipo de sistema fotovoltaico a dois estágios para o qual não se aplica o método proposto no Capítulo 3 é o sistema fotovoltaico para aquecimento de água (SFAA), o que se deve ao fato de ser um sistema *off-grid* que não utiliza baterias e, portanto, de tensão variável no barramento CC. Tomando por base este fato e considerando a escassez de métodos RPMP existentes para SFAA, um novo método deste tipo foi proposto no Capítulo 4. Sua característica distintiva é a realização do rastreamento de modo inteiramente analítico por meio de uma equação em forma fechada deduzida para estimação da impedância

de entrada do inversor, cujo valor é subsequentemente casado à resistência do ponto de máxima potência do arranjo fotovoltaico (cujo valor é estimado via medições de irradiância e temperatura). Além de possuir requisitos simples para implementação (comparáveis àqueles do algoritmo P&O), os resultados de simulação demonstraram que o método proposto é mais eficiente do que outros algoritmos anteriormente utilizados em SFAA. Características particularmente notáveis do método proposto são a sua oscilação em estado estacionário muito pequena e seu rápido rastreamento das condições ambientes, ambas das quais são consequências diretas de sua natureza analítica. Assumindo-se a disponibilidade de sensores de temperatura e irradiância com baixo custo, o método proposto poderia ser facilmente utilizado para substituir, em uma implementação prática de SFAA, os métodos RPMP menos eficientes com que foi comparado.

Apesar de seu desempenho favorável, o método RPMP proposto no Capítulo 4 tem a importante limitação de ser aplicável apenas a SFAA monofásicos. Ademais, a aproximação de ausência harmônicos na corrente de carga utilizada na estimação da impedância de entrada do inversor pode causar, para filtros de saída pequenos, significativo descasamento de carga e, por conseguinte, degradação de desempenho. Ambos problemas foram resolvidos com sucesso no Capítulo 5, em que são propostas generalizações do método que consideram sistemas trifásicos e incorporam harmônicos de corrente à estimação da impedância de entrada. Os resultados obtidos via simulação demonstraram que os algoritmos resultantes entregam desempenho similar àquele do Capítulo 4, exceto pelo fato de que é evitada a redução de eficiência devido ao descasamento em ângulos de carga pequenos. Os requisitos para implementação são essencialmente os mesmos daqueles do método com aproximação de conteúdo harmônico nulo, visto que a única complexidade adicional consiste em termos adicionais no denominador da equação para cálculo da impedância de entrada. Logo, se comparadas ao método proposto no Capítulo 4, as abordagens apresentadas no Capítulo 5 são igualmente adequadas para uso em implementações prática e de baixa complexidade.

Parte III

O método para controle de tensão descentralizado proposto no Capítulo 6 é, até onde temos conhecimento, a primeira tentativa publicada de se empregar a modelagem de Processo de Decisão de Markov Parcialmente Observável Cooperativo (PDMPO-C) ao controle da potência reativa de geradores fotovoltaicos distribuídos conectados à rede. Este *framework* de modelagem e controle é frequentemente evitado em trabalhos com viés prático em função da complexidade duplamente exponencial associada à aprendizagem de modelos PDMPO-C, a qual é incompatível com aplicações em tempo real. Esta dificuldade foi contornada no Capítulo 6 especificando-se um modelo PDMPO-C heurístico correspondente ao problema de controle de tensão e resolvendo-o *offline* por meio de um algoritmo de planejamento aproximado. Este procedimento implica duas vantagens práticas: tempo

de execução muito menor e, mais notavelmente, leis de controle em forma fechada que são atribuídas aos agentes Markov anteriormente à aplicação em tempo real. Utilizando uma métrica de distância baseada em sensibilidade de tensão, a rede foi *clusterizada* em zonas de controle atribuídas a cada agente, o que resultou no controle descentralizado, cooperativo e eficiente de tensão na rede. Os resultados de simulação confirmaram que a abordagem proposta provê perfis de tensão com melhor regulação quando comparada a outros métodos heurísticos descentralizados da literatura.

Apesar da eficácia do método proposto no Capítulo 6, é possível argumentar que sua implementação poderia acarretar dificuldades práticas. De fato, foi discutido que este método requer: medições extensivas de tensão ao longo da rede, controladores dedicados para implementação das políticas de agente e uma rede de comunicação em nível superior para cooperação entre os controladores de zona. Levando em consideração que situações práticas frequentemente implicam escassez de recursos para implementação, outro método para controle descentralizado de tensão com uso muito menos intensivo de recursos é proposto no Capítulo 7. Contrariamente ao método anterior, as zonas de controle operam de maneira não-cooperativa e controladores especiais não são necessários, já que o esquema usual de controlador *droop* dos inversores é aproveitado na compensação de potência reativa. Visando obter melhor regulação de tensão do que seria possível com controle *droop* estritamente local, medidas de tensão tomadas em apenas dois nós piloto por zona foram utilizadas como referências de tensão superior e inferior para o controle *droop* dos inversores da respectiva zona. Os requisitos de implementação mais simples sugerem que o método proposto apresentaria melhor viabilidade prática em um contexto de redes inteligentes. A validação foi realizada por meio de simulação, cujos resultados mostram que o método proposto provê desempenho superior quando comparado ao controle *droop* local e a um recente método descentralizado que utiliza um nó piloto por zona de controle.

A regulação de tensão é o único objetivo considerado pelos métodos de controle propostos nos Capítulos 6 e 7. Todavia, é de grande interesse considerar, simultaneamente, o problema de redução das perdas de potência ativa e buscar um equilíbrio entre ambos objetivos. Como os métodos dos Capítulos 6 e 7 provêem excelente regulação de tensão, a ideia por trás do Capítulo 8 foi adaptá-los de modo a reduzir as perdas ativas e manter, o quanto possível, suas propriedades favoráveis de regulação de tensão. Com esse fim, foi proposto um método que emprega uma lei de chaveamento em cada inversor para selecionar entre as soluções providas por seu respectivo controlador de zona do método PDMPO-C e por uma heurística local para minimização de perdas ativas. Ademais, os requisitos de implementação originalmente descritos no Capítulo 6 para o controle PDMPO-C são atenuados via incorporação, em cada zona de controle de tensão do método PDMPO-C, do controlador *droop* de nó piloto duplo proposto no Capítulo 7. A validação da proposta foi realizada via comparação, através de simulação, a métodos similares do estado da arte que se baseiam em leis de chaveamento e ponderação para balancear controle de tensão

local e redução de perdas. Os resultados obtidos revelaram que, em comparação a tais métodos locais, a abordagem proposta possui melhor desempenho tanto em termos da regulação de tensão quanto na redução das perdas ativas totais na rede.

Trabalhos Futuros

Breves indicações a pesquisas derivadas de cada parte desta Tese são como segue:

- Parte I: Como discutido no Capítulo 2, o modelo I-V quadrático proposto não é adequado para células solares que desviam significativamente do comportamento ODM (e.g, células com baixo fator de preenchimento e características em S). Um natural passo adiante consiste em desenvolver modelos que incorporam as vantagens analíticas do modelo quadrático e também sejam capazes de se ajustarem às características I-V destas células solares de comportamento atípico.

- Parte II: O algoritmo P&O+SFOCV proposto é uma única possível hibridização auxiliada por sensores entre algoritmos MPPT legados. Em princípio, é possível propor-se abordagens análogas que combinem um método *hill-climbing* diferente do P&O (e.g., INC e INR) com uma modificação auxiliada por sensor de um método baseado em referência de tensão/corrente diferente do FOCV (e.g., FSCC); avaliar tais possibilidades consistirá uma importante extensão do presente trabalho. Uma consideração similar aplica-se aos métodos MPPT *off-grid* que foram propostos: as equações de impedância de entrada do inversor para casamento de carga foram demonstradas para os esquemas de chaveamento e topologias de inversor mais comumente utilizados. Espera-se que alguma generalização, ou ao menos resultados adicionais para outros esquemas de inversor relevantes, possam ser obtidos.

- Parte III: Apesar dos bons desempenhos de regulação de tensão e redução de perdas providos pelos métodos baseados em MDP dos Capítulos 6 e 8, deve-se reconhecer que o modelo C-POMDP proposto é especificado de modo inteiramente heurístico. Em princípio, não se trata de um problema grave: precisamente em função da falta de algoritmos rápidos para aprendizagem C-POMDP, uma abordagem comum na literatura é especificar heuristicamente o modelo e aplicar um algoritmo de planejamento. Todavia, para a aplicação particular visada nesta Tese, permanece a possibilidade de se pesquisar o possível uso de uma abordagem mais estruturada (e.g., via simulação Monte Carlo) para que se atenue a dependência em intuição e, com isso, sejam atribuídos valores mais consistentes aos parâmetros do modelo.

Bibliography

1 TIAN, H.; MANCILLA-DAVID, F.; ELLIS, K.; MULJADI, E.; JENKINS, P. A cell-to-module-to-array detailed model for photovoltaic panels. *Solar Energy*, v. 86, n. 9, p. 2695–2706, 2012. ISSN 0038-092X. Cited 4 times in pages 41, 48, 53, and 77.

2 PINDADO, S.; CUBAS, J.; ROIBÁS-MILLÁN, E.; BUGALLO-SIEGEL, F.; SORRIBES-PALMER, F. Assessment of explicit models for different photovoltaic technologies. *Energies*, v. 11, n. 6, 2018. ISSN 1996-1073. Cited 6 times in pages 41, 44, 50, 53, 54, and 68.

3 ORTIZ-CONDE, A.; SÁNCHEZ, F. J. G.; MUCI, J. New method to extract the model parameters of solar cells from the explicit analytic solutions of their illuminated i–v characteristics. *Solar Energy Materials and Solar Cells*, v. 90, n. 3, p. 352–361, 2006. ISSN 0927-0248. Cited 2 times in pages 41 and 53.

4 PENG, L.; SUN, Y.; MENG, Z.; WANG, Y.; XU, Y. A new method for determining the characteristics of solar cells. *Journal of Power Sources*, v. 227, p. 131–136, 2013. ISSN 0378-7753. Cited 2 times in pages 41 and 53.

5 FRANCO, R.; VIEIRA, F. Analytical method for extraction of the single-diode model parameters for photovoltaic panels from datasheet data. *Electronics Letters*, v. 54, n. 8, p. 519–521, 2018. Cited 2 times in pages 41 and 53.

6 LUN, S.-X.; DU, C.-J.; YANG, G.-H.; WANG, S.; GUO, T.-T.; SANG, J.-S.; LI, J.-P. An explicit approximate i–v characteristic model of a solar cell based on padé approximants. *Solar Energy*, v. 92, p. 147–159, 2013. ISSN 0038-092X. Cited 2 times in pages 41 and 53.

7 CUBAS, J.; PINDADO, S.; VICTORIA, M. On the analytical approach for modeling photovoltaic systems behavior. *Journal of Power Sources*, v. 247, p. 467–474, 2014. ISSN 0378-7753. Cited 2 times in pages 41 and 53.

8 HARA, S. Parameter extraction of single-diode model from module datasheet information using temperature coefficients. *IEEE Journal of Photovoltaics*, v. 11, n. 1, p. 213–218, 2021. Cited 2 times in pages 41 and 53.

9 SALEEM, H.; KARMALKAR, S. An analytical method to extract the physical parameters of a solar cell from four points on the illuminated j-v curve. *IEEE Electron Device Letters*, v. 30, n. 4, p. 349–352, 2009. Cited 2 times in pages 41 and 53.

10 XIAO, W.; LIND, M.; DUNFORD, W.; CAPEL, A. Real-time identification of optimal operating points in photovoltaic power systems. *IEEE Transactions on Industrial Electronics*, v. 53, n. 4, p. 1017–1026, 2006. Cited in page 41.

11 ANDREI, H.; IVANOVICI, T.; PREDUSCA, G.; DIACONU, E.; ANDREI, P. Curve fitting method for modeling and analysis of photovoltaic cells characteristics. In: *Proceedings of 2012 IEEE International Conference on Automation, Quality and Testing, Robotics*. 2012. p. 307–312. Cited in page 41.

12 SZABO, R.; GONTEAN, A. Photovoltaic cell and module i-v characteristic approximation using bézier curves. *Applied Sciences*, v. 8, n. 5, 2018. ISSN 2076-3417. Cited in page 41.

13 DAS, A. K. An explicit j–v model of a solar cell using equivalent rational function form for simple estimation of maximum power point voltage. *Solar Energy*, v. 98, p. 400–403, 2013. ISSN 0038-092X. Cited 2 times in pages 41 and 54.

14 DAS, A. K. An explicit j–v model of a solar cell for simple fill factor calculation. *Solar Energy*, v. 85, n. 9, p. 1906–1909, 2011. ISSN 0038-092X. Cited 2 times in pages 41 and 54.

15 SAETRE, T. O.; MIDTGARD, O.-M.; YORDANOV, G. H. A new analytical solar cell i–v curve model. *Renewable Energy*, v. 36, n. 8, p. 2171–2176, 2011. ISSN 0960-1481. Cited 2 times in pages 41 and 54.

16 KARMALKAR, S.; HANEEFA, S. A physically based explicit j-v model of a solar cell for simple design calculations. *IEEE Electron Device Letters*, v. 29, n. 5, p. 449–451, 2008. Cited 5 times in pages 41, 43, 44, 49, and 54.

17 PINDADO, S.; CUBAS, J. Simple mathematical approach to solar cell/panel behavior based on datasheet information. *Renewable Energy*, v. 103, p. 729–738, 2017. ISSN 0960-1481. Cited 5 times in pages 41, 43, 44, 49, and 54.

18 AKBABA, M.; ALATTAWI, M. A. A new model for i–v characteristic of solar cell generators and its applications. *Solar Energy Materials and Solar Cells*, v. 37, n. 2, p. 123–132, 1995. ISSN 0927-0248. Cited 5 times in pages 41, 43, 44, 49, and 54.

19 JERANKO, T.; TRIBUTSCH, H.; SARICIFTCI, N.; HUMMELEN, J. Patterns of efficiency and degradation of composite polymer solar cells. *Solar Energy Materials and Solar Cells*, v. 83, n. 2, p. 247–262, 2004. ISSN 0927-0248. The development of organic and polymer photovoltaics. Cited 2 times in pages 44 and 59.

20 EASWARAKHANTHAN, T.; BOTTIN, J.; BOUHOUCH, I.; BOUTRIT, C. Nonlinear minimization algorithm for determining the solar cell parameters with microcomputers. *International Journal of Solar Energy*, Taylor & Francis, v. 4, n. 1, p. 1–12, 1986. Cited 2 times in pages 44 and 59.

21 SPECTROLAB PHOTOVOLTAIC PRODUCTS. *26.8% Improved Triple Junction (ITJ) Solar Cells*. Sylmar, CA, USA, 2008. Available at: <https://www.spectrolab.com/DataSheets/TNJCell/tnj.pdf>. Cited 3 times in pages 44, 49, and 59.

22 ROMERO, B.; POZO, G. del; ARREDONDO, B.; MARTÍN-MARTÍN, D.; GORDOA, M. P. R.; PICKERING, A.; PÉREZ-RODRÍGUEZ, A.; BARRENA, E.; GARCÍA-SÁNCHEZ, F. J. S-shaped $I - V$ characteristics of organic solar cells: Solving mazhari's lumped-parameter equivalent circuit model. *IEEE Transactions on Electron Devices*, v. 64, n. 11, p. 4622–4627, 2017. Cited 2 times in pages 48 and 67.

23 De Soto, W.; KLEIN, S.; BECKMAN, W. Improvement and validation of a model for photovoltaic array performance. *Solar Energy*, v. 80, n. 1, p. 78–88, 2006. ISSN 0038-092X. Cited 3 times in pages 48, 53, and 77.

24 SIDDIQUE, H. A. B.; XU, P.; DONCKER, R. W. D. Parameter extraction algorithm for one-diode model of pv panels based on datasheet values. In: *2013 International Conference on Clean Electrical Power (ICCEP)*. 2013. p. 7–13. Cited 3 times in pages 48, 77, and 109.

25 MASOUM, M.; DEHBONEI, H.; FUCHS, E. Theoretical and experimental analyses of photovoltaic systems with voltageand current-based maximum power-point tracking. *IEEE Transactions on Energy Conversion*, v. 17, n. 4, p. 514–522, 2002. Cited 2 times in pages 48 and 108.

26 FEDERAL UNIVERSITY OF GOIáS. *Estação Meteorológica - EMC/UFG*. Brazil, 2021. Available at: <https://sites.google.com/site/sfvemcufg/weather-station>. Cited 3 times in pages 49, 98, and 153.

27 VILLALVA, M. G.; GAZOLI, J. R.; FILHO, E. R. Comprehensive approach to modeling and simulation of photovoltaic arrays. *IEEE Transactions on Power Electronics*, v. 24, n. 5, p. 1198–1208, 2009. Cited 14 times in pages 50, 53, 54, 58, 59, 60, 61, 62, 63, 64, 65, 66, 67, and 68.

28 HUO, Y.; GRUOSSO, G. Hardware-in-the-loop framework for validation of ancillary service in microgrids: Feasibility, problems and improvement. *IEEE Access*, v. 7, p. 58104–58112, 2019. Cited in page 50.

29 MESSENGER, R.; ABTAHI, A. *Photovoltaic Systems Engineering*. : CRC Press, 2017. ISBN 9781498772808. Cited 2 times in pages 53 and 77.

30 HUMADA, A. M.; DARWEESH, S. Y.; MOHAMMED, K. G.; KAMIL, M.; MOHAMMED, S. F.; KASIM, N. K.; TAHSEEN, T. A.; AWAD, O. I.; MEKHILEF, S. Modeling of pv system and parameter extraction based on experimental data: Review and investigation. *Solar Energy*, v. 199, p. 742–760, 2020. ISSN 0038-092X. Cited in page 53.

31 ABDEL-BASSET, M.; MOHAMED, R.; MIRJALILI, S.; CHAKRABORTTY, R. K.; RYAN, M. J. Solar photovoltaic parameter estimation using an improved equilibrium optimizer. *Solar Energy*, v. 209, p. 694–708, 2020. ISSN 0038-092X. Cited in page 53.

32 CÁRDENAS, A. A.; CARRASCO, M.; MANCILLA-DAVID, F.; STREET, A.; CÁRDENAS, R. Experimental parameter extraction in the single-diode photovoltaic model via a reduced-space search. *IEEE Transactions on Industrial Electronics*, v. 64, n. 2, p. 1468–1476, 2017. Cited in page 53.

33 GUDE, S.; JANA, K. C. Parameter extraction of photovoltaic cell using an improved cuckoo search optimization. *Solar Energy*, v. 204, p. 280–293, 2020. ISSN 0038-092X. Cited in page 53.

34 IBRAHIM, I. A.; HOSSAIN, M. J.; DUCK, B. C.; FELL, C. J. An adaptive wind-driven optimization algorithm for extracting the parameters of a single-diode pv cell model. *IEEE Transactions on Sustainable Energy*, v. 11, n. 2, p. 1054–1066, 2020. Cited in page 53.

35 JIAO, S.; CHONG, G.; HUANG, C.; HU, H.; WANG, M.; HEIDARI, A. A.; CHEN, H.; ZHAO, X. Orthogonally adapted harris hawks optimization for parameter estimation of photovoltaic models. *Energy*, v. 203, p. 117804, 2020. ISSN 0360-5442. Cited in page 53.

36 KUMAR, C.; RAJ, T. D.; PREMKUMAR, M.; RAJ, T. D. A new stochastic slime mould optimization algorithm for the estimation of solar photovoltaic cell parameters. *Optik*, v. 223, p. 165277, 2020. ISSN 0030-4026. Cited in page 53.

37 MESSAOUD, R. B. Extraction of uncertain parameters of single and double diode model of a photovoltaic panel using salp swarm algorithm. *Measurement*, v. 154, p. 107446, 2020. ISSN 0263-2241. Cited in page 53.

38 PREMKUMAR, M.; BABU, T. S.; UMASHANKAR, S.; SOWMYA, R. A new metaphor-less algorithms for the photovoltaic cell parameter estimation. *Optik*, v. 208, p. 164559, 2020. ISSN 0030-4026. Cited in page 53.

39 RAM, J. P.; BABU, T. S.; DRAGICEVIC, T.; RAJASEKAR, N. A new hybrid bee pollinator flower pollination algorithm for solar pv parameter estimation. *Energy Conversion and Management*, v. 135, p. 463–476, 2017. ISSN 0196-8904. Cited in page 53.

40 SUBUDHI, B.; PRADHAN, R. Bacterial foraging optimization approach to parameter extraction of a photovoltaic module. *IEEE Transactions on Sustainable Energy*, v. 9, n. 1, p. 381–389, 2018. Cited in page 53.

41 TAO, Y.; BAI, J.; PACHAURI, R. K.; SHARMA, A. Parameter extraction of photovoltaic modules using a heuristic iterative algorithm. *Energy Conversion and Management*, v. 224, p. 113386, 2020. ISSN 0196-8904. Cited in page 53.

42 VENKATESWARI, R.; RAJASEKAR, N. Review on parameter estimation techniques of solar photovoltaic systems. *International Transactions on Electrical Energy Systems*, v. 31, n. 11, p. e13113, 2021. Cited in page 53.

43 VIEIRA, F. H. T.; CORRêA, H. P. Methods for estimating one-diode model parameters of photovoltaic panels and adjusting to non-nominal conditions. *Advances in Electrical and Computer Engineering*, v. 19, n. 1, p. 27–34, 2019. Cited 13 times in pages 53, 54, 58, 59, 60, 61, 62, 63, 64, 65, 66, 67, and 68.

44 RHOUMA, M. B.; GASTLI, A.; Ben Brahim, L.; TOUATI, F.; BENAMMAR, M. A simple method for extracting the parameters of the pv cell single-diode model. *Renewable Energy*, v. 113, p. 885–894, 2017. ISSN 0960-1481. Cited 13 times in pages 53, 54, 58, 59, 60, 61, 62, 63, 64, 65, 66, 67, and 68.

45 KOLDA, T. G.; LEWIS, R. M.; TORCZON, V. Optimization by direct search: New perspectives on some classical and modern methods. *SIAM Review*, v. 45, n. 3, p. 385–482, 2003. Cited in page 58.

46 HANHWA Q CELLS. *Full-square monocrystalline solar cell*. Bitterfeld-Wolfen, Germany, 2013. Available at: <https://www.spectrolab.com/DataSheets/TNJCell/tnj.pdf>. Cited in page 59.

47 ECKER, B.; EGELHAAF, H.-J.; STEIM, R.; PARISI, J.; HAUFF, E. von. Understanding s-shaped current–voltage characteristics in organic solar cells containing a tiox interlayer with impedance spectroscopy and equivalent circuit analysis. *The Journal of Physical Chemistry C*, v. 116, n. 31, p. 16333–16337, 2012. Cited in page 59.

48 SAIVE, R. S-shaped current–voltage characteristics in solar cells: A review. *IEEE Journal of Photovoltaics*, v. 9, n. 6, p. 1477–1484, 2019. Cited in page 67.

49 COLMENAR-SANTOS, A.; REINO-RIO, C.; BORGE-DIEZ, D.; COLLADO-FERNáNDEZ, E. Distributed generation: A review of factors that can contribute most to achieve a scenario of dg units embedded in the new distribution networks. *Renewable and Sustainable Energy Reviews*, v. 59, p. 1130 – 1148, 2016. ISSN 1364-0321. Cited 3 times in pages 71, 102, and 138.

50 ALLAN, G.; EROMENKO, I.; GILMARTIN, M.; KOCKAR, I.; MCGREGOR, P. The economics of distributed energy generation: A literature review. *Renewable and Sustainable Energy Reviews*, v. 42, p. 543 – 556, 2015. ISSN 1364-0321. Cited 3 times in pages 71, 102, and 138.

51 El Chaar, L.; LAMONT, L.; El Zein, N. Review of photovoltaic technologies. *Renewable and Sustainable Energy Reviews*, v. 15, n. 5, p. 2165 – 2175, 2011. ISSN 1364-0321. Cited 3 times in pages 71, 102, and 138.

52 CHATTERJEE, S.; KUMAR, P.; CHATTERJEE, S. A techno-commercial review on grid connected photovoltaic system. *Renewable and Sustainable Energy Reviews*, v. 81, p. 2371 – 2397, 2018. ISSN 1364-0321. Cited 3 times in pages 71, 102, and 138.

53 Pereira da Silva, P.; DANTAS, G.; PEREIRA, G. I.; CâMARA, L.; De Castro, N. J. Photovoltaic distributed generation – an international review on diffusion, support policies, and electricity sector regulatory adaptation. *Renewable and Sustainable Energy Reviews*, v. 103, p. 30 – 39, 2019. ISSN 1364-0321. Cited 3 times in pages 71, 102, and 138.

54 RIGO, P. D.; SILUK, J. C. M.; LACERDA, D. P.; ROSA, C. B.; REDISKE, G. Is the success of small-scale photovoltaic solar energy generation achievable in brazil? *Journal of Cleaner Production*, v. 240, p. 118243, 2019. ISSN 0959-6526. Cited 3 times in pages 71, 102, and 138.

55 GHAFOOR, A.; MUNIR, A. Design and economics analysis of an off-grid pv system for household electrification. *Renewable and Sustainable Energy Reviews*, v. 42, p. 496–502, 2015. ISSN 1364-0321. Cited 2 times in pages 71 and 102.

56 VENKATRAMANAN, D.; JOHN, V. Dynamic modeling and analysis of buck converter based solar pv charge controller for improved mppt performance. *IEEE Transactions on Industry Applications*, v. 55, n. 6, p. 6234–6246, 2019. Cited 2 times in pages 71 and 103.

57 ANKIT; SAHOO, S. K.; SUKCHAI, S.; YANINE, F. F. Review and comparative study of single-stage inverters for a pv system. *Renewable and Sustainable Energy Reviews*, v. 91, p. 962–986, 2018. ISSN 1364-0321. Cited 3 times in pages 71, 84, and 129.

58 KIM, K. A.; SEO, G.-S.; CHO, B.-H.; KREIN, P. T. Photovoltaic hot-spot detection for solar panel substrings using ac parameter characterization. *IEEE Transactions on Power Electronics*, v. 31, n. 2, p. 1121–1130, 2016. Cited 2 times in pages 71 and 103.

59 KIM, J.-S.; KWON, J.-M.; KWON, B.-H. High-efficiency two-stage three-level grid-connected photovoltaic inverter. *IEEE Transactions on Industrial Electronics*, v. 65, n. 3, p. 2368–2377, 2018. Cited 2 times in pages 71 and 103.

60 WU, T.-F.; CHANG, C.-H.; LIN, L.-C.; KUO, C.-L. Power loss comparison of single- and two-stage grid-connected photovoltaic systems. *IEEE Transactions on Energy Conversion*, v. 26, n. 2, p. 707–715, 2011. Cited 2 times in pages 71 and 103.

61 DING, G.; GAO, F.; TIAN, H.; MA, C.; CHEN, M.; HE, G.; LIU, Y. Adaptive dc-link voltage control of two-stage photovoltaic inverter during low voltage ride-through operation. *IEEE Transactions on Power Electronics*, v. 31, n. 6, p. 4182–4194, 2016. Cited 2 times in pages 71 and 79.

62 DEBNATH, D.; CHATTERJEE, K. Two-stage solar photovoltaic-based stand-alone scheme having battery as energy storage element for rural deployment. *IEEE Transactions on Industrial Electronics*, v. 62, n. 7, p. 4148–4157, 2015. Cited 2 times in pages 71 and 79.

63 TEODORESCU, R.; LISERRE, M.; RODRIGUEZ, P. *Grid Converters for Photovoltaic and Wind Power Systems.* : Wiley, 2011. (Wiley - IEEE). ISBN 9780470057513. Cited in page 71.

64 BOLLIPO, R. B.; MIKKILI, S.; BONTHAGORLA, P. K. Hybrid, optimal, intelligent and classical pv mppt techniques: A review. *CSEE Journal of Power and Energy Systems*, v. 7, n. 1, p. 9–33, 2021. Cited 6 times in pages 71, 72, 75, 81, 83, and 103.

65 YAP, K. Y.; SARIMUTHU, C. R.; LIM, J. M.-Y. Artificial intelligence based mppt techniques for solar power system: A review. *Journal of Modern Power Systems and Clean Energy*, v. 8, n. 6, p. 1043–1059, 2020. Cited 3 times in pages 71, 72, and 103.

66 SUBUDHI, B.; PRADHAN, R. A comparative study on maximum power point tracking techniques for photovoltaic power systems. *IEEE Transactions on Sustainable Energy*, v. 4, n. 1, p. 89–98, 2013. Cited 3 times in pages 71, 72, and 103.

67 ALI, A. I. M.; MOHAMED, H. R. A. Improved p&o mppt algorithm with efficient open-circuit voltage estimation for two-stage grid-integrated pv system under realistic solar radiation. *International Journal of Electrical Power & Energy Systems*, v. 137, p. 107805, 2022. ISSN 0142-0615. Cited 3 times in pages 72, 73, and 75.

68 JATELY, V.; AZZOPARDI, B.; JOSHI, J.; Venkateswaran V, B.; SHARMA, A.; ARORA, S. Experimental analysis of hill-climbing mppt algorithms under low irradiance levels. *Renewable and Sustainable Energy Reviews*, v. 150, p. 111467, 2021. ISSN 1364-0321. Cited 3 times in pages 72, 103, and 121.

69 ISHAQUE, K.; SALAM, Z.; LAUSS, G. The performance of perturb and observe and incremental conductance maximum power point tracking method under dynamic weather conditions. *Applied Energy*, v. 119, p. 228–236, 2014. ISSN 0306-2619. Cited in page 72.

70 ELGENDY, M. A.; ZAHAWI, B.; ATKINSON, D. J. Assessment of the incremental conductance maximum power point tracking algorithm. *IEEE Transactions on Sustainable Energy*, v. 4, n. 1, p. 108–117, 2013. Cited 3 times in pages 72, 93, and 132.

71 ELGENDY, M. A.; ZAHAWI, B.; ATKINSON, D. J. Assessment of perturb and observe mppt algorithm implementation techniques for pv pumping applications. *IEEE Transactions on Sustainable Energy*, v. 3, n. 1, p. 21–33, 2012. Cited 6 times in pages 72, 103, 110, 115, 116, and 126.

72 KAVYA, M.; JAYALALITHA, S. Developments in perturb and observe algorithm for maximum power point tracking in photo voltaic panel: A review. *Archives of Computational Methods in Engineering*, v. 28, n. 4, p. 2447–2457, Jun 2021. ISSN 1886-1784. Cited in page 72.

73 HUSAIN, M. A.; TARIQ, A.; HAMEED, S.; ARIF, M. S. B.; JAIN, A. Comparative assessment of maximum power point tracking procedures for photovoltaic systems. *Green Energy & Environment*, v. 2, n. 1, p. 5–17, 2017. ISSN 2468-0257. Cited in page 72.

74 ELBASET, A. A.; ALI, H.; SATTAR, M. A.-E.; KHALED, M. Implementation of a modified perturb and observe maximum power point tracking algorithm for photovoltaic system using an embedded microcontroller. *IET Renewable Power Generation*, v. 10, n. 4, p. 551–560, 2016. Cited 3 times in pages 72, 73, and 75.

75 KILLI, M.; SAMANTA, S. Modified perturb and observe mppt algorithm for drift avoidance in photovoltaic systems. *IEEE Transactions on Industrial Electronics*, v. 62, n. 9, p. 5549–5559, 2015. Cited 3 times in pages 72, 73, and 75.

76 GAMMOUDI, R.; BRAHMI, H.; HASNAOUI, O. Developed and stm implementation of modified p&o mppt technique for a pv system over sun. *EPE Journal*, Taylor & Francis, v. 29, n. 3, p. 99–119, 2019. Cited 4 times in pages 72, 73, 75, and 135.

77 BELKAID, A.; COLAK, I.; KAYISLI, K. Implementation of a modified p&o-mppt algorithm adapted for varying solar radiation conditions. *Electrical Engineering*, v. 99, n. 3, p. 839–846, Sep 2017. ISSN 1432-0487. Cited 3 times in pages 72, 73, and 75.

78 MAMARELIS, E.; PETRONE, G.; SPAGNUOLO, G. A two-steps algorithm improving the p&o steady state mppt efficiency. *Applied Energy*, v. 113, p. 414–421, 2014. ISSN 0306-2619. Cited 3 times in pages 72, 73, and 75.

79 CHEN, K.; TIAN, S.; CHENG, Y.; BAI, L. An improved mppt controller for photovoltaic system under partial shading condition. *IEEE Transactions on Sustainable Energy*, v. 5, n. 3, p. 978–985, 2014. Cited 3 times in pages 72, 73, and 75.

80 FEMIA, N.; GRANOZIO, D.; PETRONE, G.; SPAGNUOLO, G.; VITELLI, M. Predictive & adaptive mppt perturb and observe method. *IEEE Transactions on Aerospace and Electronic Systems*, v. 43, n. 3, p. 934–950, 2007. Cited 3 times in pages 72, 73, and 75.

81 PIEGARI, L.; RIZZO, R. Adaptive perturb and observe algorithm for photovoltaic maximum power point tracking. *IET Renewable Power Generation*, Institution of Engineering and Technology, v. 4, p. 317–328(11), July 2010. ISSN 1752-1416. Cited 3 times in pages 72, 73, and 75.

82 JIANG, Y.; QAHOUQ, J. A. A.; HASKEW, T. A. Adaptive step size with adaptive-perturbation-frequency digital mppt controller for a single-sensor photovoltaic solar system. *IEEE Transactions on Power Electronics*, v. 28, n. 7, p. 3195–3205, 2013. Cited 3 times in pages 72, 73, and 75.

83 MANOHARAN, P.; SUBRAMANIAM, U.; BABU, T. S.; PADMANABAN, S.; HOLM-NIELSEN, J. B.; MITOLO, M.; RAVICHANDRAN, S. Improved perturb and observation maximum power point tracking technique for solar photovoltaic power generation systems. *IEEE Systems Journal*, v. 15, n. 2, p. 3024–3035, 2021. Cited 3 times in pages 72, 73, and 75.

84 KUMAR, N.; SINGH, B.; PANIGRAHI, B. K. Llmlf-based control approach and lpo mppt technique for improving performance of a multifunctional three-phase two-stage grid

integrated pv system. *IEEE Transactions on Sustainable Energy*, v. 11, n. 1, p. 371–380, 2020. Cited 3 times in pages 72, 73, and 75.

85 KUMAR, N.; SINGH, B.; PANIGRAHI, B. K.; XU, L. Leaky-least-logarithmic-absolute-difference-based control algorithm and learning-based inc mppt technique for grid-integrated pv system. *IEEE Transactions on Industrial Electronics*, v. 66, n. 11, p. 9003–9012, 2019. Cited 3 times in pages 72, 73, and 75.

86 KUMAR, N.; SINGH, B.; PANIGRAHI, B. K.; CHAKRABORTY, C.; SURYAWANSHI, H. M.; VERMA, V. Integration of solar pv with low-voltage weak grid system: Using normalized laplacian kernel adaptive kalman filter and learning based inc algorithm. *IEEE Transactions on Power Electronics*, v. 34, n. 11, p. 10746–10758, 2019. Cited 3 times in pages 72, 73, and 75.

87 KUMAR, N.; SINGH, B.; WANG, J.; PANIGRAHI, B. K. A framework of l-hc and am-mkf for accurate harmonic supportive control schemes. *IEEE Transactions on Circuits and Systems I: Regular Papers*, v. 67, n. 12, p. 5246–5256, 2020. Cited 3 times in pages 72, 73, and 75.

88 KUMAR, N.; SINGH, B.; PANIGRAHI, B. K. Integration of solar pv with low-voltage weak grid system: Using maximize-m kalman filter and self-tuned p&o algorithm. *IEEE Transactions on Industrial Electronics*, v. 66, n. 11, p. 9013–9022, 2019. Cited 3 times in pages 72, 73, and 75.

89 HUSAIN, M. A.; JAIN, A.; TARIQ, A. A novel fast mutable duty (fmd) mppt technique for solar pv system with reduced searching area. *Journal of Renewable and Sustainable Energy*, v. 8, n. 5, p. 054703, 2016. Cited 2 times in pages 72 and 73.

90 HUSAIN, M. A.; JAIN, A.; TARIQ, A.; IQBAL, A. Fast and precise global maximum power point tracking techniques for photovoltaic system. *IET Renewable Power Generation*, v. 13, n. 14, p. 2569–2579, 2019. Cited 3 times in pages 72, 73, and 75.

91 BAŞOğLU, M. E. An improved 0.8 voc model based gmppt technique for module level photovoltaic power optimizers. *IEEE Transactions on Industry Applications*, v. 55, n. 2, p. 1913–1921, 2019. Cited 3 times in pages 72, 73, and 75.

92 HARRAG, A.; MESSALTI, S. Pso-based smc variable step size p&o mppt controller for pv systems under fast changing atmospheric conditions. *International Journal of Numerical Modelling: Electronic Networks, Devices and Fields*, v. 32, n. 5, p. e2603, 2019. E2603 JNM-18-0219.R1. Cited 3 times in pages 72, 74, and 75.

93 MOHAMMADINODOUSHAN, M.; ABBASSI, R.; JERBI, H.; Waly Ahmed, F.; Abdalqadir kh ahmed, H.; REZVANI, A. A new mppt design using variable step size perturb and observe method for pv system under partially shaded conditions by modified shuffled frog leaping algorithm- smc controller. *Sustainable Energy Technologies and Assessments*, v. 45, p. 101056, 2021. ISSN 2213-1388. Cited 3 times in pages 72, 74, and 75.

94 NGO, V.-Q.-B.; LATIFI, M.; ABBASSI, R.; JERBI, H.; OHSHIMA, K.; KHAKSAR, M. Improved krill herd algorithm based sliding mode mppt controller for variable step size p&o method in pv system under simultaneous change of irradiance and temperature. *Journal of the Franklin Institute*, v. 358, n. 7, p. 3491–3511, 2021. ISSN 0016-0032. Cited 3 times in pages 72, 74, and 75.

95 RADJAI, T.; GAUBERT, J. P.; RAHMANI, L.; MEKHILEF, S. Experimental verification of p&o mppt algorithm with direct control based on fuzzy logic control using cuk converter. *International Transactions on Electrical Energy Systems*, v. 25, n. 12, p. 3492–3508, 2015. Cited 3 times in pages 72, 74, and 75.

96 GOUABI, H.; HAZZAB, A.; HABBAB, M.; REZKALLAH, M.; CHANDRA, A. Experimental implementation of a novel scheduling algorithm for adaptive and modified p&o mppt controller using fuzzy logic for wecs. *International Journal of Adaptive Control and Signal Processing*, v. 35, n. 9, p. 1732–1753, 2021. Cited 3 times in pages 72, 74, and 75.

97 AURAIRAT, A.; PLANGKLANG, B. An alternative perturbation and observation modifier maximum power point tracking of pv systems. *Symmetry*, v. 14, n. 1, 2022. ISSN 2073-8994. Cited 3 times in pages 72, 74, and 75.

98 ZAINURI, M. A. A. M.; RADZI, M. A. M.; SOH, A. C.; RAHIM, N. A. Development of adaptive perturb and observe-fuzzy control maximum power point tracking for photovoltaic boost dc–dc converter. *IET Renewable Power Generation*, v. 8, n. 2, p. 183–194, 2014. Cited 3 times in pages 72, 74, and 75.

99 HASSAN, T.-u.; ABBASSI, R.; JERBI, H.; MEHMOOD, K.; TAHIR, M. F.; CHEEMA, K. M.; ELAVARASAN, R. M.; ALI, F.; KHAN, I. A. A novel algorithm for mppt of an isolated pv system using push pull converter with fuzzy logic controller. *Energies*, v. 13, n. 15, 2020. ISSN 1996-1073. Cited 3 times in pages 72, 74, and 75.

100 HARRAG, A.; MESSALTI, S. Variable step size modified p&o mppt algorithm using ga-based hybrid offline/online pid controller. *Renewable and Sustainable Energy Reviews*, v. 49, p. 1247–1260, 2015. ISSN 1364-0321. Cited 3 times in pages 72, 74, and 75.

101 MOHANTY, S.; SUBUDHI, B.; RAY, P. K. A grey wolf-assisted perturb & observe mppt algorithm for a pv system. *IEEE Transactions on Energy Conversion*, v. 32, n. 1, p. 340–347, 2017. Cited 3 times in pages 72, 74, and 75.

102 SUNDARESWARAN, K.; VIGNESHKUMAR, V.; SANKAR, P.; SIMON, S. P.; NAYAK, P. S. R.; PALANI, S. Development of an improved p&o algorithm assisted through a colony of foraging ants for mppt in pv system. *IEEE Transactions on Industrial Informatics*, v. 12, n. 1, p. 187–200, 2016. Cited 3 times in pages 72, 74, and 75.

103 PILAKKAT, D.; KANTHALAKSHMI, S. An improved p&o algorithm integrated with artificial bee colony for photovoltaic systems under partial shading conditions. *Solar Energy*, v. 178, p. 37–47, 2019. ISSN 0038-092X. Cited 3 times in pages 72, 74, and 75.

104 MATHI, D. K.; CHINTHAMALLA, R. A hybrid global maximum power point tracking method based on butterfly particle swarm optimization and perturb and observe algorithms for a photovoltaic system under partially shaded conditions. *International Transactions on Electrical Energy Systems*, v. 30, n. 10, p. e12543, 2020. Cited 3 times in pages 72, 74, and 75.

105 TESHOME, D. F.; LEE, C. H.; LIN, Y. W.; LIAN, K. L. A modified firefly algorithm for photovoltaic maximum power point tracking control under partial shading. *IEEE Journal of Emerging and Selected Topics in Power Electronics*, v. 5, n. 2, p. 661–671, 2017. Cited 3 times in pages 72, 74, and 75.

106 SHER, H. A.; MURTAZA, A. F.; NOMAN, A.; ADDOWEESH, K. E.; AL-HADDAD, K.; CHIABERGE, M. A new sensorless hybrid mppt algorithm based on fractional short-circuit current measurement and p&o mppt. *IEEE Transactions on Sustainable Energy*, v. 6, n. 4, p. 1426–1434, 2015. Cited 4 times in pages 72, 74, 75, and 76.

107 KOLLIMALLA, S. K.; MISHRA, M. K. A novel adaptive p&o mppt algorithm considering sudden changes in the irradiance. *IEEE Transactions on Energy Conversion*, v. 29, n. 3, p. 602–610, 2014. Cited 4 times in pages 72, 74, 75, and 76.

108 MORADI, M. H.; REISI, A. R. A hybrid maximum power point tracking method for photovoltaic systems. *Solar Energy*, v. 85, n. 11, p. 2965–2976, 2011. ISSN 0038-092X. Cited 10 times in pages 72, 74, 75, 76, 85, 93, 95, 96, 97, and 98.

109 BAIG, M. Q.; KHAN, H. A.; AHSAN, S. M. Evaluation of solar module equivalent models under real operating conditions—a review. *Journal of Renewable and Sustainable Energy*, v. 12, n. 1, p. 012701, 2020. Cited in page 76.

110 BLAIR, N.; DIORIO, N.; FREEMAN, J.; GILMAN, P.; JANZOU, S.; NEISES, T.; WAGNER., M. System advisor model (sam) general description (version 2017.9.5). *NREL/ TP-6A20-70414*, 2018. Cited 2 times in pages 77 and 85.

111 GLASNER, I.; APPELBAUM, J. Advantage of boost vs. buck topology for maximum power point tracker in photovoltaic systems. In: *Proceedings of 19th Convention of Electrical and Electronics Engineers in Israel*. 1996. p. 355–358. Cited in page 78.

112 MAKSIMOVIC, D.; STANKOVIC, A.; THOTTUVELIL, V.; VERGHESE, G. Modeling and simulation of power electronic converters. *Proceedings of the IEEE*, v. 89, n. 6, p. 898–912, 2001. Cited in page 78.

113 ERICKSON, R.; MAKSIMOVIĆ, D. *Fundamentals of Power Electronics*. : Springer International Publishing, 2020. ISBN 9783030438791. Cited 4 times in pages 78, 104, 105, and 127.

114 HAUKE, B. Basic calculation of a boost converter's power stage. *Application Report SLVA372C*, p. 1–49, 2014. Cited 2 times in pages 79 and 105.

115 SERBAN, E.; ORDONEZ, M.; PONDICHE, C. Dc-bus voltage range extension in 1500 v photovoltaic inverters. *IEEE Journal of Emerging and Selected Topics in Power Electronics*, v. 3, n. 4, p. 901–917, 2015. Cited in page 79.

116 PANDE, M.; JOOS, G.; JIN, H.; ZIOGAS, P. Output voltage integral control technique for compensating a non-ideal dc bus in voltage source inverters. In: *Proceedings Eighth Annual Applied Power Electronics Conference and Exposition,*. 1993. p. 761–767. Cited 2 times in pages 79 and 103.

117 ALI, M.; YAQOOB, M.; CAO, L.; LOO, K. H. Disturbance-observer-based dc-bus voltage control for ripple mitigation and improved dynamic response in two-stage single-phase inverter system. *IEEE Transactions on Industrial Electronics*, v. 66, n. 9, p. 6836–6845, 2019. Cited 2 times in pages 79 and 103.

118 LEVRON, Y.; CANADAY, S.; ERICKSON, R. W. Bus voltage control with zero distortion and high bandwidth for single-phase solar inverters. *IEEE Transactions on Power Electronics*, v. 31, n. 1, p. 258–269, 2016. Cited 3 times in pages 79, 80, and 103.

119 DAVIS, T. T.; DEY, A. Investigation on extending the dc bus utilization of a single-source five-level inverter with single capacitor-fed h-bridge per phase. *IEEE Transactions on Power Electronics*, v. 34, n. 3, p. 2914–2922, 2019. Cited 2 times in pages 79 and 103.

120 FEMIA, N.; PETRONE, G.; SPAGNUOLO, G.; VITELLI, M. A technique for improving p&o mppt performances of double-stage grid-connected photovoltaic systems. *IEEE Transactions on Industrial Electronics*, v. 56, n. 11, p. 4473–4482, 2009. Cited 3 times in pages 79, 98, and 115.

121 HUANG, Y.-P. A rapid maximum power measurement system for high-concentration photovoltaic modules using the fractional open-circuit voltage technique and controllable electronic load. *IEEE Journal of Photovoltaics*, v. 4, n. 6, p. 1610–1617, 2014. Cited in page 81.

122 MOHAPATRA, A.; NAYAK, B.; DAS, P.; MOHANTY, K. B. A review on mppt techniques of pv system under partial shading condition. *Renewable and Sustainable Energy Reviews*, v. 80, p. 854–867, 2017. ISSN 1364-0321. Cited in page 84.

123 KOUCHAKI, A.; IMAN-EINI, H.; ASAEI, B. A new maximum power point tracking strategy for pv arrays under uniform and non-uniform insolation conditions. *Solar Energy*, v. 91, p. 221–232, 2013. ISSN 0038-092X. Cited 2 times in pages 84 and 129.

124 ALQAISI, Z.; MAHMOUD, Y. Comprehensive study of partially shaded pv modules with overlapping diodes. *IEEE Access*, v. 7, p. 172665–172675, 2019. Cited 2 times in pages 85 and 129.

125 MOHAN, N.; UNDELAND, T.; ROBBINS, W. *Power Electronics: Converters, Applications, and Design.* : Wiley, 2003. (Power Electronics: Converters, Applications, and Design). ISBN 9780471429081. Cited 7 times in pages 87, 105, 107, 122, 123, 128, and 129.

126 CLIFT, D. H.; SUEHRCKE, H. Control optimization of pv powered electric storage and heat pump water heaters. *Solar Energy*, v. 226, p. 489–500, 2021. ISSN 0038-092X. Cited in page 102.

127 NORTON, B. Solar water heaters: A review of systems research and design innovation. *Green*, v. 1, n. 2, p. 189–207, 2011. Cited in page 102.

128 JOSHI, S. S.; DHOBLE, A. S. Photovoltaic -thermal systems (pvt): Technology review and future trends. *Renewable and Sustainable Energy Reviews*, v. 92, p. 848–882, 2018. ISSN 1364-0321. Cited in page 102.

129 MATUSKA, T.; SOUREK, B. Performance analysis of photovoltaic water heating system. *International Journal of Photoenergy*, Hindawi, v. 2017, p. 7540250, May 2017. ISSN 1110-662X. Cited 2 times in pages 102 and 104.

130 ALAJMI, A.; RODRíGUEZ, S.; SAILOR, D. Transforming a passive house into a net-zero energy house: a case study in the pacific northwest of the u.s. *Energy Conversion and Management*, v. 172, p. 39–49, 2018. ISSN 0196-8904. Cited in page 102.

131 LI, S.; ATTOU, A.; YANG, Y.; GENG, D. A maximum power point tracking control strategy with variable weather parameters for photovoltaic systems with dc bus. *Renewable Energy*, v. 74, p. 478–488, 2015. ISSN 0960-1481. Cited in page 103.

132 G.S. CHENG, S. L. MULKEYM e A.J. CHOW. *Smart microgrids and dual-output off-grid power inverters with DC source flexibility*. 2018. US Patent 9871379B2. Cited 3 times in pages 103, 106, and 110.

133 B. L. BUTLER. *Photovoltaic DC heater systems*. 2016. US Patent 9518759B2. Cited 2 times in pages 103 and 110.

134 A. H. FANNEY e B. P. DOUGHERTY. *Photovoltaic solar water heating system*. 1994. US Patent 5293447A. Cited 3 times in pages 103, 104, and 110.

135 M. NEWMAN e G. NEWMAN. *Solar Photovoltaic Water Heating System*. 2014. US Patent 0153913A1. Cited 2 times in pages 103 and 104.

136 CYBOENERGY. *Off-Grid CI-Mini-1200H for Electrical Water Heaters*. Rancho Cordova, CA, USA, 2019. Available at: <http://www.cyboenergy.com/products/cimini1200h_spec.html>. Cited in page 103.

137 RASHID, M. *Power Electronics: Devices, Circuits, and Applications*. : Pearson, 2014. ISBN 9780133125900. Cited 3 times in pages 105, 106, and 128.

138 AKAGI, H.; WATANABE, E.; AREDES, M. *Instantaneous Power Theory and Applications to Power Conditioning*. : Wiley, 2017. (IEEE Press Series on Power and Energy Systems). ISBN 9781119307211. Cited 2 times in pages 107 and 128.

139 CHUNWEI, C.; PUFENG, A.; YUXING, G.; FANGANG, M. Three-phase four-wire inverter topology with neutral point voltage stable module for unbalanced load inhibition. *Journal of Power Electronics*, v. 18, n. 5, p. 1315–1324, 2018. Cited in page 127.

140 LOPEZ-FLORES, D. R.; DURAN-GOMEZ, J. L.; CHACON-MURGUIA, M. I. A mechanical sensorless mppt algorithm for a wind energy conversion system based on a modular multilayer perceptron and a processor-in-the-loop approach. *Electric Power Systems Research*, v. 186, p. 106409, 2020. ISSN 0378-7796. Cited in page 134.

141 FEKKAK, B.; MENAA, M.; BOUSSAHOUA, B.; REKIOUA, D. Processor in the loop test for algorithms designed to control power electronics converters used in grid-connected photovoltaic system. *International Transactions on Electrical Energy Systems*, v. 30, n. 2, p. e12227, 2020. E12227 ITEES-19-0080.R3. Cited in page 134.

142 THOMSON, M.; INFIELD, D. Impact of widespread photovoltaics generation on distribution systems. *IET Renewable Power Generation*, Institution of Engineering and Technology, v. 1, p. 33–40(7), March 2007. ISSN 1752-1416. Cited in page 138.

143 ZHAO, C.; GU, C.; LI, F.; DALE, M. Understanding lv network voltage distribution-uk smart grid demonstration experience. In: *2015 IEEE Power Energy Society Innovative Smart Grid Technologies Conference (ISGT)*. 2015. p. 1–5. Cited in page 138.

144 DEMIROK, E.; SERA, D.; TEODORESCU, R.; RODRIGUEZ, P.; BORUP, U. Evaluation of the voltage support strategies for the low voltage grid connected pv generators. In: *2010 IEEE Energy Conversion Congress and Exposition*. 2010. p. 710–717. Cited 3 times in pages 138, 164, and 185.

145 HOSSAIN, M. I.; YAN, R.; SAHA, T. K. Investigation of the interaction between step voltage regulators and large-scale photovoltaic systems regarding voltage regulation and unbalance. *IET Renewable Power Generation*, Institution of Engineering and Technology, v. 10, p. 299–309(10), March 2016. ISSN 1752-1416. Cited 2 times in pages 138 and 152.

146 YANG, Q.; WANG, G.; SADEGHI, A.; GIANNAKIS, G. B.; SUN, J. Two-timescale voltage control in distribution grids using deep reinforcement learning. *IEEE Transactions on Smart Grid*, v. 11, n. 3, p. 2313–2323, 2020. Cited in page 138.

147 LIU, X.; AICHHORN, A.; LIU, L.; LI, H. Coordinated control of distributed energy storage system with tap changer transformers for voltage rise mitigation under high photovoltaic penetration. *IEEE Transactions on Smart Grid*, v. 3, n. 2, p. 897–906, 2012. Cited 2 times in pages 138 and 152.

148 WANG, L.; BAI, F.; YAN, R.; SAHA, T. K. Real-time coordinated voltage control of pv inverters and energy storage for weak networks with high pv penetration. *IEEE Transactions on Power Systems*, v. 33, n. 3, p. 3383–3395, 2018. Cited in page 138.

149 KRATA, J.; SAHA, T. K. Real-time coordinated voltage support with battery energy storage in a distribution grid equipped with medium-scale pv generation. *IEEE Transactions on Smart Grid*, v. 10, n. 3, p. 3486–3497, 2019. Cited in page 138.

150 GRILLO, S.; PIEVATOLO, A.; TIRONI, E. Optimal storage scheduling using markov decision processes. *IEEE Transactions on Sustainable Energy*, v. 7, n. 2, p. 755–764, 2016. Cited in page 138.

151 LAN, Y.; GUAN, X.; WU, J. Online decentralized and cooperative dispatch for multi-microgrids. *IEEE Transactions on Automation Science and Engineering*, v. 17, n. 1, p. 450–462, 2020. Cited 2 times in pages 138 and 140.

152 Wu, J.; Guan, X. Coordinated multi-microgrids optimal control algorithm for smart distribution management system. *IEEE Transactions on Smart Grid*, v. 4, n. 4, p. 2174–2181, 2013. Cited 2 times in pages 138 and 140.

153 ANTONIADOU-PLYTARIA, K. E.; KOUVELIOTIS-LYSIKATOS, I. N.; GEORGILAKIS, P. S.; HATZIARGYRIOU, N. D. Distributed and decentralized voltage control of smart distribution networks: Models, methods, and future research. *IEEE Transactions on Smart Grid*, v. 8, n. 6, p. 2999–3008, 2017. Cited 6 times in pages 138, 139, 164, 165, 185, and 186.

154 FARIVAR, M.; NEAL, R.; CLARKE, C.; LOW, S. Optimal inverter var control in distribution systems with high pv penetration. In: *2012 IEEE Power and Energy Society General Meeting*. 2012. p. 1–7. Cited 2 times in pages 138 and 164.

155 MOLINA-GARCíA, n.; MASTROMAURO, R. A.; GARCíA-SáNCHEZ, T.; PUGLIESE, S.; LISERRE, M.; STASI, S. Reactive power flow control for pv inverters voltage support in lv distribution networks. *IEEE Transactions on Smart Grid*, v. 8, n. 1, p. 447–456, 2017. Cited 3 times in pages 138, 164, and 185.

156 DESHMUKH, S.; NATARAJAN, B.; PAHWA, A. Voltage/var control in distribution networks via reactive power injection through distributed generators. *IEEE Transactions on Smart Grid*, v. 3, n. 3, p. 1226–1234, 2012. Cited 3 times in pages 138, 164, and 185.

157 Li, C.; Jin, C.; Sharma, R. Coordination of pv smart inverters using deep reinforcement learning for grid voltage regulation. In: *2019 18th IEEE International Conference On Machine Learning And Applications (ICMLA)*. 2019. p. 1930–1937. Cited 3 times in pages 138, 140, and 164.

158 HELOU, R. E.; KALATHIL, D.; XIE, L. Fully decentralized reinforcement learning-based control of photovoltaics in distribution grids for joint provision of real and reactive power. *IEEE Open Access Journal of Power and Energy*, v. 8, p. 175–185, 2021. Cited 3 times in pages 138, 140, and 165.

159 FARIVAR, M.; ZHO, X.; CHEN, L. Local voltage control in distribution systems: An incremental control algorithm. In: *2015 IEEE International Conference on Smart Grid Communications (SmartGridComm)*. 2015. p. 732–737. Cited 2 times in pages 139 and 164.

160 KEKATOS, V.; ZHANG, L.; GIANNAKIS, G. B.; BALDICK, R. Voltage regulation algorithms for multiphase power distribution grids. *IEEE Transactions on Power Systems*, v. 31, n. 5, p. 3913–3923, 2016. Cited 3 times in pages 139, 164, and 185.

161 LI, H.; LI, F.; XU, Y.; RIZY, D. T.; KUECK, J. D. Adaptive voltage control with distributed energy resources: Algorithm, theoretical analysis, simulation, and field test verification. *IEEE Transactions on Power Systems*, v. 25, n. 3, p. 1638–1647, 2010. Cited 3 times in pages 139, 164, and 185.

162 ROBBINS, B. A.; HADJICOSTIS, C. N.; DOMíNGUEZ-GARCíA, A. D. A two-stage distributed architecture for voltage control in power distribution systems. *IEEE Transactions on Power Systems*, v. 28, n. 2, p. 1470–1482, 2013. Cited 3 times in pages 139, 164, and 185.

163 YU, L.; CZARKOWSKI, D.; LEON, F. de. Optimal distributed voltage regulation for secondary networks with dgs. *IEEE Transactions on Smart Grid*, v. 3, n. 2, p. 959–967, 2012. Cited 2 times in pages 139 and 165.

164 FAZIO, A. R. D.; FUSCO, G.; RUSSO, M. Decentralized control of distributed generation for voltage profile optimization in smart feeders. *IEEE Transactions on Smart Grid*, v. 4, n. 3, p. 1586–1596, 2013. Cited 2 times in pages 139 and 165.

165 DALL'ANESE, E.; SIMONETTO, A. Optimal power flow pursuit. *IEEE Transactions on Smart Grid*, v. 9, n. 2, p. 942–952, 2018. Cited 3 times in pages 139, 165, and 188.

166 MAKNOUNINEJAD, A.; QU, Z. Realizing unified microgrid voltage profile and loss minimization: A cooperative distributed optimization and control approach. *IEEE Transactions on Smart Grid*, v. 5, n. 4, p. 1621–1630, 2014. Cited 3 times in pages 139, 165, and 186.

167 UTKARSH, K.; TRIVEDI, A.; SRINIVASAN, D.; REINDL, T. A consensus-based distributed computational intelligence technique for real-time optimal control in smart distribution grids. *IEEE Transactions on Emerging Topics in Computational Intelligence*, v. 1, n. 1, p. 51–60, 2017. Cited 3 times in pages 139, 165, and 186.

168 ZHENG, W.; WU, W.; ZHANG, B.; SUN, H.; LIU, Y. A fully distributed reactive power optimization and control method for active distribution networks. *IEEE Transactions on Smart Grid*, v. 7, n. 2, p. 1021–1033, 2016. Cited 3 times in pages 139, 165, and 186.

169 ABESSI, A.; VAHIDINASAB, V.; GHAZIZADEH, M. S. Centralized support distributed voltage control by using end-users as reactive power support. *IEEE Transactions on Smart Grid*, v. 7, n. 1, p. 178–188, 2016. Cited 3 times in pages 139, 165, and 188.

170 NAYERIPOUR, M.; FALLAHZADEH-ABARGHOUEI, H.; WAFFENSCHMIDT, E.; HASANVAND, S. Coordinated online voltage management of distributed generation using network partitioning. *Electric Power Systems Research*, v. 141, p. 202–209, 2016. ISSN 0378-7796. Cited 3 times in pages 139, 140, and 165.

171 YEH, H.-G.; GAYME, D. F.; LOW, S. H. Adaptive var control for distribution circuits with photovoltaic generators. *IEEE Transactions on Power Systems*, v. 27, n. 3, p. 1656–1663, 2012. Cited 15 times in pages 139, 140, 156, 157, 158, 159, 162, 165, 187, 189, 195, 196, 197, 198, and 199.

172 OLIVIER, F.; ARISTIDOU, P.; ERNST, D.; CUTSEM, T. V. Active management of low-voltage networks for mitigating overvoltages due to photovoltaic units. *IEEE Transactions on Smart Grid*, v. 7, n. 2, p. 926–936, 2016. Cited 11 times in pages 139, 140, 156, 157, 158, 159, 160, 162, 163, 165, and 186.

173 Corrêa, H. P.; Vieira, F. H. T. Matrix-based generalization for power-mismatch newton-raphson load flow computations with arbitrary number of phases. *IEEE Access*, v. 8, p. 40261–40268, 2020. Cited in page 141.

174 CENELEC. *EN 50438 Standard. Requirements for Micro-Generating Plants to be Connected in Parallel with Public Low-Voltage Distribution Networks*. Brussels, Belgium, 2014. Cited 2 times in pages 141 and 186.

175 MURPHY, K. *Machine Learning: A Probabilistic Perspective*. : MIT Press, 2012. (Adaptive Computation and Machine Learning series). ISBN 9780262018029. Cited in page 142.

176 BERNSTEIN, D. S.; ZILBERSTEIN, S.; IMMERMAN, N. The complexity of decentralized control of markov decision processes. In: *Proceedings of the Sixteenth Conference on Uncertainty in Artificial Intelligence*. San Francisco, CA, USA: Morgan Kaufmann Publishers Inc., 2000. (UAI'00), p. 32–37. ISBN 1558607099. Cited 2 times in pages 144 and 149.

177 DIBANGOYE, J.; BUFFET, O. Learning to act in decentralized partially observable MDPs. In: DY, J.; KRAUSE, A. (Ed.). *Proceedings of the 35th International Conference on Machine Learning*. : PMLR, 2018. (Proceedings of Machine Learning Research, v. 80), p. 1233–1242. Cited in page 144.

178 DIBANGOYE, J. S.; BUFFET, O. Learning to act in continuous dec-pomdps. In: *JFPDA*. 2018. Cited in page 144.

179 NAIR, R.; TAMBE, M.; YOKOO, M.; PYNADATH, D.; MARSELLA, S. Taming decentralized pomdps: Towards efficient policy computation for multiagent settings. In: *Proceedings of the 18th International Joint Conference on Artificial Intelligence*. San Francisco, CA, USA: Morgan Kaufmann Publishers Inc., 2003. (IJCAI'03), p. 705–711. Cited 4 times in pages 144, 145, 146, and 149.

180 Lagonotte, P.; Sabonnadiere, J. C.; Leost, J. .; Paul, J. . Structural analysis of the electrical system: application to secondary voltage control in france. *IEEE Transactions on Power Systems*, v. 4, n. 2, p. 479–486, 1989. Cited 3 times in pages 149, 170, and 236.

181 Di Fazio, A. R.; Russo, M.; De Santis, M. Zoning evaluation for voltage control in smart distribution networks. In: *2018 IEEE International Conference on Environment and Electrical Engineering and 2018 IEEE Industrial and Commercial Power Systems Europe (EEEIC / I CPS Europe)*. 2018. p. 1–6. Cited 3 times in pages 149, 150, and 169.

182 MAIMON, O.; ROKACH, L. *Data Mining and Knowledge Discovery Handbook*. : Springer US, 2006. ISBN 9780387254654. Cited 2 times in pages 150 and 170.

183 IEEE POWER ENGINEERING SOCIETY. *IEEE 123 Bus Test Feeder*. 1992. Cited 3 times in pages 151, 153, and 154.

184 BRODéN, D. A.; PARIDARI, K.; NORDSTRöM, L. Matlab applications to generate synthetic electricity load profiles of office buildings and detached houses. In: *2017 IEEE Innovative Smart Grid Technologies - Asia (ISGT-Asia)*. 2017. p. 1–6. Cited in page 153.

185 ANEEL. *Module 8 of the Procedures for Distribution of Electrical Energy in the National Electric System (PRODIST)*. 12. ed. Brazil, 2021. Cited in page 155.

186 MA, R.; CHEN, H.-H.; HUANG, Y.-R.; MENG, W. Smart grid communication: Its challenges and opportunities. *IEEE Transactions on Smart Grid*, v. 4, n. 1, p. 36–46, 2013. Cited in page 162.

187 PICCIARIELLO, A.; ALVEHAG, K.; SöDER, L. Impact of network regulation on the incentive for dg integration for the dso: Opportunities for a transition toward a smart grid. *IEEE Transactions on Smart Grid*, v. 6, n. 4, p. 1730–1739, 2015. Cited in page 162.

188 RAZAVI, S. E.; RAHIMI, E.; JAVADI, M. S.; NEZHAD, A. E.; LOTFI, M.; SHAFIE-KHAH, M.; CATALãO, J. P. Impact of distributed generation on protection and voltage regulation of distribution systems: A review. *Renewable and Sustainable Energy Reviews*, v. 105, p. 157–167, 2019. ISSN 1364-0321. Cited 2 times in pages 164 and 185.

189 TAYAB, U. B.; ROSLAN, M. A. B.; HWAI, L. J.; KASHIF, M. A review of droop control techniques for microgrid. *Renewable and Sustainable Energy Reviews*, v. 76, p. 717–727, 2017. ISSN 1364-0321. Cited 5 times in pages 164, 165, 173, 176, and 194.

190 KULMALA, A.; REPO, S.; JäRVENTAUSTA, P. Coordinated voltage control in distribution networks including several distributed energy resources. *IEEE Transactions on Smart Grid*, v. 5, n. 4, p. 2010–2020, 2014. Cited 2 times in pages 164 and 185.

191 CHAI, Y.; GUO, L.; WANG, C.; ZHAO, Z.; DU, X.; PAN, J. Network partition and voltage coordination control for distribution networks with high penetration of distributed pv units. *IEEE Transactions on Power Systems*, v. 33, n. 3, p. 3396–3407, 2018. Cited 2 times in pages 165 and 188.

192 BERNSTEIN, A.; REYES-CHAMORRO, L.; Le Boudec, J.-Y.; PAOLONE, M. A composable method for real-time control of active distribution networks with explicit power setpoints. part i: Framework. *Electric Power Systems Research*, v. 125, p. 254–264, 2015. ISSN 0378-7796. Cited 2 times in pages 165 and 188.

193 BOLOGNANI, S.; CARLI, R.; CAVRARO, G.; ZAMPIERI, S. Distributed reactive power feedback control for voltage regulation and loss minimization. *IEEE Transactions on Automatic Control*, v. 60, n. 4, p. 966–981, 2015. Cited in page 165.

194 DALL'ANESE, E.; DHOPLE, S. V.; GIANNAKIS, G. B. Photovoltaic inverter controllers seeking ac optimal power flow solutions. *IEEE Transactions on Power Systems*, v. 31, n. 4, p. 2809–2823, 2016. Cited 2 times in pages 165 and 188.

195 ROBBINS, B. A.; DOMíNGUEZ-GARCíA, A. D. Optimal reactive power dispatch for voltage regulation in unbalanced distribution systems. *IEEE Transactions on Power Systems*, v. 31, n. 4, p. 2903–2913, 2016. Cited in page 165.

196 CHAMANA, M.; CHOWDHURY, B. H.; JAHANBAKHSH, F. Distributed control of voltage regulating devices in the presence of high pv penetration to mitigate ramp-rate issues. *IEEE Transactions on Smart Grid*, v. 9, n. 2, p. 1086–1095, 2018. Cited 2 times in pages 165 and 186.

197 CHRISTAKOU, K.; TOMOZEI, D.-C.; BOUDEC, J.-Y. L.; PAOLONE, M. Gecn: Primary voltage control for active distribution networks via real-time demand-response. *IEEE Transactions on Smart Grid*, v. 5, n. 2, p. 622–631, 2014. Cited in page 165.

198 PACHANAPAN, P.; ANAYA-LARA, O.; DYSKO, A.; LO, K. L. Adaptive zone identification for voltage level control in distribution networks with dg. *IEEE Transactions on Smart Grid*, v. 3, n. 4, p. 1594–1602, 2012. Cited in page 165.

199 FAZIO, A. R. D.; RISI, C.; RUSSO, M.; SANTIS, M. D. Coordinated optimization for zone-based voltage control in distribution grids. *IEEE Transactions on Industry Applications*, v. 58, n. 1, p. 173–184, 2022. Cited 6 times in pages 165, 168, 170, 171, 173, and 176.

200 MASSOUD, S. P.; PROAKIS, J. *Digital Communications*. : McGraw-Hill Education, 2007. ISBN 9780072957167. Cited in page 169.

201 SCHNEIDER, K. P.; MATHER, B. A.; PAL, B. C.; TEN, C.-W.; SHIREK, G. J.; ZHU, H.; FULLER, J. C.; PEREIRA, J. L. R.; OCHOA, L. F.; ARAUJO, L. R. de; DUGAN, R. C.; MATTHIAS, S.; PAUDYAL, S.; MCDERMOTT, T. E.; KERSTING, W. Analytic considerations and design basis for the ieee distribution test feeders. *IEEE Transactions on Power Systems*, v. 33, n. 3, p. 3181–3188, 2018. Cited in page 174.

202 MARANO, A.; ORTEGA, J. M.; RAMOS, J. L. M.; TREBOLLE, D. Voltage control of active distribution networks by means of dispersed generation. In: *CIRED 2012 Workshop: Integration of Renewables into the Distribution Grid*. 2012. p. 1–4. Cited in page 174.

203 SINHA, R. S.; WEI, Y.; HWANG, S.-H. A survey on lpwa technology: Lora and nb-iot. *ICT Express*, v. 3, n. 1, p. 14–21, 2017. ISSN 2405-9595. Cited in page 177.

204 IEEE POWER ENGINEERING SOCIETY. *IEEE 13 Bus Test Feeder*. 1992. Cited 2 times in pages 181 and 182.

205 GUERRERO, J. M.; VASQUEZ, J. C.; MATAS, J.; VICUNA, L. G. de; CASTILLA, M. Hierarchical control of droop-controlled ac and dc microgrids—a general approach toward standardization. *IEEE Transactions on Industrial Electronics*, v. 58, n. 1, p. 158–172, 2011. Cited in page 185.

206 YAZDANIAN, M.; MEHRIZI-SANI, A. Distributed control techniques in microgrids. *IEEE Transactions on Smart Grid*, v. 5, n. 6, p. 2901–2909, 2014. Cited 2 times in pages 185 and 186.

207 ZHANG, Z.; CHOW, M.-Y. Convergence analysis of the incremental cost consensus algorithm under different communication network topologies in a smart grid. *IEEE Transactions on Power Systems*, v. 27, n. 4, p. 1761–1768, 2012. Cited in page 186.

208 CORRêA, H. P.; VIEIRA, F. H. T. Cooperative markov decision process for voltage control of grid-tied photovoltaic generators with reactive power support. *IEEE Transactions on Sustainable Energy*, v. 13, n. 2, p. 919–933, 2022. Cited 2 times in pages 186 and 198.

209 TONKOSKI, R.; LOPES, L. A. Impact of active power curtailment on overvoltage prevention and energy production of pv inverters connected to low voltage residential feeders. *Renewable Energy*, v. 36, n. 12, p. 3566–3574, 2011. ISSN 0960-1481. Cited in page 186.

210 HRAIZ, M. D.; GARCíA, J. A. M.; CASTAñEDA, R. J.; MUHSEN, H. Optimal pv size and location to reduce active power losses while achieving very high penetration level with improvement in voltage profile using modified jaya algorithm. *IEEE Journal of Photovoltaics*, v. 10, n. 4, p. 1166–1174, 2020. Cited in page 186.

211 AHN, C.; PENG, H. Decentralized voltage control to minimize distribution power loss of microgrids. *IEEE Transactions on Smart Grid*, v. 4, n. 3, p. 1297–1304, 2013. Cited 2 times in pages 187 and 188.

212 KRYONIDIS, G. C.; DEMOULIAS, C. S.; PAPAGIANNIS, G. K. A nearly decentralized voltage regulation algorithm for loss minimization in radial mv networks with high dg penetration. *IEEE Transactions on Sustainable Energy*, v. 7, n. 4, p. 1430–1439, 2016. Cited 2 times in pages 187 and 189.

213 TURITSYN, K.; SULC, P.; BACKHAUS, S.; CHERTKOV, M. Options for control of reactive power by distributed photovoltaic generators. *Proceedings of the IEEE*, v. 99, n. 6, p. 1063–1073, 2011. Cited 9 times in pages 187, 189, 190, 191, 194, 196, 197, 198, and 199.

214 TURITSYN, K.; SULC, P.; BACKHAUS, S.; CHERTKOV, M. Local control of reactive power by distributed photovoltaic generators. In: *2010 First IEEE International Conference on Smart Grid Communications*. 2010. p. 79–84. Cited 3 times in pages 187, 194, and 195.

215 MARUTHO, D.; HANDAKA, S. H.; WIJAYA, E.; MULJONO. The determination of cluster number at k-mean using elbow method and purity evaluation on headline

news. In: *2018 International Seminar on Application for Technology of Information and Communication*. 2018. p. 533–538. Cited in page 192.

216 NEWNAN, D.; LAVELLE, J.; ESCHENBACH, T. *Engineering Economic Analysis*. : Oxford University Press, 2014. ISBN 9780199339273. Cited in page 203.

217 ANEEL. *Ranking de tarifas*. Brazil, 2022. Available at: <https://portalrelatorios.aneel.gov.br/luznatarifa/rankingtarifas>. Cited in page 203.

Appendix

APPENDIX A – Constant-Power Load Impedance for Varying Power Angle

The simulations carried out in Section 5.2.3 consider fixed values of *rated* active power (P_x) and voltage (V_x) for varying load power angles. To obtain the required load impedance magnitude $|Z_l|$, let $Z_l = R_l + jX_l$. Then, $P_x = V_R^2/R$, where $V_R = (R_l/|Z_l|) \cdot V_x$. Manipulating these expressions and recalling that $R_l = |Z_l| \cos\theta_l$, it follows that:

$$|Z_l| = \frac{V_x^2}{P_x} \cos\theta_l \tag{A.1}$$

which is the required load impedance magnitude.

APPENDIX B – Proof of $\Gamma_{ij}^{rr} \geq \Gamma_{ij}^{rs}$

In what follows, the proof of **Lemma 2** makes use of the assumption that $\Gamma_{ii}^{rs} \approx \Gamma_{ii}^{sr}$ and $\Gamma_{ii}^{rr} \approx \Gamma_{ii}^{ss}$. This can be safely considered for usual power systems due to approximate symmetry of the lines connected to each phase of any given node. Hence, no loss of generality is incurred.

Lemma 2: For any $i \in \mathcal{I}$ and $r, s \in \Phi$, the sensitivity of V_i^r with respect to Q_i^s is maximum for $r = s$. In other words, at the same node, sensitivity of voltage at a given phase is greater with respect to its associated reactive power injection, i.e., $\Gamma_{ii}^{rs} \leq \Gamma_{ii}^{rr}$.

Proof: First, recall the definition of electrical distance:

$$d_{ij}^{rs} = -\ln\left(\frac{\Gamma_{ij}^{rs}\Gamma_{ji}^{sr}}{\Gamma_{ii}^{rs}\Gamma_{jj}^{rs}}\right) \tag{B.1}$$

Since Equation B.1 is a distance metric, it satisfies the triangular inequality [180]. For this reason, it is immediate that $0 = d_{ii}^{rr} \leq d_{ii}^{rs}$, which can be expanded as:

$$0 \leq -\ln\left(\frac{\Gamma_{ii}^{rs}\Gamma_{ii}^{sr}}{\Gamma_{ii}^{rr}\Gamma_{jj}^{ss}}\right) \tag{B.2}$$

Using the aforementioned assumptions that $\Gamma_{ii}^{rs} \approx \Gamma_{ii}^{sr}$ and $\Gamma_{ii}^{rr} \approx \Gamma_{ii}^{ss}$ in Equation B.2, $(\Gamma_{ii}^{rs})^2/(\Gamma_{ii}^{rr})^2 < 1$ is obtained and the proof is complete. ■

Proposition 9: For any $i, j \in \mathcal{I}$ and $r, s \in \Phi$, with $i \neq j$, $\Gamma_{ij}^{rs} \leq \Gamma_{ij}^{rr}$ is valid.

Proof: First, expand the r-th row of Equation 6.2 as:

$$Q_i^r = -B_{ii} \cdot (V_i^r)^2 + V_i^r \cdot \sum_{\substack{k \neq i \\ m \neq r}} [G_{ik}^{rm}\cos(\theta_{ik}^r) - B_{ik}^{rm}\sin(\theta_{ik}^r)]V_k^m \tag{B.3}$$

where the summations in k and m extend over all nodes and phases different from i and r, respectively. For conciseness, the summation coefficient of V_{km} in Equation B.3 is henceforth denoted as C_{km}. Accordingly, the coefficient of $(V_i^r)^2$ is C_{ir}.

Consider computing the partial derivatives of Equation B.3 with respect to Q_i^r and Q_i^s. The obtained expressions are as follows:

$$\left(2C_{ir}V_i^r + \sum_{\substack{k \neq i \\ m \neq r}} C_{km}V_k^m\right)\frac{\partial V_i^r}{\partial Q_i^r} + V_i^r \cdot \sum_{\substack{k \neq i \\ m \neq r}} C_{km}\frac{\partial V_k^m}{\partial Q_i^r} = 1 \tag{B.4}$$

$$\left(2C_{ir}V_i^r + \sum_{\substack{k\neq i\\ m\neq r}} C_{km}V_k^m\right)\frac{\partial V_i^r}{\partial Q_i^s} + V_i^r \cdot \sum_{\substack{k\neq i\\ m\neq r}} C_{km}\frac{\partial V_k^m}{\partial Q_i^s} = 0 \tag{B.5}$$

Substracting Equation B.5 from Equation B.4 and realizing from Equation 6.15 that $\partial_{Q_i^r} V_k^m = \Gamma_{ki}^{mr}/2V_k^m$ and analogously for the other partial derivatives, the following is obtained:

$$\Gamma_{ii}^{rr} - \Gamma_{ii}^{rs} = \frac{1 - V_i^r \cdot \sum\limits_{k\neq i, m\neq r} \frac{C_{km}}{2V_k^m}(\Gamma_{ki}^{mr} - \Gamma_{ki}^{ms})}{C_{ir} + \frac{1}{2V_i^r} \cdot \sum\limits_{k\neq i, m\neq r} C_{km}V_k^m} \tag{B.6}$$

Now, consider the signs of coefficients C_{ir} and C_{km}. No loss of generality occurs by adopting the power system approximations $\cos(\theta_{ik}^r) \approx 1$ and $\sin(\theta_{ik}^r) \approx 0$, since no precision in the coefficient values is required and only their signs are being analyzed. Proceeding as such and recalling from power system admittance matrix properties that $B_{ii}^{rr} < 0$ and $B_{ik}^{rm} < 0$, it is seen that $C_{ir} > 0$ and $C_{km} > 0$.

From **Lemma 2**, the right-handside of Equation B.6 must be greater than or equal to zero. Since $C_{ii} > 0$ and $C_{km} > 0$, the denominator can be disregarded and thus:

$$1 + V_i^r \cdot \sum_{\substack{k\neq i\\ m\neq r}} \frac{C_{km}}{2V_k^m}(\Gamma_{ki}^{ms} - \Gamma_{ki}^{mr}) \geq 0 \tag{B.7}$$

Recall that voltage sensitivities in Equation B.7 are functions of time n, since they are components of the power system Jacobian inverse. In this derivation, no assumptions can be made with respect to $\Gamma_{ki}^{mr}[n]$ and $\Gamma_{ki}^{ms}[n]$, for which reason they must be considered *arbitrary* time functions. Taking this into account and recalling that $C_{km} > 0$, the requirement for Equation B.7 to be valid $\forall n$ is, approximately (since $V_i^r C_{km}/2V_k^m$ is large), that $\Gamma_{ki}^{ms}[n] \geq \Gamma_{ki}^{mr}[n]$. Finally, setting $m = s$ and $k = j$ in this relation and generalizing to all nodes and phase pairs, the proof is complete. ■